# Synthesis and Processing of Nanocrystalline YAG (Yttrium Aluminium Garnet) Ceramics

**by**

**Prabhu Ramanujam**

**A Doctoral Thesis submitted in partial fulfilment of the requirements for the award of Doctor of Philosophy of Loughborough University**

**September 2014**

**Supervisors: Prof. Bala Vaidhyanathan & Prof. Jon Binner**

*To*

*My lovable wife*

*&*

*My lovable Mom and Dad*

## Acknowledgements

I would like to express my deep and sincere gratitude to my supervisors Professor Bala Vaidhyanathan and Professor Jon Binner, who have supported me throughout my PhD with patience and expertise whilst allowing me the room to work in my own independent way. I thank them not only for giving me this excellent opportunity, but also for their encouragement and guidance from the initial to this level that enabled me to develop an understanding of the subject.

I would also like to thank my sponsors Morgan Advanced Materials, Swansea, UK, in particular Dr Chris Spacie, Dr Mike Murray and Dr Roger Bayliss for their financial and technical support. I would also like to thank Loughborough University for the studentship.

I would like to acknowledge the help from Professor Mike Reece and Dr Salvatore Grasso for conducting SPS experiments at Queen Mary University of London, UK and Professor Yanqiu Zhu and Dr Hong Chang at University of Exeter, UK for conducting hot pressing experiments in this project.

I am indebted to all the staff at LMCC, especially Dr Keith Yendall and Dr Zhaoxia Zhou for their co-operation concerning X-ray diffraction and electron microscopy. I am thankful to all the staff and students from the Department of Materials for their help and support. Special thanks to Mr. Andrew Lau and my project students. I am very grateful to all the members of the Advanced Ceramic Research Group for helping me at various stages of my experiments and their moral support during my PhD. I would also appreciate my friends and my siblings for their big support.

# Journal papers and conferences

1. **'A comparative study of the synthesis of nanocrystalline Yttrium aluminium garnet using sol-gel and co-precipitation methods',** *Ramanujam P, Vaidhyanathan B, Binner JGP, Anshuman A and Spacie C,* Ceramic International, Volume 40, Issue 3, April 2014, Pages 4179–4186
2. **Preparation of high solids loading nYAG suspensions for transparent YAG ceramics**", *Ramanujam P, Bala Vaidhyanathan and Jon Binner,* 13th International Conference of the European ceramic society, Limoges, France, June 23-27, 2013
3. "**Synthesis and processing of nanostructured YAG ceramics**", *Ramanujam P, Bala Vaidhyanathan and Jon Binner,* International Conference and Exposition on Advanced Ceramics and Composites (38th ICACC), The American ceramic society, Florida, USA January 26 - 31, 2014
4. **'Mechanism and particle growth kinetics of nanocrystalline YAG using solvothermal method'** *Ramanujam P, Ghanizadeh S, Vaidhyanathan B, Binner JGP, and Spacie C, (expecting to submit in Nov 2014).*
5. **'Preparation of colloidal YAG suspensions for spray freeze drying'** *Ramanujam P, Ghanizadeh S, Vaidhyanathan B, Binner JGP, Stone M, and Spacie C, (expecting to submit in Dec 2014).*

## Abstract

Transparent ceramics are used in a variety of applications such as protective visors, thermo-graphic lens, night vision devices and windowpane of an armed vehicle, missile domes and in aircrafts. Yttrium Aluminium Garnet (YAG, $Y_3Al_5O_{12}$) exhibits uniform index of refraction without birefringence owing to its cubic crystal structure and offers a range of optical and mechanical properties that makes it suitable for transparent applications.

Processing of nanostructured YAG ceramics has not been studied in significant detail, the aim of this project is to investigate the various stages involved during the manufacturing of nano YAG (nYAG) ceramics viz., synthesis, green forming and sintering with a holistic view to assess its potential for engineering application.

The existing commercial nano and sub-micron YAG powders were identified to be heavily agglomerated, they were not found to be suitable for fabricating transparent and fine grained YAG ceramics. In the present work, soft chemical routes such as sol-gel, co-precipitation and solvothermal methods have been investigated for developing a suitable synthesis route for the preparation of nYAG powder with minimal agglomeration. Two different sources for $Al^{3+}$ ions, $Al(NO_3)_3.9H_2O$ and Al metal powder, were used in the sol-gel process. Single phase YAG was obtained regardless of the precursors, though when Al metal powder was used, the conversion yield was increased by two fold. However, the nYAG powders obtained from sol-gel process resulted in severe agglomeration due to the high temperature calcination procedures needed for complete YAG phase conversion. Further, a reverse strike co-precipitation method was investigated to reduce agglomeration. It was observed that by controlling the pH and maintaining the processing temperature in a narrow range, the precipitates of Yttrium and Aluminium ions resulted in a core/shell structure. However the crystalline nYAG powder showed severe agglomeration due to drying and calcination of the precursors. Therefore a supercritical fluid (SCF) method was employed, which involves the use of both temperature and pressure in tandem to crystallise nYAG particles in a liquid medium and these particles were kept suspended to avoid agglomeration. 1, 4 Butanediol was found successful amongst the various solvents used to crystallise the precursors into single phase YAG. When organic precursors of Y and Al were used,

the YAG particles obtained were found to be spherical with ~25 nm diameter and the BET (Brunauer-Emmett-Teller) results suggested that the extent of agglomeration is very low compared to the other powders synthesised in this project. The resultant powders from different methods were examined using X-ray diffraction, Transmission electron microscope, Scanning transmission electron microscope, Gas chromatography- Mass spectrometer, Fourier transform-infrared spectroscopy and the results compared and contrasted. The mechanism for the formation of nanocrystalline YAG was developed with corroborative analytical evidence.

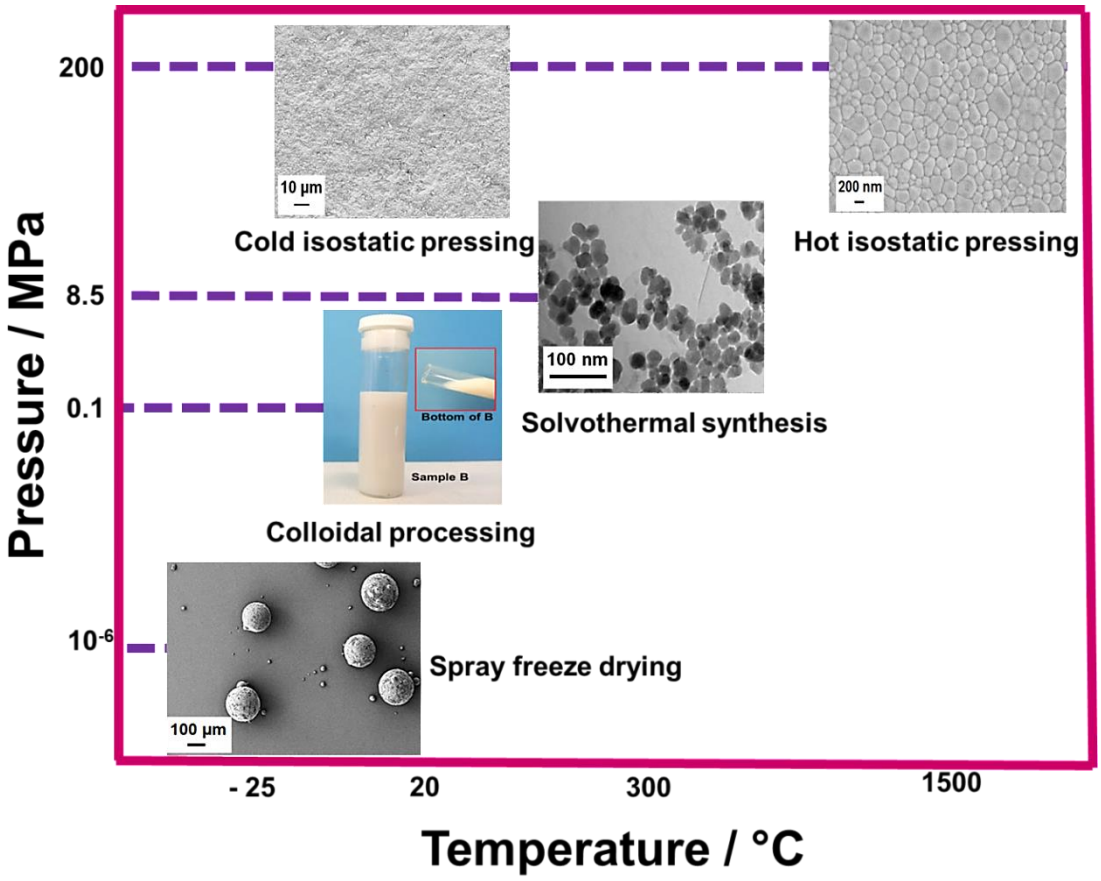


*Figure 1 Processing of YAG ceramics using pressure and temperature in tandem at different stages*

Figure 1 shows different stages of YAG processing in this project, which involves temperature and pressure in combination and the results are discussed below. The as-synthesised nYAG powder from solvothermal method was re-dispersed with ammonium polyacrylate, $NH_4PAA$, to produce colloidal nYAG suspension. The rheological behaviour and the electro-kinetic aspects of the nYAG suspensions were characterised to optimise the viscosity, desired solids content and suitable pH to

achieve maximum suspension stability. The 55 wt.% nYAG suspension was further spray-freeze dried (SFD) to produce soft and crushable granules and green compacts were made by uniaxial pressing at 75 MPa and followed by isopressing at 200 MPa. The defect free green bodies were pre-sintered to 95-99% theoretical density and further hot isostatically processed between 1500-1700°C. Nano YAG powders from different routes were also used for spark plasma sintering and hot pressing to compare the effect of various sintering methods on YAG ceramics production. The sintered samples were polished and thermally etched for microstructure analysis. Preliminary optical properties were measured using UV-Visible spectrophotometry and FT-IR to gain insights on the transmittance characteristics of the sintered samples over a wide spectral band.

Thus, in this project effective use of pressure and temperature in tandem to reduce synthesis and sintering temperature of YAG powders and ceramics was realised. More than 700°C reduction in synthesis temperature and 250°C reduction in sintering temperature were achieved that resulted in less agglomerated, more sinter-active nanocrystalline YAG powder and a fine grained fully dense YAG ceramics, respectively.

# TABLE OF CONTENTS

## LIST OF FIGURES

# LIST OF TABLES

## Glossary

**µm** – micrometer

**AIP** – American Isostatic presses, Inc

**BET** – Brunauer-Emmett-Teller

**BT-YAG** – Butanol derived Yttrium Aluminium Garnet

**C=O** – Carbonyl group

**CIP** – Cold isostatic pressing

**CP-nYAG** – Solvothermal nanocrystalline Yttrium Aluminium Garnet

**DSC** – Differential scanning calorimetry

**EDX** – Energy dispersive x-ray analysis

**ET-YAG** - Ethanol derived Yttrium Aluminium Garnet

**FAST** – Field assisted sintering techniques

**FEGSEM** – Field emission gun scanning electron microscope

**FEG-STEM** - Field emission gun Transmission electron microscope

**FT-IR** – Fourier Transform – Infra red

**GC-MS** – Gas chromatography – Mass spectroscopy

**GPa** – Giga Pascal

**HIP** – Hot isostatic pressing

**HP** – Hot pressing

**IEP** – Isoelectric point

**M** – Molarity

**m** - moles

**MPa** – Mega Pascal

**η** – Viscosity

**Nd:YAG** – Neodymium doped Yttrium aluminium garnet

**$NH_4$PAA** – Ammonium poly acrylate

**OD-YAG** – Oven dried Yttrium Aluminium Garnet powders

**pH** – potential of Hydrogen

**PoP** – Plaster of Paris

**PSD** – Particle size distribution

**SAED** – Selected Area Electron Diffraction

**SCF** – Supercritical fluids

**SFD** – Spray freeze drying

**SFD-YAG** - Spray freeze drying - Yttrium Aluminium Garnet granules

**SG-nYAG** – Sol-gel nanocrystalline Yttrium Aluminium Garnet

**SPS** – Spark Plasma Sintering

**ST-nYAG** – Solvothermal nanocrystalline Yttrium Aluminium Garnet

**ST-YAG** – Solvothermal nanocrystalline Yttrium Aluminium Garnet (nitrate route)

**SG-YAG** - Sol-gel Yttrium Aluminium Garnet (metal precursor derived)

**TEM** – Transmission electron microscope

**TGA** – Thermo gravimetric analysis

**XRD** – X- ray diffraction

**YAG** - Yttrium Aluminium Garnet

**YAH** - Yttrium Aluminium Hexagonal

**YAM** - Yttrium Aluminium Monoclinic

**YAP** - Yttrium Aluminium Perovskite

$\gamma_s$ - rocking vibration

**δ** - in-plane bending vibration

**ζ** – Zeta potential

**v** – Vibrations

$v_{as}$ - Asymmetric vibrations

$v_s$ – Symmetric vibrations

# 1 Introduction

Amongst advanced ceramics, transparent materials are finding interesting applications based on both structural and functional properties. Transparent ceramics such as ZnSe, Lead Lanthanum Zirconate Titanate (PLZT), $MgF_2$ and diamond are used as the components of electro-optics and semiconductor devices for functional applications [1]. Materials choice for structural applications include alumina ($Al_2O_3$), yttria ($Y_2O_3$), magnesium aluminate spinel ($MgAl_2O_4$) and aluminium oxynitride (AlON), which are widely used as IR domes and windows for infrared applications, face shields and protective armour for vehicles and people [2-4]. Each material is superior to the others in one particular property, but none exhibit all the properties desired [5, 6] .

The primary requirements of a material for the structural applications are optical transparency, high toughness and hardness [7]. These properties are interdependent on both the density and grain size of the polycrystalline ceramics. Due to the differences in the refractive index between the grains, the grain size must be very large or very fine to provide transparency by reducing the scattering of the incident light [8, 9] . Many transparent ceramics exhibit grain sizes ranging between 10 - 15 µm since the starting powders are in the submicron range and require high temperature sintering to achieve full density. Such large grain sizes, however, can limit the mechanical strength [10]. Moreover, multi-cation materials such as $MgAl_2O_4$ and AlON are conventionally processed using mixed oxide routes, which can result in chemical inhomogeneity and make them unsuitable for other transparent applications [11]. Fine nanocrystalline particles, with a significant level of homogeneity, have the potential to lead to fine microstructured ceramics that are both transparent and strong [8].

Over the last two decades, significant research has focused on producing nanostructured materials and a range of nanocrystalline powders of different compositions have been synthesised using methods such as sol-gel, co-precipitation, hydrothermal and combustion routes [12-15]. These bottom-up approaches have, in some cases, been used to tailor the particle characteristics to make them more suitable for different applications [16]. In addition, the nanoparticles have been processed into nanostructured ceramics components using different

processing methods, such as two step sintering, spark plasma sintering, hot pressing and hot isotactic pressing [17-20]. It has been demonstrated that nanostructured ceramics can offer improved performance for the components as diverse as bio-implants, automobiles and electronic devices [21]. In particular, the mechanical properties of the components were found to be enhanced due to the decrease in the grain size of the ceramics [22, 23].

In this present work, nanocrystalline yttrium aluminium garnet (YAG) have been investigated as an alternative material for structural applications such as riot visors and ballistic protection, window materials for armed and other security vehicles. The main goal was to synthesise YAG nanoparticles and investigate the processing methods suitable for the production of fine grained YAG ceramics.

Yttrium aluminium garnet is an excellent structural and functional material that is used in many applications [24]. Single crystal YAG is a known laser host material owing to its excellent optical properties; however, due to the recent greatly enhanced availability of high purity powders and advanced processing technologies, the use of single crystal YAG is being replaced by polycrystalline YAG, which typically contains up to 4 atomic percentage of dopant to achieve transparency. Since YAG has cubic symmetry, it does not exhibit birefringence at the grain boundaries. This results in a high in-line transmittance of about 84%, which makes polycrystalline YAG ceramics desirable for laser applications, IR domes, lenses and focused-beam applications such as automotive headlamps and photo-optic lamps [25, 26]. YAG also exhibits isotropic thermal expansion [27], meaning that there are no residual stresses at the grain boundaries in YAG ceramics and it also has a high elastic modulus [28]; this leads to YAG being a high creep resistance material at high temperatures [29]. Thus, the high mechanical strength and optical transmittance of YAG makes it a potential candidate for the applications where high transparency and mechanical performance are required.

## 1.1 Aim and objectives of the project

The main goal of the research was to synthesis high quality nanocrystalline yttrium aluminium garnet powders with minimal agglomeration and to process them into nanostructured ceramics for applications where the transparency and mechanical

performance are needed. In addition, a focus was towards reducing sintering temperatures for the production of YAG ceramics that could lead to energy and time savings. As a first step, a suitable method to produce nanocrystalline YAG powders was investigated using different methods such as sol-gel, co-precipitation and solvothermal routes. A comparison based on the resulting powder characteristics led to the advantages and disadvantages of these routes being identified. The best powder was subsequently processed via a colloidal route and a 55 wt.% suspension was used to produce soft, crushable granules using a spray freeze drying (SFD) method. Hot pressing, spark plasma sintering (SPS) and hot isostatic pressing were investigated as possible routes to fabricate transparent YAG ceramics. Further investigation of the optical properties of the sintered YAG ceramics ensued.

# 2 Literature review

## 2.1 Advanced ceramics

Advanced ceramics are finding potential applications ranging from aerospace components to bio-ceramic implants [30]. They can offer enhancements in performance, durability and reliability when compared to more traditional materials as a result of improved mechanical, physical, chemical, electrical and thermal properties [31], Figure 2.


*Figure 2 A range of applications of advanced ceramics, a) ultra-high temperature ceramics [32] , b) corrosion resistant ceramic elbows [33] , c) ceramic armour [34] , d) ceramic disc brakes [35] , e) ball bearings [36] , f) cutting tools [37] , g) photovoltaic cells [38] , h) fuel cells [39] , and i) hip joints [40] .*

With the help of advanced characterisation techniques, the understanding of ceramic powders has been improved and particle characteristics such as shape, size, agglomeration, purity and homogeneity are considered to be the primary factors that influence the properties of the end component. Therefore, quality has to be maintained throughout the ceramic production process, from synthesis, through green processing and to the final sintering stages.

In this chapter, an insight into transparent materials and their applications is provided together with a review of the different routes to synthesising YAG nanoparticles and the processing of transparent YAG ceramics.

### 2.1.1 Transparent ceramics

Most of the ceramics are intrinsically transparent since the band gap is above 2 eV, see Figure 3, otherwise all the incident light will be absorbed by electron transitions from the valance band to conduction band [41].

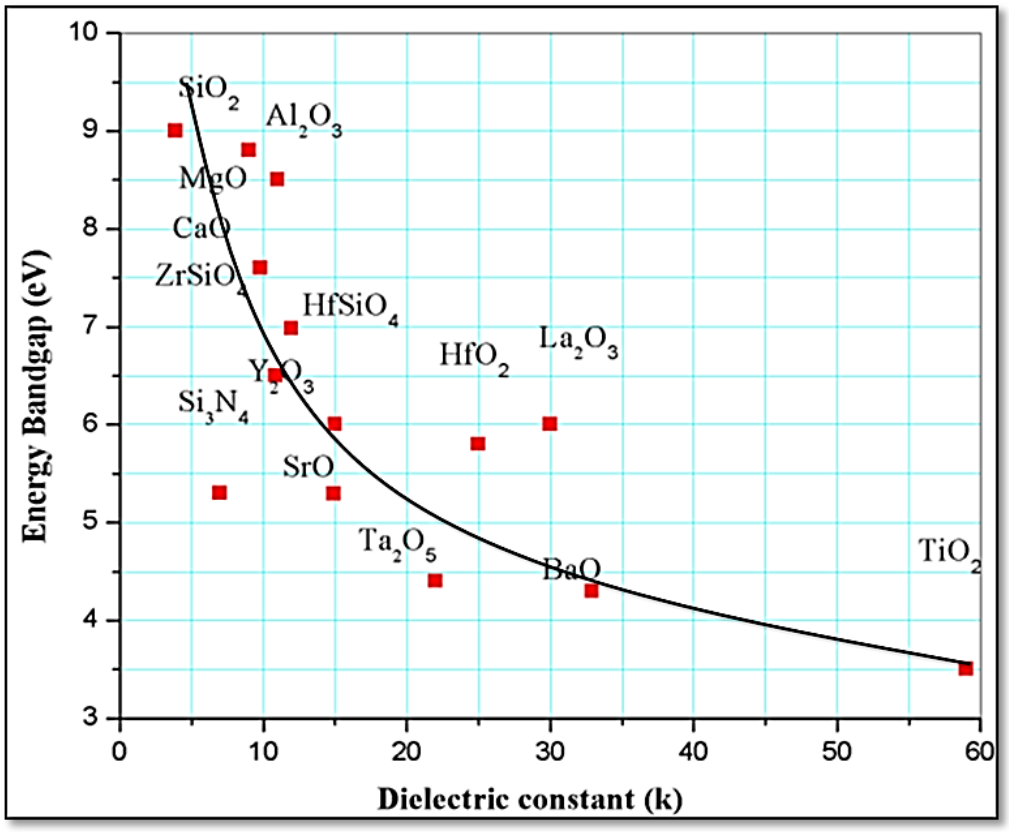


*Figure 3 Band gap of different ceramic materials [42]*

However, ceramics appear opaque because they are optically heterogeneous due to the presence of pores and grain boundaries, which scatters the light. Thus, polycrystalline ceramics that have been fabricated to reduce optical scattering and energy absorption will exhibit transparency. When a radiant flux, a measure of the total power of electromagnetic radiation, is incident upon a medium, three processes occur, transmission, absorption and reflection [43]. The latter depends on the refractive index of the material and the angle of incidence of the light [44]. The reflection losses at the surface can be minimised in two ways, either by choosing a material with low refractive index or by avoiding surface roughness [45, 46]. The other two processes, absorption and transmittance, depend on the wavelength of the incident light and the defects present in the sample [47].

Crystal structure, powder purity, powder uniformity and microstructural defects such as grain size, porosity and surface roughness are the major factors influencing transparency of ceramics [26]. Some materials exhibit different colours, which is due to the selective absorption of the photons to the corresponding wavelength of the visible light [48, 49]. Therefore, care must be taken whilst selecting the suitable dopant for a desired application. Thus, it is vital to minimise the microstructural defects and avoid impurities to obtain transparent ceramics.

Chemically synthesized nanomaterials are increasingly being investigated for their potential to fabricate transparent ceramics. However, a controlled and industrially feasible green processing route is required to produce green bodies with homogeneous nanostructures and high green density. Green forming routes such as cold pressing, cold isostatic pressing (CIP), extruding and slip casting can yield bodies of ~60% of theoretical density when conventional submicron powders are used [50] but considerable work is needed to yield routes that work for nano powders. The same is true for densification routes [51]. Whilst routes such as hot pressing, hot isostatic pressing (HIP), microwave sintering and spark plasma sintering (SPS) have all been used for making transparent ceramics, it is not an easy task especially when the powders are extremely fine. It is therefore important to understand the microstructural features that can influence the transparency of a ceramic and avoid generating them during the fabrication process.

### 2.1.2 Microstructural features that can influence transparency in ceramic materials

Although, as explained earlier, ceramic materials are intrinsically transparent, the degree of transparency exhibited is affected by a range of microstructural features. The two main factors are [52] :

1. Diffused scattering, arising from the presence of grain boundaries, porosity and defects

2. Birefringence, arising from a non-cubic crystal structure

The former is independent of crystal structure and takes place at the sites of secondary phases such as rough surfaces, pores, additives and impurities with different refractive indices, Figure 4. Surface roughness often scatters the incident light and reduces the inline transmittance of the light, whilst pores act as scattering centers and diffuse the incident light. Grain boundaries allied to grain size, also play a vital role in optical transmittance in ceramics. Grain boundaries can reflect the incident light due to the difference in the refractive indices of the adjacent grains, since grains are usually oriented randomly, leading to optical anisotropy. This grain boundary factor can be eliminated by two ways. One is by adopting cubic structured materials, which are optically isotropic and hence do not exhibit birefringence, see later, whilst the other method is by altering the grain size, either making it very large and hence reducing the fraction of grain boundaries, or by keeping it less than the wavelength of visible light, which avoids the scattering effect [46].

For instance, non-cubic $Al_2O_3$, Figure 5a, can exhibit a low in-line transmission coefficient due to its non-isometric structure and exhibit birefringence effect. The main issue with the birefringence effect is the thickness. Alumina samples with different thickness are shown in Figure 5a, which are of produced using identical conditions, but lack in transparency. This is a main disadvantage for making large components for structural applications. In the case of cubic structured materials like $MgAl_2O_4$, Figure 5b, and YAG, birefringence is absent, and there is no effect of thickness, only the diffuse scattering takes place; this can be eliminated by controlling the grain size and porosity.

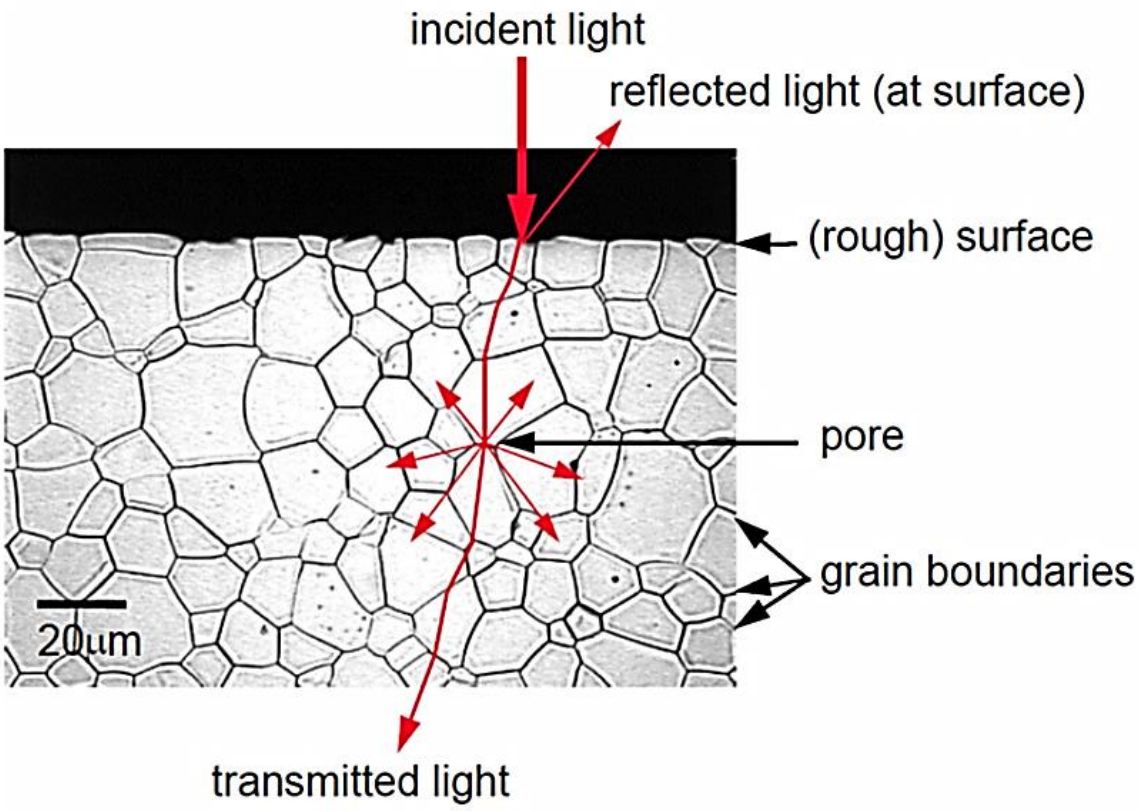


*Figure 4 Light transmissions through a non-cubic ceramic material [52]*

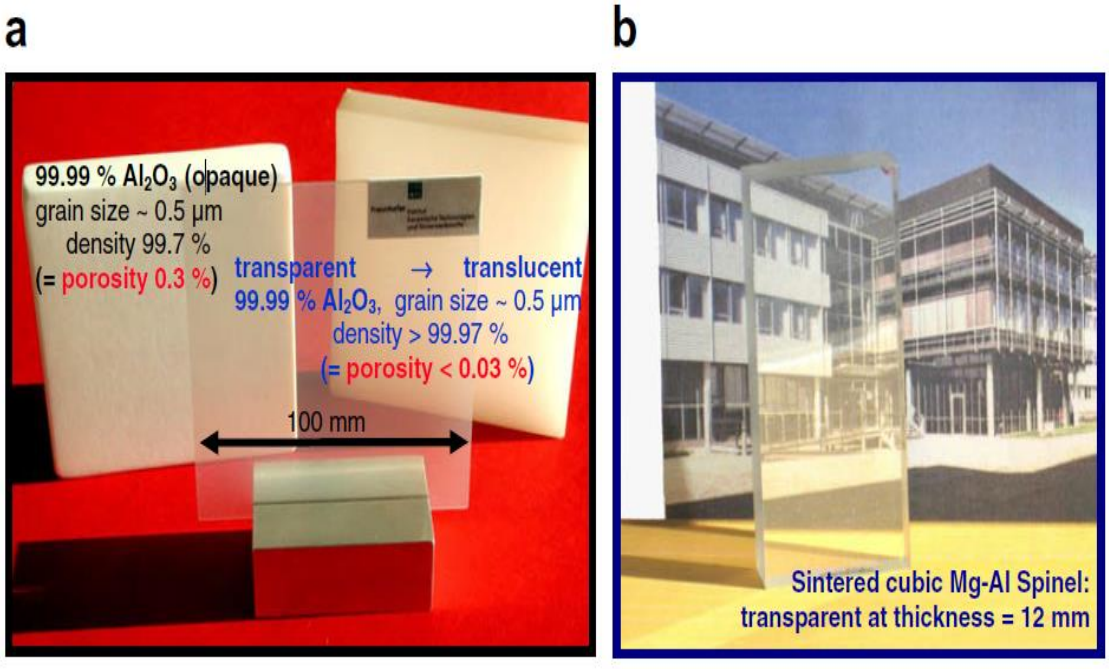


.

*Figure 5 Transparent ceramics (a) alumina ($Al_2O_3$) (b) spinel ($MgAl_2O_4$) [46]*

Generally, the poor optical transmittance of $Al_2O_3$, $CeO_2$ and other non-cubic ceramics generally makes them unsuitable for applications such as displays, light sources and radar windows. On the other hand, cubic $MgAl_2O_4$, which is transparent, appears light brown after irradiation by X-ray or gamma rays [53], due to the excitation of some electrons into the conduction band, leaving voids in the valance band, which act as colour centers. This coloration of the spinal reduces its optical transparency and it has been reported that $MgAl_2O_4$ exhibits an inherent birefringence (IBR) at short UV wavelengths about 200 nm [54], despite it having a cubic structure. This clearly shows that both cubic and non-cubic ceramic materials can have limitations.

Yttrium aluminium garnet (YAG) is an alternative material, which has a cubic structure and is already used in applications involving radiation such as solid-state lasers, UV, and X-ray detectors and fluorescent displays [55]. Whilst it can be produced in single crystal form, it is more often polycrystalline, but with a large grain size. This limits its mechanical performance, however [10, 23, 28].

### 2.1.3 Application of Transparent Ceramics

Amongst advanced ceramic materials, the interest in transparent ceramics is increasing due to the range of application; some of these are listed in Table 1 and shown in Figure 6.

Single crystal Nd:YAG possess a high radiation resistance, which is often used in high power laser applications such as remote sensing, laser particle acceleration, gravitational wave interferometers and also in medical treatments [56]. However, the processing of single crystal Nd:YAG has many disadvantages, such as processing time, high cost and size; this limits the use of single crystals in many circumstances. The polycrystalline version offers several key advantages over single crystals, including the possibility of increasing the neodymium doping concentration to >4 atomic % compared to melt grown material, which makes it possible to miniaturise the laser host [57].

The combination of suitable dopants and fine microstructures has allowed the optical performance to be equivalent to single crystals [58]. This has allowed the polycrystalline ceramics to replace single crystals by offering similar physical, chemical and thermal properties but at lower cost. Ceramics with high in-line

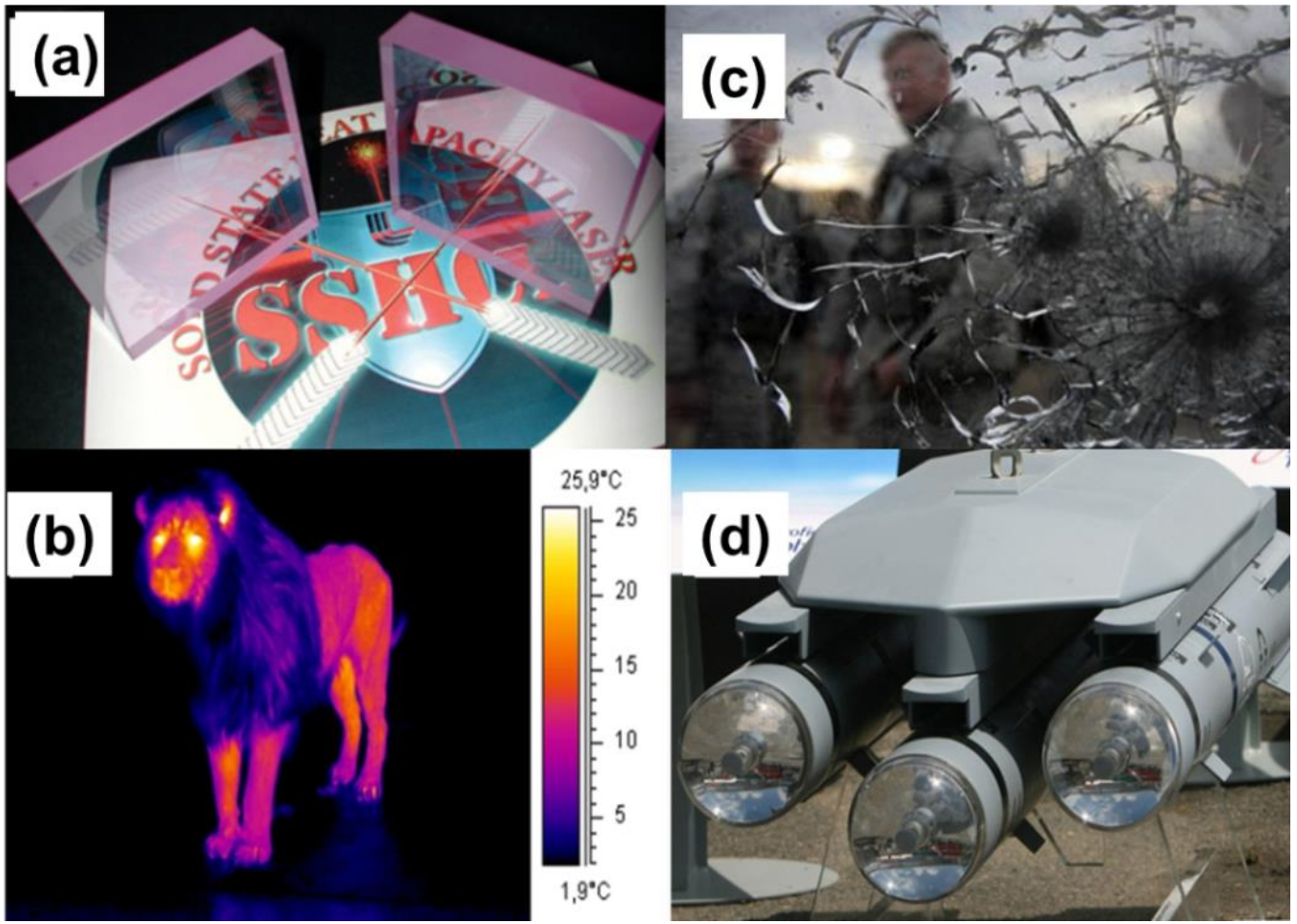


*Figure 6 Applications of transparent ceramics, (a) laser host materials [59] , (b) thermographic lenses [60] , (c) transparent armour [61] and (d) missile domes [62]*

transmittance combined with high mechanical properties such as hardness, strength and toughness can be used in structural applications such as riot visors, radomes, IR domes, sensor protection, multispectral windows [63] and windows for armed vehicles and high protection cars [5].

*Table 1 Applications of different transparent ceramics by transmission wavelength*

| **Transparent Ceramics** | **Transmission wavelength** | **Functional Applications** | **Structural Applications** |
|---|---|---|---|
| Glass [64] | Visible | Lenses and prisms | Windows |
| CdTe [65], MgO [66], fused $SiO_2$ [67], Ge [68], $MgF_2$ [69], ZnS [70] and PLZT [71] | Ultra violet and infrared | Magnetic materials, LEDs, X-ray detectors & junction devices | Electro-optic windows |
| Nd:$Y_3Al_5O_{12}$ [72], YAG:Tb, YAG:$Ce^{3+}$ and YAG:$Eu^{3+}$ | Visible and near infrared | Laser host materials for lasers and phosphors screens | IR domes and radomes |
| Diamond [73] | Visible and infrared | Semiconductors | Electro-optic windows |
| Glass [63], $Al_2O_3$ [74], AlON [75], $Y_2O_3$ [76] and $MgAl_2O_4$ [77] | Visible and infrared | Lenses | Radomes, riot visors, missile domes and transparent armours |

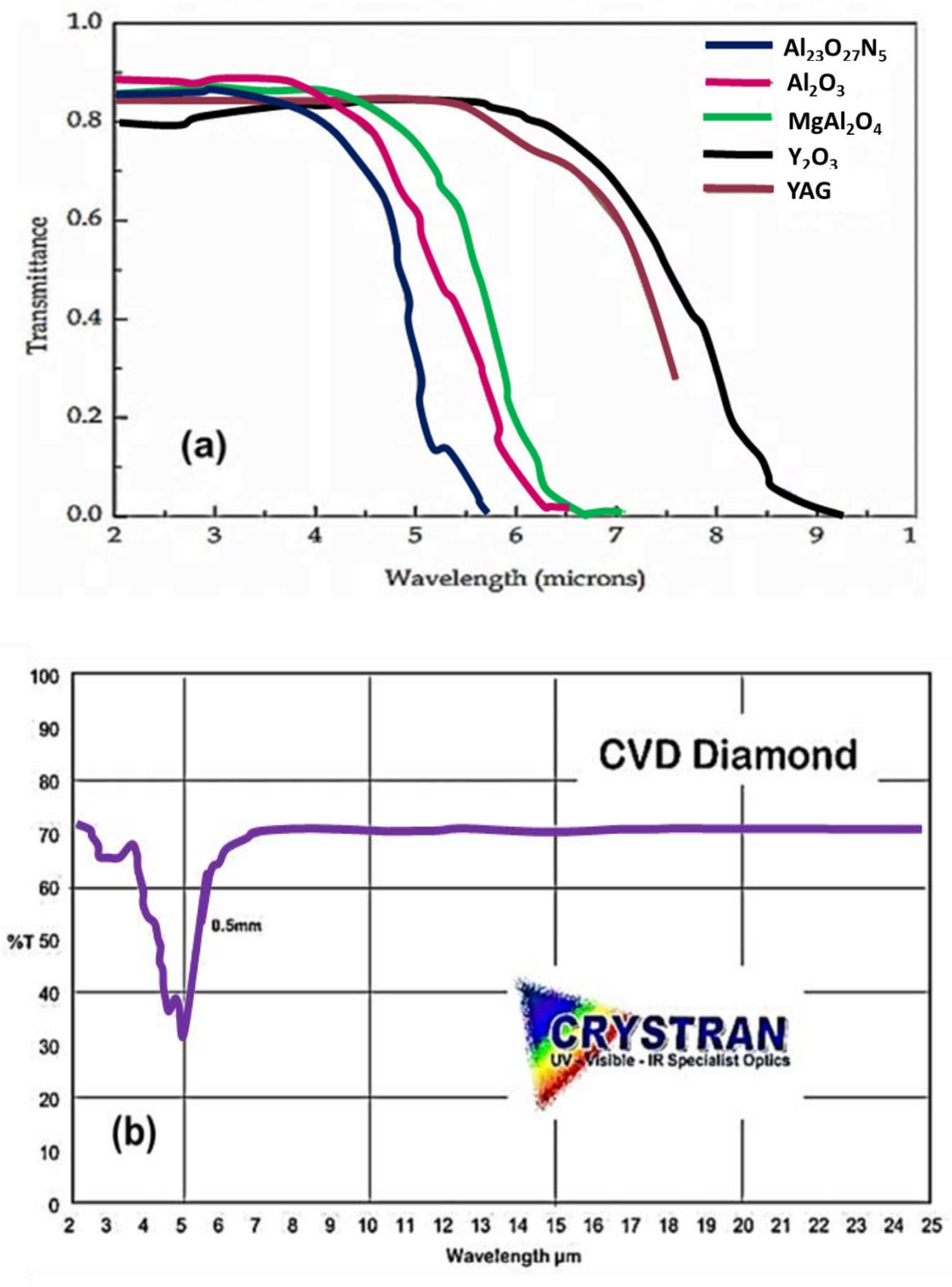


*Figure 7 IR transmittance of (a) different ceramics [26] and (b) diamond [78] .*

An excellent material for these applications is diamond, which offers a broad IR transmission range (8-14 µm) and excellent mechanical and thermal properties. However, the processing cost of diamond limits its usage. Although it is a hard

material, alumina has a very low IR transmittance range (2-4 μm), whilst yttria has a desirable IR transmittance range (2-7 μm), but lacks the required mechanical and thermal properties. ALON and spinel both offers attractive properties, but the transmittance range is less when compared to YAG, see Figure 7 [26]. Single phase yttrium aluminium garnet, YAG, offers higher transmittance than alumina and adequate mechanical and thermal properties, though these might be improved by reducing the grain size.

## 2.2 Nanostructured ceramics

Nanostructured materials are generally classified by their structural features, where at least one of their dimensions should be less than 100 nm. These structural differences can result in unusual and novel properties, for example, both nano YSZ [79] and $Si_3N_4$/SiC [80], exhibit plastic deformation at high temperatures by grain boundary sliding, known as superplasticity, it can be used to join nanostructured and large grained ceramics and also used to produce engine components via moulding at elevated temperatures [80]. In addition, bulk nanostructured ceramics can show unique optical [81], electrical [82], thermal [83], magnetic [84] and mechanical properties [85, 86]. Another potential benefit during processing nanostructured ceramics is energy savings resulting from low temperature sintering [87]. This occurs due to changes in the kinetics of the atomic processes, e.g diffusion, grain growth and plasticity during densification of the highly reactive nanoparticles [51, 88]. This must be balanced, however, by higher processing costs. The exploitation of the potential offered by nano powders is also hindered by challenges related to the effects of agglomeration and poor flow characteristics [89, 90]. In addition, with nano powders there are significant health and safety issues. These will be reviewed later in this literature survey, for now, however, the focus will be on YAG as a ceramic material.

## 2.3 Yttrium aluminium garnet (YAG)

### 2.3.1 Chemical structure of YAG

The basic elemental constituents of YAG are yttrium, aluminium and oxygen. According to the bond strength, chemical bonds are grouped into primary and secondary bonding. Primary bonds such as ionic and covalent bonding, have bond

energies in the range 100-1000 kJ $mol^{-1}$, in YAG, ionic bonding of the oppositely charged ions is produced by the transfer of electrons between $Y^{3+}$, $Al^{3+}$ and $O^{2-}$ ions [91] yielding a stable crystal structure.

### 2.3.2 Crystal structure of YAG and $Y_2O_3$-$Al_2O_3$ Phase Diagram

Garnets are usually a group of silicate minerals used as gem stones and abrasives since Bronze Age [92] . The crystal structure of garnet was first identified by Menzer (1928). Materials which belongs to the chemical formula $A_3B_2(BO_4)_3$ or $A_3B_5O_{12}$ are usually called as garnets. YAG belongs to the garnet structure, a body centered cubic structure [93].

Ceramic powder processing within the $Y_2O_3$-$Al_2O_3$ system has largely been intended for functional and structural applications. Figure 8 shows phase diagram of the $Y_2O_3$-$Al_2O_3$ system.

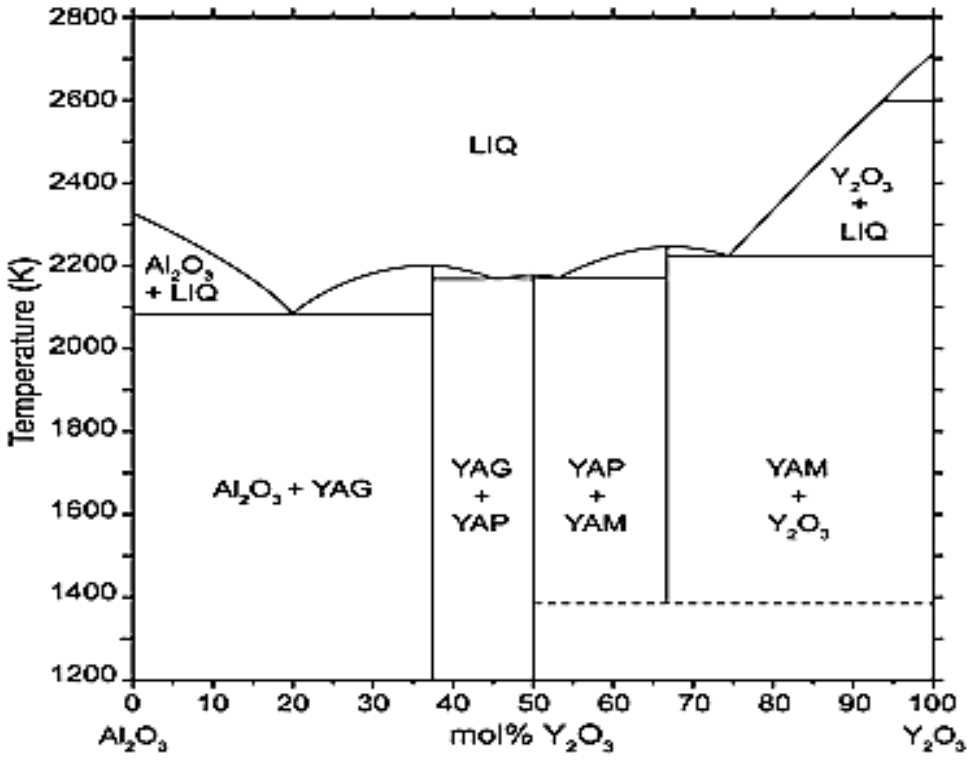


*Figure 8 Pseudo-binary phase diagram of $Y_2O_3$-$Al_2O_3$ system [94]*

The $Y_2O_3$-$Al_2O_3$ phase diagram exhibits compounds [94] of the two end members, $Y_2O_3$ is cubic and $Al_2O_3$ is hexagonal in structure. In this system, three stable yttrium aluminates exist with different polymorphs, garnet $Y_3A1_5O_{12}$ (YAG), perovskite-based

orthorhombic $YAlO_3$ (YAP) and monoclinic $Y_4Al_2O_9$ (YAM) [95]. A hexagonal $YAlO_3$ (YAH) has also been identified as an intermediate metastable phase during the processing of YAG [96]. The YAG composition is rich in $Al_2O_3$ and crystallises with cubic symmetry. It does not exhibit any birefringence effects at the grain boundaries and hence results in high in-line transparency with rare earth dopants.

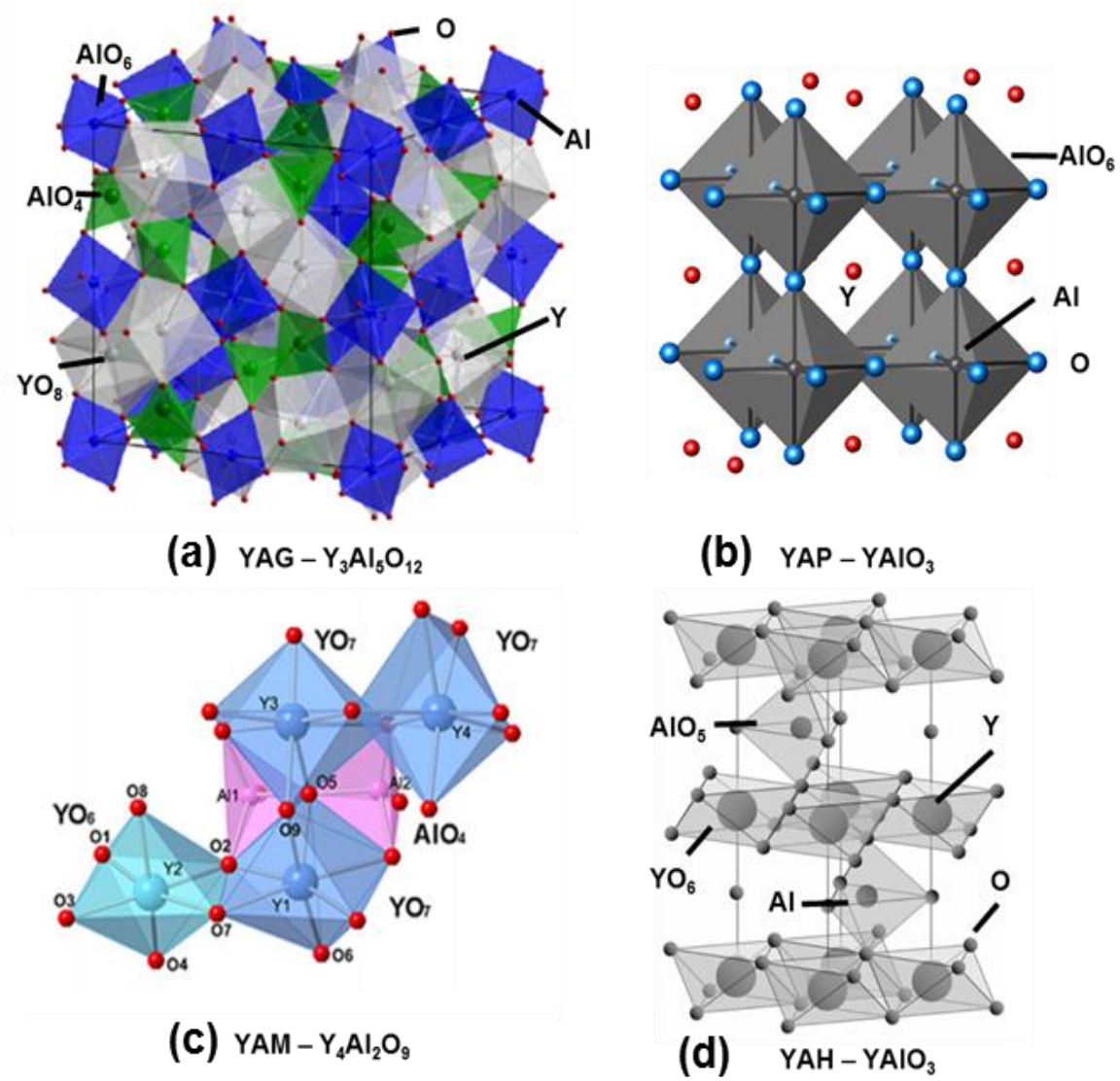


*Figure 9 Atomic structures of YAG, YAP, YAM and YAH, compiled from [97-99]*

YAG contains 37.5 mol% $Y_2O_3$ and 62.5 mol% $Al_2O_3$. It has a cubic structure, Figure 9a, with two aluminium sites ($AlO_4$ tetrahedral and $AlO_6$ octahedral), one yttrium site ($YO_8$ dodecahedron) and an oxygen site ($OY_2Al_{12}$). The unit cell of YAG contains 160 atoms, which are positioned in eight formula units [100]. Figure 9a shows the arrangement of the cationic sites, the $Y^{3+}$ ions occupy the dodecahedral positions

whilst the $Al^{3+}$ ions occupy two different positions, the octahedral and tetrahedral sites, in the lattice.

The perovskite phase, YAP, $YAlO_3$, contains 50 mol% $Y_2O_3$ is orthorhombic structure with a single aluminium site ($AlO_4$ tetrahedral), one yttrium site ($YO_8$) and two oxygen sites ($OY_2Al_{12}$ and $OY_3Al_{12}$), see Figure 9b. The third compound in the phase diagram is YAM with 66.67 mol% $Y_2O_3$, is monoclinic structure with two aluminium sites ($AlO_4$ tetrahedral) and four yttrium sites, two each in ($YO_6$ and $YO_7$) sites [97], Figure 9c. It is also reported that there is a metastable phase YAH (hexagonal), Figure 9d, with four octahedral yttrium sites ($YO_6$) co-ordinated with a five-fold trigonal polyhedron ($AlO_5$) aluminium sites encountered during processing of YAG [101]. This clearly reveals that a slight change in chemical composition would result in structural inhomogeneity of the resultant YAG powder. Therefore, atomic level mixing is required at the initial stage of the powder synthesis process.

### 2.3.3 Physical properties of YAG

Table 2 illustrates the physical properties of single crystal and polycrystalline YAG ceramics. The physical properties of single crystal YAG remain unclear. Here, the mechanical properties of polycrystalline ceramics are better than those of single crystals because the former are aggregates of randomly oriented crystalline grains [102]. When compared with $Y_2O_3$ and $Al_2O_3$, YAG is stiffer than yttria (160 GPa), but more compliant than alumina (360 GPa) [92] . Nevertheless, significant improvement in the mechanical properties is required for YAG ceramics to make it suitable for structural applications. From the literature, it is believed that fabrication of nanostructured YAG ceramics could possibly improve the physical properties further.

*Table 2 Physical properties of single crystal and polycrystalline YAG [compiled from [103, 104]*

| Properties | Single crystal YAG | Polycrystalline YAG |
|---|---|---|
| Young's modulus(E) | 279.9 GPa | 283.3 GPa |
| Bulk modulus (B) | 173.4 GPa | 178.2 GPa |
| Shear modulus (μ) | 113.8 GPa | 115.7 GPa |
| Poisson's ratio (v) | 0.230 | 0.226 |
| Hardness (Vickers) | - | 14.7 GPa |
| Fracture toughness (Vickers) | 1.48 MPa m1/2 | 1.59 MPa m1/2 |
| Flexural strength (S) | 252 MPa | 341 MPa |
| Thermal conductivity | - | 12.9 W/mK |
| Thermal expansion | - | 7.8×10-6/°C |
| Transmission range | - | 0.2 – 5 μm |
| Enthalpy of fusion | - | 420 kJ mol-1 |

## 2.4 Synthesis of high quality nanocrystalline YAG powders

The choice of powder synthesis route has a significant effect on powder characteristics such as particle size, shape, distribution and the extent of agglomeration, each of which greatly influences the microstructural homogeneity of the resulting ceramics [105]. Each factor has the potential to introduce an adverse effect on densification and microstructural development of the ceramics. The presence of particle agglomeration, for example, is a well-known source of inhomogeneity, and hence defects, in the final microstructure of the ceramic components [106].

The traditionally mixed oxide method [107] usually requires long duration and high temperature heat treatments to obtain phase-pure YAG powder, so particle size and particle size distribution cannot be readily controlled. Therefore, wet chemical processes such as combustion synthesis [108, 109], plasma spray pyrolysis [110, 111] solvothermal synthesis [112], sol-gel synthesis [113] and co-precipitation synthesis [114-116], with higher reaction rates and lower synthesis temperatures are often used for synthesising nanocrystalline YAG. These chemical processes achieve intimate mixing of reactant cations at the atomic level, which yield excellent chemical homogeneity of the final product for multi-cation ceramics.

### 2.4.1 Solid state reaction method of YAG

The $Al_2O_3$-$Y_2O_3$ system is a pseudo binary system, which is influenced by temperature, pressure and composition. In this system, yttria and alumina react to form three congruent intermediate compounds, mentioned in section 2.3.2, occurring at $Y_2O_3$:$Al_2O_3$ ratios of 3:5 (YAG), 1:1 (YAP) and 2:1 (YAM). The YAP and YAM intermediate compounds are stable only over a limited temperature range, 900 - 1400°C, however, YAG can be formed by a solid state reaction between yttria and alumina in the appropriate molar ratio at high temperatures, 1400 - 1700°C. Mixing of the ingredients can be achieved either through dry or wet routes. The density difference of the constituents is an important parameter to be considered for wet mixing, since yttria (5.1 g $cm^{-3}$) is denser than alumina (3.9 g $cm^{-3}$). Hence $Y_2O_3$ can settle faster than $Al_2O_3$, leading to a non-uniform distribution in the green body that can result in a non-stoichiometric compound [107].

Early researchers found that the reaction sequence proceeds by a series of reaction steps from equation 1, 2 and 3 [107, 117]. The reaction between alumina and yttria occurs by the ionic diffusion. The first phase to be developed during heat treatment is the yttrium-rich YAM phase; this reaction begins at 900°C. At about 1100°C, the $Al^{3+}$ ions not only continue to react with the free yttria, but also diffuse into the YAM to form the YAP phase.

$$2Y_2O_3 + Al_2O_3 \rightarrow Y_4Al_2O_9\ (YAM)\ (900 - 1100°C) \qquad Eqn\ 1$$

$$Y_4Al_2O_9 + Al_2O_3 \rightarrow 4YAlO_3\ (YAP)\ (1100 - 1250°C) \qquad Eqn\ 2$$

$$3YAlO_3 + Al_2O_3 \rightarrow Y_3Al_5O_{12}\ (YAG)\ (1400 - 1700°C) \qquad Eqn\ 3$$

Finally, the alumina reacts with YAP at ~1400°C to yield YAG. It was observed that single phase YAG is only achieved when the temperature was around 1700°C using solid state reaction.

Lei et al. [118] successfully fabricated YAG by a solid-state reaction method using high purity α-$Al_2O_3$ and $Y_2O_3$ powders as starting materials. However, the final microstructures and the property of the ceramics were not adequate to fulfil the requirements for structural and mechanical properties. In general, this route is not known for producing high quality ceramic powders in any system since homogeneity cannot be guaranteed [119].

### 2.4.2 Combustion synthesis of nanocrystalline YAG

Combustion-based techniques are classified as conventional combustion synthesis (CS), volume combustion synthesis (VCS) and solution combustion synthesis (SCS). Combustion synthesis involves an exothermic reaction that releases heat, which enhances the kinetics of the reaction; a substantial increase in temperature of the reactant stimulates the process to combust and results in a fluffy powder [109].

The starting precursors play a vital role in the synthesis of YAG because the combustion reaction mechanism is relatively complex. The reaction kinetics are altered by the type of oxidizer and fuel, fuel to oxidizer ratio, ignition temperature and water content of the precursor mixture.

YAG powder was synthesised using nitrate (oxidizer) solutions of yttrium and aluminium with specific fuel-molar ratios [15, 109]. The molar ratio is vital for a complete combustion of precursors, which in turn will yield contamination less YAG powders. Slight deviation in the ratios will result in partial combustion of the fuel and result in unreacted carbonaceous products. Ramanathan et al. [109] studied the effect of fuel to oxidizer ratio in the range of 0.1–0.56. When glycine was used a fuel, the glycine to nitrate ratio of 0.18 was found successful in producing single phase YAG on subsequent calcination. The combustion reaction was initiated on a hot plate at an ignition temperature of about ~500°C and an additional heat treatment to obtain single phase YAG. The XRD pattern obtained at 920°C showed YAG phase with YAP as an intermediate. At 1050°C, the precursor was completely transformed into a single phase YAG, which is a stable phase in the $Y_2O_3$-$Al_2O_3$ system. This suggests that the phase transformation followed a reaction sequence similar to the mixed oxide route and could possibly result in structural inhomogeneity. This is because the chemical potential energy released from the exothermic reaction between the metal nitrates and fuel can rapidly heat the system locally to high temperatures, ~1600°C, without an external heat source [120]. On the other hand, the particle morphology obtained using this route showed a significant level of agglomeration. This had reflected in their microstructure of the sintered samples at 1600°C showing a large grain size of about 3-5 μm.

In summary to the combustion synthesis, the powders have higher surface areas than the powders prepared by conventional solid-state methods. However, the intense local heating can also result in particle agglomeration and chemical inhomogeneity of the final products. Moreover, this method is not a safe approach and for bulk production the evolution of gas will be very intense and has a high risk in combusting explosive reactants such as ammonium nitrate.

### 2.4.3 Sol-gel synthesis of nanocrystalline YAG

The last two methods are unlikely to produce agglomeration free single phase YAG particles. Furthermore, the combustion synthesis is not a safe approach since the precursors such as glycine and ammonium nitrate are explosive precursors. Therefore, sol-gel method has been considered as an alternative route to produce YAG powders in a safe mode with lesser extent of agglomeration compared to the aforementioned methods. The term sol-gel is generally used to refer colloids and macromolecular systems [121], where the molecular interactions are governed by short range forces such as surface charge and van der Waals attraction. Thus the gravitational forces are negligible and the particles can be easily suspended in the colloidal medium called a sol. The sol-gel process is the conversion of the sol to a gel by subsequent drying and calcination. Gelation is obtained by adding a complexing agent to a solution of inorganic metal salts. This method facilitates the molecular level mixing of the chemicals, hence high chemical homogeneity.

The citrate-gel method of synthesizing YAG [122] has an advantage of controlling the stoichiometry, as the chelating agent (citric acid) reacts with all the metal ions in the solution. Moreover, chelating agent separates a metallic ion from a salt solution and the insoluble compound can be removed by washing it away with water. The chelating agent or ligand must have at least two functional groups (COOH in citric acid) called bi-dentate, which is capable of bonding with the metal atom. In this bond, the ligand is an electron-pair donor and the metal is an electron-pair acceptor. This is known as co-ordination bonding. The functional groups can be either acidic or basic. Citric acid is a weak acid, which loses its protons and coordinates with metal atoms.

Metal inorganic precursors such as yttrium nitrate hexahydrate and aluminium nitrate nonahydrate are mixed in a solvent with an organic poly functional acid group, such as citric acid [123-125]. The sol from the dissolved cationic mixture ensures the atomic scale mixing and is partially hydrolyzed to form a cross-linked polymer chain. This polymerization reaction forms three-dimensional network structures and helps to avoid segregation. The obtained gel is dehydrated at low temperature and subsequently pyrolysed into a crystalline YAG powder. By using this Y–Al mixed citrate precursor, the crystallization of YAG is initiated at temperatures as low as 600°C in the air and single phase YAG is synthesized at 800°C for 1 h [126].

Nevertheless, the particle characteristics were not discussed and no evidence of particle morphology was given.

Recently, Yang et al. [12] optimised the solvent concentration and calcination conditions to achieve nano YAG with soft agglomerates using a sol-gel method. This work confirmed that the molar concentration ratio of citrate to nitrate ratio (n=citric acid/Yttrium and aluminium nitrate) has a significant effect on particle size. They varied the ratio from 0 – 10 and investigated the extent of agglomeration. When the ratio was 3, the YAG particles were soft and fluffy. The XRD obtained using this process resulted in single phase YAG at 900°C, regardless of the concentration they used in their process. This research proved that the concentration ratio does not influence the degree of crystallinity of the precursor, but the TEM image clearly showed the particles were necked after calcination.

From sol-gel synthesis, the use of nitrate precursors and citric acid showed promising results on the degree of crystallinity, since the atomic level of mixing solves the issues associated with the chemical homogeneity in the mixed oxides route and combustion synthesis. However, particle agglomeration is the major issue in the final powders being synthesised using the sol-gel method. Therefore, significant investigation is still required with a view to produce agglomeration free YAG particles by sol-gel approach.

### 2.4.4 Co-precipitation technique of nanocrystalline YAG

Like sol-gel synthesis, the atomic level mixing of the precursors is achieved prior to the co-precipitation step. In YAG synthesis, it has been reported that the presence of $Y^{3+}$ (or hydroxide of $Y^{3+}$) inhibits the crystallization of $Al^{3+}$ (Bayerite and Boehmite) during the precipitation. These coated $Y^{3+}$ions on $Al^{3+}$ ions act as a capping agent to minimize grain growth and reduce particle-particle coalescence during calcination. This leads to the preparation of YAG nanoparticles with soft agglomerates [101]. Therefore, there is potential to investigate the suitable condition for the formation of core-shell structured precipitates. This could be a challenging task to achieve core-shell structure during precipitation whilst maintaining the precursor concentration less than 3 and allowing very little pH fluctuation.

Co-precipitates of metal ions ($Y^{3+}$ and $Al^{3+}$) in a solution can be achieved if the precipitant is insoluble in the precursor solution and makes precipitation kinetics

rapid. Chemical precipitation reaction can be performed by a normal strike method [127] (adding a precipitant solution to a salt solution) or by a reverse strike technique [101] (adding the salt solution to the precipitant solution). The main difference between these two methods is the rate at which the pH of the salt solution changes as a function of time, because $Y(OH)_3$ precipitates at pH 8.1, whereas $Al(OH)_3$ precipitates at pH 3.5 [128]. For multi-cation materials like YAG, the reverse strike co-precipitation technique has the advantage of higher cation homogeneity in the precursor and results in finer particles. In the normal strike method, the exchange of ions from the surrounding salt solution is different due to different solubility of aluminium and yttrium in the solvent, which results in non-stoichiometric compound. However, a drop wise addition of the salt solution onto the precipitant solution would result in rapid fluctuation of the pH, surpassing the precipitation conditions of both aluminium and yttrium solution to maintain the cation stoichiometry is necessary. Nevertheless, the soft agglomerates formed during co-precipitation tend to transform to hard agglomerates during the calcination step.

Another factor that influences the agglomeration of particles is the concentration of the precursors. Wang et al. [129] studied the effect of different concentrations of the precursor solution for the co-precipitation synthesis of YAG nano powder. They achieved 20-30 nm particles using a precursor solution ratio of <1 and calcination for 2 hours at 900°C.

The uses of different precipitants [130] and pH conditions [128, 131, 132] have also been studied; these are considered to be very important factors governing particle morphology with the co-precipitation method. Li et al [130] studied the effect of precipitants using ammonium hydroxide and ammonium hydrogen carbonate (AHC) with a precursor solution ratio of about 1.5 at pH 9. Their comparative study suggests that the YAG powder synthesized using AHC resulted in less agglomeration with crystallite size of about 52 nm. However, neither the precursor concentration, nor the control over the pH was optimized. Apte and Vrolijk [128, 133] investigated the best pH range for the precipitating YAG using ammonium hydroxide and suggested that it was pH 7 – 9.

These results suggest that identification of the most suitable processing conditions is still required for the production of fine nanocrystalline YAG powder with little agglomeration.

### 2.4.5 Supercritical and subcritical synthesis of nanocrystalline YAG

Supercritical fluid technology to synthesis ceramic particles involves pressure and temperature in tandem, which significantly change the crystallisation kinetics and its reaction pathways. Figure 10 illustrates the phase changes as a function of pressure and temperature in the liquid-gas-solid system.

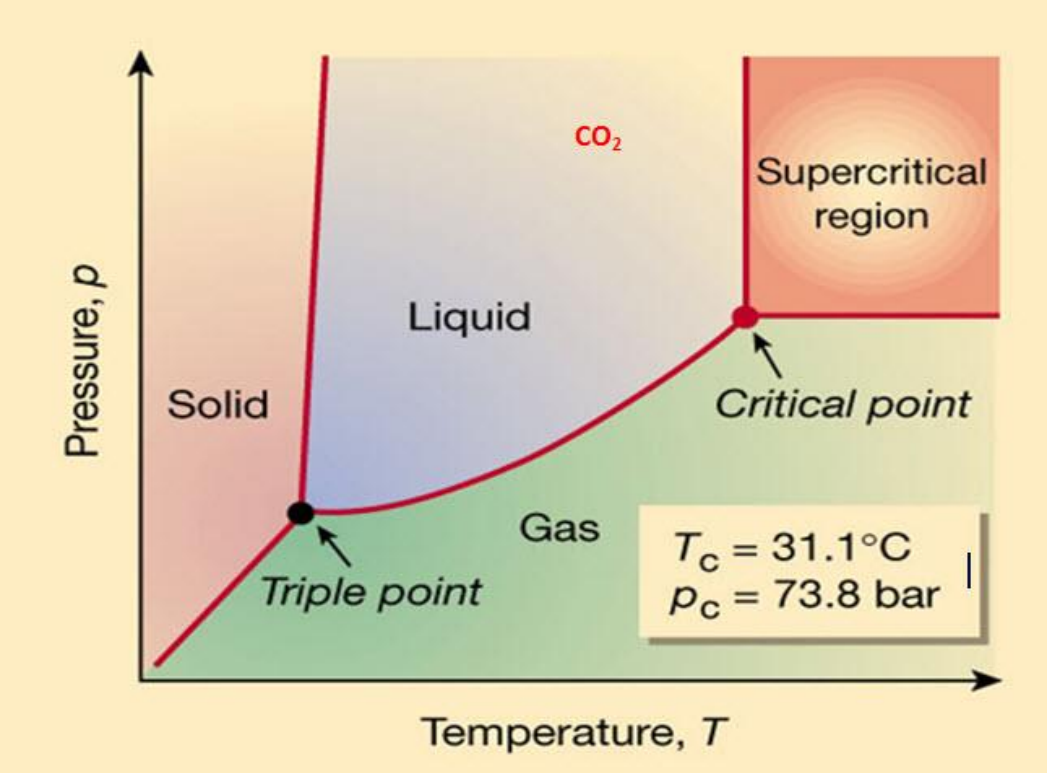


*Figure 10 PT - phase diagram for a liquid-gas-solid system [134]*

An autogenous pressure generated as a function of temperature influences the matter to change its state from liquid to gas-like behaviour at supercritical conditions. When a solvent exceeds the critical point, it becomes supercritical fluid and attains larger volume than the normal fluids and hence become highly compressible, Figure 11. Consequently, the abrupt change in solvent properties, Table 3, such as density, viscosity and the diffusivity equivalent to gaseous state makes supercritical fluids potentially a superior and attractive solvent media for synthesising nanoscale particles, rods, wires and films.

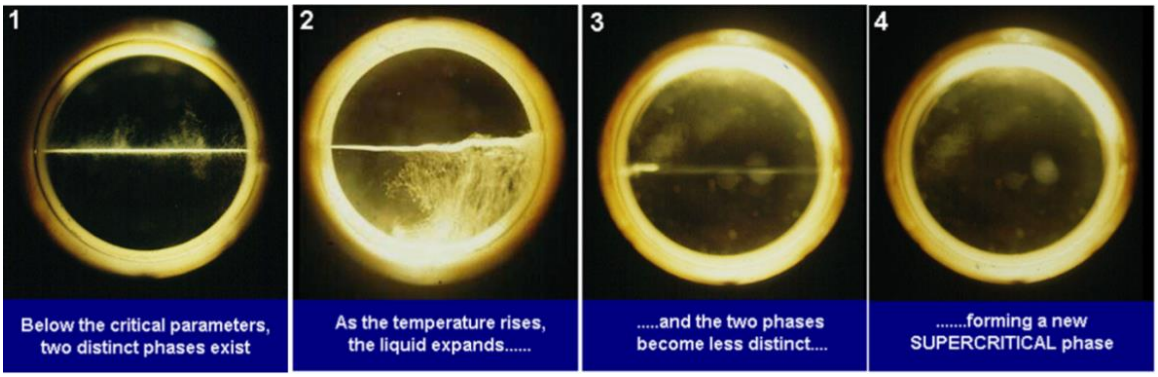


*Figure 11 Change in phase from $CO_2$ liquid to supercritical fluid with increase in temperature and pressure [135]*

Recently, subcritical and supercritical fluids have been intensively applied for chemical synthesis. In solvothermal synthesis, precipitation is initiated from the precursor solution and the hydrothermal crystallization occurs from the hydroxide gels or precipitates. The major advantage of this method is that the high temperature calcination is not required for the formation of crystalline oxides. The particles are crystallised whilst suspended in a liquid medium, which in turn facilitates the formation of agglomeration free colloids directly.

*Table 3 Properties comparison of typical gases, SCF and liquids [136]*

| **State of matter** | **Density / g cm$^{-3}$** | **Viscosity / µPa s** | **Diffusivity / mm$^2$ s$^{-1}$** |
|---|---|---|---|
| Gas | 1 | 0.01 | 1-10 |
| SCF | 0.1 – 0.5 | 0.05 - 0.1 | 0.01-0.1 |
| Liquid | $10^{-3}$ | 0.5-1.0 | 0.001 |

For instance, YAG submicron and nanoparticles can be obtained in a single step by the rapid hydrolysis and dehydration of a solution of yttrium and aluminium nitrates. When the water is heated above its supercritical conditions [137] , ($T_c$ = 400°C, $P_c$ = 30 MPa), the super saturated solution precipitates into small particles of metal hydroxides, $Y(OH)_3$ and $Al(OH)_3$, which undergo rapid dehydration and form single-phase YAG with a particle size range from 40 – 140 nm using hydrothermal

synthesis [137]. Sahraneshin et al. [138, 139] studied the effect of surfactants on the particle morphology of YAG using hydrothermal synthesis. Spherical and rod like morphologies with particle sizes of about 400 nm were obtained when oleic acid and oleylamine were used as the surface modifiers, respectively.

Like surfactants, the effect of solvents and the type of precursors on the particle morphology were studied by Poliakoff and co-workers [137] at Nottingham. They produced single phase YAG in ethanol (EtOH) and water mixtures using continuous supercritical hydrothermal synthesis at relatively low temperature and pressure, 385°C and 24 MPa. Both organic (yttrium acetate and aluminium isopropoxide) and inorganic (yttrium and aluminium nitrate) precursors were precipitated using ammonia solution and the obtained precipitates were dispersed with different concentration of alcohol- water mixtures (60-90) vol.% EtOH in $H_2O$). Their study suggest that the use of water alone resulted in cubic particle morphology with 120 nm in size and the mixture of water and ethanol (60-90 vol.%) in smaller particles of about 50 nm with irregular particle morphology regardless of the precursor types being used. This clearly showed that the solvent is highly influential than the precursors being used.

Li et al. [108, 140] further reduced the water content and maintained a ratio of 2:1 EtOH–$H_2O$ mixture using nitrate precursor, which reduced the processing conditions to 290°C and 10 MPa for YAG synthesis and resulted in monodispersed spherical particles with a mean particle size of about 60 nm particles. On the other hand, Inoue et al. [141] synthesised YAG using the organic precursors, yttrium acetate and aluminium isopropoxide, with ethylene glycol (EG) and 1, 4 butanediol as the solvent medium to crystallise YAG nanoparticles. The former resulted in amorphous phase and the latter successfully resulted in phase pure YAG with a mean particle size of about 20 nm at 300°C and 5 MPa pressure for two hours.

Replacing water content with other solvents significantly influenced to produce smaller particles. Very little literature was available on the mechanism for the formation of YAG nanoparticles using 1, 4 butanediol. Therefore, a detailed study on the solvothermal process is still required to produce fine particles without agglomeration of the fine particles. The disadvantages of this process are safety issues and capital cost of the equipment [142]. During the powder synthesis, the

precursors undergo extreme pressures and resulting severe exothermic reactions. Therefore, it requires more attention during the process and it is more important to work within the pressure limit of the autoclave and a proper cooling system is required [142, 143].

### 2.4.6 Summary of YAG synthesis

A comparison of YAG synthesis procedures and their quality of the YAG powders obtained are listed in Table 4. The particle size and shape of the YAG powders were found to be uniform in sol-gel and co-precipitation and solvothermal methods, which also require low temperatures for the synthesis. This gives a clear knowledge about the precursors that are compatible with the solvents for a suitable process for producing high quality nanopowders.

*Table 4 Overview of YAG synthesis and the characteristics of YAG powder produced*

| **Synthesis routes** | **Particle size** | **Homogeneity** | **Heat treatment** | **Agglomeration** | **Cost** |
|---|---|---|---|---|---|
| Mixed oxides | ~1 µm | Poor | 1600°C | High | Low to moderate |
| Combustion | ~20 nm | Very good | 950°C | High | Moderate |
| Sol-gel | 10-50 nm | Very good | 900°C | Moderate | Low to moderate |
| Co-precipitation | ~60 nm | Good | 950°C | Low | Low to moderate |
| Solvothermal | ~30 nm | Very good | 300°C | Low | Moderate |

## 2.5 Colloidal processing of ceramic suspensions

A colloidal system consists of two different phases; a continuous phase, which acts as a dispersion medium, and a dispersed phase, which is usually having a physical dimension ranging between 1 - 1000 nm [144, 145]. Table 5 shows the relationship between the continuous phase and the dispersed phase to form corresponding colloids [144].

*Table 5 A combination of different forms of dispersed phases and continuous phases, compiled from [144, 146]*

| **Phases** | | **Continuous phase** | | |
|---|---|---|---|---|
| | | **Gaseous** | **Liquid** | **Solid** |
| Dispersed phase | Gaseous | None | Foam (cream) | Solid foam |
| | Liquid | Liquid aerosol (fog) | Emulsion (milk) | Gel (agar) |
| | Solid | Solid aerosol (air particulate) | Sol (colloidal silica) | Solid sol (gold ruby glass) |

In advanced ceramic processing, colloidal suspensions, solid-liquid phase, are used to produce nanostructured ceramics using both wet and dry processing [87, 147]. Whilst comparing the conventional ceramic processing, consolidation of ceramics using colloidal methods resulted in better packing in the green bodies, which leads to a better microstructure during sintering. This in turn offers unusual physical and chemical properties of the sintered ceramics for different applications. In ceramic processing, high solids loading colloidal suspensions are required for slip casting and granulation processes for dry pressing methods. However, the stability of colloidal suspensions with high solids loadings is very difficult which is controlled by their physicochemical properties, detailed in the following section.

### 2.5.1 Stability of colloidal suspensions

Colloidal particles in a dispersed medium involve continuous collision between them and transfer the kinetic energy to the colliding particle and exhibits zigzag movement called Brownian motion. This depends on the viscosity of the dispersion medium because the viscous force hinders the movement of the colloidal particles and results in coagulation of the suspension. This kind of behaviour usually happens during the concentration of colloidal suspension to achieve high solids loadings. Therefore, stability of the suspension is considered to be an important factor in the colloidal processing of ceramics.

The stability of colloids is dominated by the interaction energies based on the attractive and repulsive forces between the particles. When the latter dominates in the colloidal system, the particles are well dispersed, resulting in a stable state. When the former dominates, particle-particle coalescence is predominant and results in an unstable dispersion state [148] caused by sedimentation and aggregation of the particles in the colloidal suspension.

Figure 12 shows the difference between a stable and an unstable colloidal suspension, which is caused by aggregation and sedimentation. Aggregation mainly arises from the attraction of the particles in the colloids due to lack of repulsive forces between them, whilst sedimentation is mainly caused by agglomerated particles, which will have a different specific gravity compared to the dispersed particles in a continuous phase [149]

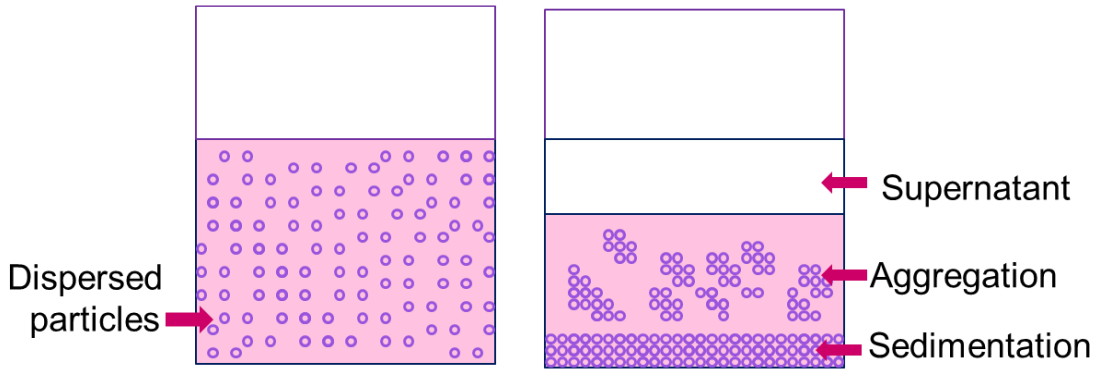


*Figure 12 Example of a stable and an unstable colloidal suspensions [150]*

### 2.5.2 Factors influencing the stability of the suspensions

The colloidal stability of the suspension has been determined the balance between repulsive and attractive forces. The significant energies that influence the colloidal stability of a mono dispersed suspension are gravity, buoyance, Van der Waals force and repulsive energy by double layer. The sum of these forces governs the stability of the colloidal system and the total inter-particle potential energy $V_{total}$ is described by the equation 4 and 5 [147]:

$$V_{total} = V_{attractive} + V_{repulsive} \qquad Eqn\ 4$$

$$V_{total} = V_{vdw} + (V_{elect} + V_{steric} + V_{ele\text{-}steric}) \qquad Eqn\ 5$$

All the energies are particle size dependant, the potential energies decreasing with a decrease in particle size. Therefore, the stability of the nano-dispersions is very difficult and requires more repulsive force to counteract the attractive force.

#### *2.5.2.1 Van der Waals Forces*

Van der Waals forces are short-range attractive and abundant forces, which originate from the interaction between the dipoles within the media. Different methods are used to minimise the influences of Van der Waals forces to produce a stable colloidal suspension.

One possible method to make attraction free colloids is by matching the refractive index of the dispersed particles with the solvents [151, 152]. However, this method is limited for most ceramic powders due to their high refractive index. Thus, the alternative method to prevent colloids from aggregation is by generating an electrical charge at the solid-liquid interface by functionalising surface active agents on the particle surface to prevail over Van der Waals forces of attraction. This can be achieved through electro–steric mechanism, a combination of electrostatic and steric stabilisation imparted by the polyelectrolytes.

### *2.5.2.2 Electrostatic Forces*

The fundamental mechanism of the electrostatic force is the repulsion of the like charges. When ceramic particles suspended in a liquid, it generates interfacial charges at the solid-liquid interface due to the ionisation of the reactants into ions ($H^+$ or $OH^-$), which are adsorbed on the surface of the particles. Most of the metal oxides contain surface passivation of $OH^-$ groups in the polar solvents, which are amphoteric in nature and can either protonated in acidic pH or deprotonated in alkaline pH, equation 6 and 7 [153]. This results in the ceramic particles becoming electrically charged at the surface.

$$MeOH + H^+ \text{-----> } MeOH_2^+ \quad \textit{(Positively charged surface)} \qquad \textit{Eqn 6}$$

$$MeOH \text{-----> } MeO^- + H^+ \quad \textit{(negatively charged surface)} \qquad \textit{Eqn 7}$$

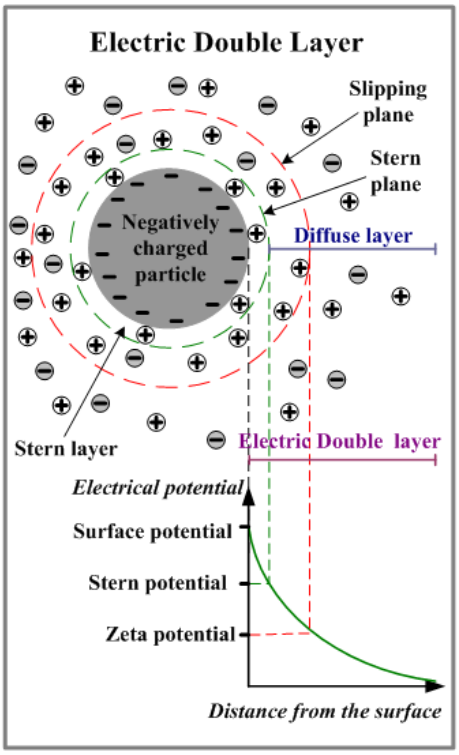


*Figure 13 Illustration of electrostatic length scale and potential energy [154]*

The charged electrical layers thus surrounded by the ceramic particles are called the electric double layer; a schematic of the double layer is shown in Figure 13. The ions in the first Stern layer are strongly bound to the particles and the second diffuse layer is less firmly associated with the particles. Within the diffuse layer there is another boundary forming a stable entity, which facilitates the double layer repulsion and the potential it offers at the boundary is called the zeta potential. However, the surface potential offered by the electrostatic force on the particle surface may be too low to triumph the attractive force. Thus, other forces balancing the conditions are needed to increase the inter-particle potential energy.

#### *2.5.2.3 Steric Forces*

Steric-stabilization is an additional option to stabilise the ceramic suspension by covering each surface of the particle with a polymer. The adsorbed polymer should offer sufficient thickness and density to overcome the attractive forces to maintain the stability of the suspension. Depending on the molecular weight and the functional groups, polymer configuration may vary from homo-polymers, di-block copolymers, comb-like co-polymers, and functionalized short-chain dispersants, illustrated in Figure 14a.

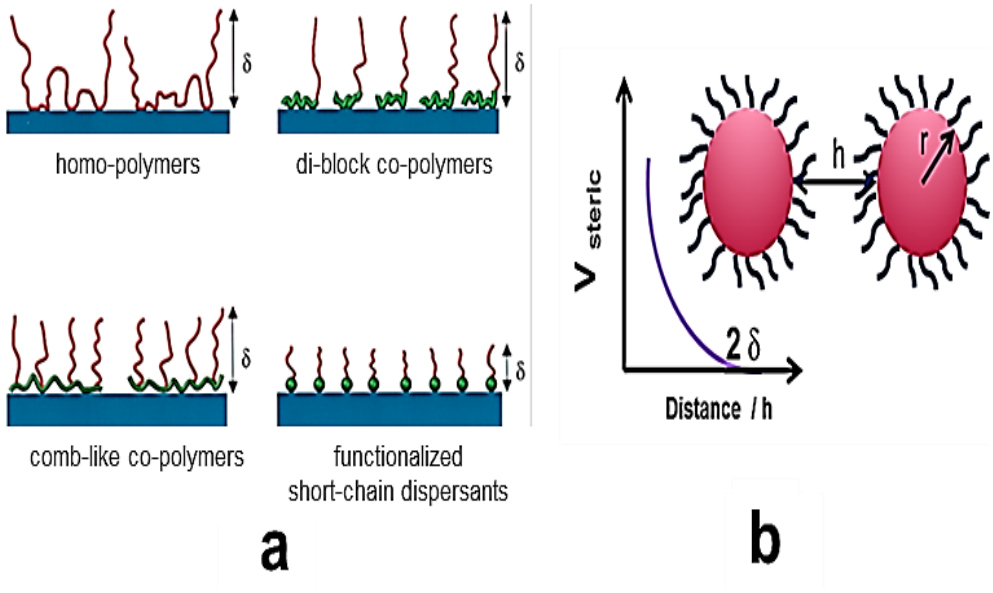


*Figure 14 (a) Illustration of dispersant configuration on ceramic layer and (b) steric length scale and potential energy [147]*

Steric interactions happen only when the particles are separated by a distance (h) less than twice the adsorbed polymer layer (adlayer) thickness (δ). The relationship between V steric and adlayer thickness is shown in Figure 14b. According to this theory and the illustration, the system requires sufficient distance from the particles to maintain stable suspension. Therefore, steric stabilisation is not suitable for highly concentrated nanodispersions due to the volume restrictions.

#### *2.5.2.4 Electro-steric Forces*

Electro–steric mechanism is the tandem of electrostatic and steric stabilisation imparted by the polyelectrolytes [155]. It requires the existence of adsorbed polymers on the particle surface and significant double layer repulsion between the particles. This mechanism is more suitable for highly concentrated nano-suspensions because the stability depends on the ionic strength and the pH of the suspension, see Figure 15.

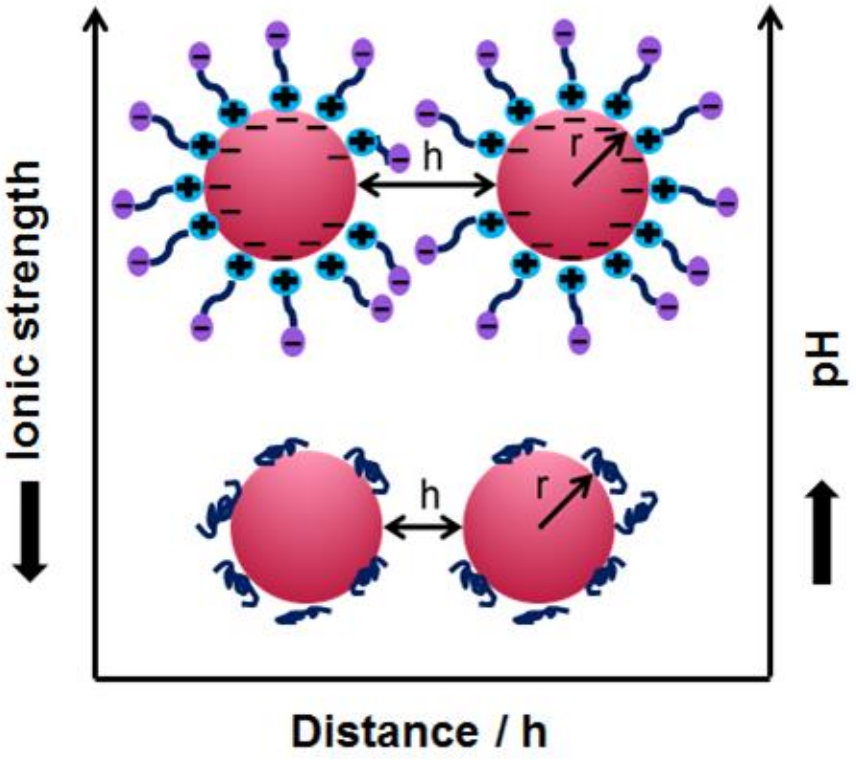


*Figure 15 Illustration of electro-steric mechanism [147]*

The electrochemical properties of the material affect the degree of absorption of the polymer on the surface. As shown in Figure 19, the degree of ionization for most

polyelectrolytes is directly proportional to the pH. Also, with an increase in the pH, the length of interaction enhances between negatively charged particles and vice versa for positively charged particles, providing a high enough zeta potential to maintain the stability of the suspension. The dissociation of the polyelectrolyte form charged polymers helps to develop electrostatic charges.

From this review, it is very clear that electro-steric mechanism is more suitable for stabilising highly concentrated colloidal ceramic suspensions. However, the adsorption of the polyelectrolytes on the ceramic particles depends upon several factors such as molecular weight, ionic strength and pH of the dispersion medium. Once the electro kinetics has been determined, there are lots of dispersants available to stabilise the ceramic suspensions.

### 2.5.3 Dispersants for YAG suspensions

Dispersants or surfactants are a substance used in low concentrations to influence the surfaces and interfaces of the adsorbate and to alter its physical properties. Measurements of the zeta potential as a function of dispersant concentration and an optimum amount of dispersant will be determined at the point where the zeta potential becomes stable, meaning that the dispersant molecules covered the surface of the particles. Usually zeta potential of about 30 mV charge (both positive and negative) is required to produce a stable suspension [156]. The chemical structure of a dispersant is usually composed of a hydrocarbon or fluorocarbon chain associated with a tail group (COO-, $SO_4^{2-}$, $PO_4^{3-}$, $SO_2O^-$) and a head group ($Na^+$, $NH_4^+$, $Cl^-$, $Br^-$), which act as lyophobic and lyophilic groups, respectively. This structure is known as amphipathic structure. When a dispersant of this structure is dissolved in an aqueous medium, the lyophobic (tail group) distorts the structure of water to reduce the surface tension and the lyophilic (head group) attracts the surface of the particles and protects the particles from coagulation.

Table 6 shows the different classifications of dispersants based on the hydrophilic groups. Anionic dispersants are suitable for negatively charged particles and cationic for positively charged and zwitterionic for both the charges. Ceramic particles such as alumina and YAG exhibits negative charge above pH 7, and anionic dispersants are largely used to stabilise the suspensions. However, the use of $Na^+$ based dispersants acts as a flux and weakens the grain boundaries of the ceramics, which

leads to poor mechanical properties. Moreover, fluorocarbon chain based dispersants and $SO_4^{2-}$, $PO_4^{3-}$ and $SO_2O$ based tail group dispersants are likely to contaminate the elemental composition of the ceramics. These ions can diffuse into the crystal lattice and result in non-stoichiometric compositions of the sintered ceramics. Therefore, for processing components of high mechanical and optical performance, dispersants with both part of polar head group having $NH_4^+$ and $COO^-$ molecules are usually preferred, even though the ionic strength of it is lower than the aforementioned.

*Table 6 Dispersant classification*

| **Metal oxide surface** | **Suitable dispersant type** | **Dispersants** |
|---|---|---|
| Negatively charged surface ($MeO^-$) | Anionic | $RCOO^-Na^+$, $RCOO^-NH_4^+$ Mw (~10,000), $RSO_3^-$ $NH_4^+$, |
| $MeOH_2^+$ (Positively charged surface) | Cationic | $RN^+Cl^-$, $RNH_3^+Cl^-$, $RN(CH_3)_3^+Cl^-$ |
| Both positive and negatively charged surfaces | Zwitterionic | $RN^+H_2CH_2COO$-, $RN^+(CH_3)_2CH_2CH_2SO_3$ |

Generally, polyacrylic acids (PAA, anionic dispersants) are used to produce co-dispersed $Y_2O_3$-$Al_2O_3$ suspensions for transparent YAG ceramics since the surface charge is negative. Appiagyei et al. [157] used PAA with an average molecular weight of about ~450,000 and found, with the addition of 0.1 wt.% PAA, a maximum zeta potential of about -45 mV was achieved, shifting the isoelectric point (IEP) towards the acidic region. Their use of PAA has shown to produce well-dispersed, high solids loading, stable suspensions with near Newtonian behaviour. Yaohui et al. [158] used the $NH_4^+$ salt of PAA ($NH_4$PAA) as a dispersant for co-dispersed neodymia-yttria-alumina suspensions. Their work has shown that a maximum zeta

potential of -85 mV was achieved at a pH of 10.5 with 5.2 wt.% of $NH_4$PAA. Under these conditions they were able to produce a fully dense transparent sintered body. Likewise, Li et al. [159] used $NH_4$PAA, but with lesser Mw (~10,000) to produce single phase YAG suspensions with 40 nm sized particles. Their work has shown that a lower molecular weight dispersant with lesser concentrations of about 1.5 wt.% dispersant at pH 10 produced -47 mV zeta potential, producing a stable nano YAG suspension.

From this literature, it is very clear that $NH_4$PAA is suitable for producing stable YAG suspensions. For nano-suspensions, the particle-particle interactions are much higher than for the suspensions with coarser particles, van der Waals force become predominant due to the very large surface area to volume ratio of the nanoparticles, which results in high suspension viscosities.

Therefore, the nanoparticles must be functionalised with a proper repulsive mechanism to offer Brownian motion and the particles will remain dispersed in an unsheared suspension, which could result in low viscosity of the suspension.

### 2.5.4 Rheological properties of colloidal suspensions

Rheology is the study of flow behaviour and deformation of matter. Understanding the rheology of colloids suspensions is of great importance before storing, atomising or forming a ceramic system [159].

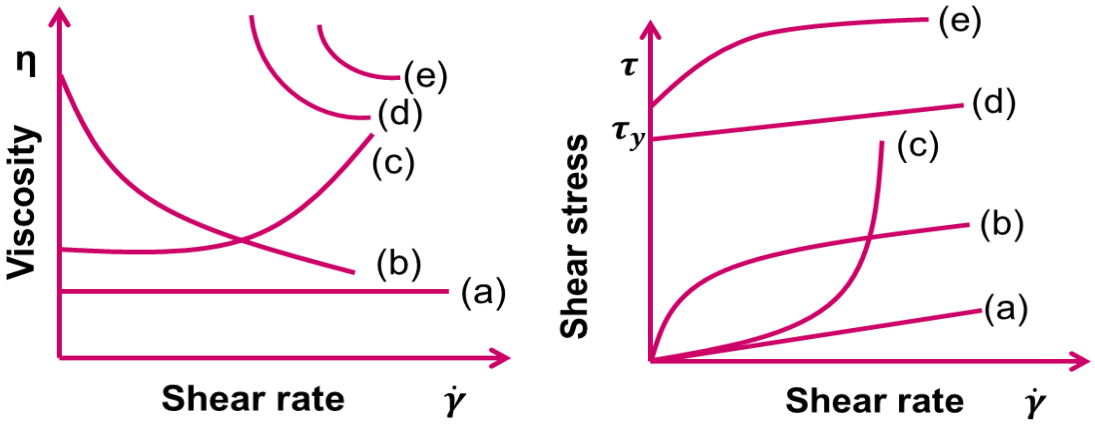


*Figure 16 Flow with rheological behaviours (ζ/γ) : (a) Newtonian; (b) shear thinning; (c) shear thickening; (d) Bingham; (e) shear thinning with a yield stress. [160].*

Based on the rheological properties, suspensions are classified into a) Newtonian, b) shear thinning, c) shear thickening, d) Bingham and e) shear thinning with yield stress. The respective rheological characteristics are shown in Figure 16.

Newtonian suspensions are independent of shear load to viscosity and maintain a constant viscosity with respect to shear rate and the stress will fall zero instantly after the shearing is stopped. In any subsequent shearing, the viscosity will be same as previously measured and the effect of aging makes no difference in the rheology of the suspensions.

The viscosity of a shear-thinning suspension is dependent on the shear load (shear rate or shear stress) and the flow behaviour can be either time dependent or time independent. Generically, a shear-thinning suspension would exhibit a lower viscosity with an increasing shear load. Therefore, suspensions with shear thinning behaviour are usually used for wet forming routes such as slip casting and to produce granules using spray drying and spray freeze drying techniques.

As discussed earlier, particle-particle interactions and the Brownian motion plays a vital role in a suspension's viscosity. An additional factor called 'suspension structure' significantly influences the rheology of the concentrated ceramic suspensions [161]. The suspension structure is clearly dependent on the particle shape and the particle size distribution. This means that when the average distance between the particles in the suspension is reduced it would cause double layer overlap, which subsequently increases the viscosity. Therefore, a narrow size distribution of spherical particles allows maximum packing efficiency when compared to the particles of irregular shapes or agglomerates to achieve high solids loading. This is considered as an important factor because high concentrations of the suspension allow high slip density or tap density for green processing.

Noticeably, factors such as temperature, particle size, surface area to volume ratio, and shear rates determine the viscosity of the suspensions. Therefore, colloidal systems require a precise investigation on rheological properties (viscosity and shear stress), which can provide an insight over controlling the stability and behaviour of colloidal suspensions for a given ceramic processing method [160]. As described, one must tailor inter-particle forces, suspension rheology, etc. to achieve the optimal suspension for a given application such as slip casting, granulation or glazing.

## 2.6 Green forming of ceramics

The green samples are processed using both wet and dry forming routes. The latter is a simple industrially viable ceramic forming route, which requires powder or granules to prepare samples. The former is a complicated route and used to make complex shapes which consequences excellent microstructures of the sintered ceramics. Detailed studies on both the forming routes are discussed below.

### 2.6.1 Wet forming routes

Microstructural defects discussed in dry processing routes can be avoided by using wet forming methods, in which the colloidal stability of the suspension influences the microstructure of the green body. However, voids due to air bubbles are the problem in suspensions which leads to microstructural flaws. These voids can be eliminated by proper de-airing of the slurry and by using controlled flow rate during casting. The common wet forming routes are slip casting and tape casting in which additives such as binders, dispersants and plasticizers are used to suspend the particles in a colloidal medium. Homogeneous particle packing and high green density can be achieved by controlling the suspension characteristics such as colloidal interactions between the particles and the suspension rheology. The term rheology refers to the deformation and flow characteristics of the matter. Rheological parameters such as viscosity, yield stress and viscoelastic properties are used to characterize colloidal suspensions. For slip casting and tape casting, suspensions with high solid loading and low viscosity are desirable for green processing.

### 2.6.2 Slip casting

Slip casting is a common wet forming method in which a suspension is poured into a porous permeable mould made of Plaster of Paris, PoP, [162]. A capillary suction pressure of about ~0.1 to 0.2 MPa is provided by the micropores in the mould which draws the solvent from the suspension into the mould [90]. An immediate consolidated layer is formed on the walls of the mould during slip casting and the surplus slips are drained slowly in order to produce hollowware for making cups, if a solid piece is desired this stage is omitted. The consolidation rate is controlled by the drain rate in which the solvent is removed through the filter formed by the consolidated layer consisting of packed particles, shown in Figure 17. Once the cast

is dried, it shrinks out of the mould wall and the cast can be easily removed from the mould.

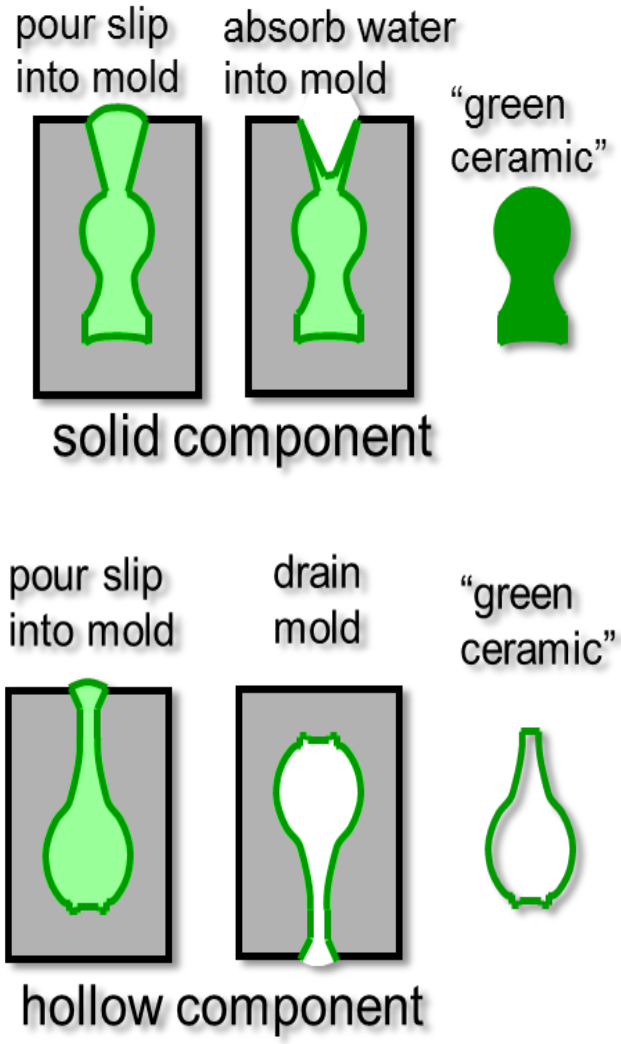


*Figure 17 Schematic diagram of slip casting [163]*

Flocculated slip usually leads to porous green bodies, whilst a well dispersed slip with a stabilized repulsive potential energy (electrostatic or steric) leads to the formation of homogenous green. Factors such as particle size and shape highly influence the packing density of the slip cast bodies. When the particle size is less than 1 µm, the ceramics resulted in high packing density and yields low pore volume due to the higher degree of dispersion compared to a unstable suspension. These results in achieving fine microstructured of the sintered slip cast samples.

### 2.6.3 Dry forming routes

Uniaxial pressing and cold isostatic pressing are the common dry forming routes to form simple shapes such as circular discs, cubes and rectangular bars with accurate dimensions. Dry forming involves shaping the powders or granules with or without additives by applying mechanical pressure. The applied pressure rearranges the powders or granules into a packed compact with increase in coordination number and uniform density. This is possible in isostatic pressing but not possible in uniaxial pressing due to the pressure gradients generated by frictional forces between particles and particle-die wall. This leads to microstructural defects such as density variation and laminar effects in the sample. These effects can be controlled by using lubricants on the die wall, adding binders to the powders or by using particles between 50-150 μm [106].

### 2.6.4 Granulation

The primary issue in manufacturing industries is the dust that comprised of nanoparticles, which can have a negative impact on the health of workers dealing with such materials. Owing to the large surface area of the nanoparticles other processing issues also come into the picture, such as large volume to compaction ratios, inhomogeneous die filling of the ceramic powders, delamination and low green densities. These medical and technical problems limit the usage of nanoparticles for the processing of ceramics in large scale. For these reasons, a granulation step is of enormous importance.

Granulation is the process of transforming ceramic suspensions into spherical aggregates for dry processing routes [164]. Granulation facilitates transportation, storage and easy processing of fine particles in a safe approach. Granulates need to exhibit the following properties:

1. Spherical shape and good flowability are required for homogenous die filling
2. High crushability [87, 165], to avoid uncrushed granules and their remnants in the green compacts [166]. The former leads to excess grain growth and the latter contributes to the formation of cracks in the sintered bodies, which can act as Griffith flaws and hence decrease their overall strength.

3. Low amount of dust, which will reduce medical problems

4. Minimal segregation in the binder mix and avoid microstructural defects such as cracking and forming voids after binder removal [166]

5. Easy storage since the powders are in the form of granules and therefore no agglomeration

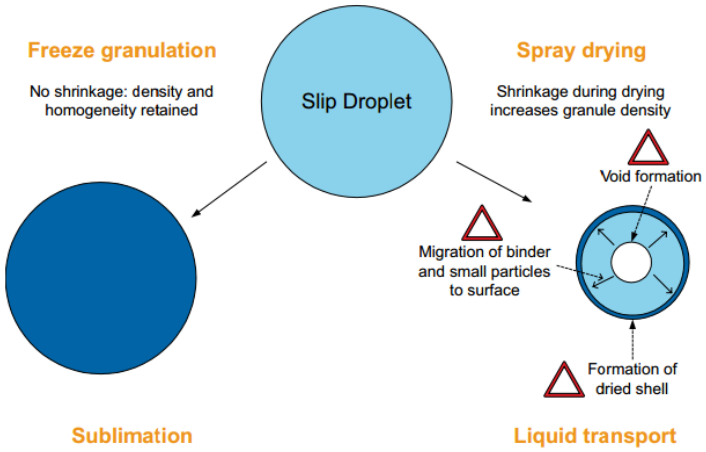


*Figure 18 Spray drying and freeze drying principle [167]*

Spray drying and spray freeze drying (SFD) are the two processes to produce ceramic granules, Figure 18. The former is widely used in industries for the production of ceramic granules. It is a continuous process, which transforms the suspension into dried particulates by spraying the feed into to a hot dry medium. Due to the large surface area created by atomisation of the liquid feed and a high heat transfer generated amongst the granules and easily decomposes the organics persists in the latter. This results in high production rate, flexible for automation and allows controlling the granule size distribution. However, [168] capillary forces appear due to the removal of the organics during drying, causing heavy shrinkage and severe hardening of the granules, which makes it difficult to crush back into fine particles in the green samples. The SFD route involves both pressure and temperature in tandem to sublimate the solvent in the suspensions to produce spherical, porous and soft granules. This allows the granules to maintain the density and homogeneity of the granule without shrinkage, giving better green compaction. The main disadvantage of this process is the time required for drying, it takes 2-3 days to dry under vacuum pressure.

### 2.6.5 Spray-freeze-drying (SFD)

Spray freeze drying is an approach that involves controlling temperature and pressure in tandem. However, this approach happens at the other extreme of the P-V diagram, below the triple junction, see Figure 19. This condition is used to freeze the water phase in the ceramic suspension and then dry the powder through a sublimation process.

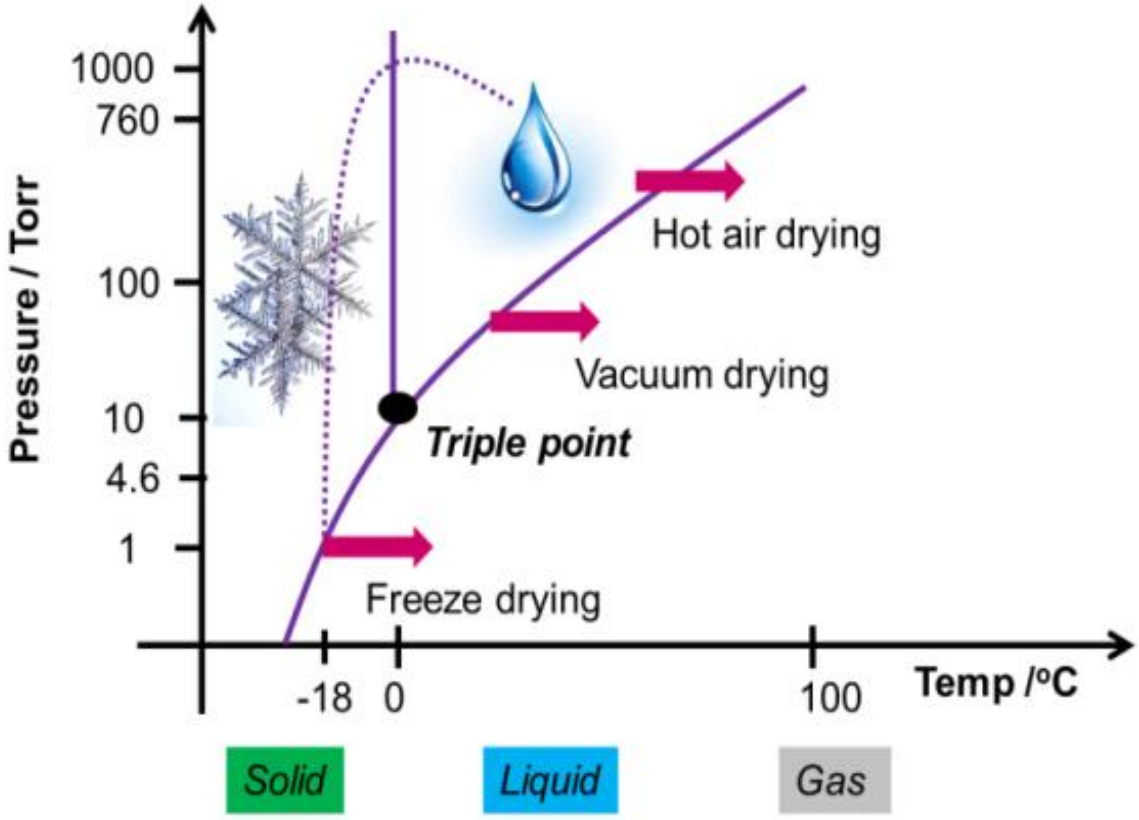


*Figure 19 Phase diagram of water, different types of drying [169]*

It is important to understand the critical properties of the formulation in the ceramic suspension when producing SFD granules because different solvents have different critical properties and hence require different freezing conditions. Surpassing the freezing condition is essential to avoid reversing the frozen ice back into liquid form. This is important because the amount of liquid phase in the ceramic suspension determines the porous structure in the final granules by subliming under vacuum pressure.

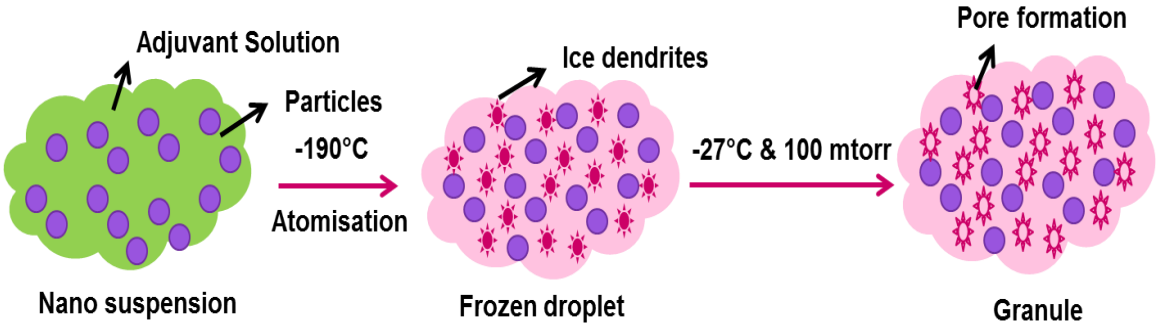


*Figure 20 Mechanism of pore formation in spray freeze dried granules [170]*

In general, the spray freeze drying process involves subsequent steps such as spray-freezing and freeze drying to produce soft ceramic granules. The former involves atomisation of nano-suspensions into fine droplets and subsequent freezing in a liquid nitrogen bath. This result in the formation of ice dendrites, see Figure 20. The latter process is also called lyophilisation. This process consists of three stages, i) pre-freezing, ii) primary drying and iii) secondary drying. These are discussed below.

#### *2.6.5.1 Spray-freezing*

The first step in the SFD process is spray-freezing; this consists of two consecutive steps. The spray process is designed to atomise the suspension into fine droplets; the shape of the droplet is determined by the solids loading and the surface tension of the adjuvant solution in the suspension. The spraying can be done using either a twin fluid nozzle or an ultrasound nozzle. The former enables to yield more granules in the desired size range with good flowabilty and crushabilty.

The next step is pre-freezing. Here, the atomised droplets are subsequently pre-frozen to produce a structurally intact product. The majority of products subjected to the freeze-drying process consist of water + a solvent (adjuvant solution) and the particles that are suspended in the adjuvant solution. This forms a eutectic mixture and it should be treated below its eutectic temperature prior to freeze drying. During freezing, the nucleation of ice crystals is thermodynamically favoured because the liquid nitrogen is at -190°C and provides nucleation sites for the formation of ice dendrites. At such low temperatures the granules are instantly frozen, promoting the formation of ice dendrites [168]. It has been reported that in using such a method the suspension results in softer granules because of the rapid freezing prevents the

formation of elongated ice crystals [168]. After the granules are effectively frozen, they are transferred into glass jars and subsequently freeze dried in order to retain the softness of the granules.

#### *2.6.5.2 Freeze drying*

After pre-freezing the suspension, suitable conditions must be provided in order to remove the frozen adjuvant solution (ice dendrites) phase by sublimation. This is achieved by drying, which takes place in two stages; primary and secondary drying.

Primary drying is the most important step in the SFD process. The primary drying is usually performed at a low pressure of about ~100 mTorr to improve the sublimation rate of the ice. The sublimation rate is determined by several factors, such as chamber pressure ($P_c$), self-temperature, heat transfer coefficient of the jars, sample volume and product resistance.

The main driving force for the ice sublimation is the pressure difference between the vapour pressure of the ice and the partial pressure of the water in the chamber. Therefore, only a very low vacuum pump pressure, in the order of a few milliTorrs (<80 mTorr), is required for fast freeze drying. Overloading of the sample in a jar will certainly reduce the difference in the vapour pressure and reverse the process back to suspension state by melting the ice, which would render the product unusable. Moreover, the rate of primary drying also depends on the shape and size of the product being dried. A greater surface area translates to quicker drying because of the larger area available to the granules leaving the system.

According to Tang and Pikal [171], the pore size of the product is also considered to be an important factor in the primary drying of the product, since the sublimation rate is directly associated with the dry layer resistance of the product. If the suspension is too concentrated, the pores created in the solute matrix by the ice crystals would be smaller, which in turn increases the resistance of the water vapour flow from the product, reducing the sublimation rate. Therefore, a moderate concentration of the suspension (50 - 55% solids loading) would be appropriate for spray freeze drying ceramic granules.

Overall, the sublimation rate determines the endpoint of the primary drying. Different methods are employed to detect the end point of primary drying. The simplest

approach is by checking the jars, if there are no ices lumps present it means the product has reached the end point of the primary drying. This means that the product temperature has been increased to the shelf temperature and the solute phase is converted into a gaseous state [172].

Secondary drying eliminates the residual moisture content of about 7-8 % in the product after primary drying [173] . At this stage, water that does not freeze or the moisture adsorbed from the atmosphere are removed by desorption from the solute phase. To get rid of the residual moisture, external heat is supplied. However, keep in mind that too high a temperature can also harden the granules. This process is called isothermal desorption.

#### *2.6.5.3 Granule characteristics*

The properties of granules are influenced by the suspension viscosity, solids content loading, geometric parameters of the nozzle and spraying parameters. The freezing rate has a very significant effect on the granule characteristics. The materials which are frozen slowly exhibit higher tap densities after drying. This phenomenon has been explained by the growth of elongated ice crystals, which densify the powder particles of the suspension during the freezing process [168]. Increasing the freezing rate suppresses the elongation of the ice crystals. Granule strength increases with increasing solids content loading. The reason is that during the spray drying process the evaporation of the suspension media causes capillary forces which pull the particles into closer contact in an already dense suspension. High solids content also results in better flowability of the granules [174].

The role of the foaming agents has also been envisaged to avoid particle-particle coalescing during freeze drying. The selection of the foaming agents has also been observed to govern the resultant structure of the granules formed. Nanocrystalline yttria doped zirconia granules have been found to exhibit better flowability and increased softness upon the addition of sublimable additive [175] to the starting suspension [164]. Relic-free green bodies of densities as high as 55% of the theoretical density were obtained using pressures as low as 250 MPa. The sublimable additive, which is a foaming agent, reduces the strength of the granules thus, making it easier to crush them while still maintaining the free-flowing nature of the granules into the die. Thus, it can be clearly seen that foaming agents have the

ability to enhance the flowability and softness of nano sized ceramic powders, making their use very desirable in the spray freeze drying suspensions.

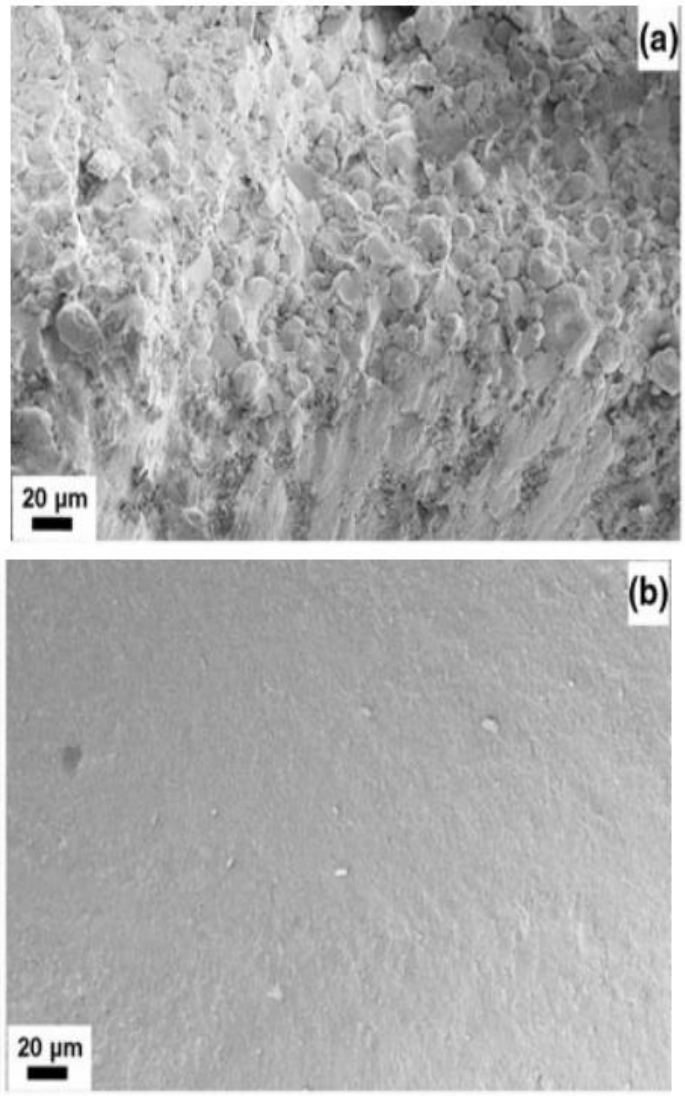


*Figure 21 Fracture surfaces of green compacts obtained from (a) spray dried and (b) spray freeze dried granules [176]*

For instance, Raghupathy et al. [176] proved that the spray dried granules of yttria stabilised zirconia were too hard to be crushed even under pressures as high as 380 MPa. From the micrograph in Figure 24a, it is clear that the spray drying process resulted in uncrushed granules remaining in the green compacts, lowering the green density. Conversely, Figure 24b shows that the spray freeze dried granules resulted in a defect free green microstructure where no uncrushed granules were seen. It is worth nothing that compacts containing uncrushed granules would require higher

temperatures to sinter than the more homogenous green bodies. In addition, the uncrushed granules would preferentially sinter, causing excess grain growth of the ceramics during densification. Therefore, the spray freeze drying process is advantageous in producing nanostructured ceramics.

### 2.6.6 Die pressing

In die pressing, a powder or a granular material undergoes uniaxial pressing usually at room temperature. The process consists of lubricating and subsequent drying of the die followed by die filling, compacting and ejecting the compact. Lubricants such as stearic acid reduce the friction between powder and die-wall during compaction and ejection of the green body, Figure 22.

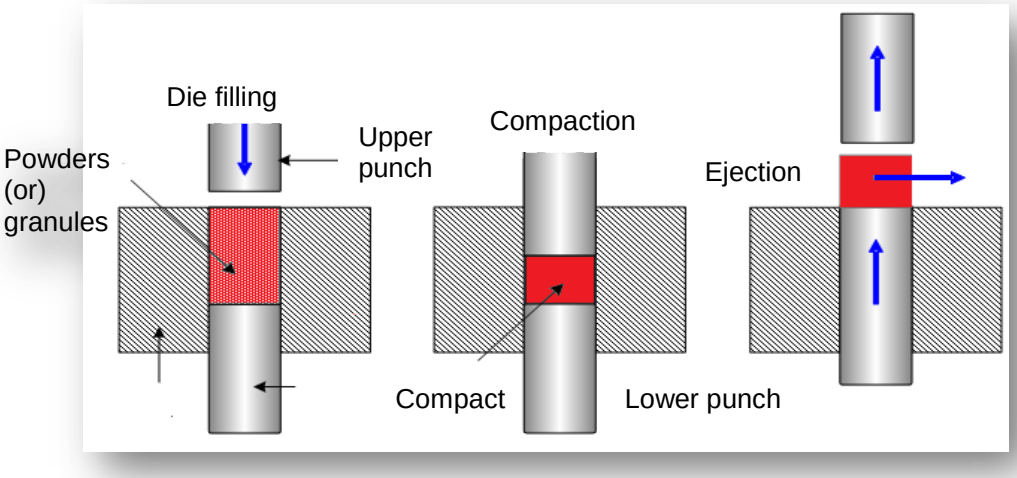


*Figure 22 Schematic of die pressing [177]*

The main issue in die compaction is the die wall friction; it doesn't transmit the applied pressure to the powder completely due to the friction between the powder and the die wall, which results in density gradients of the resultant compacts. Strijbos et al. [178] investigated the frictional behaviour of fine and coarse particles with the use of lubricants on the die wall. They found that the coefficient of friction for fine particles was less when the lubricant thickness was increased. Since the contact between coarse powder and the die wall is less, the frictional coefficient was found less. In summary to the die wall friction, the major factors such as hardness of the powder and the die wall, particle size and the use of lubricant types play a vital role in die compaction. For these reasons, the granulation process is vital, when soft

granules were used, the surface of the granules reduces the friction between the granules and the die wall and resulting homogenous green bodies.

The use of granules certainly helps in reducing the common defects such as cracks, delamination, end capping and ring capping during uniaxial pressing. However, this can be eliminated by using cold isostatic pressing of powder compacts.

### 2.6.7 Cold isostatic pressing (CIP)

The prime advantage of cold isostatic pressing is the compaction of powders with the pressures in all directions and no lubricants are required, which results in homogenous green bodies with uniform density. This process eliminates the defects associated with the green samples compacted uniaxially in rigid dies, however, delamination still occurs if the pressure is too high. CIP is widely accepted as an effective powder forming technology to compress the powder contained in a flexible leak proof polymer container into required shapes by applying uniform hydrostatic pressure. There are two modes of isostatic pressing; dry-bag pressing and wet-bag pressing are shown in Figure 23.

Wet-bag pressing is used for making complex shapes and large size samples. In this process, a rubber mould filled with powder is immersed in a pressure vessel, filled with oil, and the powder is pressed isostatically. After iso-pressing, the mould is removed and the green body is taken out. However, dry-bag pressing is easier to automate than wet-bag pressing; the flaw formation is less in isostatic pressing compared to uniaxial pressing due to the absence of die wall friction and lack of homogenous pressure across the samples.

In dry-bag press, a rubber mould is fixed in a pressure vessel and the pressure that applied to the mould is transmitted to the powder, thus keeping the mould dry. The green body is retrieved from the vessel after releasing the pressure. Dry-bag presses are limited to small size and for simple shapes. Moreover, it is a batch type process; however, multiple cassettes are used simultaneously to increase the production rate. It has been widely used to produce spark plugs for automotive industries.

In addition to these processes, green samples can also be prepared by using both uniaxial pressing at low pressure and isostatically pressed at higher pressure to attain a homogeneous density across the samples.

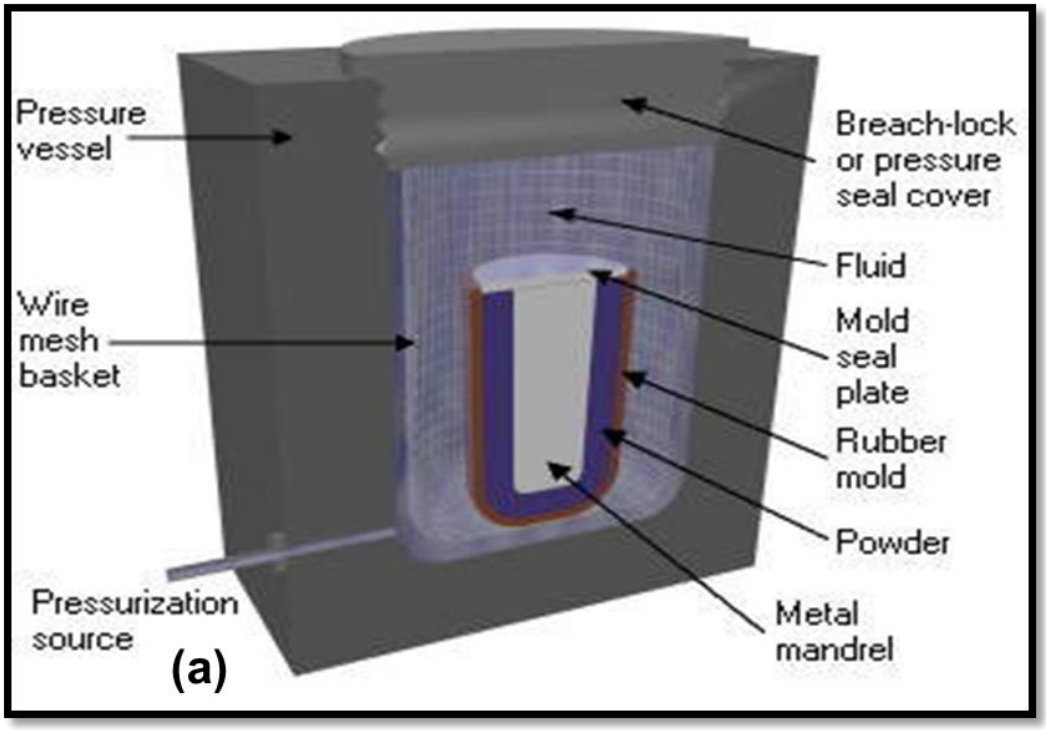


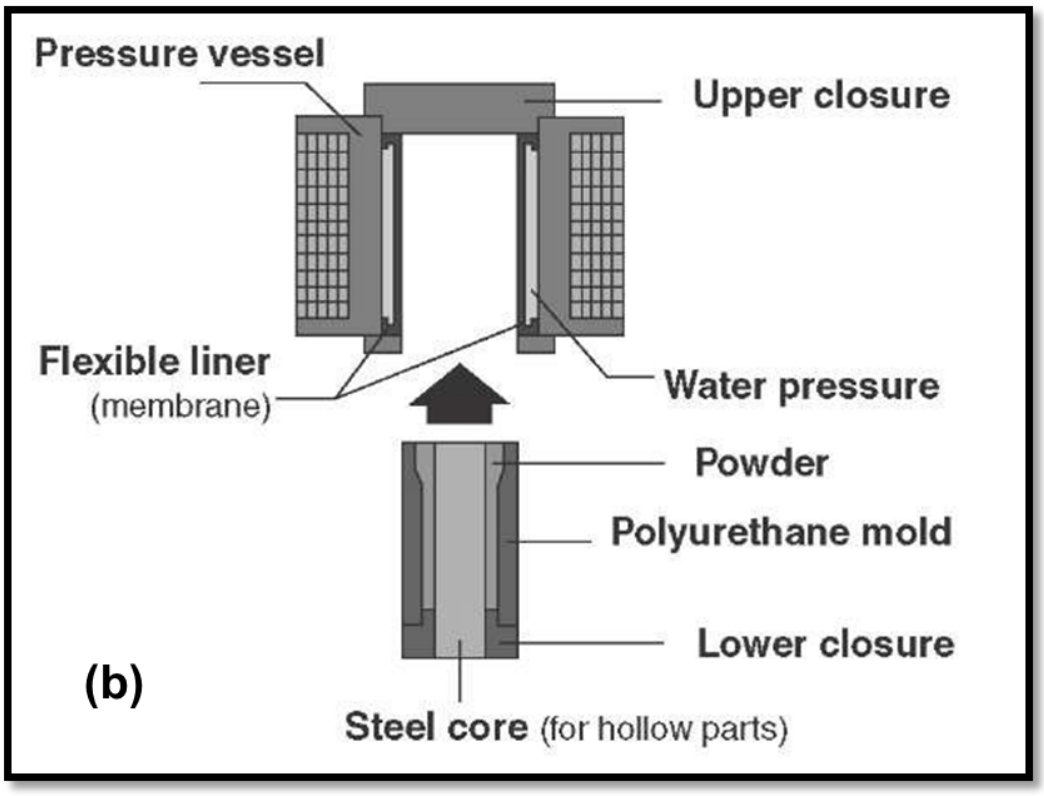


*Figure 23 Cold isostatic pressing, a) wet-bag [179] and b) dry-bag pressing [180]*

## 2.7 Sintering of transparent YAG ceramics

Classical fabrication routes for ceramics are powder based methods, which employ binders and sintering aids to produce ceramic components. Fabrication of transparent ceramics requires tight control of limiting factors such as scattering pores, second phase formation, grain boundary segregation and the presence of point defects. To eliminate these factors, special processes such as vacuum assisted pressureless-sintering are used in an attempt to achieve the theoretical density of the sintered body.

In general, densification is the process of removing residual pores in a ceramic by particle necking and grain growth, while grain coarsening is due to the mass transportation of inter-particles, which results in larger particles without densification [181]. Figure 24 illustrates both densification and grain coarsening processes of ceramics.

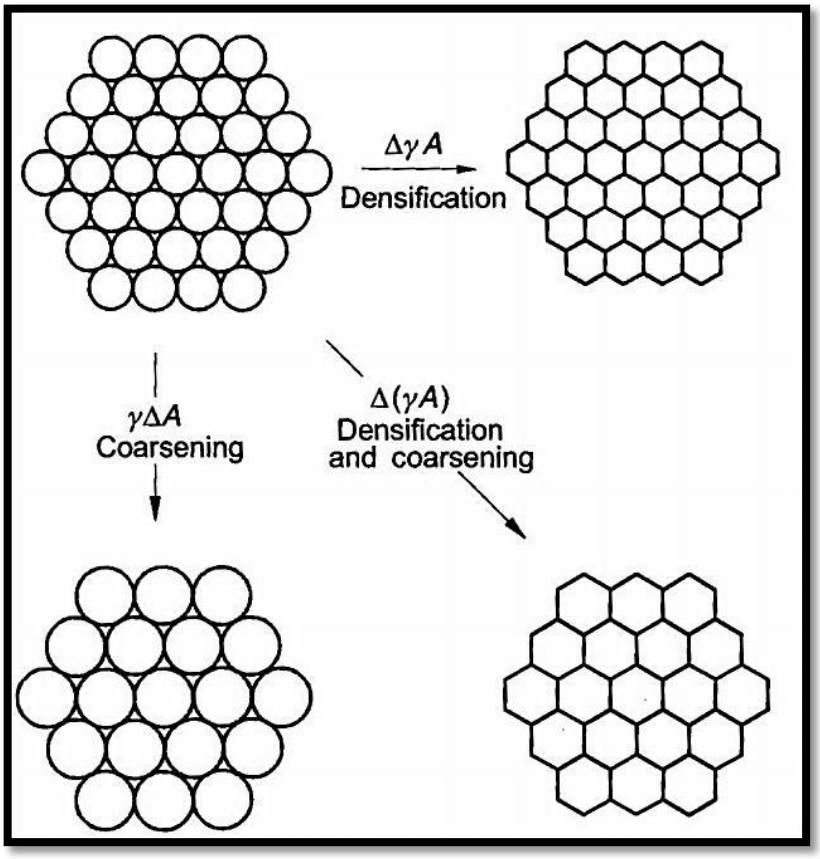


*Figure 24 Sintering mechanisms of ceramics [182]*

Two basic criteria must be satisfied by a material to be sintered:

I. Existence of material transport

II. Driving force to enhance the material transportation

Defects in crystals determine the path of material transport in solid state sintering mechanisms. The driving force for solid state sintering is the result of a capillary pressure difference due to the reduction in radius of curvature of the particle surface and the neck. Figure 25 illustrates the densification mechanism, which happens due to plastic flow, volume diffusion and grain boundary diffusion of the adjacent particles.

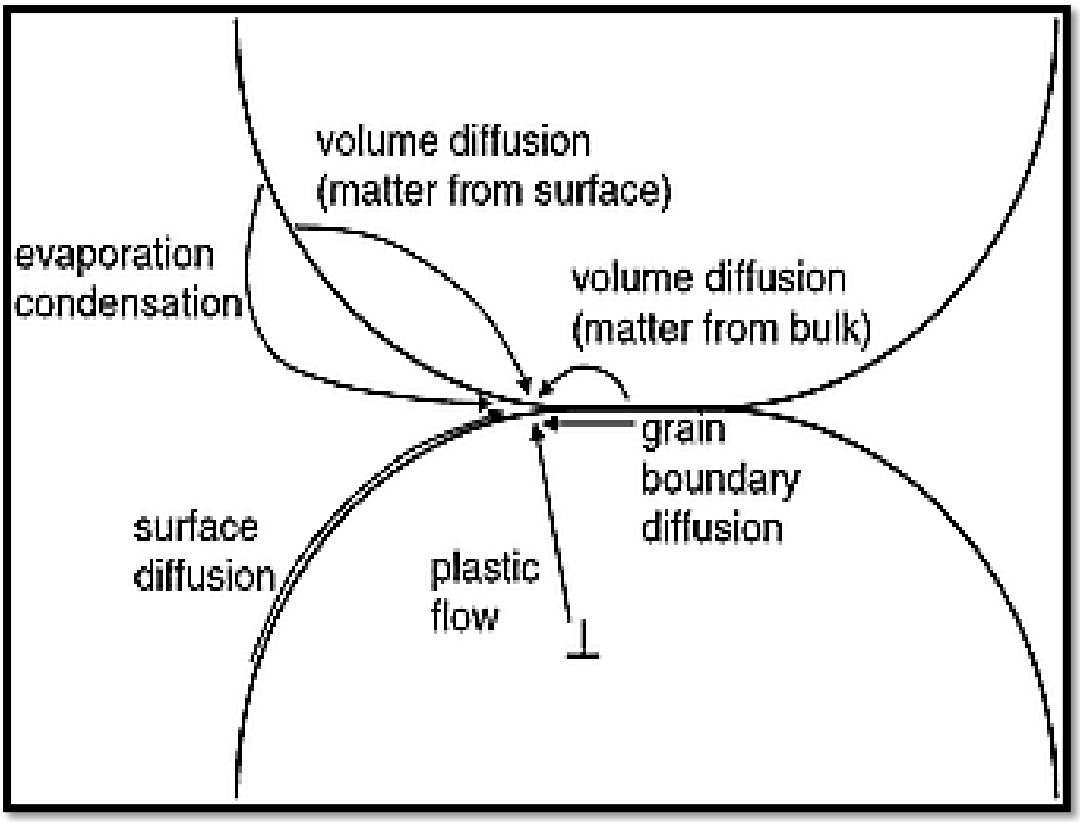


*Figure 25 Transport mechanism model of two particles in solid state sintering [183]*

The driving force for the material transportation is accomplished by the reduction in interfacial energy offered by the surface area of the particles. The total interfacial free energy $\Delta(\gamma A)$ is defined as the minimum amount of work required to create the interface between the adjacent particles.

Therefore, the reduction in the total energy is the sum of changes in the interfacial energy (causing densification) and the change in interfacial area (due to grain coarsening), equation 8 [182]

$$. \Delta(\gamma A) = \Delta\gamma A + \gamma \Delta A \qquad Eqn\ 8$$

where, $\gamma$ is the interfacial (surface) energy and A is the specific surface area of the compact.

For a typical ceramic powder, the particle size is about 1 - 10 µm and the respective surface energy ($\gamma$) is about 50 – 5 J $mol^{-1}$, which is low when compared with the energy offered by chemical reactions (300 - 1500 k J $mol^{-1}$) [182]. The large particles consume more energy without assisting densification and result in grain coarsening. Such a process requires very high temperatures and external pressures. If one uses nanoparticles of 10 nm in size, the surface energy will be about 5000 J $mol^{-1}$, which will enhance the driving force to sinter at lower temperatures and offer nanostructured ceramics. Therefore, the driving force can be enhanced by using highly reactive powders [184] (surface area >20 $m^2g^{-1}$), applying external pressure and by chemical reactions.

### 2.7.1 Sintering stages and mechanisms

Three different stages are used to explain the sintering mechanism involved, shown in Figure 26. A schematic of different stages of solid state sintering are shown in Figure 27.

Initial stage (900-1100°C) involves the rearrangement of particles by the movement of adjacent particles, which increases the coordination number of the particle, causing neck formation. This involves a slight increase in the density of the compact. Intermediate stage (1100-1400°C) involves volume shrinkage and neck growth by reducing the surface energy of the particles. Both these steps result in the transformation of continuous open pores and isolates into closed pores at the grain boundaries due to volume diffusion. The final stage of sintering (1400-1780°C)

involves the removal of entrapped pores in the triple junction and in the grains by vacancy diffusion.

The driving force during the final stage of sintering for the closure of pores at the triple junction can be written as, equation 9

$$Driving\ force\ (P) = \frac{2\gamma_{sv}}{r} \qquad Eqn\ 9$$

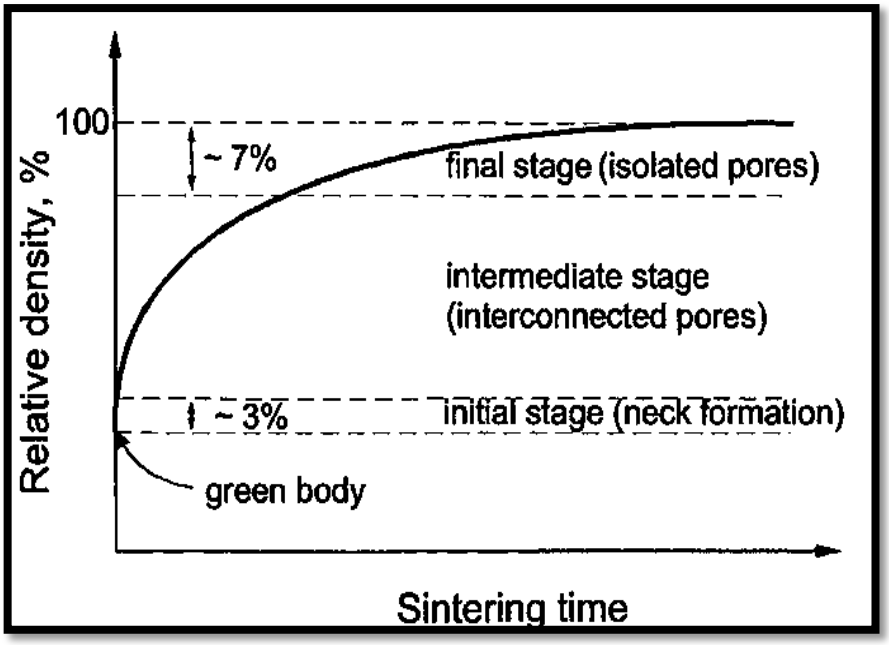


*Figure 26 Densification of green compact displaying various stages of sintering [182]*

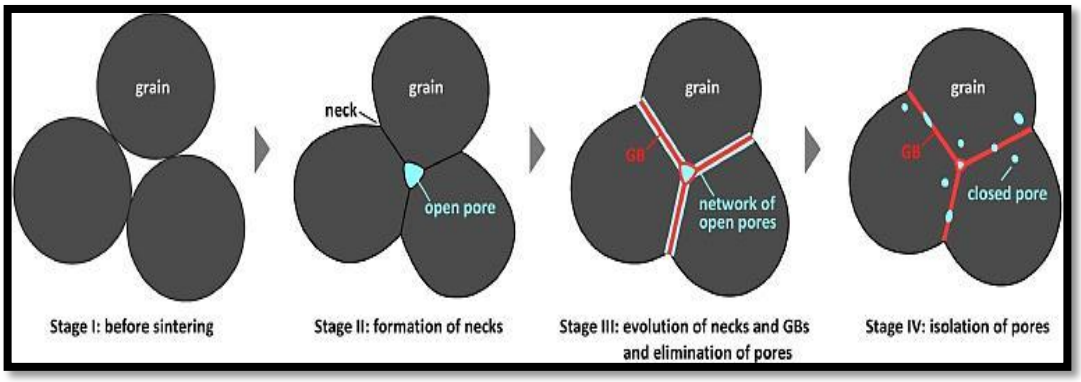


*Figure 27 Schematic diagrams of stages in solid-state self-sintering [185]*

where, $\gamma_{sv}$ is the surface energy of the pore surfaces and r is the radius of curvature of the pores. This shows that the pressure at the surface curvature migrates from the boundary towards the centre of the curvature (triple junction), filling the voids by consuming its surface energy. By assuming the surface energy $\gamma_{sv}$ = 1 J $m^{-2}$ and r = 0.5 µm, Lee et al. [186] was able to approximate the capillary driving force, p = 4 MPa, based on the equation 18. This equation also suggested that the driving force can be enhanced by using nanoparticles which provide high surface energies, thus requiring less energy to fill in the void by the migration of the nanoparticles.

The other factor that involves enhancing the driving force is the applied external pressures ($P_{appl}$). Therefore the equation 9 can be rewritten as

$$Driving\ force\ (P) = \frac{2\gamma_{sv}}{r} + P_{appl} \qquad Eqn\ 10$$

The equation 10 shows that the driving force for sintering is the sum of capillary and external pressure. Other methods such as hot isostatic pressing use external pressure of about 200 MPa would increase the densification rate by 50 times based on the previous assumption. In addition, the total sintering pressure will become the sum of the capillary and external pressures. Spark plasma sintering is another technique which involves an electric field, along with an external force, which further increases the densification rate. In this case, the driving force for sintering is the sum of the capillary force, external pressure and electric field. These methods are discussed as follows with the relevant literatures on the processing of transparent YAG.

#### *2.7.1.1 Grain growth*

Grain growth occurs due to the closure of isolated pores during the final stage of sintering. When the porosity decreases, it subsequently reduces the surface area of the pores, where the latter retards the grain growth. This results in decreasing grain boundary energy and provides the driving force for the grains to grow rapidly as the sample approaches full density.

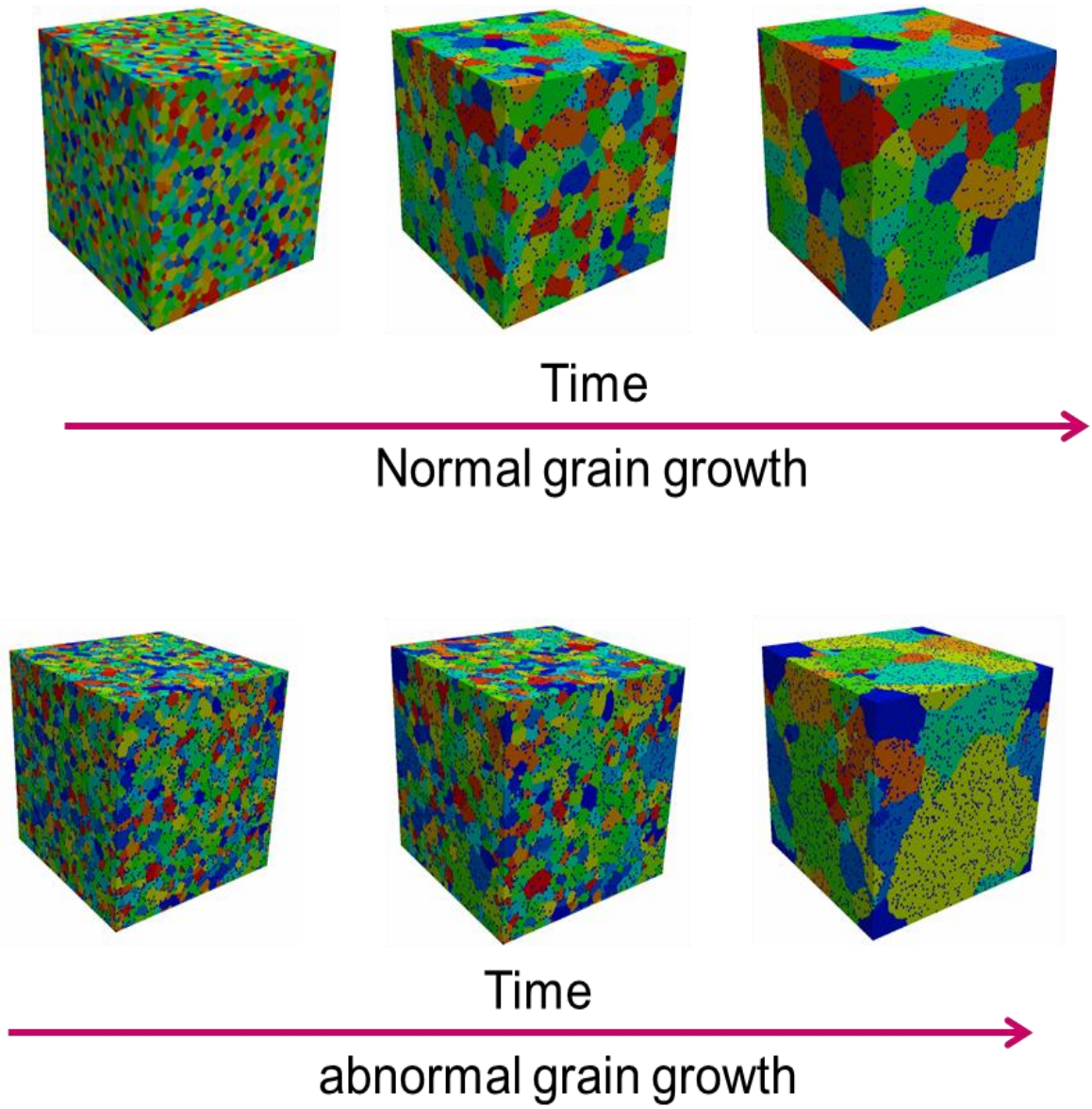


*Figure 28 Grain growth behavior of Nd:YAG as a function of silica content and temperature [187]*

Grain growth can be classified into normal and abnormal (or exaggerated) grain growth. The former is simple and the relative grain sizes are consistent with the annealing time, while the latter occurs by the development of some extremely large grains in a matrix of fine grains and results in a bimodal distribution of grains structure, Figure 28.

Several mechanisms have been studied and suggested different conditions favouring grain growth. These conditions are as follows:

1. Grain growth happens due to the migration of grain boundaries, but not because of the grain coalescence between the adjacent grains.
2. If the grain boundary migration is discontinuous, direction may change unexpectedly;
3. Curved grain boundaries migrate towards its centre of curvature due to the pressure exerted by the atoms in the grain boundaries.
4. The grain consumption rate becomes significant as the grains are about to disappear;

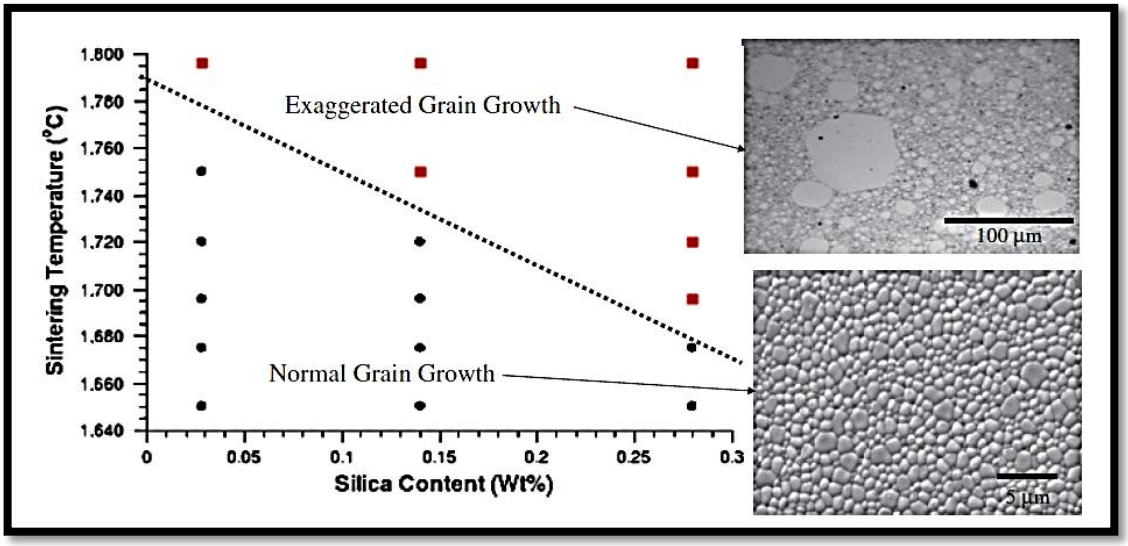


*Figure 29 Grain growth behavior of Nd:YAG as a function of silica content and temperature [186]*

On the other hand, when second phases are present in the grain boundaries, it reduces the grain mobility and so does the grain growth. This effect is limited to certain additives, however. When additives like silica were added into the ceramic matrix, an adverse effect is possible if the conditions are not optimised. Lee et al. [186] studied the effect of grain growth in Nd:YAG ceramics, their results suggest that the silica addition effectively changes the mass transport mechanism at the grain boundaries and results in abnormal grain growth with varying silica content and temperature conditions of the Nd:YAG ceramics, Figure 29. Therefore, it is vital to know about the sintering aids and their kinetics and grain growth mechanism for the fabrication of fine microstructured ceramics.

### 2.7.2 Sintering of transparent YAG ceramics

Transparent YAG has been fabricated using powders that have been synthesized by both chemical and solid state reactions. In both cases, this was achieved using vacuum sintering at temperatures between 1600°C to 1780°C under a vacuum of $5\times10^{-6}$ Torr over long holding periods. The vacuum sintering avoids oxidative degradation and helps in maintaining the chemical composition to avoid phase change of YAG [145]. As discussed earlier in the section 2.7, the basic mechanism in solid state sintering is the transport of material through volume diffusion along grain boundaries or through lattice dislocations. Sintering occurs according to the physical changes at different temperatures, essentially the removal of pores and strong bonding between the particles.

### 2.7.3 Pressure less sintering of YAG ceramics

Conventional sintering with a normal heat and soak temperature profile is called single step sintering. In this method, the green compacts are heated to a high temperature known as $T_1$ and held for several hours before being cooled to room temperature. This temperature profile is illustrated schematically in Figure 30 and the final density is achieved through solid state sintering as discussed above.

Conventional sintering with a modified temperature profile, Figure 30, is called two step sintering [87]. In this method, the green compacts are rapidly heated to a high temperature known as $T_1$, without a dwell period and then rapidly cooled down to a lower temperature known as $T_2$, and held at $T_2$ for a longer period. The first step is considered to be a pre-coarsening treatment where the closure of integral pores in the compact are delayed, creating a smoother pore channel. This results in all pores becoming subcritical and unstable against shrinkage due to the capillary forces. During the second step, the smoother pore channel delays the isolation of closed pores, allowing the controlled grain-boundary migration to facilitate grain-boundary diffusion of smaller grains with a uniform distribution. Thus the green body can be sintered without grain growth and can maintain the necessary nanostructure whilst exhibiting an increase in the final density.

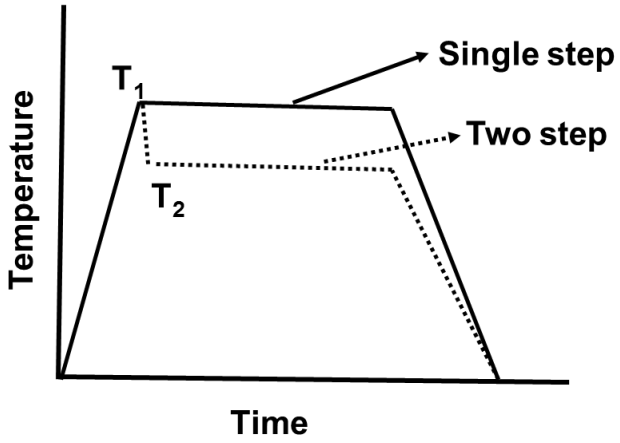


*Figure 30 Schematic diagram of conventional and two step sintering profiles*

Chen et al. [188] compared the calculated densification rate from two step sintering with the normalized Herrings model and found that the frozen microstructures decreased by a factor of 30 during the final densification from 85% to 99%. They reported that a high starting density at temperature $T_1$ ($T_1$ = 1700, 1750, 1800°C) was sufficient for the pores in YAG to become subcritical and unstable against shrinkage. Due to this, a smoother pore channel was formed amongst the YAG grains. The activation energy for the grain boundary diffusion was provided over the dwell period at temperature $T_2$ ($T_2$ = 1500, 1550, 1600°C). Therefore, full density of YAG was achieved by the controlled grain-boundary kinetics instead of thermo-dynamic diffusion.

### 2.7.4 Pressure assisted sintering of YAG ceramics

This process involves pressure and temperature in tandem, which allows the sample to sinter at lower temperatures when compared to the conventional sintering. Here, the pressure increases the driving force and reduces the sintering temperatures of the ceramic, which leads to fine microstructure of the ceramics after sintering. Hot pressing, HP, and Hot isotactic pressing, HIP, are the two common techniques, which uses pressure and temperature for sintering ceramics. In the last decade, electric field has also been used in combination with pressure and temperature in a process called spark plasma sintering (SPS). These techniques are used for producing transparent ceramics, which are discussed in this section.

### *2.7.4.1 Hot pressing of YAG ceramics*

Hot pressing technique has been used for sintering metals, intermetallic compounds and ceramics. However, hot pressed products are limited to simple geometries and they are often small billets to be machined to final shape. In this process, a uniaxial pressure of about 20 – 50 MPa is used in combination with high temperatures. Powder sample were prepressed at low pressures in a graphite die and loaded between two graphite punches in vacuum or inert atmosphere.

The heat is transferred by the induction coil surrounding the graphite die and to the sample via radiation/convection, Figure 31. On the application of pressure at the sintering temperatures, a diffusional material transport from grain boundary to neck, which is similar to the diffusional creep of ceramics, accelerates the sintering kinetics and resulted in full densification [182].

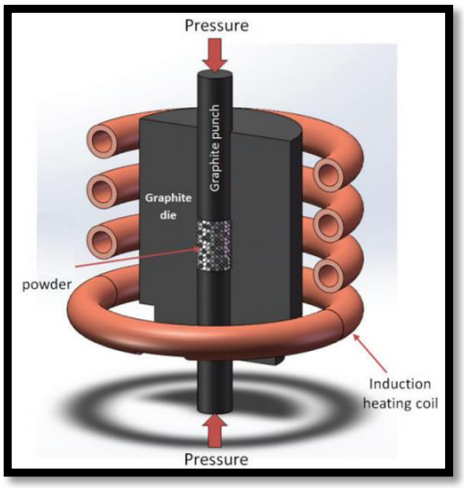


*Figure 31 Schematic of hot pressing [189]*

Very little research has been carried out using hot pressing of YAG ceramics. Naga et al. [190] fabricated Nd:YAG ceramics using the hot pressing approach. Their results suggest that the optical properties of the Nd:YAG samples with 0.5 wt % tetraethyl orthosilicate (TEOS) as sintering aid were equivalent to the single crystals when the samples were hot pressed at 1700°C for 1 h. They obtained a pore free microstructure with mean grain size of about 10 µm. This coarse grain structure is due to the inadequacy of pressure in this approach, hence, a high pressure technique is required to achieve fine microstructured ceramics.

### *2.7.4.2 Spark plasma sintering (SPS) of YAG ceramics*

Since the pressure is too low in hot pressing, the samples results in large grain sizes, which negatively influences the mechanical properties of transparent YAG. Therefore, a field assisted sintering (FAST) method under vacuum atmosphere has been employed to reduce grain growth and furthermore, to remove the entrapped pores in the grains and at triple junctions by grains migration [18]. However, instead of using very high temperatures, an applied pressure in tandem with an electrical current (DC, pulsed DC, or AC) is used in the SPS technique which results in smaller grains [191]. In SPS, the electric field is applied through an electrically conducting graphite pressure die, see Figure 32.

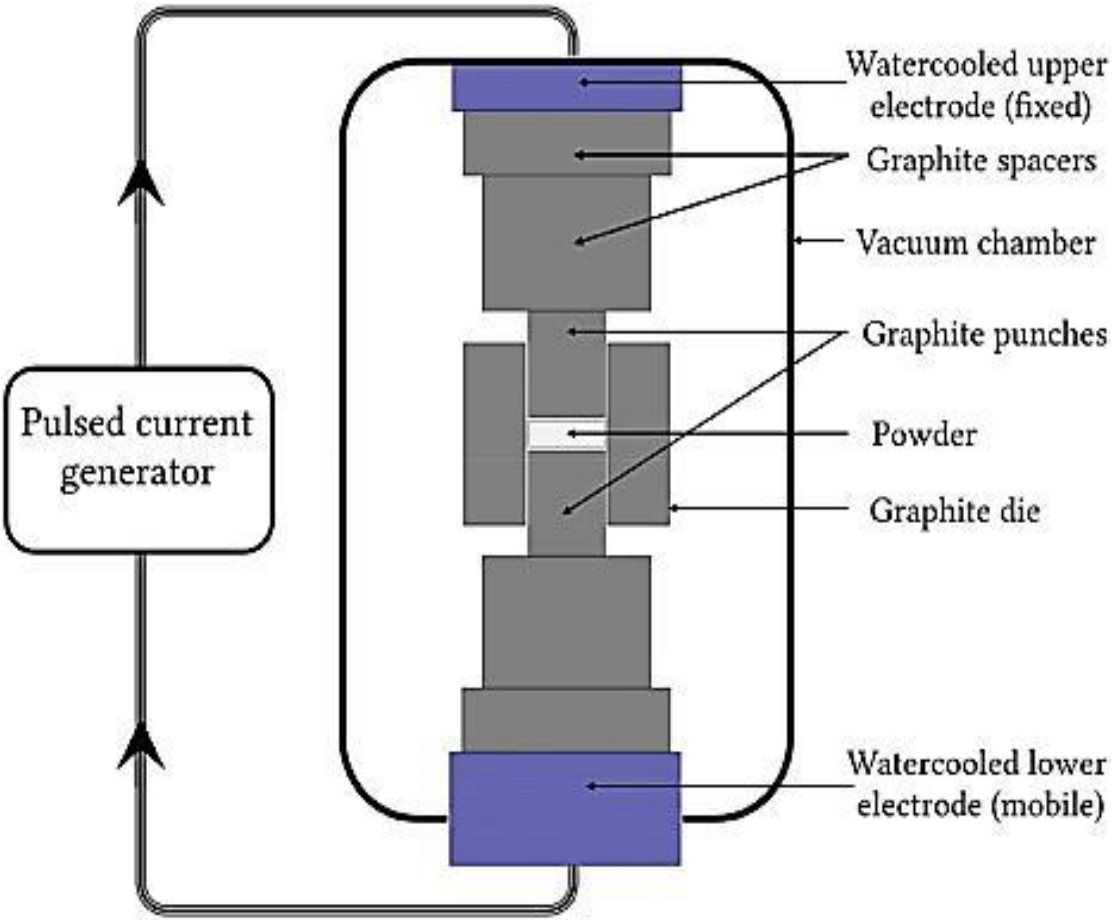


*Figure 32 Schematic of SPS setup [192]*

The local electric discharge takes place, leading to heat and mass transport. Hubert et al. [193] studied different experimental methods such as in situ AES, atomic emission spectroscopy, during spark plasma sintering. Their result concluded that

neither spark nor plasma generated throughout the sintering process. The rapid heating and cooling during the process might play a vital role in consolidating efficiently with fine microstructures. This also significantly reduces the processing time and therefore allows the ceramics to achieve their theoretical densities at a lower temperature compared to other more conventional processes. But the down side is carbon contamination from the graphite foils used in the SPS system, shown in Figure 32, which act as a sacrificing layer to avoid direct interaction of graphite punches with the sample.

Chaim et al. [194] investigated the feasibility of spark plasma sintering (SPS) for the fabrication of transparent YAG using a commercial YAG powder from Tal Materials Inc. They studied the effect of SPS duration and pressure and concluded that the densification mechanism depends on atomic transport at the particle interfaces, which also helps in retarding the grain growth of the sintered samples. Nevertheless, a YAG sample polished to 0.5 mm thickness reported very low in line transmission, ranging from 20-30% of the single crystal. The authors claimed that the low transmittance was due to the Rayleigh scattering at residual pores in the sintered samples after annealing. However, they completely ignored the carbon contamination from the graphite layers, which penetrates into the crystal lattice and very difficult to remove them even after polishing and annealing.

Frage et al. [195] addressed issues associated with the carbon contamination during SPS and concluded that the residual pores were due to the decomposition of entrapped carbon inclusions at the grain boundaries after annealing. They adapted their previous approach to produce transparent spinal using LiF (Lithium fluoride) as a cleansing agent [196], which reduced the carbon by volatilising CF (carbon - fluoride) species during annealing. They used a commercial YAG powder with a particle size of about 50 nm and varied the LiF content from 0.25 to 4 wt.%. However, increasing the LiF content significantly increased the grain size of the sintered samples and also increased the risk of sample fracture due to liquid phase sintering. They found 0.25 wt.% was suitable for producing crack-free, transparent YAG ceramics with a grain size of ~1.5 µm.

### *2.7.4.3 Hot isostatic pressing of YAG ceramics*

The problem associated with SPS can be resolved by using hot isostatic pressing (HIP). The main advantage of this process is the production of complex and large components, which makes it commercially used route. This process also involves pressure and temperature in tandem, which allows the sample to sinter at lower temperatures when compared to pressure-less sintering. Moreover, the pressure distribution across the sample is uniform, unlike SPS and hot pressing, both of which apply uniaxial pressure on the sample.

There are three methods to consolidate ceramics using hot isostatic pressing, as shown in Figure 33. In the encapsulation method, a pre-consolidated sample is enclosed in a glass or a metal container under vacuum and placed in a pressure vessel [197]. The compact is heated to the sintering temperature. When the gas pressure is increased to a predetermined threshold, the container shrinks around the sample and applies an isostatic pressure onto the green compact. Thus, the residual pores in the samples are eliminated by the application of compressive pressure to the sample whilst heating. The glass or metal layer does require subsequent removal, however.

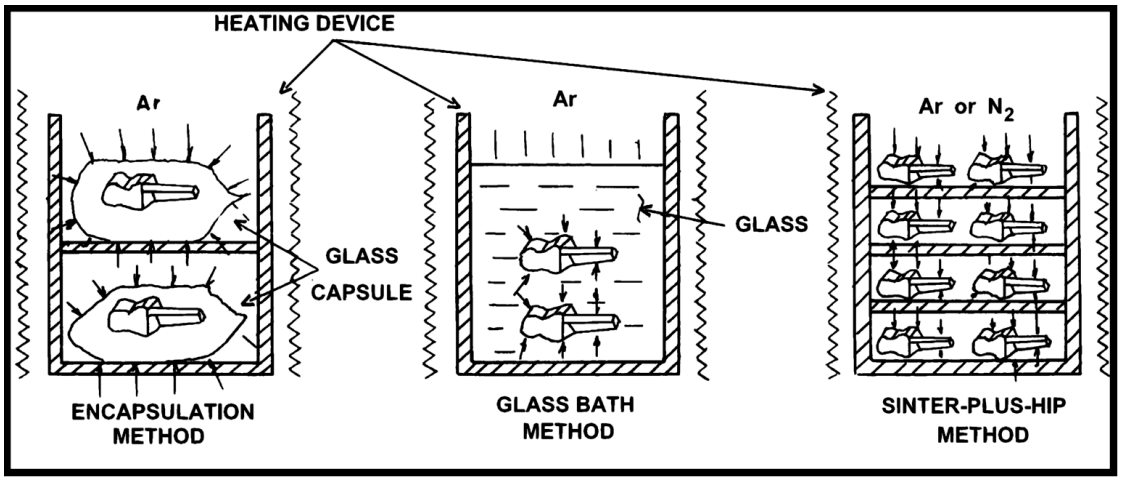


*Figure 33 Different methods of hot isostatic pressing [197]*

The second method is the glass bath method. Here, a green body is sintered isostatically whilst immersed in a powdered glass bath at a low softening temperature. It is similar to the previous method, but avoids the complicated encapsulation technique. On the other hand, low density samples can float on the

glass melt and the melt can also penetrate into them. Once again, the glass layer requires removal after the process is complete.

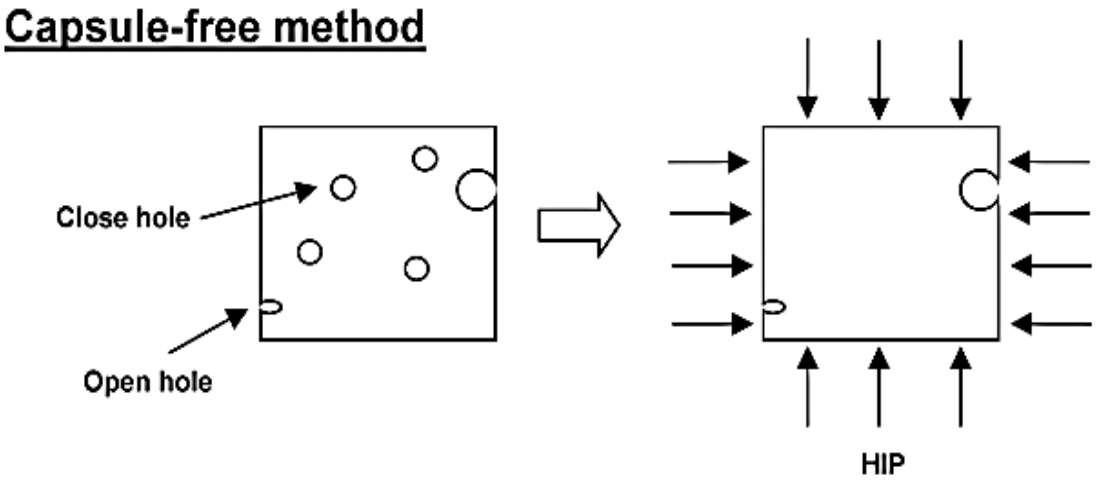


*Figure 34 Capsule free methods in HIP [197]*

To solve such problems, capsule free methods are highly preferable. This avoids sample contamination from the capsule and saves the cost of encapsulation. In addition, a large quantity of small components which have isotropic mechanical properties and high reliability can be produced using the HIP process [198, 199]. This technique evokes plastic deformation and creep deformation, which is induced by diffusion processes that are responsible for the removal of micro or nano pores in the pre-sintered ceramics [41]. The only disadvantage of the method is that pre-sintering of ceramics to close any porosity is required prior to HIP, see Figure 34, which can lead to unwanted grain growth. However, this process is more likely to produce homogeneous ceramic microstructures without any defects.

Figure 35 describes the microstructural model for removing the pores by the HIPing process [200]. It is very important to analyse the microstructure of the pre-sintered ceramics before HIP. It is very clear from the model that low temperature pre-treatment process isolates the pores at the triple junctions and during HIPing the latter can be completely eliminated to achieve full density [201]. High temperature pre-treatments can result in intragranular pores and it is an arduous task to remove them during HIP processing [186]. Note that intragranular pores can also form if hard agglomerates or uncrushed granules persist in the green samples.

Scientists further developed a continuous process combining pressureless-sintering followed by a HIP cycle, without intermediate cooling of the compact, called the ‘sinter plus HIP’ method. This is more advantageous than capsule free method because, with an intermediate cooling stage, grain coarsening is possible during the reheating stage. The lack of the intermediate stage limits grain growth and enhances the ability to produce fine microstructured ceramics.

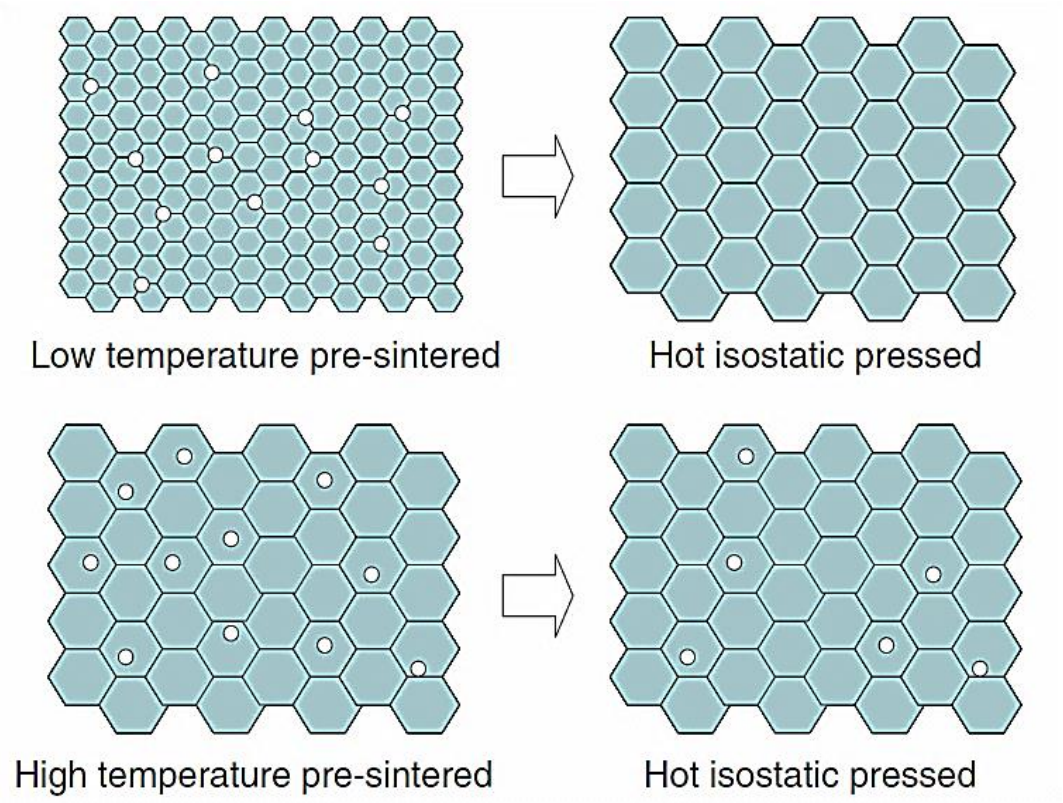


*Figure 35 Microstructure model for pore elimination by HIP [200]*

Since there are very limited publications on HIPing of pure YAG ceramics, the densification of Nd:YAG is briefly discussed here. Lee et al. [186] demonstrated the production of transparent Nd:YAG ceramics with 0.02 wt.% of $SiO_2$ doping using HIPing. They optimised the silica content to achieve dissolution in the YAG lattice and produced ceramics with a mean grain size of 2-3 microns. The pre-die pressed samples were pre-sintered to 98% density, to achieve closed porosity, in a vacuum furnace at 1600°C for 2 h and subsequently HIPed at 1750°C for 2 h at 200 MPa.

# 3 Experimental

This chapter describes the experimental procedure involved in this project. Figure 36 explains the complete work flow and the different characterisation techniques involved in each process. Initially, the YAG nano particles were synthesised using a number of different techniques and characterised completely. The best powder was then made into a colloidal suspension, which was further characterised to optimise the conditions suitable for spray freeze granulation. Then the granules were used to produce sintered samples using different sintering techniques to identify the best sintering route to produce fine microstructured ceramics.

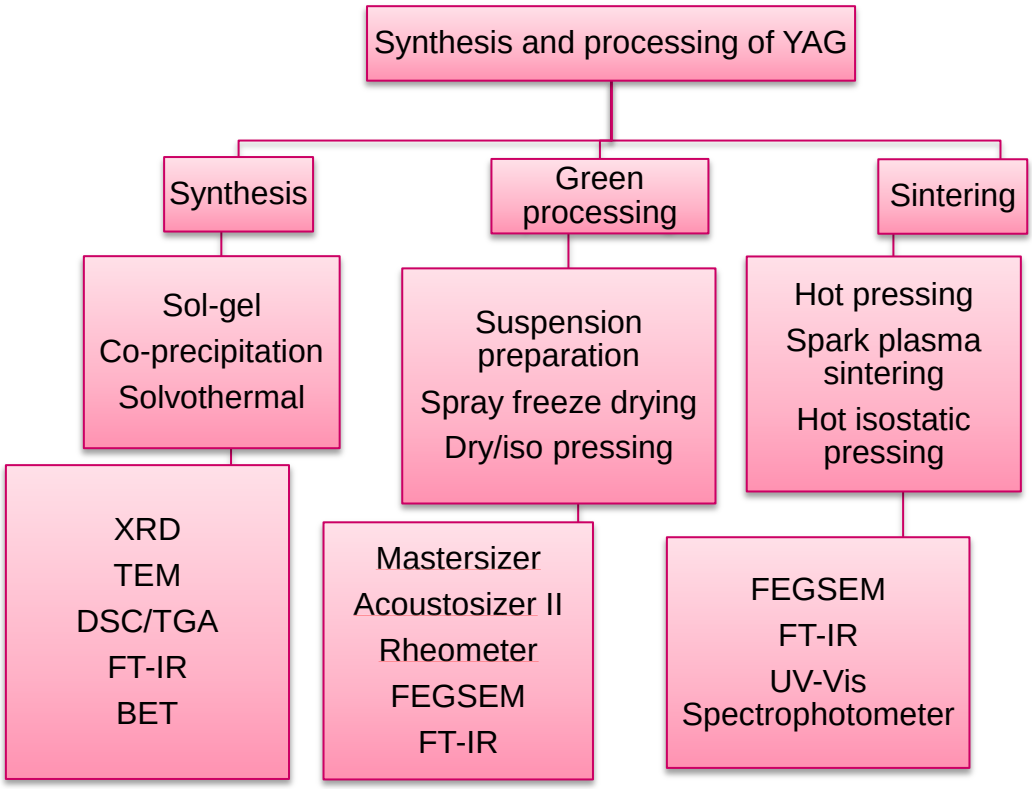


*Figure 36 Flowchart of overall experimental work*

All the synthesis experiments were performed inside a fume hood with proper extraction facilities. Precursors, chemicals and their role in this study are listed in Table 7. Moreover, general lab practice for the safe use and handling of chemicals were followed. Gloves, face mask (a particulate respirator, 9200 series-N95, Fisher scientific, Loughborough, UK), goggles, masks and lab coat were worn at all times when handling the chemicals and the nanoparticles.

*Table 7 Raw materials used in this project (*LR, laboratory reagent grade)*

| Technique | Chemicals | Molecular formula | Product source | Purity | Role |
|---|---|---|---|---|---|
| Sol-gel | Yttrium nitrate | $Y(NO_3)_3.6H_2O$ | Sigma Aldrich | 99.9 % | Source of $Y^{3+}$ ions |
| | Aluminium nitrate | $Al(NO_3)_3.9H_2O$ | Sigma Aldrich | ≥98.0 % | Source of $Al^{3+}$ ions |
| | Al metal powder | Al | Fisher Chemicals | *LR | Source of $Al^{3+}$ ions |
| | Citric acid | $C_3H_4OH\ (COOH)_3)$ | Sigma Aldrich | 99.5 % | Chelating agent |
| | Hydrochloric acid | HCl | Fisher Chemicals | 32.0% | Dissolve Al powder |
| Co-precipitation | Yttrium nitrate | $Y(NO_3)_3.6H_2O$ | Sigma Aldrich | 99.9 % | Source of $Y^{3+}$ ions |
| | Aluminium nitrate | $Al(NO_3)_3.9H_2O$ | Sigma Aldrich | ≥98 % | Source of $Al^{3+}$ ions |
| | Ammonium hydroxide | $NH_4OH$ | Fisher Chemicals | 35.0% | Precipitant |
| | Butanol | $CH_3\ (CH_2)_3\ OH$ | Fisher Chemicals | 99% | Azeotrope |
| Solvothermal | Yttrium nitrate | $Y(NO_3)_3.6H_2O$ | Sigma Aldrich | 99.9 % | Source of $Y^{3+}$ ions |
| | Aluminium nitrate | $Al(NO_3)_3.9H_2O$ | Sigma Aldrich | ≥98.0 % | Source of $Al^{3+}$ ions |
| | Yttrium acetate | $(CH_3CO_2)_3Y.6H_2O$ | Sigma Aldrich | 99.9 % | Source of $Y^{3+}$ ions |
| | Aluminium isoproxide | $Al[OCH(CH_3)_2]_3$ | Sigma Aldrich | ≥98 % | Source of $Al^{3+}$ ions |
| | Ethanol | $CH_3\ CH_2OH$ | Sigma Aldrich | 99.9 % | Supercritical solvent |
| | Isopropanol | $CH_3\ (CH_2)_2\ OH$ | Sigma Aldrich | 99.9 % | Supercritical solvent |
| | 1, 4 butanediol | $HOCH_2CH_2CH_2CH_2OH$ | Sigma Aldrich | 99.0 % | Subcritical solvent |

## 3.1 Commercial YAG

A commercial YAG obtained from (DGTec, France) was used for the initial experiments. To begin with, the commercial YAG powder was fully characterized using XRD, FEGSEM, Malvern Mastersizer and TEM. The powder characteristics of the commercial YAG are discussed in the next chapter. Since they were found heavily agglomerated we begin to synthesis own YAG powders as below

## 3.2 Synthesis of yttrium aluminium garnet (YAG) powders

After a detailed literature review on YAG synthesis, sol-gel and co-precipitation methods were found to offer the potential to be economical amongst the range of wet chemical routes to synthesise nanocrystalline YAG and hence these were investigated. Solvothermal synthesis, which requires expensive autoclaves to synthesise YAG nanoparticles, was also examined because the focus of the project was to investigate the effect of nanoparticles on reducing sintering to achieve fine microstructured ceramics without compromising their quality. The comparison of the three processes gave a clear indication of the potential alternatives for the production of nanoparticles with minimal agglomeration in an effective way.

### 3.2.1 Sol-gel synthesis of YAG using nitrate precursors

Yttrium nitrate, $Y(NO_3)_3.6H_2O$, and aluminium nitrate, $Al(NO_3)_3.9H_2O$, were used as the source of $Y^{3+}$ and $Al^{3+}$ for synthesising YAG ($Y_3Al_5O_{12}$) using the sol-gel method and citric acid was used as a chelating agent. A stoichiometric ratio of 3:5 (Y:Al) was prepared by mixing 0.6M $Y(NO_3)_3.6H_2O$ and 1M $Al(NO_3)_3.9H_2O$ in a 1M citric acid solution. The schematic representation of the sol-gel process is shown in Figure 37.

Initially, citric acid ($C_3H_4OH\ (COOH)_3$) was mixed with deionised water ($H_2O$) to prepare the 1M citrate solution. This resulted in partial dissociation of $H^+$ ions from the functional group ligands (COOH) and protonation of the water. The reaction during the initial mixing is given in equation 11.

$$\boldsymbol{C_3H_4OH(COOH)_3 + H_2O \rightarrow C_3H_4OH(COO^-)_3 + H_3O^+} \quad \textit{Eqn 11}$$

The solvation of the metal cations, introduced as an aqueous metal nitrate solution is described by equation 12 [144].

$$\begin{pmatrix} \boldsymbol{Al(NO_3)_3.9H_2O} + \\ \boldsymbol{Y(NO_3)_3.9H_2O} + \boldsymbol{H_2O} \end{pmatrix} \rightarrow \begin{pmatrix} \left(((\boldsymbol{OH_2})\,\boldsymbol{Al})^{1+} - (\boldsymbol{Y}\,(\boldsymbol{OH_2}))^{1+}\right)_{\boldsymbol{aq}} \\ +\,2\,\boldsymbol{NO_3^-} + \boldsymbol{H_2O} \end{pmatrix} \quad \textit{Eqn 12}$$

The next step was adding the nitrate solution of $Y(NO_3)_3.6H_2O$ and $Al(NO_3)_3.9H_2O$ into the citrate solution in a round bottom flask, which was equipped with a magnetic stirrer and a refluxing condenser. The reaction flask was immersed in a thermostatic oil bath and refluxed at 90±10°C for 24 hours to achieve homogenous mixing. The transparent precursor sol obtained underwent a substitution reaction, which reacted to form yttrium-aluminium citrate by replacing hydroxyl ions.

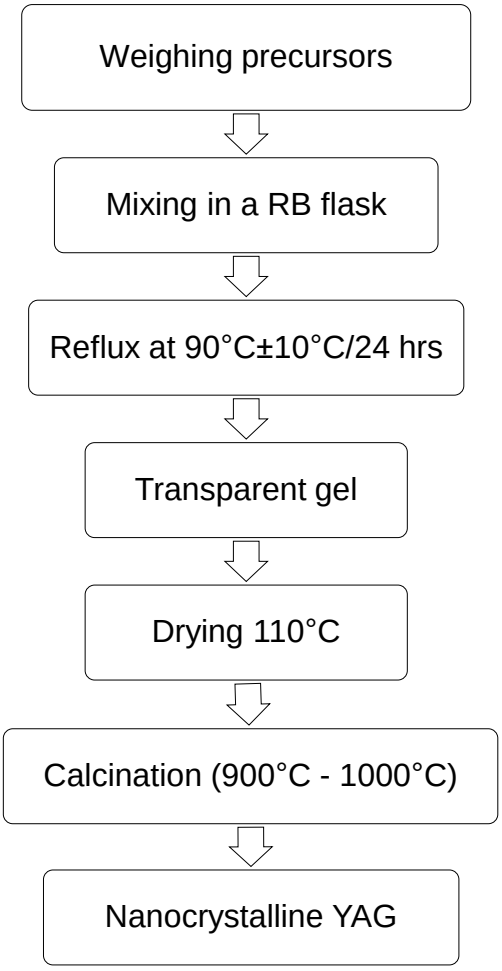


*Figure 37 Flow chart of the sol-gel process (nitrate precursor route)*

The formation of bonding between the citrate anions and metal cations at the molecular level, which forms a co-ordinate complex structure between the metal cations [202], is described by the overall hydrolysis (substitution) reaction given in equation 13.

$$\begin{pmatrix} (((\boldsymbol{OH_2})\,\boldsymbol{Al})^{1+} - (\boldsymbol{Y}\,(\boldsymbol{OH_2}))^{1+})_{\boldsymbol{aq}} + \\ 2\boldsymbol{NO_3^-} + \boldsymbol{C_3H_4OH}(\boldsymbol{COO^-})^{3-} + \boldsymbol{H_3O^+} \end{pmatrix} \rightarrow \begin{pmatrix} (\boldsymbol{COO^-})^{\boldsymbol{3}}\boldsymbol{Al^{3+}} - \boldsymbol{Y^{3+}}(\boldsymbol{COO^-})^{\boldsymbol{3}} \\ +\, 2\boldsymbol{NO_3^-} + \boldsymbol{H_2O} + \boldsymbol{H_3O^+} \end{pmatrix} \quad \textit{Eqn 13}$$

After mixing, the precursor sol was transformed into a gel matrix due to the rapid increase in viscosity of the sol at 100±5°C, which was accompanied by the evaporation of solvent molecules. During gelation, polymerisation was initiated and formed a three-dimensional coordinate complex structure between the metal cations and citrate anions [203].

The transparent gel obtained was oven dried at 110°C for 24 h to form a fluffy mass and subsequently ground using a pestle and mortar. The resultant powder was calcined in a silica crucible at temperatures in the range 950 - 1000°C in air at a heating/cooling rate of 10°C $min^{-1}$ to obtain single phase YAG. Calcination was performed in a box furnace equipped with SiC heating elements.

### 3.2.2 Sol-gel synthesis of YAG using metal precursors

The main aim of this approach was to replace the $Al(NO_3)_3.9H_2O$ used in section 3.1.1 with Al metal powder, a cheaper alternative with a view to producing high quality YAG nanoparticles at a lower cost.

The different weight fractions of Al:$Al(NO_3)_3.9H_2O$ used in this synthesis route are given in Table 8. In the process of replacing the Al metal powder, an intermediate metal-hydrochloric acid treatment was introduced, Figure 38, to remove the passive oxide layer on the surface and to dissolve the Al metal powder afterwards. Since citric acid is a weak acid, the concentration of 1M citric acid reported by Qingmei et al. [204] was found to be inadequate to react with the passive oxide layer of the Al metal powder.

*Table 8 Chemical composition of sol-gel YAG using metal precursor*

| **Precursors** | **0% Al metal** | **17% Al metal** | **34% Al metal** | **67% Al metal** | **100% Al metal** |
|---|---|---|---|---|---|
| Al (powder) | - | 0.2 M | 0.4 M | 0.6 M | 1 M |
| $Al(NO_3)_3 .9H_2O$ | 1 M | 0.8 M | 0.6 M | 0.4 M | - |
| $Y(NO_3)_3 .6H_2O$ | 0.6 M | 0.6 M | 0.6 M | 0.6 M | 0.6 M |
| $H_2O$ | 4 M | 4 M | 4 M | 4 M | 4 M |
| Citric acid | 1 M | - | - | - | - |
| HCl | - | 6 M | 6 M | 6 M | 6 M |

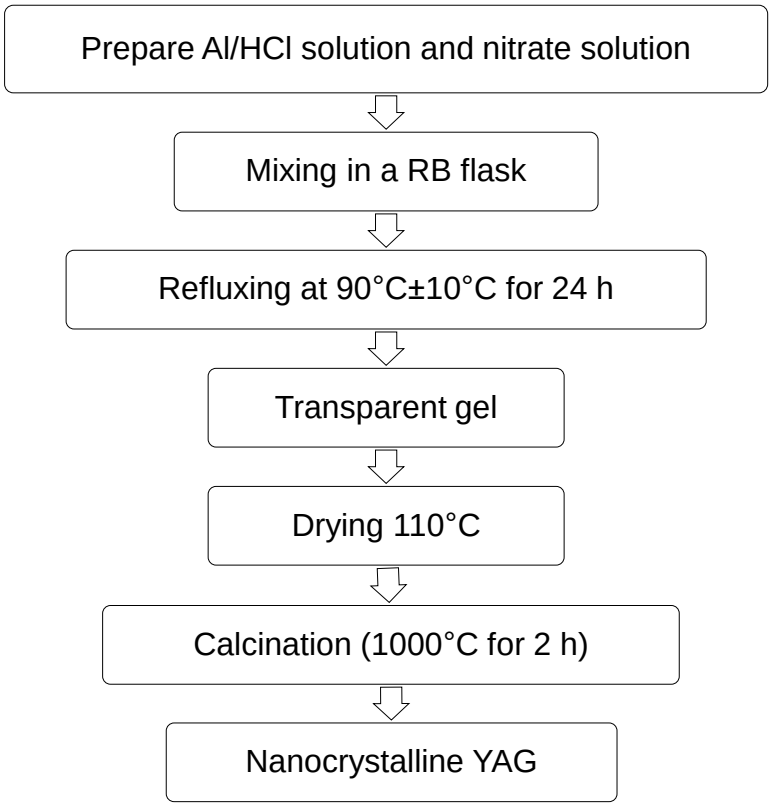


*Figure 38 Flow chart of the sol-gel process (metal precursor route)*

Therefore, the Al metal powder was dissolved in 6M HCl solution (strong acid) under mild stirring at room temperature; the powder was gradually added into the HCl to avoid a vigorous exothermic reaction between Al and HCl [205], as given by

equation 14. This was found to dissolve the oxide layer successfully and the Al metal powder thereafter [206].

$$2Al + 6HCl \rightarrow 2AlCl_3 + 3H_2 \qquad Eqn\ 14$$

Then the nitrate solution of yttrium and aluminium ions (after 30 min of mixing) was added to the Al/HCl solution (only yttrium nitrate solution was added to the 100% Al metal precursor batch). As for the route involving aluminium nitrate, homogenous mixing was achieved in a round bottom flask under refluxing conditions in a thermostatic oil bath at 90±10°C for 24 hours. In the beginning, the precursor sol was black in colour. As the reaction proceeded the sol turned transparent, this was an indication of homogenous mixing and the complete dissolution of Al in the solvent. In addition, the nitrate ions react with the chloride ions to form NOCl; a brown gas evolved during refluxing the sol indicating the latter occurred [207].

Hydrolysis and condensation reactions of mixed metal-nitrate precursor

$$\begin{pmatrix} AlCl_3 + Al(NO_3)_3.9H_2O + \\ Y(NO_3)_3.9H_2O + H_2O \end{pmatrix} \rightarrow \begin{pmatrix} (((OH_2)\,Al)^{1+} - (Y\,(OH_2))^{1+})_{aq} \\ + NO_3^- + H_2O + H_3O^+ + (NOCl)_g \uparrow \end{pmatrix} \qquad Eqn\ 15$$

Hydrolysis reaction and condensation reactions of 100 % metal precursor

$$\begin{pmatrix} AlCl_3 + Y(NO_3)_3.9H_2O \\ + H_2O \end{pmatrix} \rightarrow \begin{pmatrix} (((OH_2)\,Al)^{1+} - (Y\,(OH_2))^{1+})_{aq} \\ + NO_3^- + H_2O + H_3O^+ + (NOCl)_g \uparrow \end{pmatrix} \qquad Eqn\ 16$$

During refluxing, the $H_2O$ molecules broke into aqueous protons ($H^+$) and hydroxo ($OH^-$) ligands [208, 209]. The metal ions in the solution act as a Lewis acid (an electron pair acceptor) and draw the broken hydroxo ligands to form metal hydroxides ($Al(OH)_2$ and $Y(OH)_2$.

The $OH^-$ ligands that were present in the co-ordination sphere of metal ions acts as an attacking group and the condensation reaction proceeds further [144]; this resulted in gelation of the transparent sol, which was accompanied by the rapid increase in viscosity of the sol at 110°C. The hydrolysis and condensation reactions for the $Al/Al(NO_3)_3.9H_2O$ mixed fractions are expected to follow equation 15 and for 100% Al metal precursor, the reaction could follow equation 16. The transparent gel matrix was further dried at 110°C for 24 h into a fluffy mass and subsequently ground using a pestle and mortar prior to calcination at 1000°C for 1 h.

### 3.2.3 Co-precipitation synthesis of YAG using nitrate precursors

The reverse strike co-precipitation method was employed to synthesis nanocrystalline YAG particles. This method was chosen as an alternative synthesis route to those described earlier due to its potential to work in alkaline conditions involving multi-cation materials such as YAG ($Y_3Al_5O_{12}$) and $BaTiO_3$ etc.

The schematic representation of the co-precipitation process is shown in Figure 39. $Y(NO_3)_3.6H_2O$ and $Al(NO_3)_3.9H_2O$ were used as the source of $Y^{3+}$ and $Al^{3+}$ions and $NH_4OH$ was used as a precipitant solution. By this method, the precipitates were tailored to form a core shell structure in a way that the precursors themselves reduce agglomeration during calcination at high temperatures.

Since the precipitating conditions for $Y^{3+}$ and $Al^{3+}$ ions are different, $Y^{3+}$ ions precipitates at pH 8.1 whilst $Al^{3+}$ precipitates at pH 3.5 [128], controlling pH is considered to be the most important factor during co-precipitation reactions. If the pH of the precipitant solution ($NH_4OH$) is not maintained uniformly, heterogeneous precipitation is possible, which could lead to the formation of intermediate phases in the resultant YAG powder.

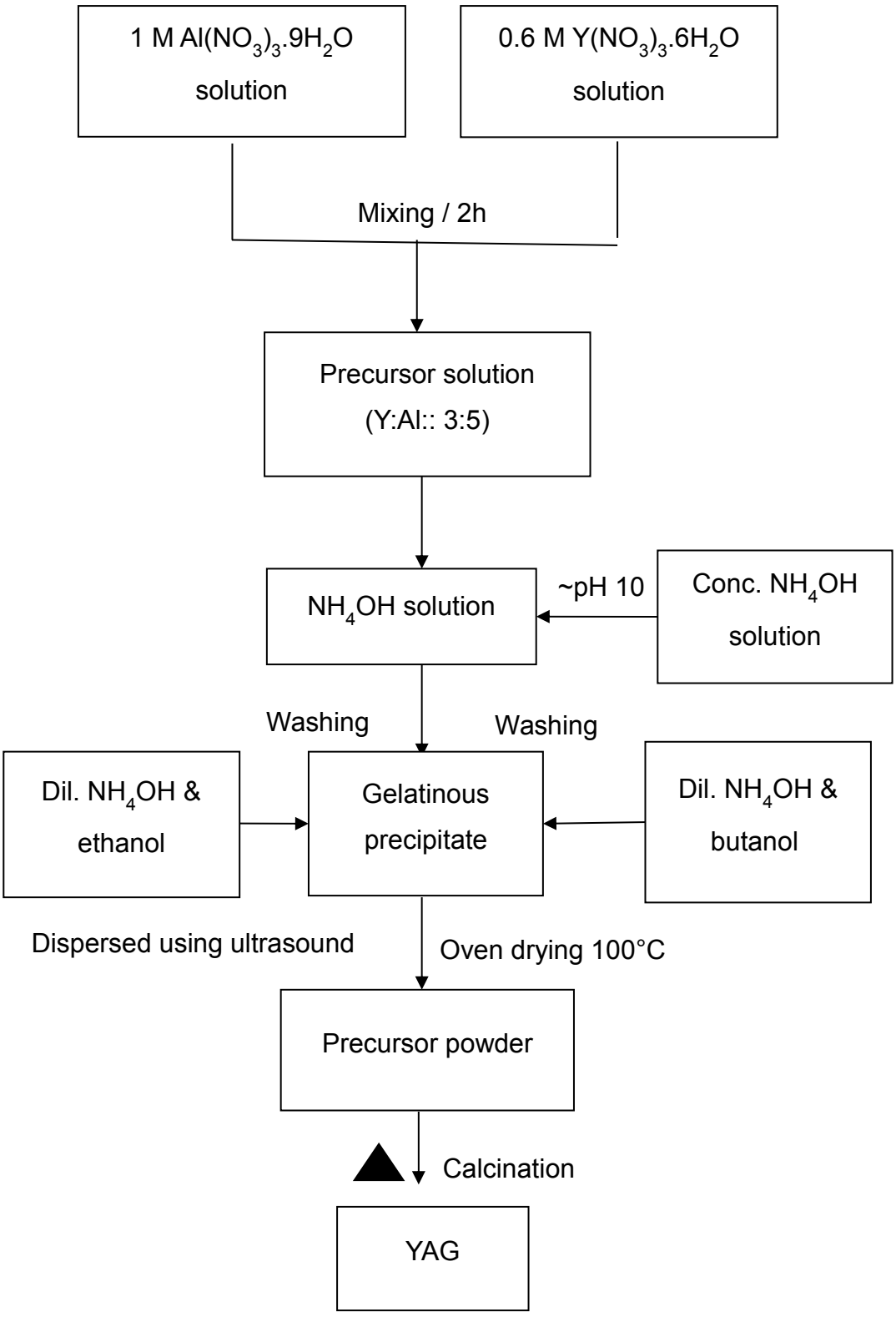


*Figure 39 Schematic representation of co-precipitation process*

The precursor solution of $Y^{3+}$ and $Al^{3+}$ ions was prepared by mixing 1M $Al(NO_3)_3.9H_2O$ and 0.6M $Y(NO_3)_3.6H_2O$ aqueous solutions for 2 hours, equation 17. Then the resulting solution was taken in a burette and added drop-wise onto 200 ml of aqueous $NH_4OH$ precipitant solution whilst simultaneously stirring and maintaining the pH at 8.20±0.05. The presence of nitrate ions in the precursor solution makes it even more critical to sustain the pH for precipitation; therefore concentrated $NH_4OH$ solution of pH 10 was added concurrently to maintain the pH. In the present work, the concentration ratio of the precursor solution (Y:Al) was kept at <1, a narrow pH window (±0.05) was maintained and a precipitation rate of about 4 ml $min^{-1}$ was used to control the nucleation and growth of the homogenous precipitates.

$$\begin{pmatrix} \boldsymbol{Al(NO_3)_3.9H_2O} + \\ \boldsymbol{Y(NO_3)_3.9H_2O} + \boldsymbol{H_2O} \end{pmatrix} \rightarrow \begin{pmatrix} (((\boldsymbol{OH_2})\,\boldsymbol{Al})^{1+} - (\boldsymbol{Y}\,(\boldsymbol{OH_2}))^{1+})_{\boldsymbol{aq}} \\ +\,2\boldsymbol{NO_3^-} + \boldsymbol{H_2O} \end{pmatrix} \qquad \textit{Eqn 17}$$

The effect of water removal in the precipitates was also investigated by using two different washing media, ethanol and butanol. The resultant precipitate was filtered, washed three times with dilute ammonia solution of pH 8.2 to remove nitrate residues, and then the filtered precipitate was dispersed with 20 ml of *n*-butanol or ethanol using ultrasound for two minutes via a KS150 ultrasonicator (Kerry Ultrasonics Ltd., Skipton, U.K.). Note that an ultrasound probe with a power of 75 W and amplitude of about 14 mm was used for all the ultrasonic dispersions involved in this project. The dispersed precipitate was dried at 100°C for 24 h in an oven drier and the resultant dried mass was gently ground using the pestle and mortar. The ground precursor powder was calcined in a silica crucible between 900 - 1000°C in air at a heating/cooling rate of 10°C $min^{-1}$ in a box furnace fitted with SiC heating elements.

### 3.2.4 Solvothermal synthesis of nanocrystalline YAG

In the previous methods, only the effect of temperature during the calcination stage was used to crystallise the YAG nanoparticles. This resulted in severe agglomeration due to the drying and calcination steps. In this approach, the latter steps were avoided and the nanoparticles were crystallised in a liquid medium and kept suspended to avoid the agglomeration.

#### *3.2.4.1 Solvothermal synthesis using inorganic (nitrate) precursors*

The precipitates of yttrium and aluminium hydroxide were prepared using the same reverse strike co-precipitation procedure outlined in section 3.2.3 and the resultant precipitate was filtered and washed three times with water to remove nitrate and ammonium residues. Then the filtered precipitate was redispersed with different solvents including ethanol, propanol and 1, 4 butanediol using ultrasound for 5 minutes. The resultant precipitate solutions were processed in an autoclave with a 400 ml volume reactor (Amar Equipment PVT Ltd, India) at different temperatures and pressures to investigate the formation of YAG nanoparticles. The experimental conditions investigated on different solvents with nitrate precursors are tabulated in Table 9. Note that only less than half of the volume (<200 ml) of the autoclave was filled with the dispersed precipitate for any given experiment. The yellow suspension obtained in each case after the process was subsequently centrifuged at 3500 rpm and washed three times using ethanol to remove the residues. The suspension became white after washing and was subsequently dried at 60°C for 24 hours and ground using the agate pestle and mortar for further analysis.

#### *3.2.4.2 Solvothermal synthesis using organic precursors*

A simple protocol was used to prepare YAG nanoparticles using organic precursors; no tight control of precipitation or vigorous acidic mixing was involved in this approach. The stoichiometric ratio of 3Y : 5Al was prepared by mixing the calculated amounts of 0.6M $Y(CH_3CO_2)_3.6H_2O$ and 1M $Al(OCH(CH_3)_2)_3$ metal organic precursors mixture in 1M 1, 4 butanediol (1, 4 BD) solvent.

The mixture was taken in the autoclave chamber and processed at different temperatures and pressures to investigate the formation of YAG nanoparticles, Table 9. The resulting white suspension obtained after the process was subsequently centrifuged at 3500 rpm and washed three times using ethanol to remove the

residues. The washed YAG suspension was dried at 60°C for 24 hours and ground using the agate pestle and mortar for further analysis.

*Table 9 Experimental conditions investigated for inorganic and organic precursors with different solvents*

| Precursor type | Solvent | Conditions |
|---|---|---|
| Inorganic precursors (yttrium nitrate and aluminium nitrate) | Ethanol | 270°C for 2 h and 7.9 MPa |
| | | 270°C for 2 h and 8.5 MPa |
| | | 275°C for 2 h and 8.5 MPa |
| | 2-propanol | 270°C for 2 h and 8.5 MPa |
| | | 290°C for 2 h and 8.5 MPa |
| | | 300°C for 2 h and 8.2 MPa |
| | | 300°C for 2 h and 8.5 MPa |
| | 1-4 butanediol | 300°C for 2 h and 8.5 MPa |
| Organic precursors (yttrium acetate and aluminium isopropoxide) | Ethanol | - |
| | 2-propanol | 300°C for 2 h and 8.5 MPa |
| | 1-4 butanediol | 270°C for 2 h and 2.0 MPa |
| | | 280°C for 2 h and 6.0 MPa |
| | | 300°C for 2 h and 6.0 MPa |
| | | 300°C for 2 h and 7.0 MPa |
| | | 300°C for 2 h and 8.5 MPa |

Note: All characterisation of the YAG powders is described in section 3.7

## 3.3 Suspension preparation

Based on the subsequent characterisation of each nanopowder, those synthesised using the solvothermal approach with the organic precursors (section 3.1.5) were considered the best quality YAG powders. This synthesis route yielded a non-aqueous suspension; this was in turn used to produce an aqueous suspension, Figure 40.

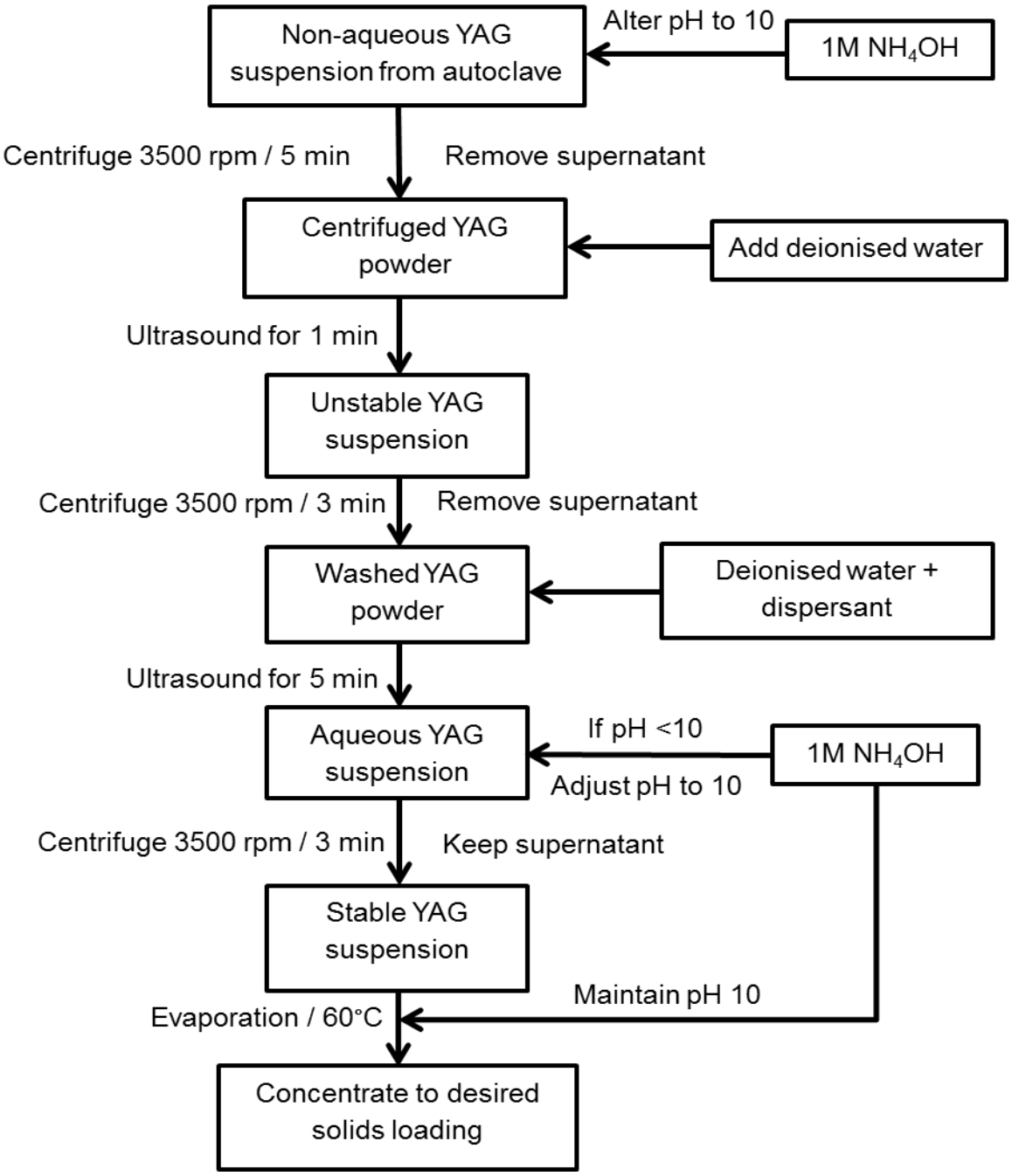


*Figure 40 Flowchart of YAG suspension preparation*

In order to avoid the agglomeration that occurs naturally due to drying, the as-synthesised suspension was centrifuged, however since this was difficult the suspension was initially treated with $NH_4OH$, Fisher Chemicals, Loughborough, UK, to modify the pH from 3 to 10 and then centrifuged at 3500 rpm for 5 minutes. This separated the YAG particles from the solvent medium used for synthesis. The supernatant was then decanted to leave behind the YAG powder sediment and deionised water added; the sediment was subsequenty dispersed with ultrasound for 1 minute**.** The resultant unstable YAG suspension was then centrifuged a second time to eliminate the residual solvents and leave a washed YAG sediment. This step was repeated a further three times. Then a desired volume of $NH_4PAA$ (Dispex A40, 40% ammonium polyacrylate of average molecular weight ~3500, BASF, Bradford, UK) mixed with deionised water for 30 minutes was added to the washed YAG sediment, which was dispersed again with ultrasound for 5 minutes to form a stable aqueous YAG suspension. The latter was once again centrifuged, this time however the YAG particles stayed dispersed and only inclusions were removed.

Table 10 shows the quantities of dispersant, deionised water and the YAG powders taken to produce suspension in this project. The suspension prepared up to this stage in the process was dilute, with a solids content of about 5 wt.% and a pH of about 10. This suspension was then concentrated by evaporation at 60$^{o}$C up to a solids loading of 50 – 60 wt.%. During the concentration 1M $NH_4OH$ was added concurrently to maintain the pH of the suspension at 10.

*Table 10 Quantities of the ingredients for the preparation of YAG suspensions*

| **$NH_4PAA$** | **Deionised water** | **ST-nYAG powders** |
|---|---|---|
| 1.5 wt % | 93.5 wt % | 5 wt % |
| 3.0 wt % | 92.0 wt % | 5 wt % |
| 5.0 wt % | 90.0 wt % | 5 wt % |

### 3.3.1 Rheology of the suspensions

The rheological behaviour of the YAG suspensions was studied by measuring the viscosity and shear stress at varying shear rates using an Anton Paar Rheolab QC viscometer (Anton Paar GmbH, Österreich, Austria), which was equipped with a computer for data acquisition. A concentric cylinder was used as a sample container in which a 20 ml YAG suspension was placed for the measurements. The viscosity (η) and shear stress (τ) were measured as a function of increasing and decreasing shear stress from 1 $s^{-1}$ to 1000 $s^{-1}$ and the effect of ultrasound, solids loading and ageing on the rheology of the YAG suspensions were also studied. A KS150 ultrasound probe (Kerry Ultrasonics Ltd., Skipton, U.K.) was used to disperse the suspensions. Note that the concentrated suspension was taken in a beaker and placed in a water bath to avoid excessive heating of the suspension during irradiation of the ultrasound. The rheology of the suspensions was performed at room temperature and three trials were carried out for each suspension to minimise the error.

### 3.3.2 Particle Size Distribution

The particle size distribution from 0.2 to 2000 µm of the YAG suspension was determined using a dynamic laser light scattering technique (Malvern Mastersizer 2000, UK). This method requires physical properties such as density (4.55 g $cm^{-3}$) and the refractive index (1.83) of the material being measured. After initialising the equipment, 800 ml of water was taken in a beaker and the background of the bubbles generated during the process was eliminated and then two drops of YAG suspension was added into the beaker. The Mastersizer measured the intensity of the light scattered as a beam passed through the dispersed particles and the data was analysed to calculate the particle size distribution using the Mastersizer software.

### 3.3.3 Zeta potential measurements of the suspensions

The electro-kinetic behaviour of the suspensions was characterised using an Acoustosizer II (Colloidal Dynamics, Florida, USA). Two modes of experiments were conducted;

1. Concentration series

2. Potentiometric titration

In the concentration series, a dilute YAG suspension of 5 wt.% solids loading was used to optimise the ammonium polyacrylate content required to generate a very high zeta potential at the surface of the particles via an electro-steric mechanism. Since the viscosity of the as-received dispersant was very high, the ammonium polyacrylate was diluted to 20 wt.% and titrated with the suspension to record the increase in zetapotential as a function of dispersant content. The zeta potential was recorded for every 0.5 wt.% of dispersant added to the suspension up to 5 wt.%. This analysis provided the change in electro kinetics associated with the interaction of the dispersant with the ceramic particles and identified the most effective concentration of a dispersant to produce stable suspension.

Potentiometric titration was performed to optimise the pH to maintain a stable suspension. Automatic titration of acid and base were performed using the Acoustosizer II; this facilitated the measurement of zeta potential over a wide range of pH from 2 to 12. In the potentiometric measurement, the dilute YAG suspension with the optimised amount of dispersant from the concentration series was used to prepare the suspension. The pH of the suspension was altered using 0.1 M HCl/NaOH solution (Fisher, UK) and the change in the zeta potential was measured. This helped to identify the isoelectric point (IEP) of the YAG suspension, which was an important factor for avoiding flocculation of the particles and to alter the viscosity of the suspensions.

### 3.3.4 Addition of foaming agent

To assist with the production of flowable, crushable granules via spray freeze drying (see section 3.4), a foaming agent (from the patent by Ketharam et al. [175] at Loughborough, UK, hereafter called sublimable additive) of 2 vol % [164] was mixed with the concentrated suspension at room temperature for 30 minutes in a beaker covered with a parafilm prior to SFD. The addition of foaming agent weaken the granules on freeze drying and helps in crushing the granules into fine particles at low pressure, ~250 MPa, during compaction.

## 3.4 Spray freeze drying of granules

As described in section 2.6.3, flowable and crushable granules are required for dry forming. With nanoparticles this is not easy to achieve, but work by other researchers at LU has resulted in a patented spray freeze drying (SFD) process, section 2.5 [164, 176, 210]. The schematic representation of the process is shown in Figure 41.

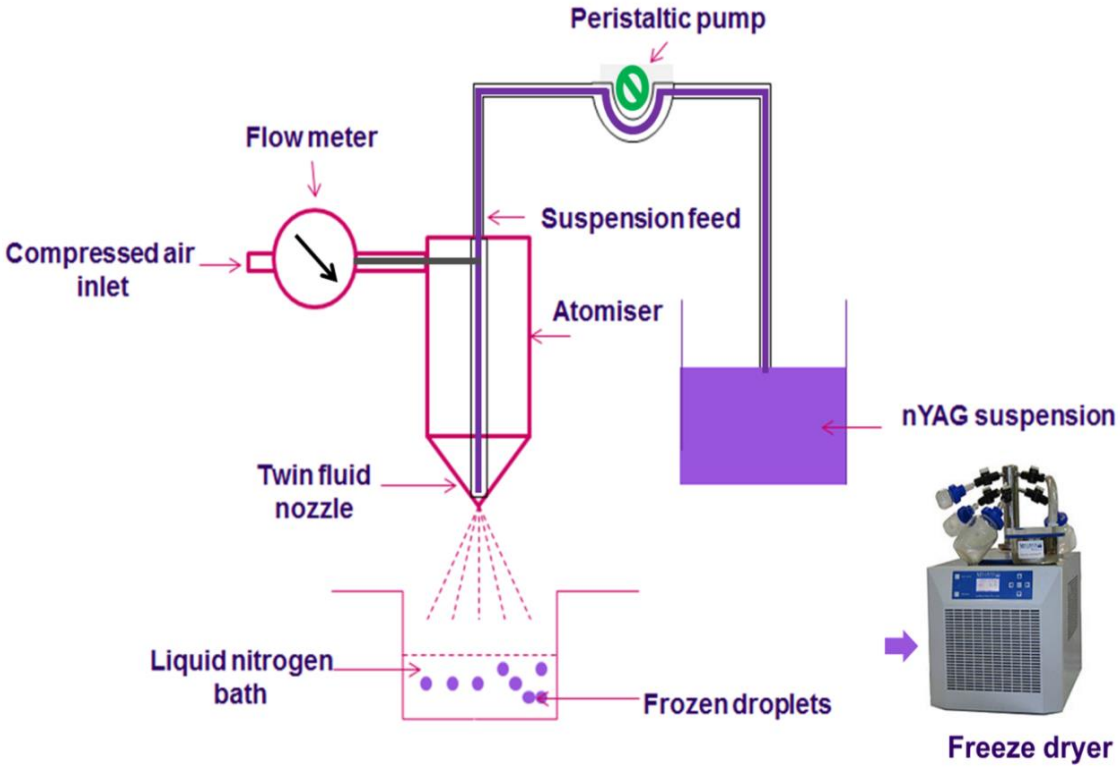


*Figure 41 Schematic representation of SFD process at LU*

In this work, the concentrated YAG suspension described in section 3.3 with ~55 wt.% solids loading and containing 2 vol% of the sublimable additive was used to produce SFD granules. The suspension was fed into an atomiser with the help of a peristaltic pump, (a Masterflex peristaltic pump, Cole-Parmer, London, UK), at a flow rate of ~10 ml $min^{-1}$ and the compressed air with a flow rate of 4 L $min^{-1}$ was used to split the suspension into fine droplets, which was sprayed into liquid nitrogen using a twin fluid nozzle. The distance between the nozzle and the liquid nitrogen level was about 15 cm, which had been determined by other researchers at LU to produce spherical granules [210]. The frozen granules were collected in a glass beaker and freeze dried using a freeze dryer, Virtis bechtop SLC, Newyork, USA. Note that, the

excess liquid nitrogen in the glass beaker was evaporated prior to being dried in the freeze drier. The freeze dryer was maintained below - 30°C and 100 mTorr and the granules were dried for 48 hours. The freeze dried granules were then oven dried in air at a temperature of about 60°C for an hour to remove the excess moisture. The dried granules were sieved and the granules of diameter between 75 µm and 250 µm were separated out using British standard sieves for green processing. Since the granules were produced in a very small scale, about 25 g, a wide range of granules being used without compromising flowability and crushabilty.

## 3.5 Green processing (dry pressing)

Dry pressing was used to produce green samples for sintering. The SFD granules and the as-synthesised powders were both used to produce separate green compacts. Initially, about 0.5 g of granules or powders was uniaxially pressed at 70 MPa for 1 min in a 10 mm inner diameter steel die. Stearic acid (96%, Acros Organics, Fisher scientific, UK) dissolved in acetone was used as a lubricant to avoid die wall friction. The resultant compacts were vacuum sealed in a polymer bag and subsequently isopressed at 200 MPa for 2 min using a Stansted cold isostatic press, Essex, UK. After isostatic pressing, the samples attained green density about 52-53% of TD (Theoretical density).

The green samples were heat treated at 700°C to remove all the organics that had been added during the powder synthesis, suspension preparation and the SFD processes. Even though the YAG powder was washed three times, there was a chance of solvent remaining in the powders and, moreover, the dispersant and the foaming agent are removed at temperatures ranging from 80 - 650°C, as confirmed by TGA/DSC data, Figure 42. The TGA curve showed a total weight loss of about 3.3 wt.% caused by the decomposition of the dispersant (3.0 wt.%) and the residual organics persisted in the granules. The weight loss in the TGA curve coincides with the endothermic and exothermic peaks from the DSC analysis. The two exothermic peaks near 80°C correspond to the decomposition of the residual $NH_3$ and the foaming agent used. The endothermic peak near 240°C and the exothermic peak near 430°C could be attributed to the decomposition of chemisorbed $NH_4$ ions and the carboxylate ions [15] from the dispersant, $NH_4$PAA, respectively.

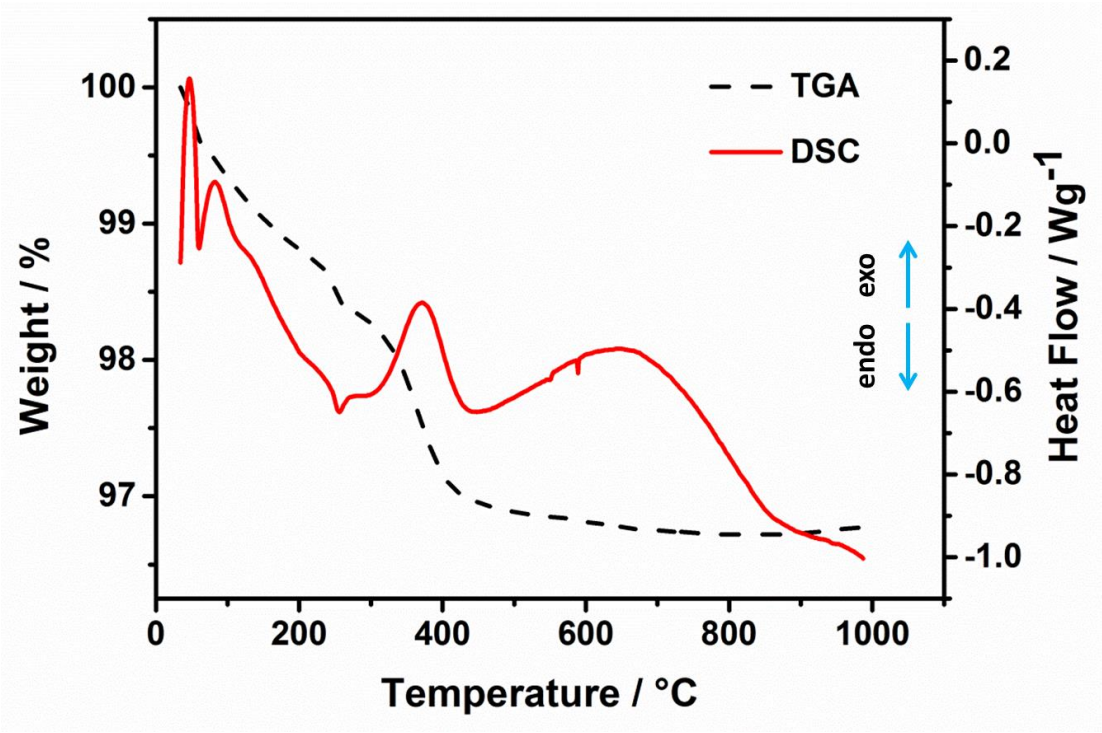


*Figure 42 TGA/DSC of the spray freeze dried YAG granules*

Therefore, a slow heating/cooling rate of 0.5°C $min^{-1}$ cycle was designed to produce crack free samples. Each sample was heated to 100°C and held for 30 minutes to remove the physisorbed organics and then heated further to 400°C for 30 min to remove the chemisorbed organics and finally to 700°C for 2 h to remove the residual organics in the samples.

## 3.6 Densification

### 3.6.1 Hot pressing (HP)

Co-precipitated YAG powder was used for the initial experiments aimed at producing fine microstructured ceramics using a hot press. Hot pressing was performed at Exeter University using a model HP W25, FCT Systeme GmbH, Germany, which was equipped with a computer to program the sintering cycle and to acquire data. The inner cavity of the hot press is shown in the Figure 43a. About 25 g of YAG powder was used to produce 50 mm square samples. Graphite sheets were used as a sacrificial layer to avoid damaging the graphite die, Figure 43b.

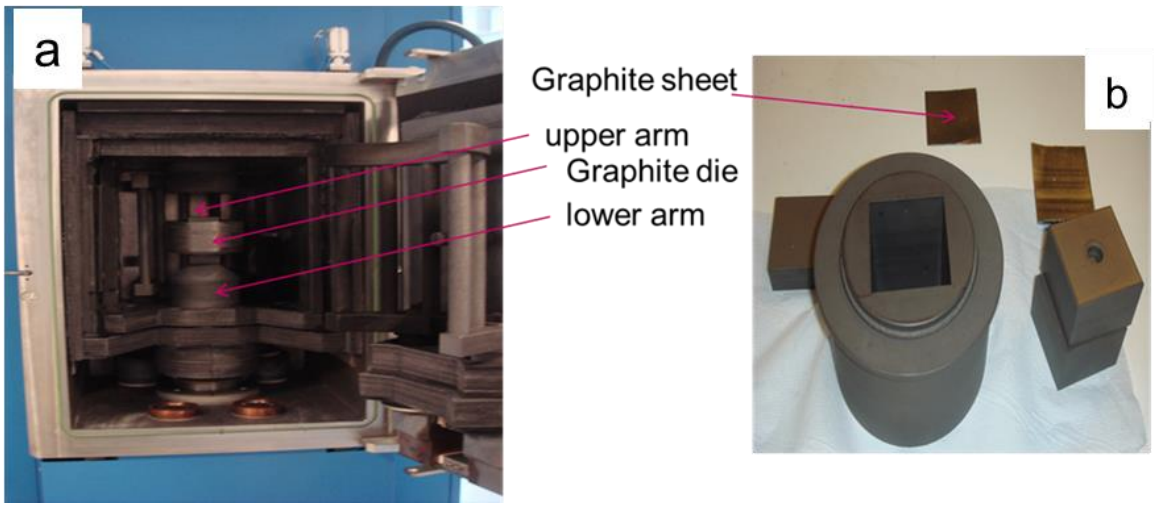


*Figure 43 (a) Inner cavity of the hot press and (b) the graphite die usedfor the process, Exeter University*

A K type thermocouple was used to monitor the temperature until 600°C and a radiation pyrometer was used to measure the temperature above this temperature. Loose YAG powder was poured into the die and gently tapped to form a flat surface on the powders and then pre-pressed at 3.9 Pa to form a green shape. Then the die was placed in the hot press cavity between the lower and the upper punches. A typical hot pressing profile was used to produce YAG ceramics; an hydraulic pressure of about 8.5 MPa was applied initially and the pressure was maintained until the temperature reached the sintering temperature, 1650 or 1700°C. Then the pressure was increased to 50 MPa at a rate of 8.3 MPa $min^{-1}$ and the sample soaked for 3 hours at the sintering temperature. A controlled atmosphere was maintained to avoid damaging the graphite die; a pressure of about 20 mbar was maintained until the temperature reached 900°C and then an argon 1022 mbar atmosphere was maintained throughout the sintering cycle above 900°C. Finally the hot press was allowed to cool back to room temperature. Table 11 lists the experimental conditions used.

*Table 11 Experimental conditions of three different sintering techniques used to produce YAG ceramics*

| **Hot pressing** | **Spark plasma sintering** | | **Hot isostatic pressing** | | | |
|---|---|---|---|---|---|---|
| **CP-YAG powder** | **Calcined CP-YAG granules and ST-nYAG granules** | **ST-nYAG powder** | **ST-nYAG granules** | | **ST-nYAG powder** | |
| | | | **Single step sintering** | **Two step sintering** | **Single step sintering** | **Two step sintering** |
| - | - | 1300°C for 15 min / 300 MPa | - | | | |
| - | 1400°C for 15 min / 70 MPa | 1400°C for 15 min / 70 MPa | - | | | |
| - | - | - | 1500°C for 3 h / 200 MPa | | | |
| - | - | - | 1550°C for 3 h / 200 MPa | | | |
| - | - | - | 1550°C for 5 h / 200 MPa | | | |
| - | - | - | 1550°C for 5 h / 300 MPa | | | |
| 1650°C for 3 h / 50 MPa | - | - | 1650°C for 5 h / 300 MPa | | | |
| 1700°C for 3 h / 50 MPa | - | - | 1700°C for 5 h / 300 MPa | | | |

### 3.6.2 Spark Plasma Sintering (SPS)

Since hot pressing is limited to relatively low pressures, 50 MPa is a typical maximum for laboratory equipment, YAG ceramics were also densified using spark plasma sintering. In SPS, an electric field is applied in tandem with pressure and temperature which results in the FAST sintering phenomena (see section 2.7.4). The SPS trials were performed at Queen Mary University, UK using a FCT HP D20 model, FCT Systeme GmbH, Germany, which was also computerised for data processing. A procedure similar to that used for hot pressing was followed, however graphite dies with different diameters were used to modify the applied pressure. Both loose YAG powders and calcined YAG granules (due to restrictions with the equipment, all organics in the granules were removed at 700°C) were used. The atmospheric control and the temperature monitoring system were similar to that for the hot press, since both the HP and SPS units were produced by the same manufacturer. The heating profile for the SPS involved a hydraulic pressure of about 12 MPa being applied prior to heating and the pressure remained unchanged until the sintering temperature was reached. The heating rate was 100°C $min^{-1}$ up to 1100°C and then 10°C $min^{-1}$ to the sintering temperature, which ranged from 1350 - 1700°C. The resultant samples were subsequently annealed at 200°C using a box furnace at a slow heating/cooling rate 5°C $min^{-1}$. Table 11 lists the experimental conditions used.

### 3.6.3 Hot isostatic pressing (HIP) of YAG ceramics

Since carbon contamination from the die was severe in the SPS process, pre-sintered YAG samples were also sintered to theoretical density using hot isostatic pressing. With this technique, unless the samples are to be encapsulated, a pre-sintering process is required to close the porosity so that an external pressure can be applied to the sample.

#### *3.6.3.1 Pre-sintering*

Both single step and two step sintering were performed to sinter the YAG samples, Table 12, using a conventional box type furnace (Carbolite Ltd., U.K) fitted with SiC heating elements. A K-type thermocouple was used to measure the temperature and a Eurotherm 902 temperature controller (Eurotherm Ltd., U.K) was used to program

the heating cycles. Pre-sintering was designed to achieve 93 – 99% of theoretical density (TD).

*Table 12 Pre-sintering profile for YAG samples.*

| Segment | Single step sintering | Two step sintering |
|---|---|---|
| 1 | 0.5°C $min^{-1}$ upto 100°C hold for 30 min | |
| 2 | 0.5°C $min^{-1}$ upto 400°C hold for 30 min | |
| 3 | 0.5°C $min^{-1}$ upto 700°C hold for 2 h | |
| 4 | 5°C $min^{-1}$ upto $T_1$°C hold for 3 h | 5°C $min^{-1}$ upto $T_1$°C hold for 0 min |
| 5 | 5°C $min^{-1}$ down to 20°C | 10°C $min^{-1}$ down to $T_2$°C hold for 3 h |
| 6 | | 5°C $min^{-1}$ down to 20°C |

In order to avoid coarsening of the YAG nanoparticles during the heat treatment to remove the organics in the green sample, the heat treatment profile was combined with the sintering profile without allowing the samples to cool down to room temperature.

After pre-sintering the samples were visually examined for any visible defects and the grain sizes and densities of the samples were measured prior to HIPing.

#### *3.6.3.2 HIPing*

The ST-nYAG granules and powders that were successfully pre-sintered to 93-99% of TD, see Table 20 shows the density of the pre-sintered YAG samples produced using both SFD granules (SFD-YAG) and oven dried powder (OD-YAG) both derived from solvothermal approach. The table clearly shows that the samples attained ~95% of TD at 1350°C for 0 h ($T_1$) and 1100°C for 3 h ($T_2$) using the two step sintering process. Other conditions exhibited higher densities and the focus was to obtain ~95% of TD under the lowest sintering temperature conditions to achieve minimal grain growth.

Table 20 in section 4.10.3, were used for hot isostatic pressing. The HIP treatment was done with argon as the media and a pressure of 200 – 300 MPa was applied at different sintering temperatures, Table 11. HIP treatments from 1500 - 1700°C and 200 - 300 MPa pressure were performed at the American Isostatic Presses (AIP), Columbus, USA, using an AIP10-30H HIPing unit, which was also facilitated by computer-aided programming cycles and data logging.

*Figure 44 HIP facility used to sinter YAG samples at AIP, AIP 6-45H, Colombus, USA*

*Table 13 Typical sintering profile used in HIP*

| **Segment** | **Operation** |
|---|---|
| 1 | Flushed with argon 3 times |
| 2 | Heated to sintering temperature at 5°C $min^{-1}$ |
| 3 | Pressure increased from 0 – 300 MPa |
| 4 | Pressure and temperature held |
| 5 | Cooled to 30°C at 5°C $min^{-1}$ + pressure gradually decreased to atmospheric pressure |

A typical HIP sintering profile is given in Table 13. The HIP chamber was flushed three times with argon prior to heating to avoid gas contamination from the previous runs. The samples with different densities were stacked at different levels in the chamber and sintered using a heating / cooling rate of 5°C $min^{-1}$. After reaching the sintering temperature, the pressure was gradually applied using argon and the samples were soaked for different durations. The resultant samples were annealed at a temperature 200°C less than the sintering temperature.

## 3.7 Sample characterization

### 3.7.1 Thermal analyses (TGA/DSC)

Thermal analysis of the as-synthesized precursor powders from the sol-gel and co-precipitation routes and the granules produced from the solvothermal route were performed using simultaneous TGA/DSC (SDT 2960, TA Instruments, USA). The powders/granules were weighed to ~5 mg and placed into an alumina sample pan and TGA/DSC traces were recorded between 25°C and 1000°C at a ramp rate of 10°C $min^{-1}$; an empty alumina pan was used as a reference. The instrument measures the weight loss and the change in heat flow between the sample and the reference material. Graphs of % weight loss and heat flow as a function of temperature were plotted to show the exothermic and endothermic reactions associated with the weight loss of the precursors.

### 3.7.2 X-ray powder diffraction (XRD)

Crystalline structures based on the elastic scattering of X-rays from the individual atoms in the YAG powders were determined using X-ray diffractometry (Bruker, model D8 diffractometer, Bruker AXS GmbH, Karlsruhe, Germany, fitted with a quarter-circle Eulerian cradle). $CuK\alpha^1$ radiation with a wavelength of 1.5406 Å was used. Since information such as peak positions, peak intensities and peak shape depend on the sample preparation; the powder samples were ground finely and mounted on a sample holder with a flat surface to achieve the required uniform distribution of lattice orientations. All the powder samples were analysed at a step size of 0.02° increment in 2θ with a step scan of 1 s and the XRD patterns were recorded from 20° to 90° degree angle of 2θ.

### 3.7.3 Transmission electron microscopy (TEM)

Transmission electron microscopy was performed to find the primary particle size of the powder particles and to obtain an indication of particle agglomeration. A JEOL JEM 2000FX (JEOL Ltd. Tokyo, Japan) TEM was used for this study. The samples for TEM were prepared by dispersing the powders in an alcohol medium using ultrasound and then by depositing a drop of the suspension on a copper mesh (Agar carbon film, 200 Mesh Cu (50) coated with a carbon film. The samples were dried in a laboratory oven at 60°C for 15 minutes and loaded in a single tilt holder. The TEM was operated at 200 kV and images were obtained at various magnifications.

### 3.7.4 BET Surface area measurements

The BET surface area (S) of the YAG nanoparticles synthesised using the different methods was measured using an automated gas adsorption analyser, a Tristar™ 3000 instruments (Micrometrics Instrument Corporation, USA). The surface area of the nanoparticles gives an indication of the reactivity of the powders; a surface area of more than about 20 $m^2g^{-1}$ is usually considered to indicate a highly reactive powder. Moreover, this also provides an insight into the extent of agglomeration of the particles by measuring the particle size, from equation 18, and comparing it to that obtained from TEM. If the calculated surface area matches with the TEM particle size, then the particles can generally be considered to be non-agglomerated.

$$\boldsymbol{Particle\ size\ (d_{BET})} = \frac{\mathbf{6}}{\boldsymbol{\rho \times S}} \times \mathbf{1000} \qquad \textit{Eqn 18}$$

where, S is the specific surface area and $\rho$ is the theoretical density of the material.

To obtain the measurements, ~1.0 g of the dried YAG powders were placed in the equipment's glass tubes and the samples were loaded into the sample ports. Then, the samples were evacuated to less than 20 µm Hg vacuum and the temperature was cooled down to -196°C using liquid nitrogen and then >99.99% purity nitrogen was dosed in a predefined manner. The amount of nitrogen adsorbed on the particle surface at -196°C with respect to the relative pressure and saturation vapour pressure was used to estimate the surface area of the particles.

### 3.7.5 Density measurements

The green densities of the YAG compacts were measured using a volumetric method. The sample dimensions of radius (r) and thickness (h) were measured using a Vernier calliper and screw gauge respectively and the sample mass (m) also obtained. All measurements were to two decimal places and the density was calculated from equation 19.

$$\boldsymbol{green\ density\ (GD)} = \frac{\boldsymbol{mass}}{\boldsymbol{volume}} = \frac{\boldsymbol{m}}{\boldsymbol{\pi r^2 h}} \qquad \textit{Eqn 19}$$

The bulk density of the sintered samples was measured using the Archimedes water displacement method. The dry weight ($M_1$) and the suspended weight ($M_2$) of the sintered samples were taken along with the density of water ($\rho$) to calculate the bulk density using equation 20.

$$\boldsymbol{bulk\ density\ (BD)} = \frac{\boldsymbol{M_1 \times \rho}}{\boldsymbol{M_1 - M_2}} \qquad \textit{Eqn 20}$$

The percentage of theoretical density was calculated using the equation 21.

$$\%\ \boldsymbol{of\ theoretical\ density\ (\%\ TD)} = \frac{\boldsymbol{GD\ or\ BD}}{\boldsymbol{4.55}} \times \boldsymbol{100} \qquad \textit{Eqn 21}$$

where, 4.55 g $cm^{-3}$ was taken as the theoretical density of YAG.

### 3.7.6 Sample mounting and polishing

Mounting and polishing were performed for the microstructural and optical measurements of the sintered samples obtained using HP, SPS and HIP. The samples were mounted using epoxy resin and hardener mixture (Epofix, Struers Ltd., Solihull, UK) in a 25:3 weight ratio, respectively, and excellent adhesion to the samples was achieved after 12 hours of curing. Grinding and polishing were

performed using a semi-automated polishing machine equipped with an automatic diamond slurry feeding system, Tegramin-25, Struers Ltd., Solihull, UK.

The polishing cycle for the YAG samples is given in Table 14. After removing the specimen from the mounting cups, the specimens were cleaned and placed in the sample holder. Care was taken whilst using the polishing cloths; the specimen edges were rounded off to avoid tearing the cloths. In addition, the specimens were washed with deionised water after every step. The specimens were subjected to ultrasound for 2 minutes and wiped with acetone to clean the surface of the samples after the final step. To remove the samples from the mounting material, a heat treatment was used in an air oven at 200°C for 5 min. The polished samples were thermally etched for 30 minutes at temperatures 200°C lower than the corresponding sintering temperatures of the samples for the microstructural evolution.

*Table 14 Grinding and polishing cycle for YAG samples*

| Process | Polishing disc | Polishing media | Duration |
|---|---|---|---|
| Grinding | MD-Piano 220 | Water | 3 min |
| Grinding | MD-Piano 600 | Water | 5 min |
| Grinding | MD-Piano 1200 | Water | 5 min |
| Polishing | MD-Plan | DP-suspension (9 µm) | 5 min |
| Polishing | MD-Dac | DP-suspension (3 µm) | 5 min |
| Polishing | MD-Floc | DP-suspension (1 µm) | 5 min |

### 3.7.7 Field emission gun scanning electron microscopy (FEGSEM)

The morphology of the granules, fracture surfaces of the green samples and the microstructure of the sintered YAG samples were analysed using FEGSEM (Carl Zeiss Leo 1530VP FEGSEM, Oberkochen, Germany) at different magnifications.

The granulated powder was sprinkled onto a conducting carbon film mounted on aluminium stubs and gold sputtered for 90 seconds prior to the analysis to make them conductive and hence to prevent them from charging. The fracture surfaces of

the YAG green samples and the polished sintered compacts were glued on the carbon film for FEGSEM. The samples were gold sputtered for 60 seconds and silver paint was used to connect the top surface to the carbon film to prevent charging effects. A secondary electron detector (SE2) operated at 5 kV accelerating voltage was used to obtain images for the granules and the fractured surfaces of the green samples. The microstructure of the sintered samples was obtained using the in-lens detector at 5 kV accelerating voltage.

The grain sizes of the sintered samples were determined from the FEGSEM images using a line intercept method (ASTM E 112-96). At least three micrographs and a total of 300 grains were evaluated from the intercepts/intersections that intersects three or more parallel lines drawn across the micrograph covering most of the grains and the average grain size (D) was calculated according to equation 22,

$$\boldsymbol{Average\ grain\ size}\ (\boldsymbol{D}) = \frac{\boldsymbol{L}\times\mathbf{1.56}}{\boldsymbol{M}\times\boldsymbol{N}} \qquad \textit{Eqn 22}$$

where, L is the length of the line, M is the magnification (dimensionless) and N is the number of intercepts/intersections (the number of grains or grain boundaries). A shape correction factor of 1.56 was used to obtain the apparent grain size value after the work of Chen et al. [211].

### 3.7.8 Fourier Transform Infra-red spectroscopy

FT-IR (FT-IR 8400S, Shimadzu, Maryland, USA) was used to identify the functional groups present in the samples and to observe the IR transmission of the sintered samples. About 500 MPa uniaxial pressure was applied to produce thin translucent pellets of 15 mm diameter for the analysis. The liquid samples were dropped in between two NaCl crystals to form a thin film for the analysis. After initialising the equipment, the sample holder was fixed and background correction performed to avoid the $CO_2$ peak in the resultant spectra [212] . FT-IR was used to analyse the YAG suspension with and without the dispersants to determine the adsorption of the dispersant on the particle surface and to study the effects caused by the functional groups present in the suspension.

The IR transmittance of the sintered ceramics was also measured using FT-IR from 0.7 µm to 16 µm wavelength to get an overview about the transmittance of the sintered ceramics.

### 3.7.9 UV-Visible spectrophotometer

UV-visible spectrophotometer (Lambda 35 Perkin-Elmer UV-visible spectrophotometer, Shelton, CT, USA) was used to measure the transmittance of the sintered YAG samples to cover visible region 300 nm to 800 nm. After installing the integrated sphere, the sample was mounted on the transmittance port and spectralon, a fluropolymer, was placed on the reflectance port to get 100% reflectance back into the integrating sphere. Lambda 35 S software was used to retrieve the transmittance data. After initialising the equipment, background correction was performed without samples to confirm 100% reflectance from the spectrolon. A dark environment was created by enclosing the entire setup in black box. Then the samples were scanned in the transmission mode over a desired spectral range to obtain the transmittance data.

# 4 Results and Discussion

Nanocrystalline YAG powder is not commonly available as a commercial product and there can be quality issues. In this study, a commercial nano YAG powder from DGTec, France, was initially characterised to gain an insight into the particle characteristics and assess the quality of the material.

## 4.1 Characteristic features of commercial YAG powders

### 4.1.1 XRD analysis

Figure 45 shows the XRD pattern of the commercial YAG, which matches the reference JCPDS card: #33-0040. This indicates it was phase pure YAG, crystallised in a cubic structure and with no other secondary phases within the detection limits of XRD.

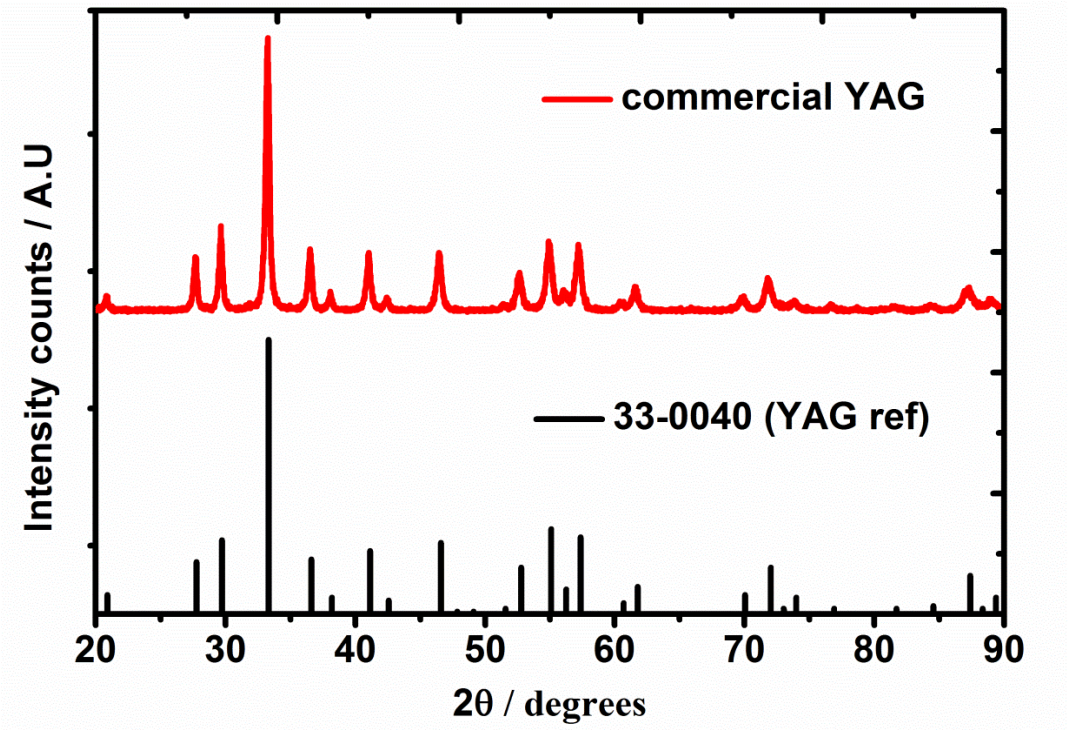


*Figure 45 XRD pattern of commercial YAG*

### 4.1.2 Particle size characteristics

Figure 46 reveals the particle morphology of the commercial YAG powder. The primary particles were in the range 30-35 nm, however it can also be seen that the

particles were highly agglomerated. There is some evidence in Figure 46 that some of the particles exhibited necking (circled) and hence formed strong agglomerates.

Analysis by FESEM, Figure 47a, confirm the observation that the powder was heavily agglomerated. To get an indication of how strong the agglomerates were, they were crushed using both a pestle and mortar and a microniser, in each case for 15 min. Figure 47 b and c show that, whilst the size of the agglomerates was reduced upon grinding/milling, not all of them could be broken.

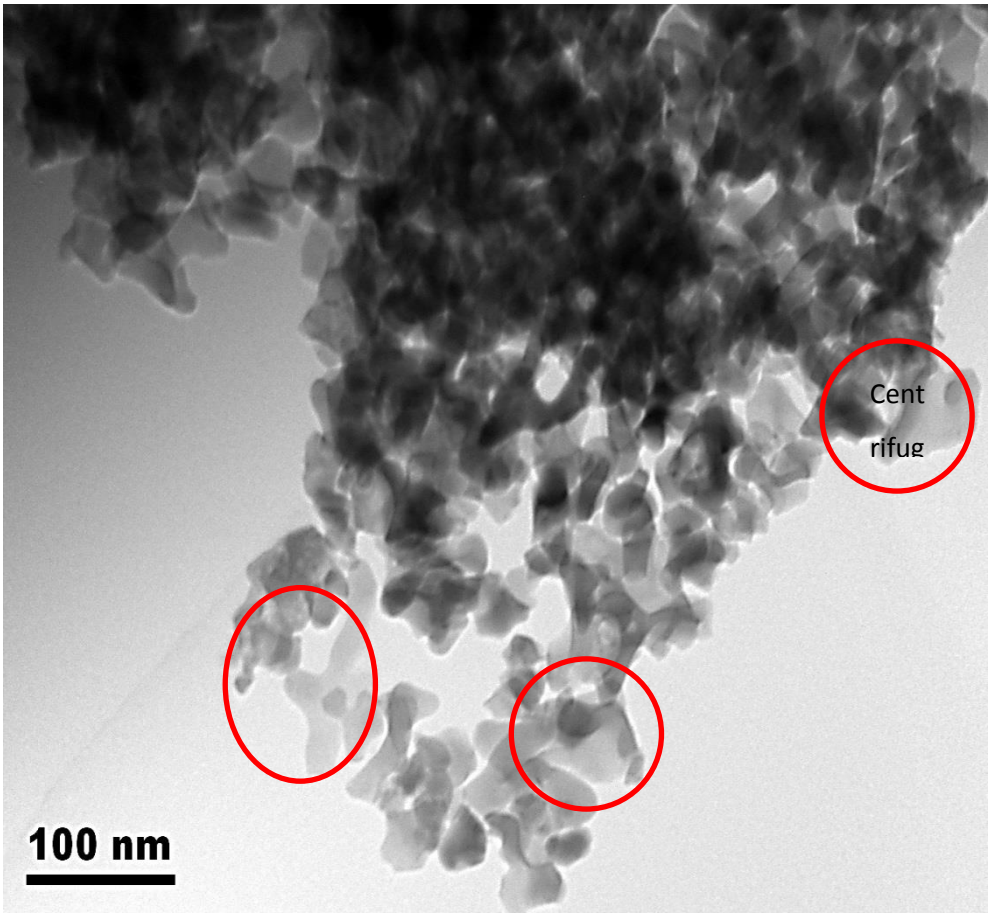


*Figure 46 TEM image of the commercial YAG, circle showing particle necking.*

The FEGSEM results were also supported by the particle size distribution plots obtained using a Malvern Mastersizer-2000, Figure 48. The as-received YAG powder displayed a broad size distribution (blue curve), ranging between 1 μm and 1000 μm. A small reduction in agglomerate size was observed when the powder was ground using the pestle and mortar; the larger particles were reduced to ~100 μm (green curve).

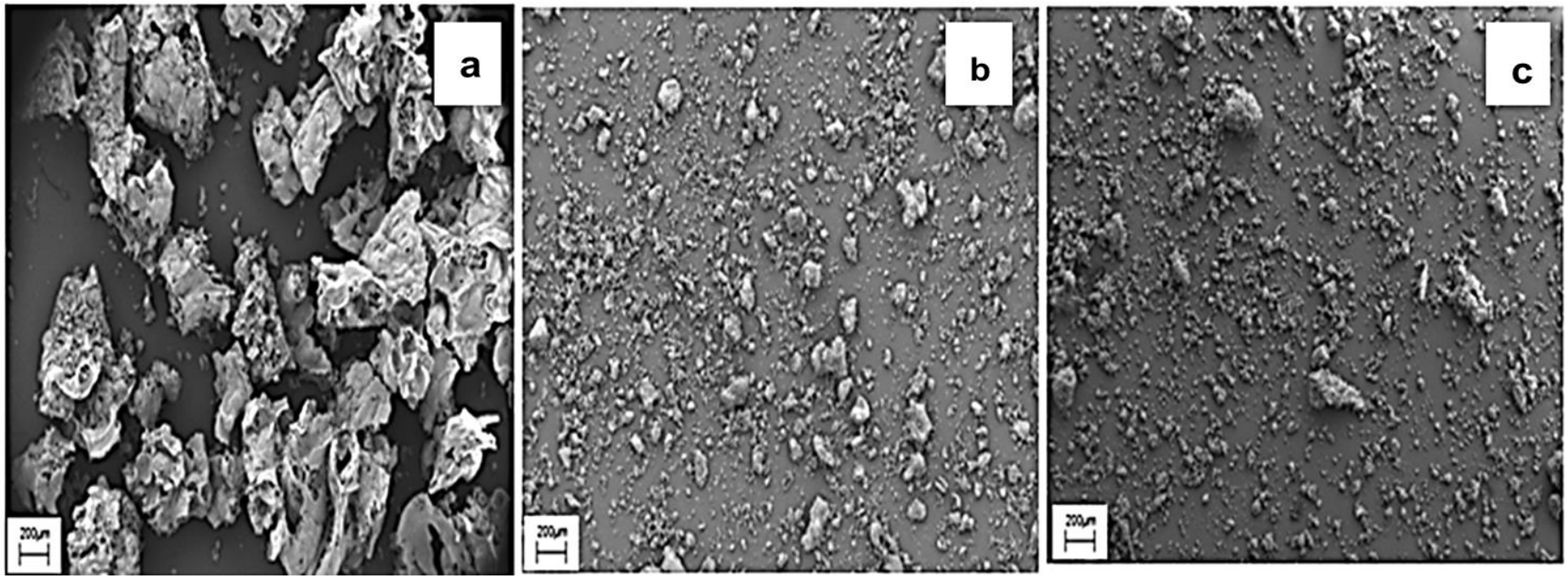


*Figure 47 FEGSEM images of the commercial YAG powder (a) as received, (b) after grinding using pestle & mortar for 15 min and (c) after using a microniser for 15 min*

A noticeable reduction in the size of the agglomerates was observed when the powder was milled using the microniser (red curve), usually microniser is used for short duration and longer duration could possibly include contamination from the milling media. A predominantly bimodal distribution indicating that there was still a significant level of agglomeration present in the powder. This also supports the view that the agglomerates were hard. In order to obtain nanostructured ceramics powders without agglomeration are preferred, the latter can lead to preferential grain growth during sintering and end up with large grains during the final stage of sintering.

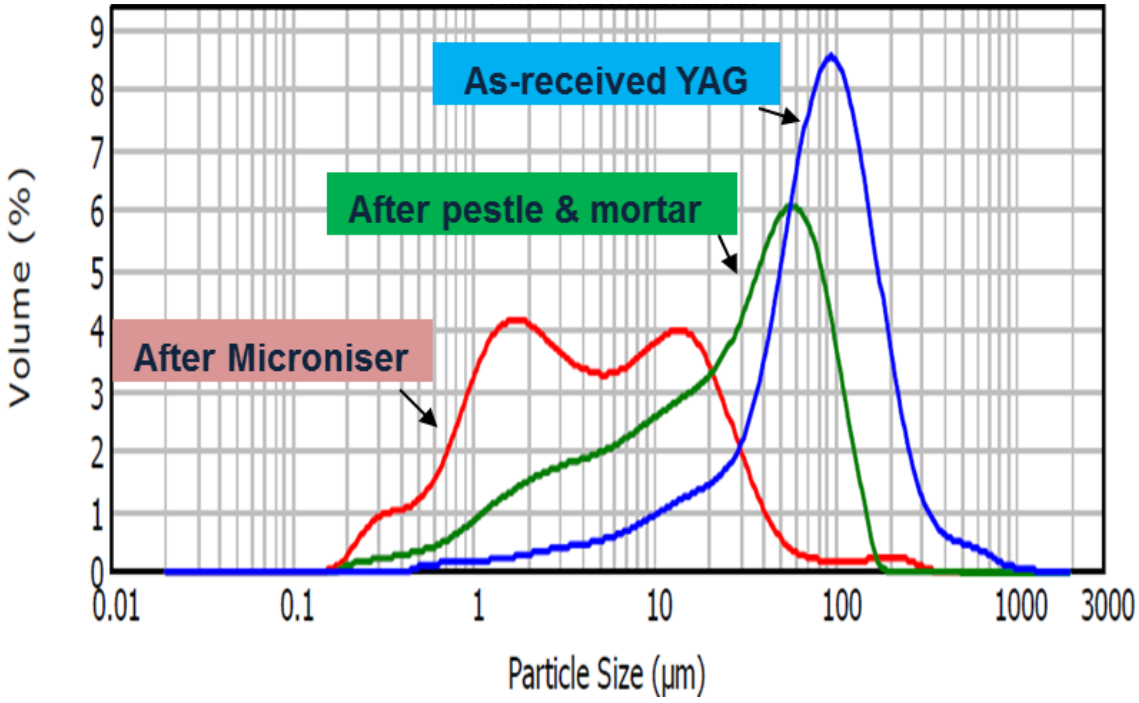


*Figure 48 Particle size distribution of commercial YAG (blue – as received, green – crushed using a pestle & mortar, red – micronised)*

Due to the presence of significant agglomeration of the particles, the commercial YAG could not be used for the production of nanostructured transparent YAG in this project. Thus, in-house chemical syntheses of nanocrystalline YAG were pursued.

## 4.2 Sol-gel synthesis of YAG powders

### 4.2.1 Sol-gel synthesis of YAG using nitrate precursors

#### *4.2.1.1 Thermal analysis and crystallization kinetics*

Thermal analysis curves of the precursor gel dried at 100°C are shown in Figure 49. A total weight loss of about ~59% is indicated by the TGA curve from 100 - 500°C, this could be due to the decomposition of organics such as moisture, nitrates and carboxylate ions from the precursors. The abrupt weight loss in the TGA curve coincides with the endothermic and exothermic peaks from the DSC analysis. The first endothermic peak near 180°C corresponds to the evaporation of water molecules and the tertiary alcohol groups present in the citrate solution [213]. An exothermic peak near 300°C corresponds to the evolution of residual $NO_3^-$ and $CO_2$ [204]. The second endothermic peak at 450°C is attributed to the oxidation of free carbon from the incomplete combustion of carboxylate groups in the citric acid [15].

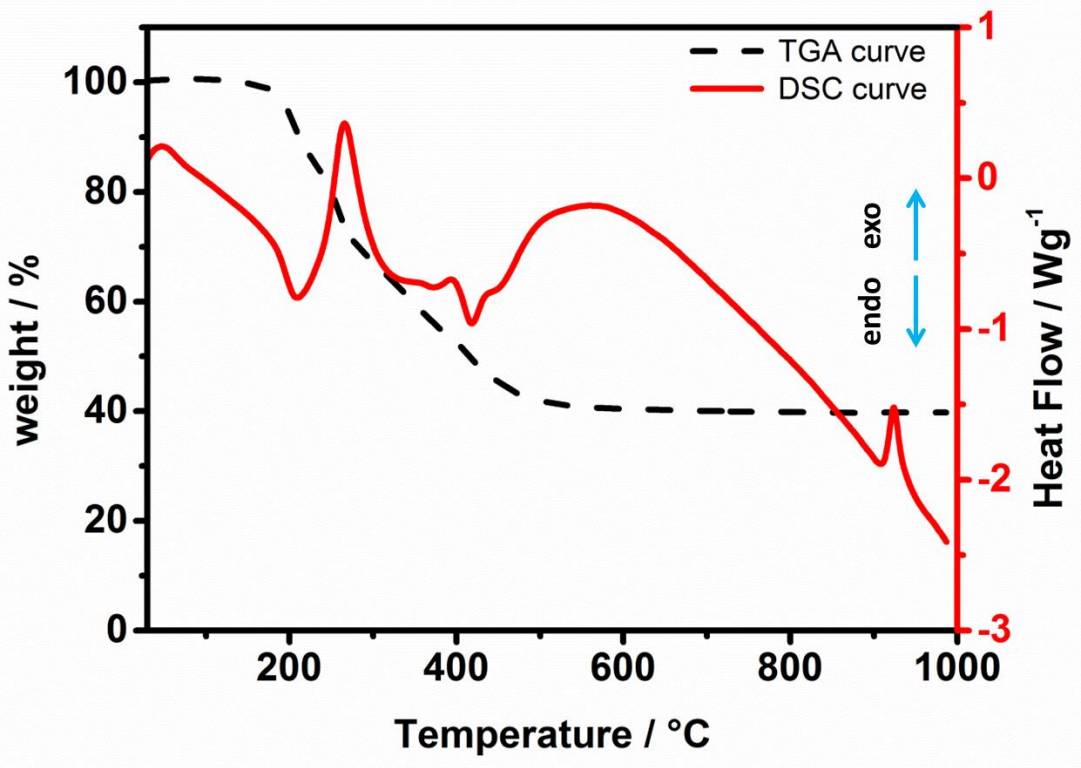


*Figure 49 TGA/DSC analysis of the dried gel synthesized using nitrate precursors*

As the temperature exceeds 600°C, the weight loss becomes negligible and the sample undergoes a continuous change in heat capacity (which corresponds to the change in the heat flow curve). The final exothermic peak observed near 917°C is

attributed to the onset of crystallization temperature ($T_c$) of the precursor to form YAG [214].

#### *4.2.1.2 FT-IR analysis*

Further investigation of the crystalline transition and the decomposition pathways of the two powders were performed using FT-IR spectroscopy. The goal was to obtain an improved understanding of the crystallisation kinetics and the relevant formation mechanisms.

FT-IR spectra from 4000 - 400 $cm^{-1}$ for the precursor powders heat treated at different temperatures are shown in Figure 50. The broad absorption bands near ~3450 $cm^{-1}$ and ~1630 $cm^{-1}$ in the powder heat treated at 100°C is associated with the O-H stretching vibrations of co-ordinated water molecules and the characteristics of H–O–H bending modes of molecular water [96, 215].

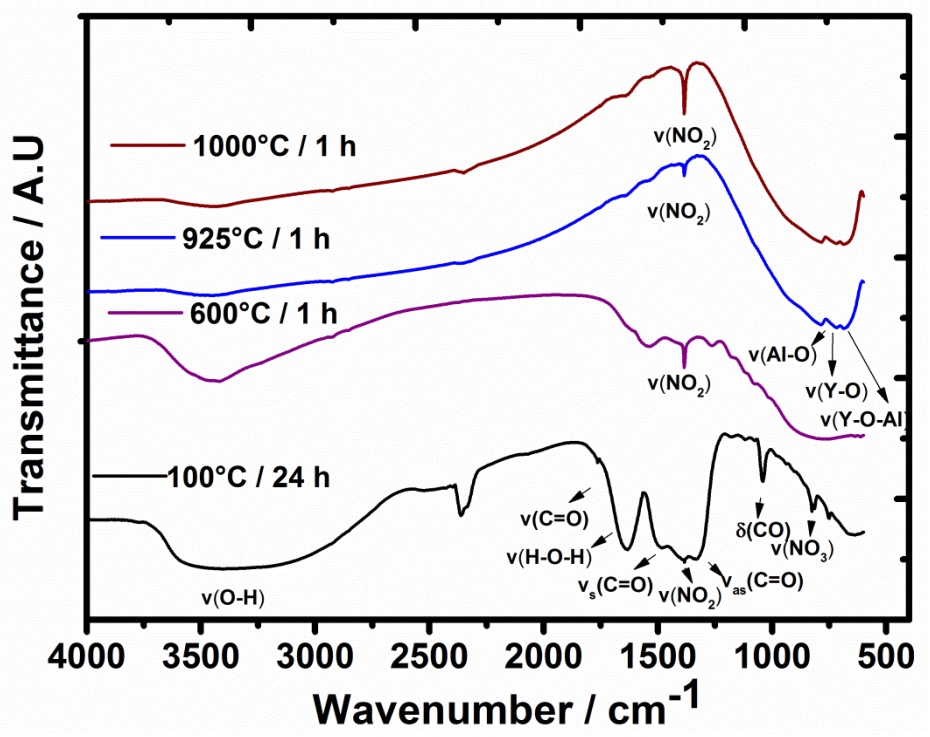


*Figure 50 FT-IR spectra of SG-nYAG precursor powders heat treated at different temperatures*

The COOH functional groups, chelating ligands, near ~1729, ~1450 and ~1323 $cm^{-1}$ in the powder after drying at 100°C are associated with the carboxyl vibrations of the citric acid. The weak band near ~1729 $cm^{-1}$ coincides with v(C=O) stretching [216],

which suggests that not all the carboxyl groups are bonding with the metal cations or free v(C=O) exist. The other two bands near ~1450 $cm^{-1}$ and ~1323 $cm^{-1}$ are associated with the symmetric $v_s$(C=O) and asymmetric $v_{as}$(C=O) vibrations [123, 217], which implies that the dissociated carboxylic ions from the citric acid react to form bonds with the $Al^{3+}$ and $Y^{3+}$ ions, forming a coordinating complex structure between the ligands and the metal ions [96, 218]. The nitrate groups were also observed at ~1380 $cm^{-1}$ and ~825 $cm^{-1}$, which corresponds to v($NO_2$) and v($NO_3$), respectively [219].

After heat treatment at 600°C, the unreacted v(C=O), v($NO_3$) and δ(CO) scissoring band (~1037 $cm^{-1}$) disappeared and some traces of the $v_{as}$ and $v_s$ of C=O, along with v($NO_2$) vibrations, were still present in the powder. This demonstrates that $v_{as}$ and $v_s$ (C=O) and v($NO_2$) were involved in the redox reaction [219] and also supplements the thermal analysis results for the nitrate precursor powder.

After heat treatment at 925°C, the new bands near ~783, ~713 and ~680 $cm^{-1}$, associated with the metal–oxygen vibration characteristics of Al–O, Y–O, and Y–O–Al stretching, confirm the formation of the YAG phase and also coincides with the onset crystallisation peak observed from the DSC results. Nevertheless, the v($NO_2$) vibration is still present in the precursor YAG powder after heat treatment at 1000°C for 1 h, which suggests that some traces of nitrate persists, even after calcination with the sol-gel route.

Based on the thermal analysis and the FT-IR results, the calcination of the dried precursor powder is suggested to follow the reactions indicated in equation 23 and 24:

$$\begin{pmatrix} (\boldsymbol{COO^-})^3\boldsymbol{Al^{3+}} - \boldsymbol{Y^{3+}}(\boldsymbol{COO^-})^3 \\ +\boldsymbol{HNO_3} + \boldsymbol{H_3O^+} + \boldsymbol{H_2O} \end{pmatrix} \overset{600°C}{\underset{\Delta}{\rightarrow}} \begin{pmatrix} (\boldsymbol{COO^-})^3\boldsymbol{Al^{3+}} - \boldsymbol{Y^{3+}}(\boldsymbol{COO^-})^3 \\ +(\boldsymbol{CO_2} + \boldsymbol{NO_2^-} + \boldsymbol{H_2})\uparrow \end{pmatrix} \quad \textit{Eqn 23}$$

$$(\boldsymbol{COO^-})^3\boldsymbol{Al^{3+}} - \boldsymbol{Y^{3+}}(\boldsymbol{COO^-})^3 \quad \overset{1000°C}{\underset{\Delta}{\rightarrow}} \quad \boldsymbol{Y_3Al_3O_{12}} + \boldsymbol{NO_2^-} \qquad \textit{Eqn 24}$$

During calcination, a thermally induced anionic redox (reduction and oxidation) reaction took place between the $(COO^-)_3$ and the $NO_2^-$, with the citrate acting as a reductant and the nitrate as an oxidant [219], as described in equation 24. This overall reaction is accompanied by the decomposition of chemisorbed water molecules, nitrates and carboxyl groups present in the precursor powder, Figure 49. On further heat treatment to 1000°C, equation 24, transformation of amorphous Y-O-Al (M-O-M network, M= metal ions $Y^{3+}$ or $Al^{3+}$) to crystalline YAG takes place due to the periodic arrangement of atoms, Figure 50.

The reaction sequence indicated in equation 25 is further supported by the XRD results of the precursors calcined at different temperatures described in the section given below, 4.2.1.3.

#### *4.2.1.3 XRD analysis*

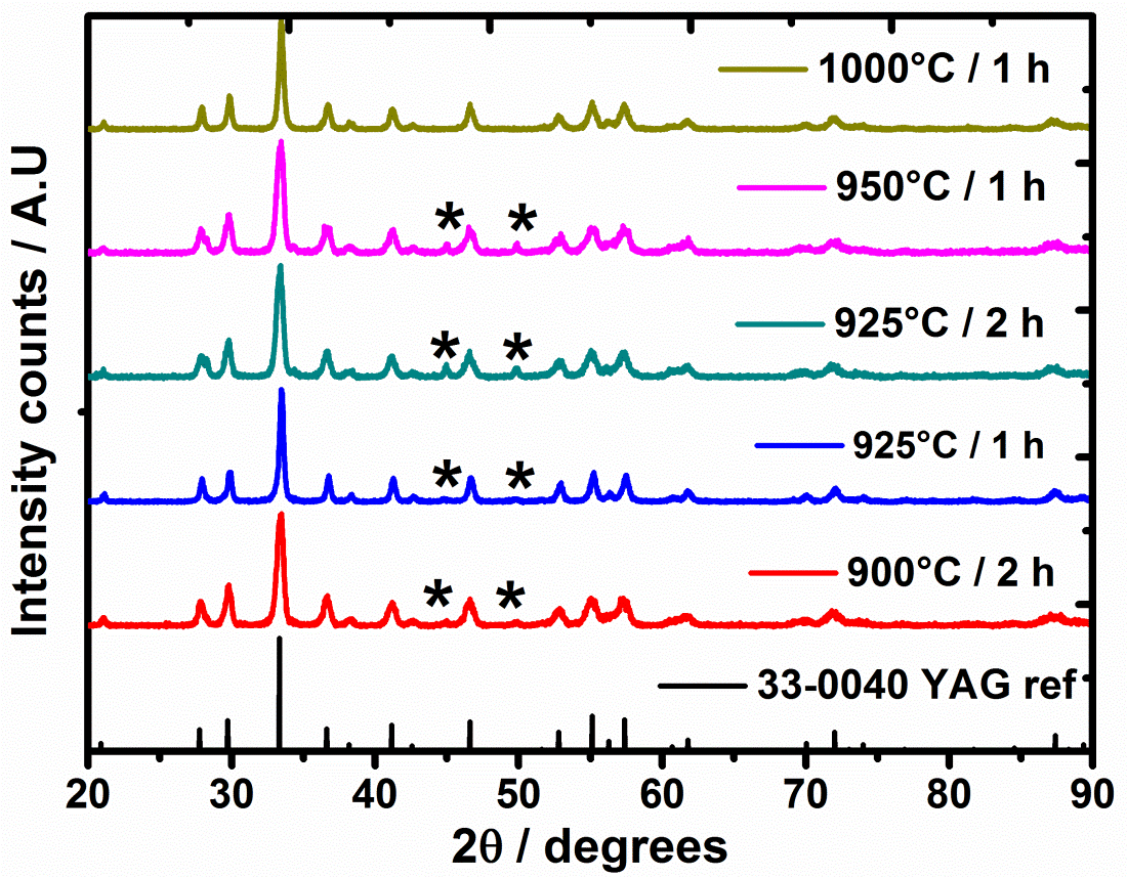


*Figure 51 XRD patterns of SG-nYAG precursor powders calcined at different temperatures (* YAH - h-$YAlO_3$)*

Figure 51 shows the XRD patterns of the precursor powders calcined from 900 to 1000°C. The peaks obtained are compared with the standard JCPDS card no: 33-

0040. After being heat-treated at 950°C for 1 h, a small amount of metastable yttrium aluminium hexagonal (h-$YAlO_3$) phase was identified within the XRD detection limit. Therefore, the precursor powder was heat-treated at 1000°C for 1 h, which resulted in single-phase YAG and all the peak positions matched with the standard diffraction reference pattern. It is important to note here that at 950°C no other stable intermediate phases such as $Y_4Al_2O_9$ (monoclinic yttrium aluminate - YAM) and $YAlO_3$ (yttrium aluminium perovskite - YAP) were formed, which will have hampered the conversion yield of YAG. Only metastable (hexagonal) h-$YAlO_3$ forms as an intermediate, which can transform to YAG at high temperatures [101].

#### *4.2.1.4 Particle size characteristics*

The TEM analysis confirmed the primary particle size and the extent of agglomeration of the primary particles, Figure 52; data was obtained at two different magnifications. It is evident from the micrographs that the primary particles were in the range between 20-25 nm and had a spherical shape. It is well known that, in general, nanoparticles have a strong tendency to agglomerate [220]. Hence it is not surprising that the synthesised SG-nYAG particles were very fine and heavily agglomerated. In addition to TEM results, the BET data suggest that the surface area was very low, 1.9 $m^2g^{-1}$, which yielded a calculated particle size of 694 nm. This clearly shows that the nanoparticles were coalesced into large agglomerates. This could be due to the high temperature heat treatment at 1000°C for 1 h.

Vaqueiro et al. [221] and Zarzecka et al. [125] observed rod shaped YAG particles ranging between 30-40 nm with a high degree of agglomeration in their work, which was based on using nitrate precursors and citric acid. In contrast, the YAG synthesised in the present study provided primary particle sizes ranging from 20-25 nm with regular shape. However, the downsides were a high degree of agglomeration and a low conversion yield (~20%), as noticed by others [122, 125, 221].

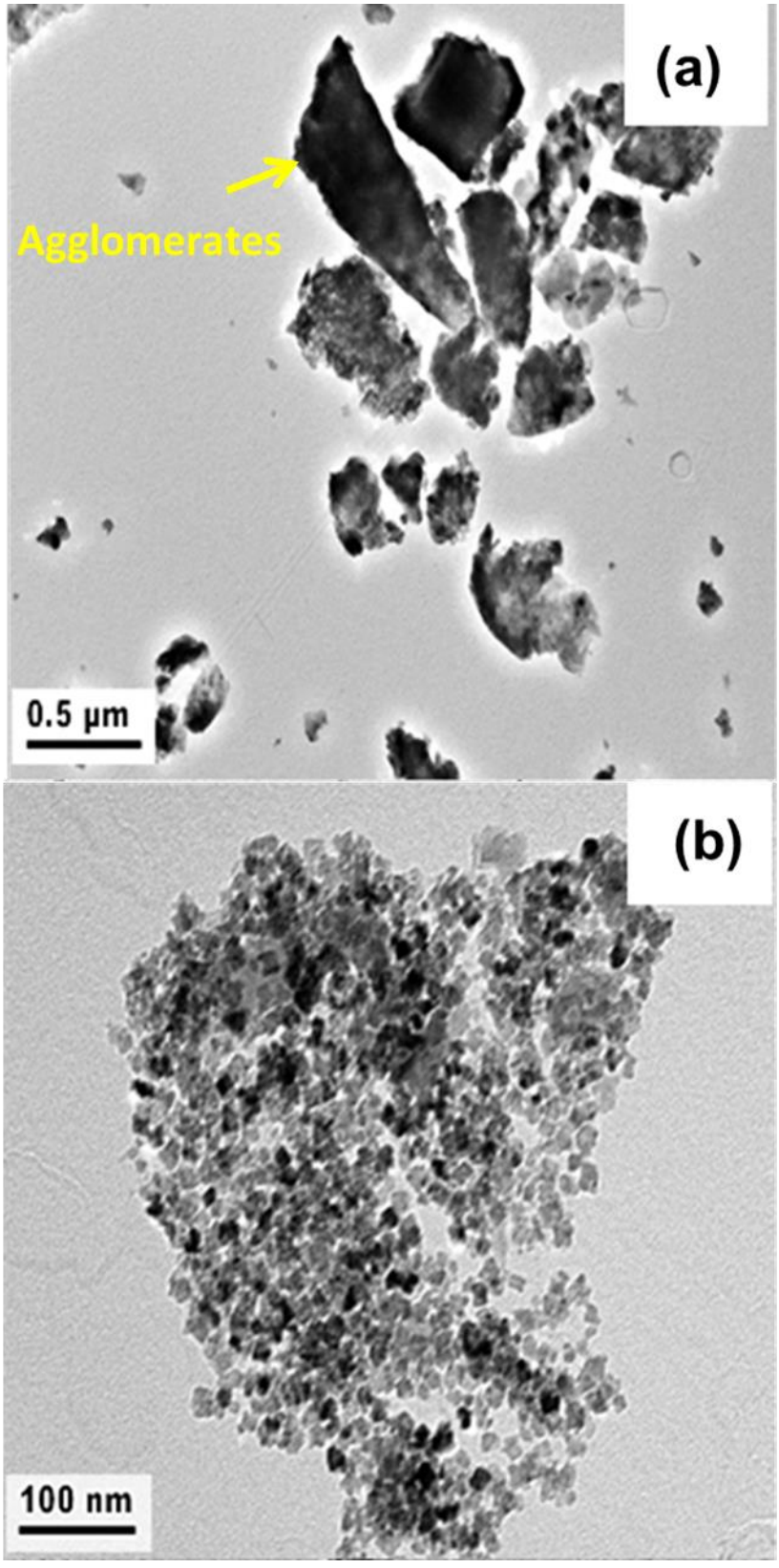


*Figure 52 TEM micrograph of SG-nYAG powder using nitrate precursor (a) low and (a) high magnifications.*

### 4.2.2 Sol-gel synthesis of YAG using metal powder

#### *4.2.2.1 Thermal analysis and crystallization kinetics*

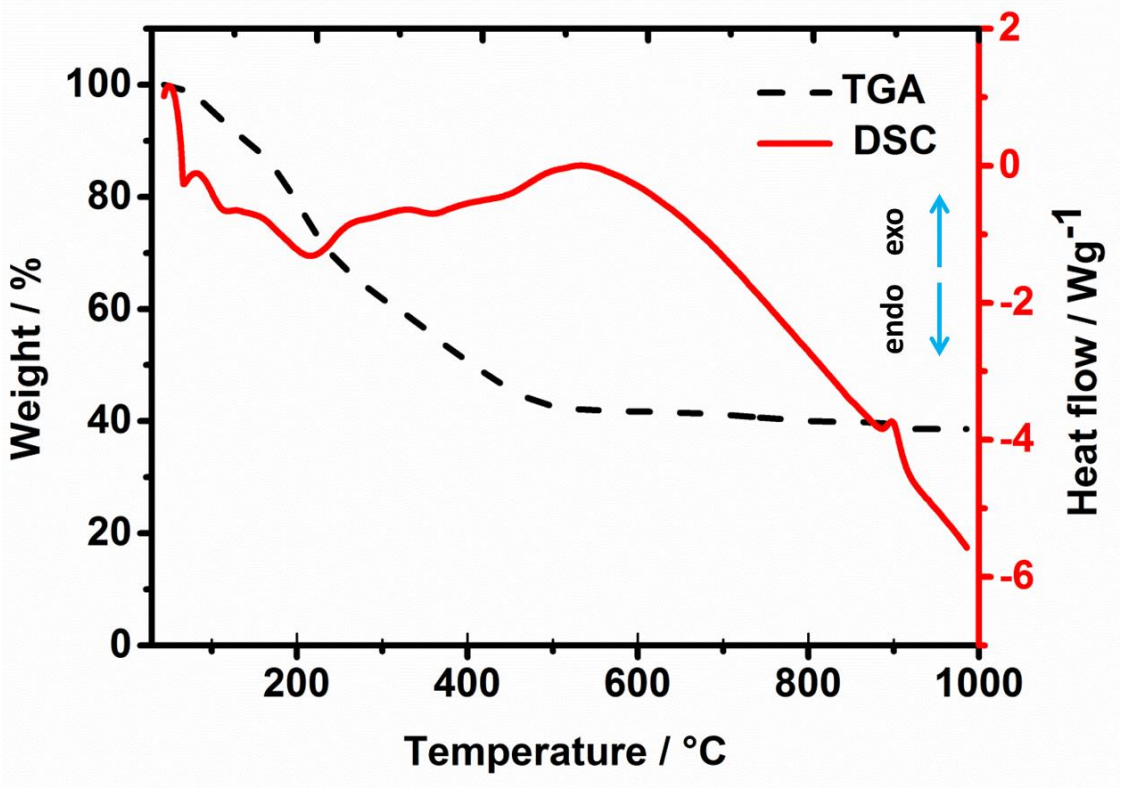


*Figure 53 TGA/DSC analysis of the dried gel synthesized using 100% Al metal precursor*

TGA/DSC curves of the 100% Al metal precursor gel dried at 100°C are shown in Figure 53. The TGA curve shows a 59% weight loss at 500°C during thermal decomposition. However, the conversion yield obtained through this approach shows a twofold increase when compared with the pure nitrate precursor route. The endothermic and exothermic curves of the DSC analysis correlate with the reactions occurring during calcination. The endothermic peak at 230°C is attributed to the decomposition of the residual water molecules and NOCl present in the sample. A small exothermic peak near 340°C corresponds to decomposition of $NO_3^-$ and the endothermic peak near 480°C is attributed to the sublimation of residual chlorine [205] in the dried gel. The final weight loss of the dried gel may be caused by the decomposition of hydroxyl groups to form metal-oxide bonding. The weight loss becomes negligible after 600°C. The transformation of crystalline phase coincides with the exothermic peak at 897°C.

It is useful to note that the crystallisation temperature ($T_c$) observed with the 100% Al metal precursor route is 20°C less than for the pure nitrate precursor method. This could be due to the change in enthalpy, $\Delta H = -3.23 \times 10^{14}$ kJ $mol^{-1}$ [205] and the reaction kinetics between precursors and the solvents.

#### *4.2.2.2 XRD analysis*

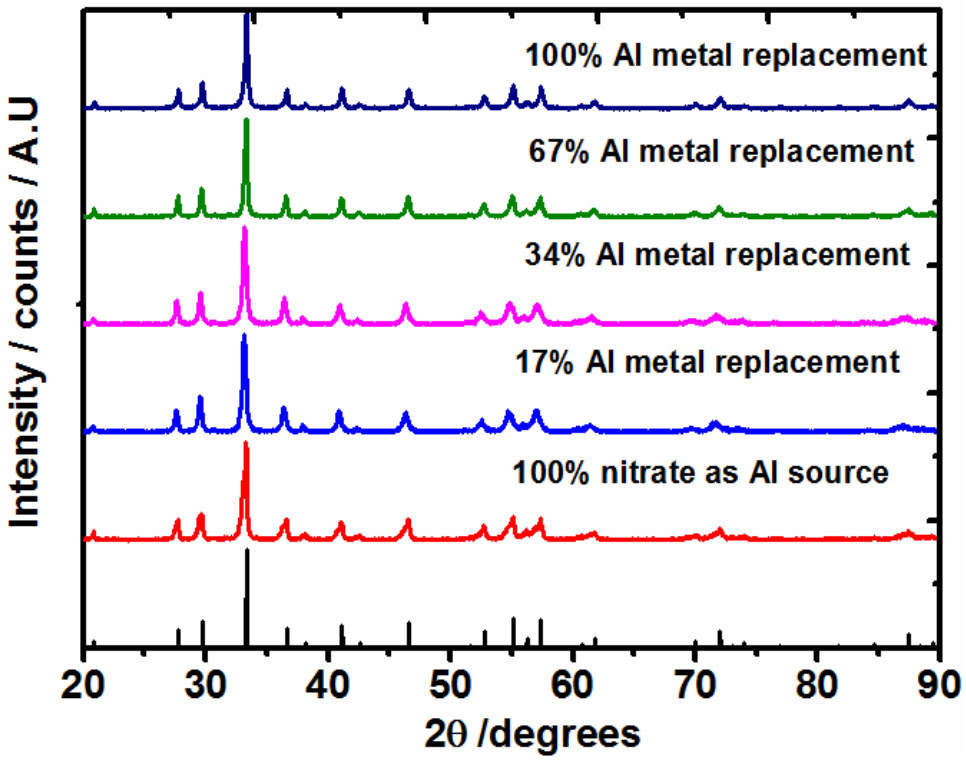


*Figure 54 XRD patterns of SG-YAG precursors calcined at 1000°C for 1 h as a function of Al metal replacement*

The XRD patterns of the precursor powders calcined at 1000°C for 1 h, with the successive replacement of $Al(NO_3)_3.9H_2O$ by Al metal, are shown in Figure 54. The peaks obtained are compared with the 100% nitrate YAG precursor and the standard JCPDS.

This shows that YAG powder synthesised using the sol-gel method exhibits phase purity and a high degree of crystallinity in all cases without any detectable amount of second phases. This result also suggests that a complete replacement of Al metal precursor is possible and YAG can be synthesised using Al metal powder as a source. It is believed that 100% metal replacement has not been reported in the literature before.

$$\begin{pmatrix} \left((OH_2)Al - Y\,(OH_2)\right)_{aq} \\ +\,HNO_3 + H_3O^+ \end{pmatrix} \overset{600°C}{\underset{\Delta}{\rightarrow}} \begin{pmatrix} (Al - O - Y)_{aq} \\ +(\,(NO_2)_g + (H_2O)_g)\uparrow \end{pmatrix} \quad \textit{Eqn 25}$$

$$Al - O - Y \overset{1000°C}{\underset{\Delta}{\rightarrow}} Y_3Al_3O_{12} \qquad \textit{Eqn 26}$$

From the thermal analysis, the dried precursor powder decomposed the volatiles and formed oxide bonding between the metal ions after 600°C, given in equation 25. The XRD results suggest that the exothermic peak at 897°C obtained in the DSC curve is the onset of crystallisation of YAG, however on further heat treatment to 1000°C for 1 h, amorphous oxides were completely crystallized into single phase YAG as per equation 26.

#### *4.2.2.3 Particle size characteristics*

The TEM study performed on sol-gel synthesized YAG powders using the metal precursors (SG-YAG) are shown in Figure 55. It is apparent from the micrographs that the primary particle size is increased with the replacement of Al metal. This could be attributed to the high calcination temperature (1000°C for 1 h) used and the Al metal precursor converted to YAG at a lower temperature ($T_c$ = 875°C) than the nitrate precursor ($T_c$ = 917°C). The possible reason for Al metal precursor resulted in low Tc is due to the presence of chloride ions, which could have influenced. When only Al metal powder was used, Figure 55d, this yielded irregular-shaped particles with large agglomerates and the mean primary particle size was found to be >90 nm. The YAG powders synthesized with mixtures of the two precursors showed intermediate behaviour when compared to 100% nitrate precursor YAG, which resulted in the smallest primary particles, Figure 52.

This suggests that using Al metal powder allows the conversion yield to be increased significantly, however the particle size characteristics were poor when compared to the citric acid route and the approach involved a lot of risk factors such as HCl handling and the vigorous reaction between HCl and Al metal powder during the initial stages of the process.

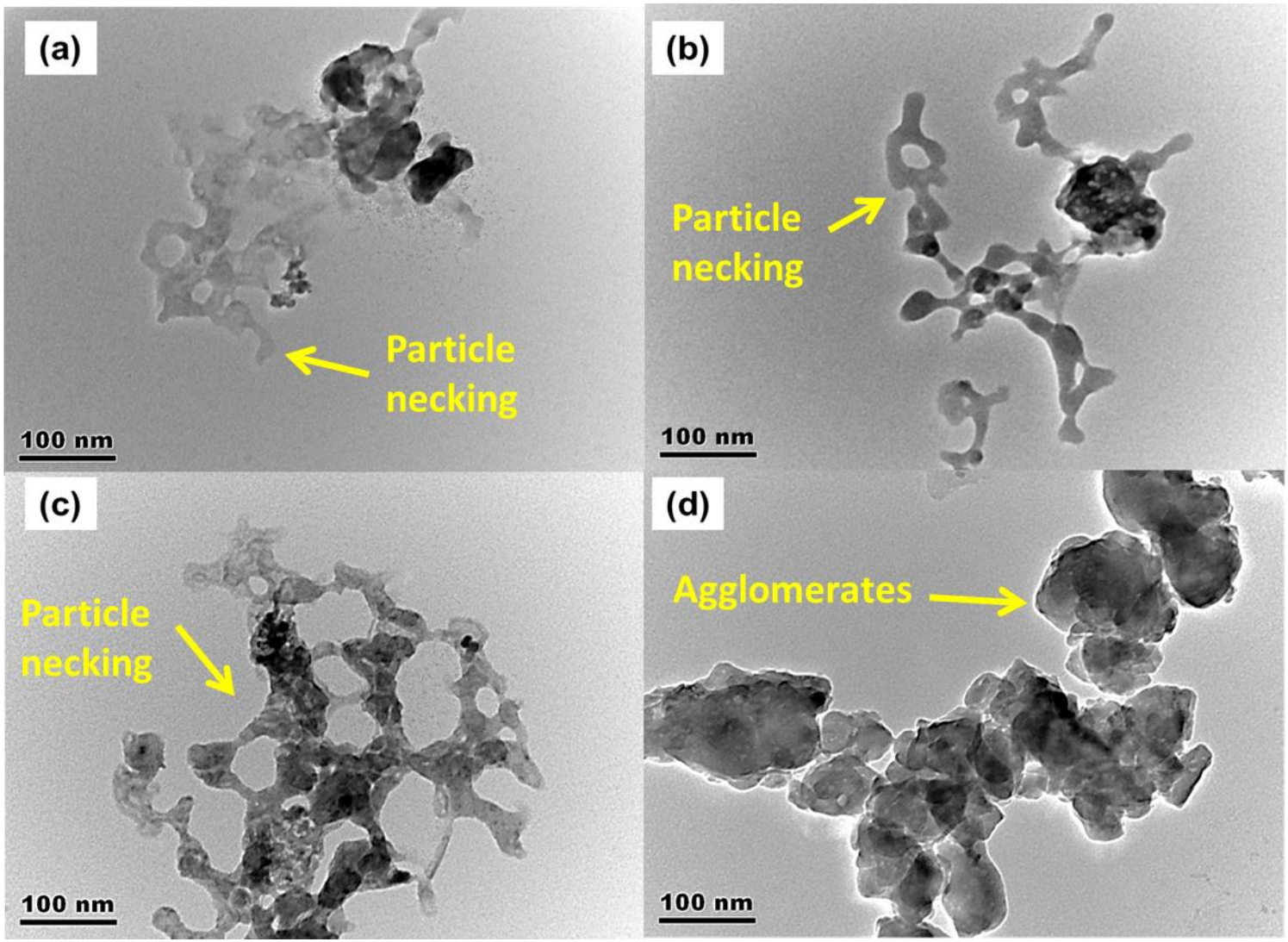


*Figure 55 TEM micrographs of SG-YAG powders as a function of Al metal replacement (a) 17%, (b) 34%, (c) 67% and (d) 100%*

## 4.3 Co-precipitation synthesis of YAG powders

The co-precipitation method was investigated to explore the potential of using an alkaline medium to synthesis YAG nano particles. In this method, the precipitates were tailored to form a core shell structure so that the precursors themselves reduced agglomeration during calcination at high temperatures.

### 4.3.1 Effect of processing conditions during precipitation

It was observed that when the pH of the precipitant solution increased or decreased by just 0.10, both the homogeneity and the morphology of the precipitates changed, Figure 56.

From Figure 56a, it is clear that whilst the precipitates were approximately spherical, there was a significant variation in their size, which is due to the difference in precipitating conditions of $Y^{3+}$ and $Al^{3+}$ ions. When the pH was maintained at 8.20±0.05, Figure 56b, the hydroxides of the mixed metal cations displayed a stable nanostructure and the precipitates were found to be discrete and to have a uniform size distribution.

In contrast, bulk precipitation morphology is displayed in Figure 56c. When the pH was increased to 8.30±0.05, the precipitation reaction resulted in agglomeration of the precipitates. Besides controlling the pH, temperature had a pronounced influence on the formation of precipitates due to nitrification of the precipitant ammonia solution at 30°C, where nitrification is the process by which ammonia is converted into nitrites ($NO^{2-}$) or nitrates ($NO^{3-}$) [222] and react to form nitric acid ($HNO_3$). This change in reaction due to the temperature could significantly influence the pH of precipitant solution.

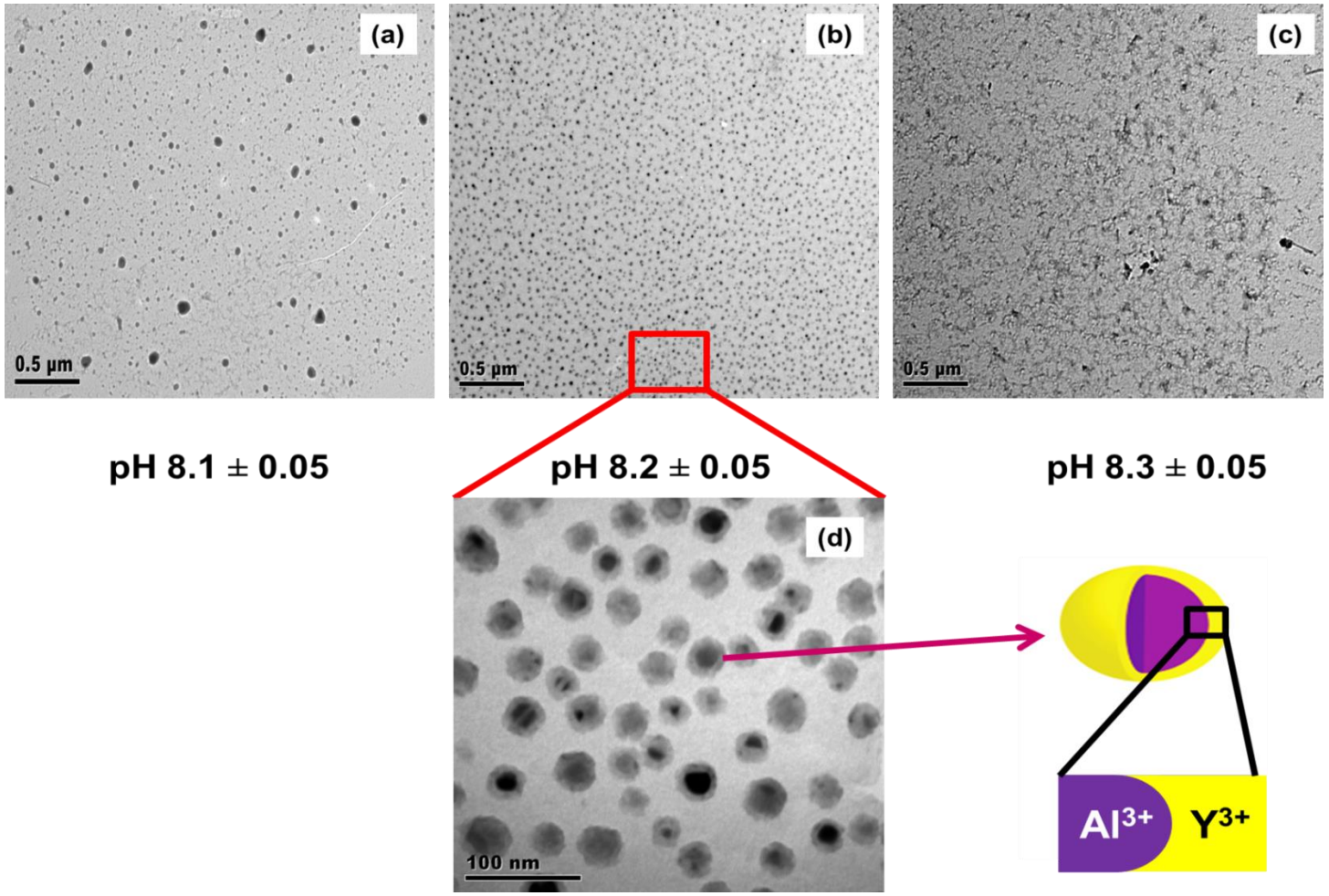


*Figure 56 TEM images of YAG precipitates obtained at different pH conditions (a) pH 8.1±0.05 (b) pH 8.2±0.05 (c) pH 8.3±0.05 and d) Core/shell structure.*

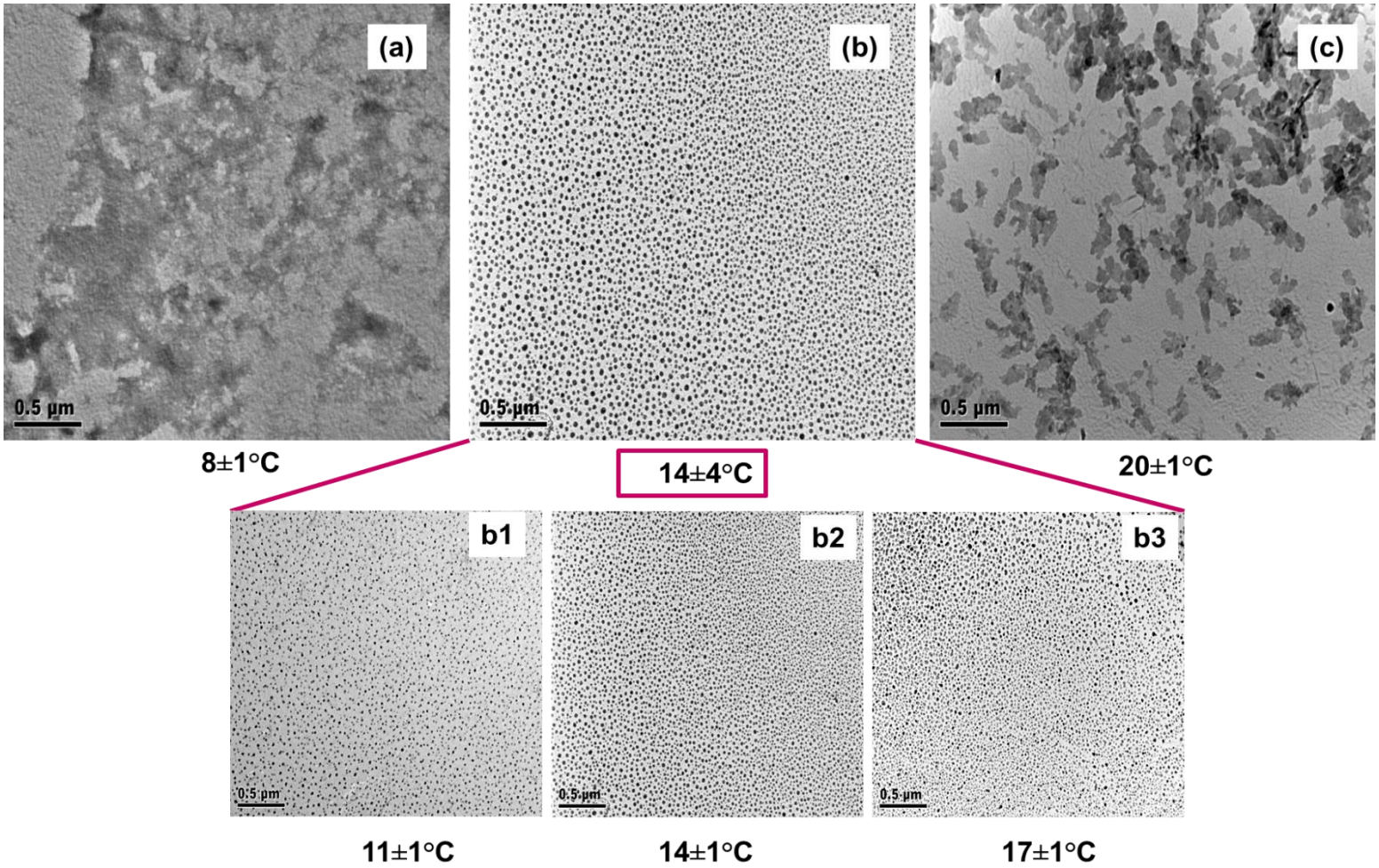


*Figure 57 TEM images of YAG precipitates obtained at different temperatures (a) 8±1 °C, (b) 14±4°C {b1 - 11±1°C, b2 - 11±1°C & b3 - 17±1°C } and (c) 20±1°C*

It has been reported that as the temperature increases from 10°C, the $NH^{4+}$ ions transform to $NH_3$ and into nitrates at 30°C [223]. This significantly influenced the change in morphology of the precipitates. From the TEM images, it is evident that thermal conditions such as 10±1°C and 20±1°C, Figure 57 a and c, resulted in heterogeneous precipitation, which could result in composition inhomogeneity and particle agglomeration. When the precipitates were processed at 10±1°C, a sudden increase in pH was noticed resulting in bulk precipitation, meaning that the precipitation occurs in a localised area not having proper structure; this could be due to the presence of excess hydroxyl molecules ($OH^-$) at this temperature. Whereas, at 20±1°C the pH dropped gradually and required a higher concentration, or larger amount of $NH_4OH$ solution, to maintain the pH at 8.20±0.05, see section 3.2.3 for pH controlling procedures. This severe fluctuation resulted in leaf-like structures due to the lack of the hydroxyl ions, which could be influenced by the formation of $HNO_3$ at this temperature. This shows that the nucleation of the precipitates is sensitive to the temperature fluctuations. However, the precipitates processed between these intermediate conditions, e.g. at 14±4°C, Figure 57 b, offered homogeneous precipitation, where both the $Y^{3+}$ and $Al^{3+}$ ions were precipitated to form a core/shell structure. Note that the temperature window was optimised based on the three different temperatures with ±1°C difference shown in the insert, Figure 57 b1, b2 and b3. The TEM results conclude that the processing temperature has a significant influence on obtaining homogenous precipitates.

### 4.3.2 Effect of water removal in the precipitates using ethanol and butanol

#### *4.3.2.1 Thermal analysis and crystallization kinetics*

Thermal analyses of the dried precipitates treated with n-butanol (BT-YAG precursor) and ethanol (ET-YAG precursor) at 100°C are shown in Figure 58. A noticeable difference of 21% weight loss was observed between ethanol and butanol treated precipitates, as indicated by the TGA curves, Figure 58a. This is associated with the removal of water and $NO_3^-$ during the filtering stage and the decomposition of volatiles at 200 - 500°C for 10°C $min^{-1}$.

This difference in weight loss from the TGA curves exhibits a strong correlation with the endothermic and exothermic peaks of the DSC analyses, Figure 58b. For ET-YAG precursor, the first endothermic peak near 100°C corresponds to the

decomposition of ethanol and water. This is absent in the BT-YAG precursor due to the large amount of hydroxyl species removal during the filtering stage.

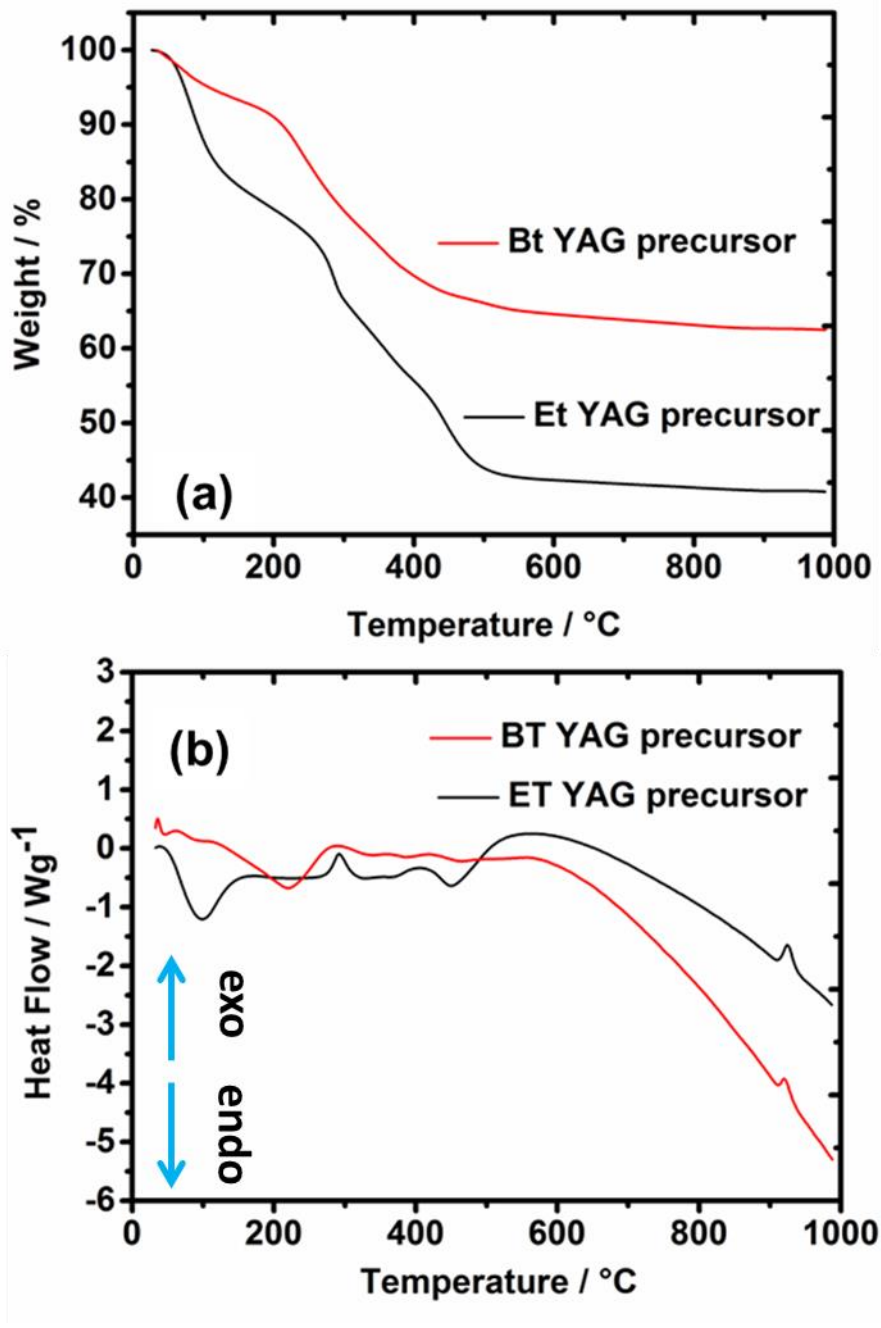


*Figure 58 Thermal analyses of the dried precipitates treated with n-butanol (BT-YAG precursor) and ethanol (ET-YAG precursor) a) TGA analysis and b) DSC analysis*

An endothermic peak is present in the BT-YAG precursor, which is attributed to the boiling point of butanol at 110°C. The exothermic peaks (for both BT & ET YAG precursors) near 300°C and 400°C correspond to the evolution of residual $NO_3^-$ and

$NH_3$ [224] in the precursors, respectively. The endothermic peak at 450°C in the ET-YAG precursor (which is absent in BT-YAG precursor) is attributed to the difference in final weight loss between the two precursors, which is caused by the decomposition of excess hydroxyl groups. Moreover, the onset crystallisation temperature for YAG formation is observed at 915 ± 5°C for both BT & ET YAG precursors.

#### *4.3.2.2 XRD analysis*

Figure 59 shows the XRD traces of YAG precursor powders calcined at 900°C. In both the butanol (BT) and ethanol (ET) treated precursor powders calcined at 900°C, some minor amounts of (YAH) h-$YAlO_3$ metastable phase were found and all the peaks were found to match with the standard reference diffraction pattern. However, no significant difference was found in the XRD results between the YAG powders. Therefore, it was important to analyse the particle characteristics of the particles to determine the best route forward.

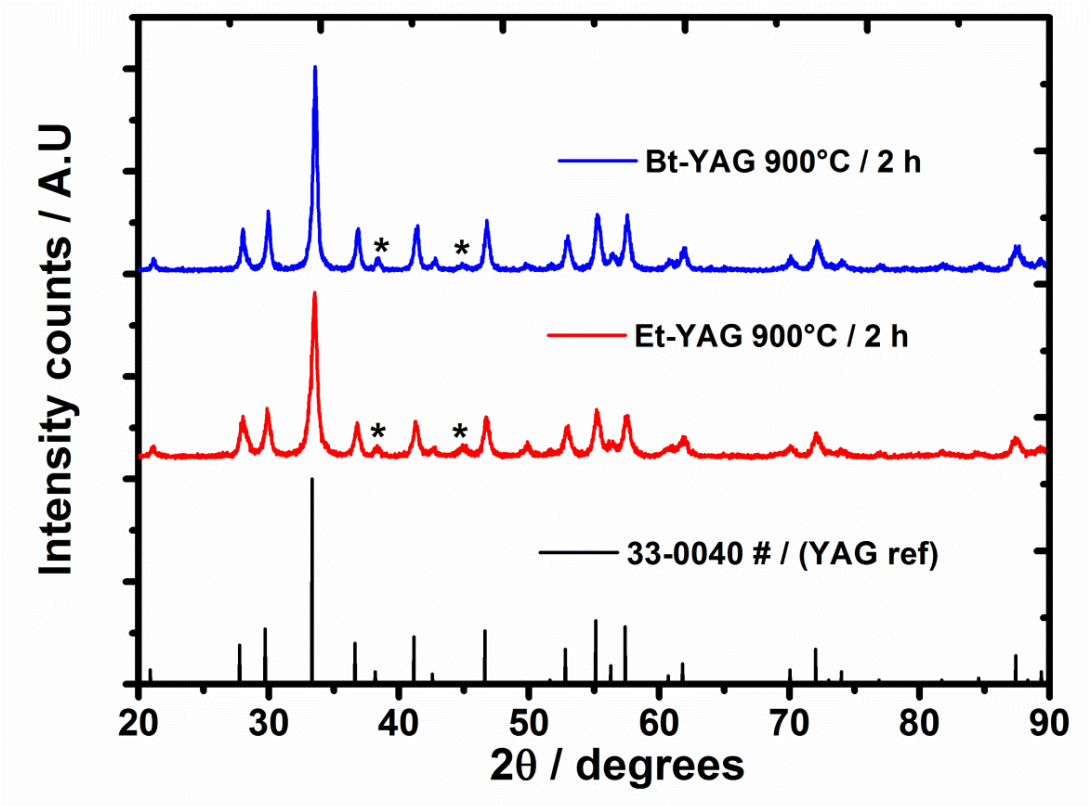


*Figure 59 XRD patterns of YAG precursor powders calcined at different temperatures (* H-$YAlO_3$)*

#### *4.3.2.3 Particle characteristics of co-precipitated YAG*

TEM analysis was performed to confirm the primary particle size and the extent of agglomeration in the co-precipitated YAG, Figure 60. It is evident from the micrographs that the primary particles were in the range from 15-20 nm in both ethanol-, Figure 60a, and butanol-treated, Figure 60b, YAG powders. However, the particles obtained from the ethanol-treated powder showed severe particle coalescence when compared to those obtained using butanol.

It is also observed from the TEM images that the extent of agglomeration is reduced with the co-precipitation method when compared to the sol-gel synthesised YAG particles. This could be attributed to the *n*-butanol treatment; the surface hydroxyl groups were replaced by the butoxyl groups and thus formed an azeotropic layer [225], which acted as a potential barrier between the particles. Due to the low surface tension of *n*-butanol compared to water, the binding force between the particles decreased whilst drying and so the hard agglomeration caused by the capillary forces was avoided. Consequently, depletion of the excess $OH^-$ ions in the precipitates controlled the agglomeration during drying and resulted in soft agglomerates of the dried precipitates.

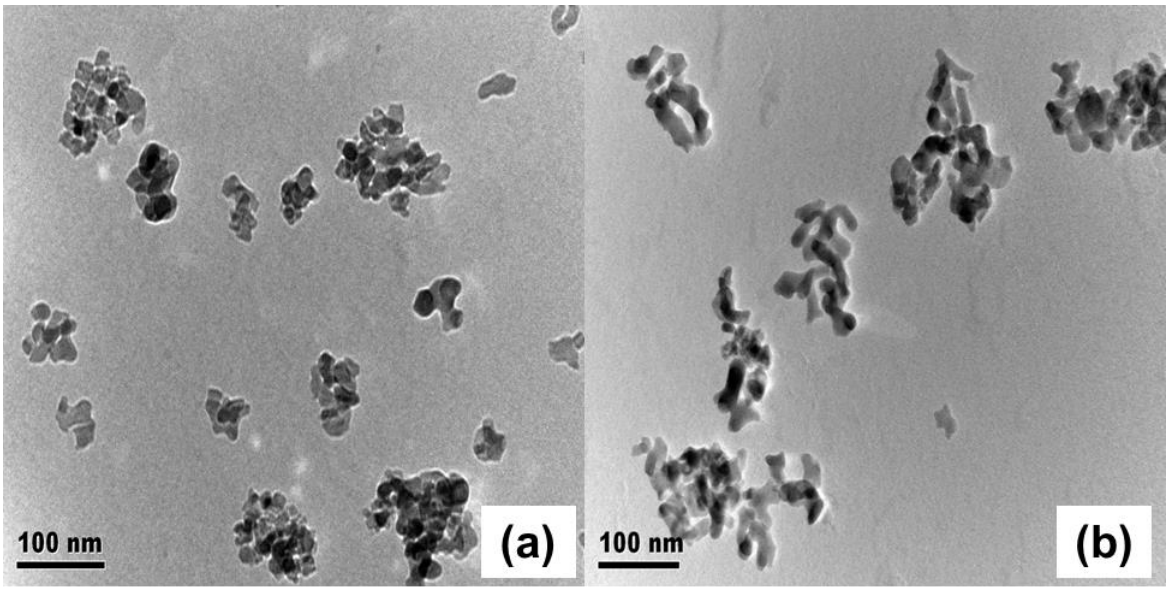


*Figure 60 TEM images of nanocrystalline YAG a) ethanol treated and b) butanol treated*

In order to obtain single phase YAG and to probe the mechanism for the formation of YAG using the co-precipitation method, the butanol treated precursor powders (hereafter called CP-nYAG) were further heat treated and characterised thoroughly using FT-IR, XRD and TEM.

#### *4.3.2.4 FT-IR spectra – effect of temperature*

The FT-IR spectra for the as-dried CP-nYAG powder, Figure 61, displayed very few functional groups when compared to the dried SG-nYAG powder.

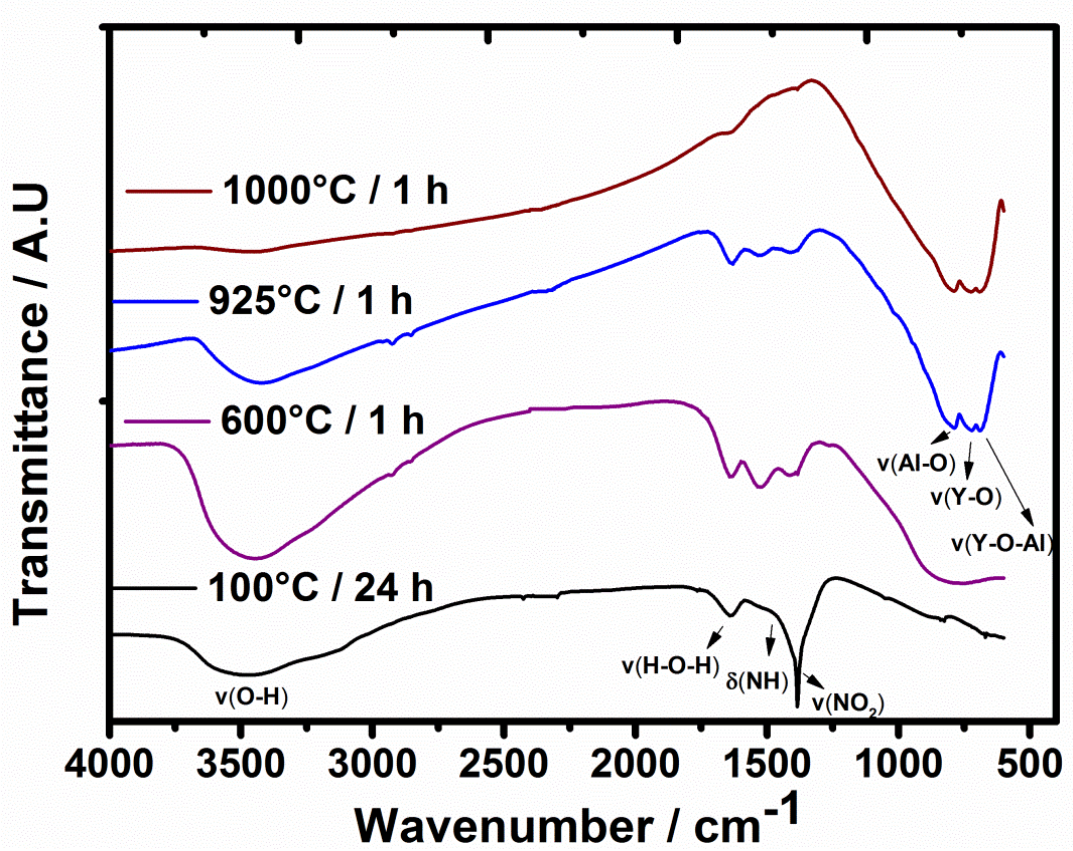


*Figure 61 FT-IR spectra of CP-nYAG precursor powders heat treated at different temperatures*

This also confirmed that the reaction mechanism between the precipitations was simple and most of the organics were removed during the washing process. The bands at ~1460 $cm^{-1}$ and ~1380 $cm^{-1}$ are associated with the vibrations of v(NH) and v($NO_2$) [226], whilst the peak intensities of the H–O–H bending modes (~1630 $cm^{-1}$) and v($NO_2$) were apparently low and the v($NO_3$) vibrations present in the SG-nYAG (100°C) trace were absent in the equivalent CP-nYAG curve. This could be due to

the effect of ammonia washing and the dehydration effect of the *n*-butanol treatment on the precipitates. The intensities of these bands were further reduced in the CP-nYAG curve after heat treatment at 600°C and there was also agreement with the thermal decomposition results. On further heat treatment at 925°C, the triplet bands formed between 800 - 600 $cm^{-1}$ correspond to the vibrations of Al-O, Y-O and Y-O-Al stretching, which coincide with the crystallisation peak of the DSC analysis. Moreover, the $v(NO_2)$ band present in the SG-nYAG after calcination at 1000°C for 1 hour is absent in the equivalent curve for the CP-nYAG powder, which confirms that the nitrate ions were removed during the co-precipitation synthesis method.

#### *4.3.2.5 XRD – effect of temperature*

After being heat-treated at 900°C for 2 h and 925°C for 1 h, some traces of the metastable hexagonal h-$YAlO_3$ (YAH) phase were observed in the CP-nYAG powders, Figure 62.

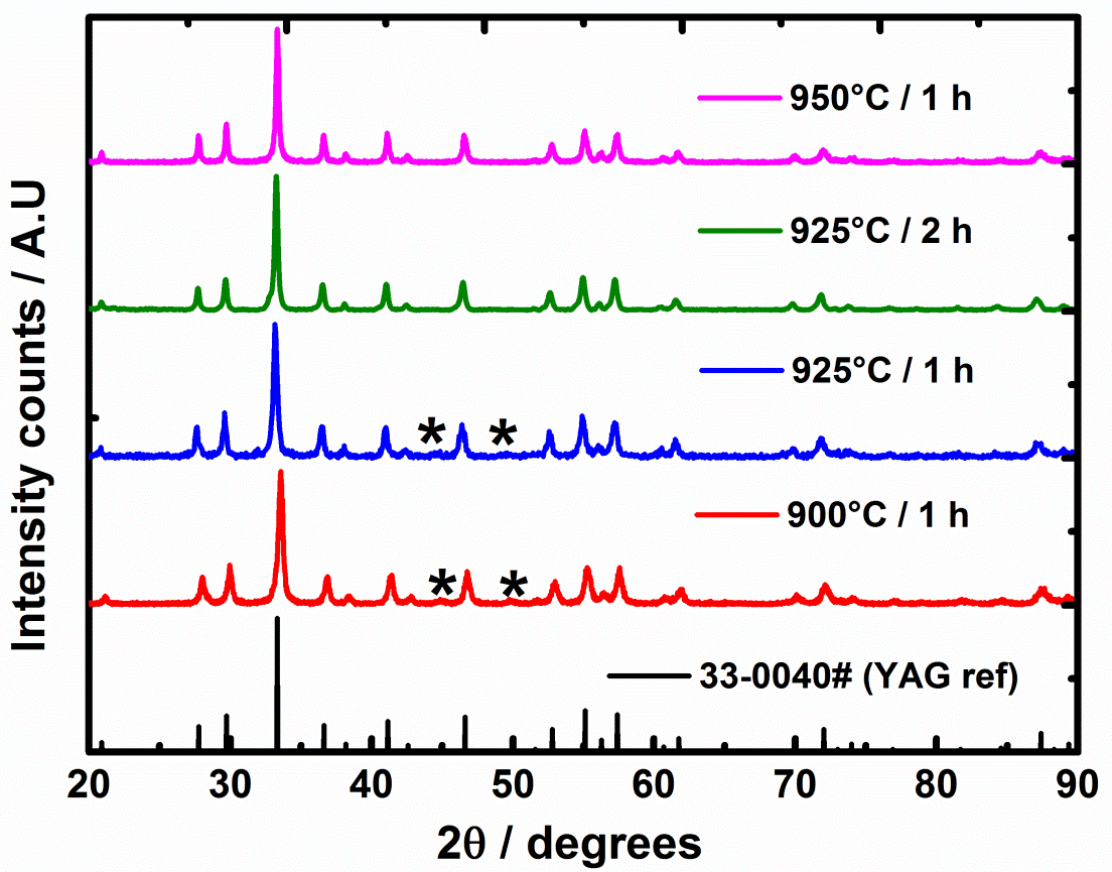


*Figure 62 XRD patterns of CP-nYAG precursor powders calcined at different temperatures (* H-$YAlO_3$)*

However, after heat treating at 925°C for 2 h, no detectable YAH phase was observed for the CP-nYAG powder; whilst the SG-nYAG powder had displayed characteristic peaks of the YAH phase. Note that all the peak positions matched with the standard YAG diffraction reference pattern and no intermediate phases such as YAM or YAP were observed. Only the metastable YAH formed as an intermediate at 900°C for 2 h, which subsequently transformed to YAG at elevated temperatures. It is important to note that the calcination temperature used in the co-precipitation method was 75°C less than that of the sol-gel method to obtain phase pure YAG. This also confirms the direct crystallisation without any stable intermediate phases, whereas in solid state methods, it undergoes transformation into YAP, YAM and YAG [95].

$$\begin{pmatrix} \left((OH)_3Al - Y(OH)_3\right)_{aq} \\ +\left((NO_2)_g + (H_2O)_g\right)\uparrow \end{pmatrix} \overset{600^\circ C}{\underset{\Delta}{\rightarrow}} Al-O-Y \overset{925^\circ C}{\underset{\Delta}{\rightarrow}} Y_3Al_3O_{12} \qquad \textit{Eqn 27}$$

Equation 27 describes the possible reaction mechanism during calcination. The metal hydroxides were oxidized to form an amorphous Y-O-Al (M-O-M bonding) network and the atomic diffusion between them transformed to a crystalline YAG phase at 925°C. The overall reaction is accompanied by the thermal decomposition of the volatiles and crystallisation kinetics of the YAG precursor as obtained from thermal analysis, FT-IR and XRD results.

#### *4.3.2.6 Morphology of YAG nanoparticles – effect of temperature*

Figure 63 shows the TEM images of the CP-nYAG powders obtained at different temperatures. For the particles obtained at 925°C for 2 h, the primary particle size was in the range between 20-30 nm. The particles obtained at 900°C clearly showed necking between the primary particles and as the temperature increased to 950°C to obtain single phase YAG, the particles are coalesced into agglomerates. When the results obtained in the present work are compared to the literature, the particle size observed by Chen and Wang et al. [129, 226] using co-precipitation was in a similar region, 30-60 nm, but their powders displayed a higher degree of agglomeration. .

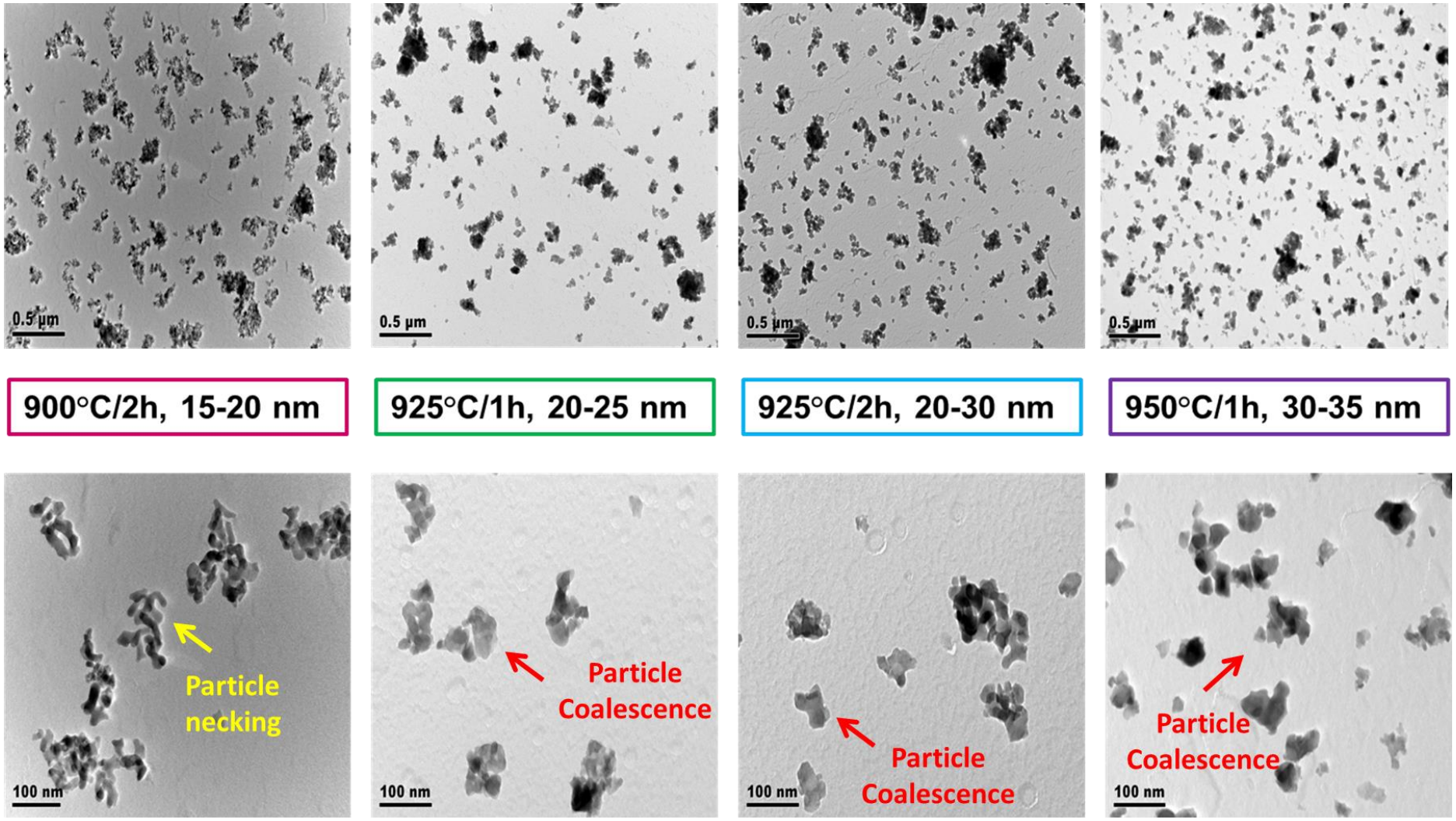


*Figure 63 TEM images of CP-nYAG powders obtained at different temperatures*

It is also observed from the TEM images that the extent of agglomeration is less with the co-precipitation method when compared to the sol-gel synthesised YAG particles. This could be attributed to three possible effects;

1. Control of agglomeration during the initial stages of drying
2. The effective core/shell mechanisms involved during precipitation that could prevent agglomeration drying and calcination
3. The lower processing temperature used compared to the sol-gel method.

However, the surface area that was measured using the BET technique suggested that the powders obtained from both the sol-gel and co-precipitation routes exhibited very low surface areas, 1.9 and 3.8 $m^2g^{-1}$, respectively. It has already been mentioned earlier (section 3.7.4) that highly reactive powders typically have surface areas of >20 $m^2g^{-1}$. Moreover, the particle sizes calculated from the BET formula were 694 nm and 380 nm for sol-gel and co-precipitation YAG powders, respectively. This clearly supports the features of the particles obtained using TEM, Figure 63, and it is more evident that the particles are coalesced and reduced their surface energy by forming agglomeration. This suggested strongly that the YAG particles synthesised by both routes suffered from significant agglomeration due to the heat treatment involved in both the approaches.

Conventional wet chemical synthesis routes such as sol-gel and co-precipitation involves only temperature as the key source to crystallise the YAG nanoparticles. Due to prolonged drying and calcination of the precursor powders the nanoparticles naturally agglomerated to a severe extent, however these steps are essential to achieve crystalline powders for both routes. Therefore, a new route was required to crystallise the nanoparticles without drying and calcination.

## 4.4 Solvothermal synthesis of YAG powders

Table 1 summarises the effect of precursors with different solvents on the synthesis of YAG nanoparticles using the solvothermal method. The table clearly shows that the particle characteristics were highly influenced by a change in precursors, solvents and the conditions being used. These results are discussed below.

*Table 15 Effect of different precursors and solvents on the particle characteristics of YAG in this study.*

| **Precursor** | **Solvent** | ****Temp at 8.5 MPa (working limit)** | **Phase-XRD** | **TEM - Particle** | |
|---|---|---|---|---|---|
| | | | | **Shape** | **Size** |
| Inorganic precursors | Ethanol | 275°C | AlO(OH), YO(OH), YAG & YAH | cubes, spheres & rods | - |
| | 2-Propanol | 300°C | YAG, YAH | sphere | ~8 nm |
| | 1, 4 BD* | 300°C | YAG | cubes & platelets | ~120 nm |
| Organic precursors | Ethanol | - | - | - | - |
| | 2-Propanol | 300°C | AlO(OH), YO(OH), YAG & YAH | - | - |
| | 1, 4 BD* | 300°C | YAG | sphere | ~27 nm |

*1, 4 BD, 1, 4 butanediol and ** temperature reached at the maximum pressure (working limit of the autoclave)

### 4.4.1 Effect of different solvents on the synthesis of YAG using inorganic (nitrate) precursors

#### *4.4.1.1 Effect of ethanol*

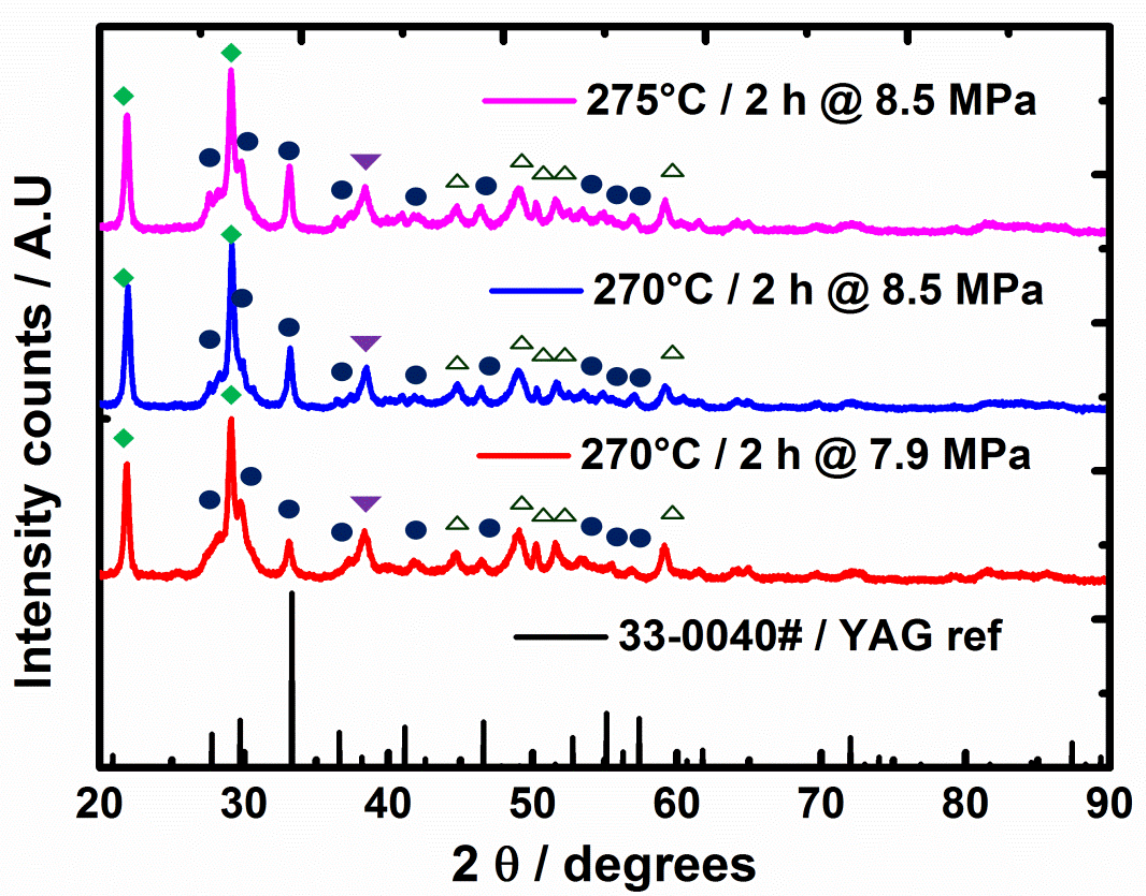


*Figure 64 XRD pattern of resultant powder synthesised using ethanol ( ◆YO(OH), ● YAG, ▼AlO(OH) and △YAH)*

Figure 64 shows the XRD patterns of the resultant powders when the precipitates of inorganic precursors were treated with ethanol under different conditions. It is very clear that only the hydroxyl derivatives of aluminium and yttrium elements were revealed; no significant improvement in the crystallinity of the precursors was observed, even after being treated at 270°C for 2 h and 8.5 MPa pressure.

Similar results were obtained by Li et al. [140] when the hydroxide mixtures (nitrate precursors) were treated with ethanol below 280°C and their results suggested that the single phase YAG was obtained only above 300°C and 10 MPa pressure.

This clearly showed that the temperature and pressure that has been used in this study were not enough to convert the hydroxide precipitates into crystalline powders.

When the precipitates treated with ethanol were processed at temperatures higher than 275°C, the autogenous pressure of the autoclave was found to increase beyond its working limit (8.5 MPa) Therefore, the capacity of the autoclave limited further exploration with the use of ethanol.

In this case, even though, ethanol had reached the supercritical condition, Table 16; the other ingredients such as hydroxyl molecules and the residual $NH_4OH$ species present in the precursor precipitates required pressures higher than 8.5 MPa for further crystallisation of the precursors.

*Table 16 Critical constants of different SCF solvents*

| **Solvent** | **Vapour pressure at 20°C / MPa** | **Critical temperature $T_c$ /°C** | **Critical pressure $P_c$ / MPa** | **Boiling Point /°C** |
|---|---|---|---|---|
| Water | ~0.0023 | 374 | 22.06 | 100 |
| Ethanol | ~0.0058 | 243.1 | 6.40 | 78.3 |
| 2-Propanol | ~0.0026 | 235.1 | 4.76 | 82.5 |
| 1, 4 butanediol | ~0.0001 | 450.65 | 5.52 | 235 |
| Ammonia | ~0.8570 | 133 | 11.3 | -33.34 |

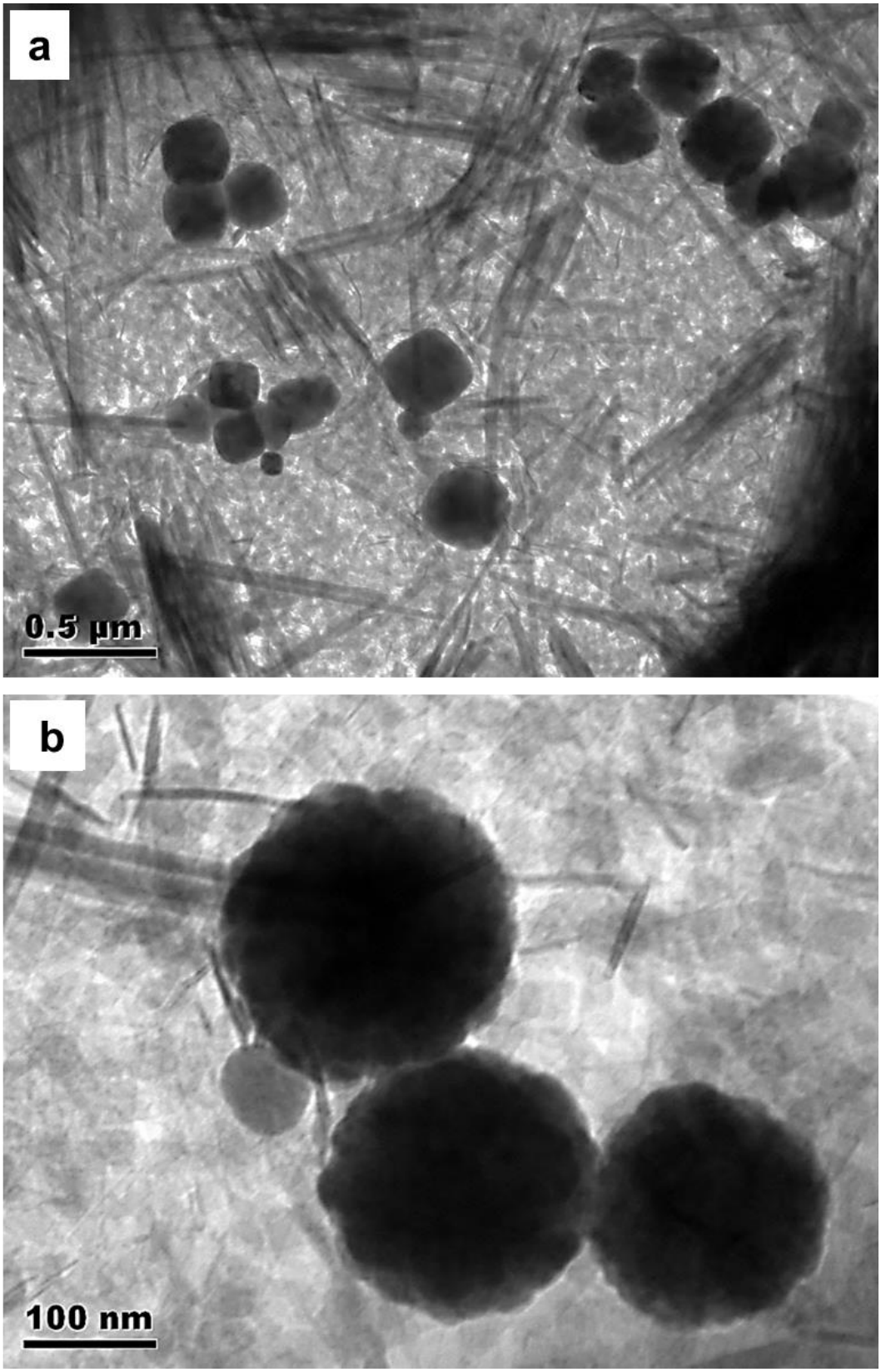


*Figure 65 TEM images of the particles obtained using ethanol (a) low and (b) high magnifications*

Figure 65 shows the TEM morphology of the particles obtained at 270°C for 2 h and 8.5 MPa. Despite the lack of crystallinity, the particles obtained from ethanol were ~120 nm in size and exhibited a heterogeneous morphology such as rods and plate-like structures. A very few particles were cubic in structure. Similar cubic particles were obtained with a high degree of crystallinity by Poliakoff et al. [137] and Li et al. [140] when they synthesised submicron YAG using ethanol or ethanol-water mixtures at temperatures above 300°C and 10 MPa.

The present study also supports previous findings that YAG particles synthesised using ethanol often formed cube-like particles with a size ranging from 60 -150 nm. Nevertheless, particles with spherical morphology and smaller sizes are much preferred for the production of fine microstructured ceramics.

#### *4.4.1.2 Effect of 2-propanol*

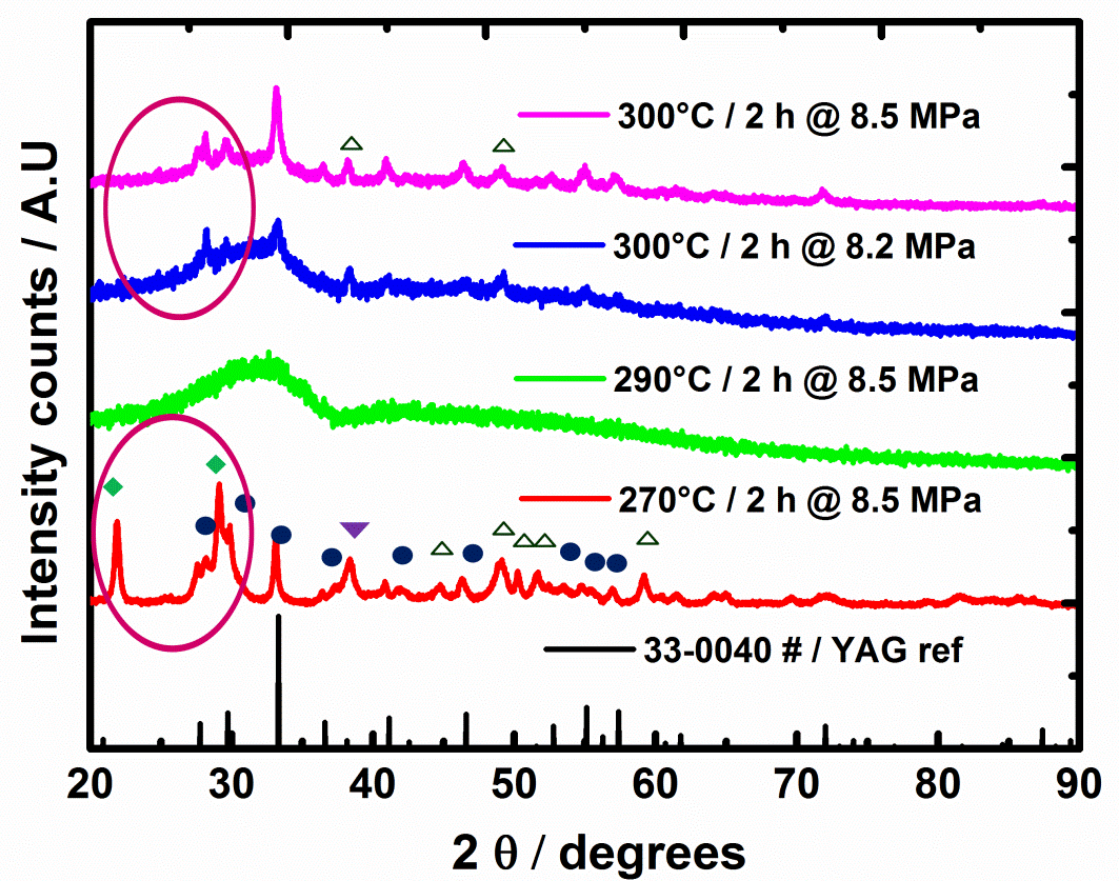


*Figure 66 XRD pattern of powders synthesised using 2-propanol (◆YO(OH), ●YAG, ▼ AlO(OH) and △YAH)*

Figure 66 shows the XRD patterns when 2-propanol (isopropanol) was used as the supercritical solvent to crystallise the inorganic precursors. When the precipitates were treated at 270°C for 2 h and 8.5 MPa, only the hydroxyl derivatives of aluminium and yttrium elements were observed. Since the vapour pressure of the propanol was lower than for ethanol, it allowed the autoclave to reach 300°C at the maximum allowed pressure of 8.5 MPa. The XRD pattern obtained from 290°C for 2 hour and 8.5 MPa showed a completely amorphous structure, which indicated the complete dissolution of the hydroxyl derivatives and the onset of YAG crystallisation, Figure 66. When the precursor was subjected to 300°C for 2 h and 8.5 MPa pressure, the predominant hydroxide peaks (circled) were transformed into yttrium aluminates; some traces of the YAG and metastable hexagonal h-$YAlO_3$ (YAH) phases were observed. However, the intensities of the peaks in the XRD patterns were very low due to the lack of crystallinity, which could be attributed to the inadequacy of the pressure required for the other species to reach supercritical conditions.

Figure 67 shows the TEM morphologies of the resultant ST-n(YAG+YAH) powder synthesised using isopropanol at 300°C for 2 h and 8.5 MPa pressure. A substantial difference in particle morphology was observed when 2-propanol was used as the supercritical solvent with the nitrate precursors. Very fine particles of about 8 ± 2 nm were observed, together with the formation of a minor amount of YAG, Figure 67. The reduction in the particle size could be due to differences in the solvent characteristics. The morphology of the particles was ellipsoidal-like structures; similar morphology was observed by Santos et al. [227] when aluminium isopropoxide and yttrium acetate were used to produce Y-rich boehmite particles via SCF process. This clearly shows that the isopropyl molecules can cause ellipsoidal-like particles and the XRD suggested that the particles were chemically inhomogeneous. The surface area determined using BET was found to be 160.1 $m^2 g^{-1}$ and the particle size calculated from equation 19 was 8 nm. It is worthwhile remembering that the surface area of the particles obtained from the sol-gel and co-precipitation routes were only 1.9 and 3.8 $m^2g^{-1}$, respectively. This clearly shows that the extent of agglomeration of the YAG particles from the SCF route is far less than for the other routes investigated in this project. Nevertheless, owing to the lack of crystallinity, green processing using these particles was not performed.

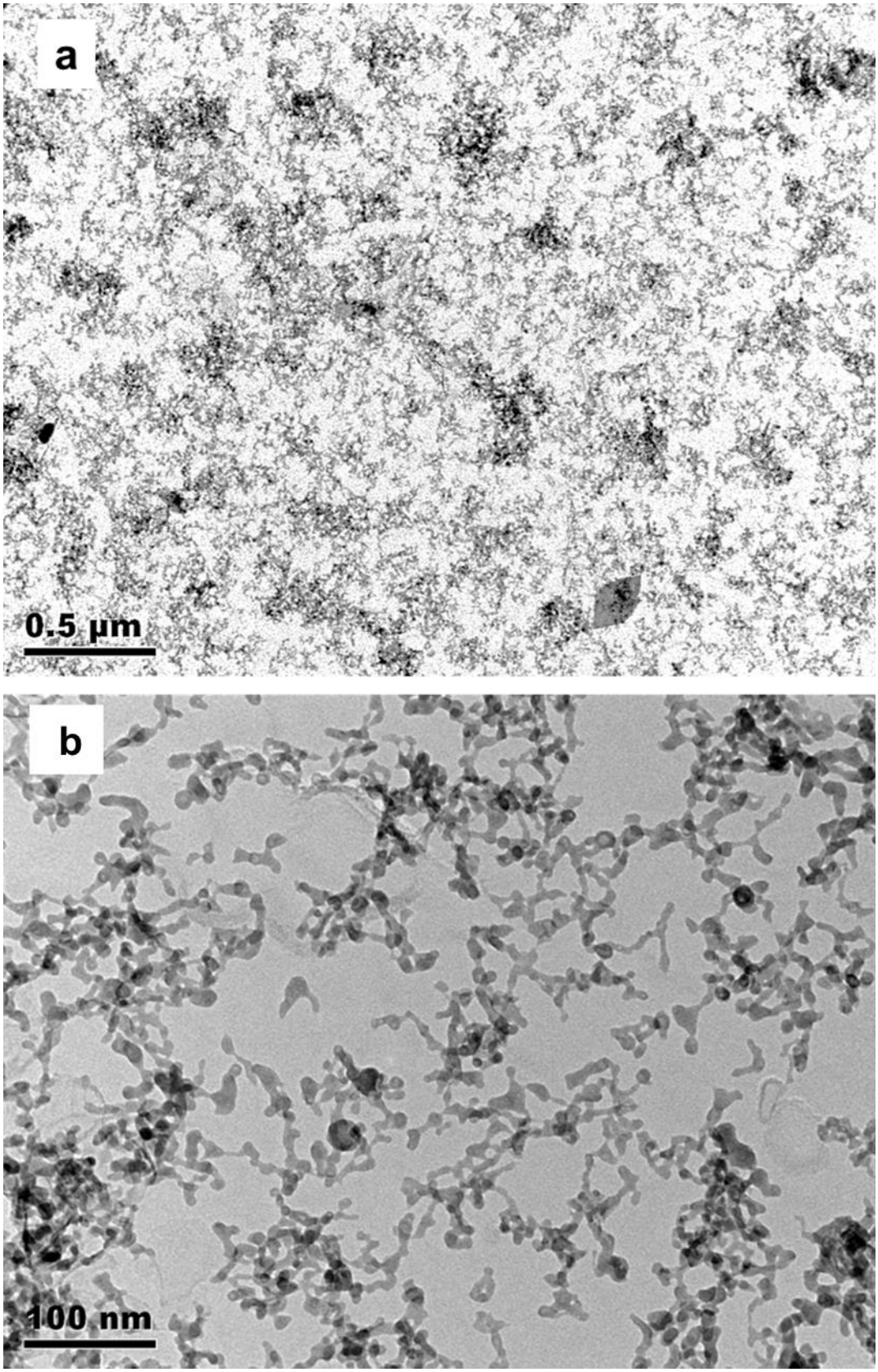


*Figure 67 TEM images of the ST-n(YAG+YAH) particles obtained using 2-propanol (a) low and (b) high magnifications*

#### *4.4.1.3 Effect of 1, 4 butanediol*

Figure 68 shows the XRD pattern of the hydroxides synthesised using 1, 4 butanediol. In contrast to the previous results, single phase YAG with a high degree of crystallinity was obtained for the precipitates of nitrate precursors. Moreover, the obtained spectra exactly matched with the YAG reference (33-0040 JCPDS). This confirmed that the use of 1, 4 butanediol, even at subcritical conditions of 300°C and 8.5 MPa, greatly influenced the degree of crystallinity. Note that the supercritical conditions for 1, 4 butanediol are ~450°C and 5.5 MPa pressure, Table 16.

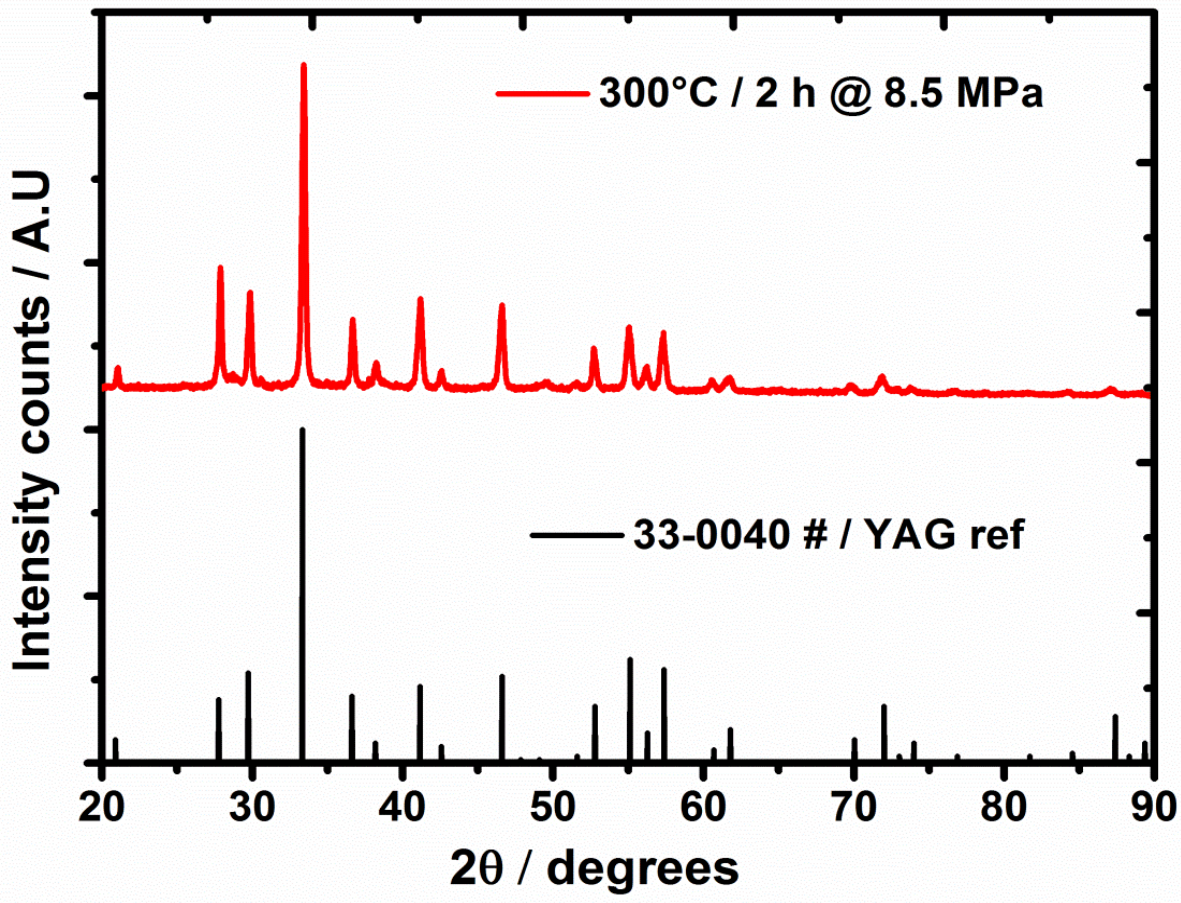


*Figure 68 XRD patterns of ST-YAG powder processed using nitrate precursors and 1, 4 butanediol at 300°C and 8.5 MPa pressure.*

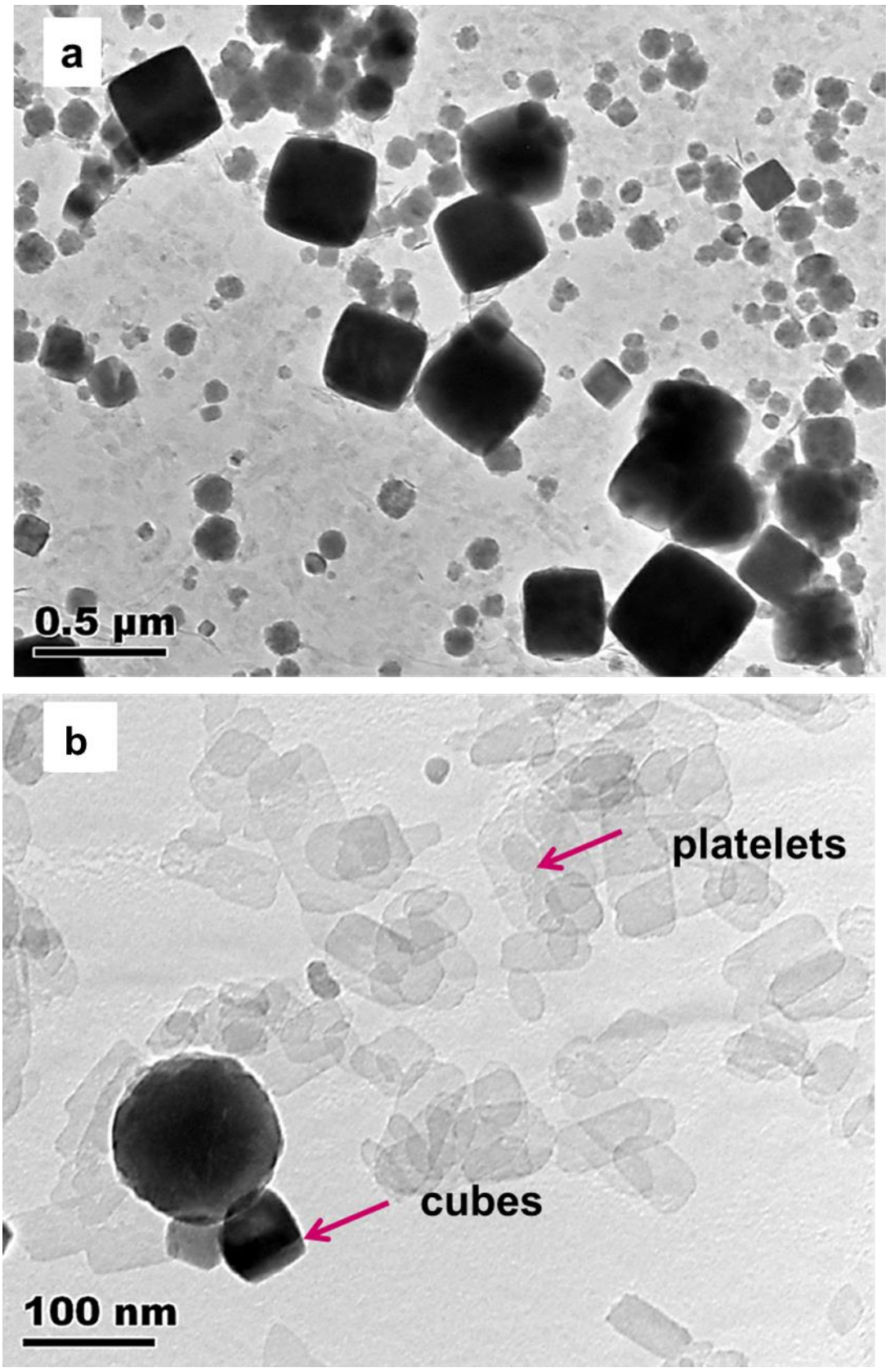


*Figure 69 TEM images of the ST-YAG particles obtained using nitrate precursors and 1, 4 butanediol (a) low and (b) high magnifications*

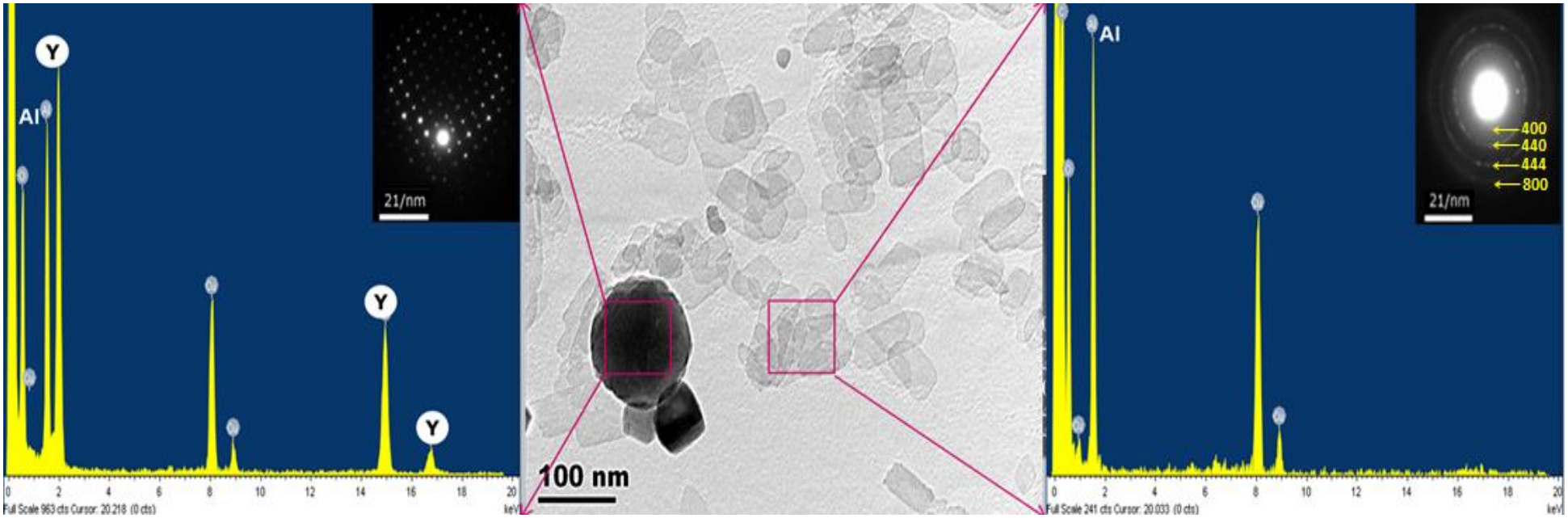


*Figure 70 EDX and SAED pattern of the particles obtained using 1, 4 butanediol with nitrate precursors*

Figure 69 shows the TEM morphologies of the resultant ST-YAG particles obtained using the 1, 4 butanediol. Whilst the XRD pattern showed a strong single phase YAG peak, the TEM results revealed two different particle morphologies, cube-like particles and platelets, Figure 69 a and b. The cube-like particles were similar to the particles obtained using ethanol, which were rich in crystallinity. EDX analysis performed on both types of particles revealed that the cube-like particles were single crystal YAG but that the platelets were deficient in yttrium. This was more evident from the EDX graphs and the indexed SAED pattern, Figure 70, on the platelets showed γ- alumina [228]. Similar results were observed by Nyman et al. [229] when they synthesised Ce:YAG using 1, 4 butanediol. They found that layered alumina was formed as an intermediate phase during the synthesis, which was found to be insoluble at the end of the reaction.

Their results suggested that the precipitates of yttrium and aluminium hydroxides in this work were partially crystallized into single phase YAG and the platelets obtained could be the undissolved layered alumina. The surface area determined using BET was found to be 22.4 $m^2 g^{-1}$ and the calculated particle size was 59 nm.

From this study, it is very clear that the shape and size of the particles and the chemical homogeneity were not only influenced by the solvent characteristics, but also by the precursors used for the synthesis via the SCF route.

### 4.4.2 Effect of different solvents on the synthesis of YAG using organic precursors

#### *4.4.2.1 Effect of 2-propanol*

The XRD pattern obtained using the 2-propanol revealed only the hydroxyl derivatives when the organic precursors were treated at 300°C for 2 h at 8.5 MPa pressure, Figure 71. This clearly shows that the dissolution and crystallisation of the organic precursors wasn't favoured when 2-propanol was used, whereas, the inorganic precursors under the same conditions had dissolved and started the crystallisation process, Figure 66. This suggests that the organic precursors required even higher temperatures and pressures to produce single phase YAG nanoparticles, but the autoclave limitations prevented further investigation.

This study also concluded that, regardless of the precursor type, the use of ethanol and propanol required conditions higher than 300°C and 8.5 MPa to synthesis YAG.

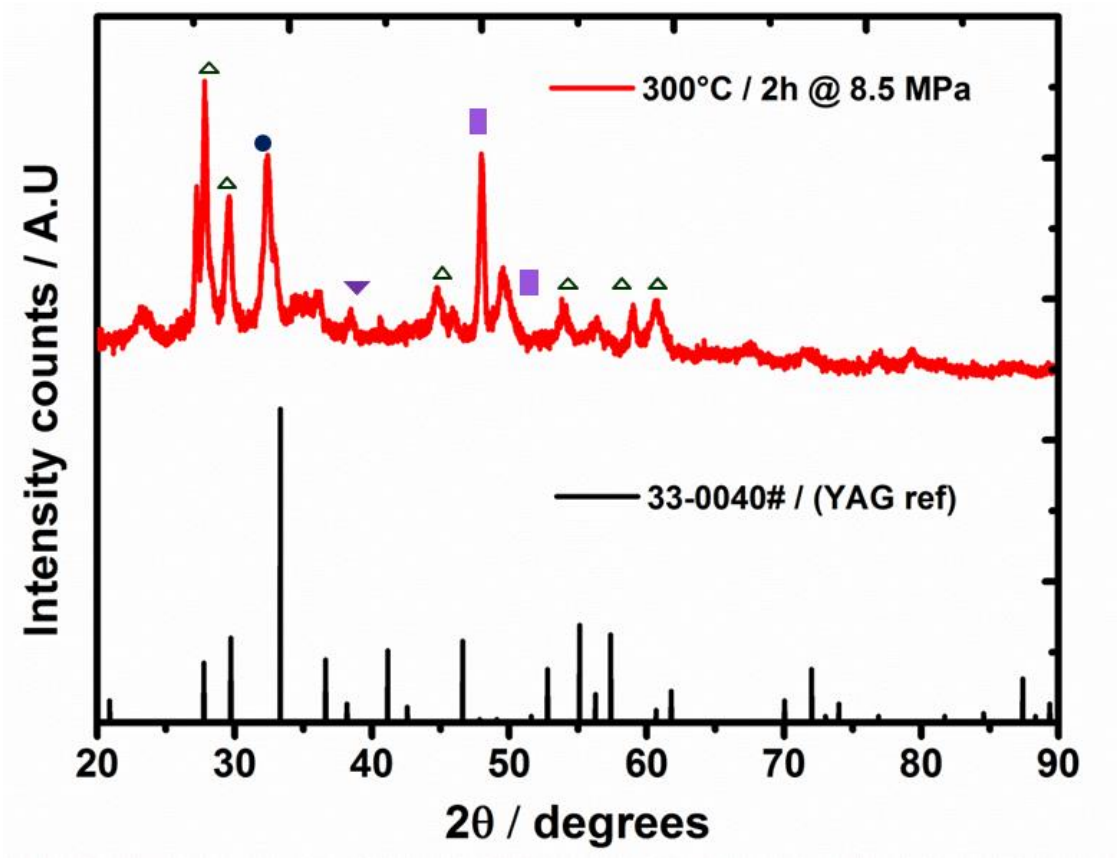


*Figure 71 XRD pattern of organic precursors treated with 2-propanol ( ■YAM, ● YAG, ▼ AlO(OH) and △ YAH)*

#### *4.4.2.2 Effect of 1, 4 butanediol*

The XRD patterns, Figure 72, revealed single phase YAG at three different conditions from 270°C – 300°C with varying autogenous pressures. The only difference amongst them is the degree of crystallinity, which is more evident from the differences in the relative intensities of XRD patterns and no intermediate phases such as YAH, YAM or YAP could be observed. This indicated that the use of highly reactive 1, 4 butanediol caused crystallisation into the YAG structure, even at 270°C and 2 MPa pressure. Moreover, the solvent didn't even require supercritical conditions, Table 16, to crystallise YAG particles for organic precursors.

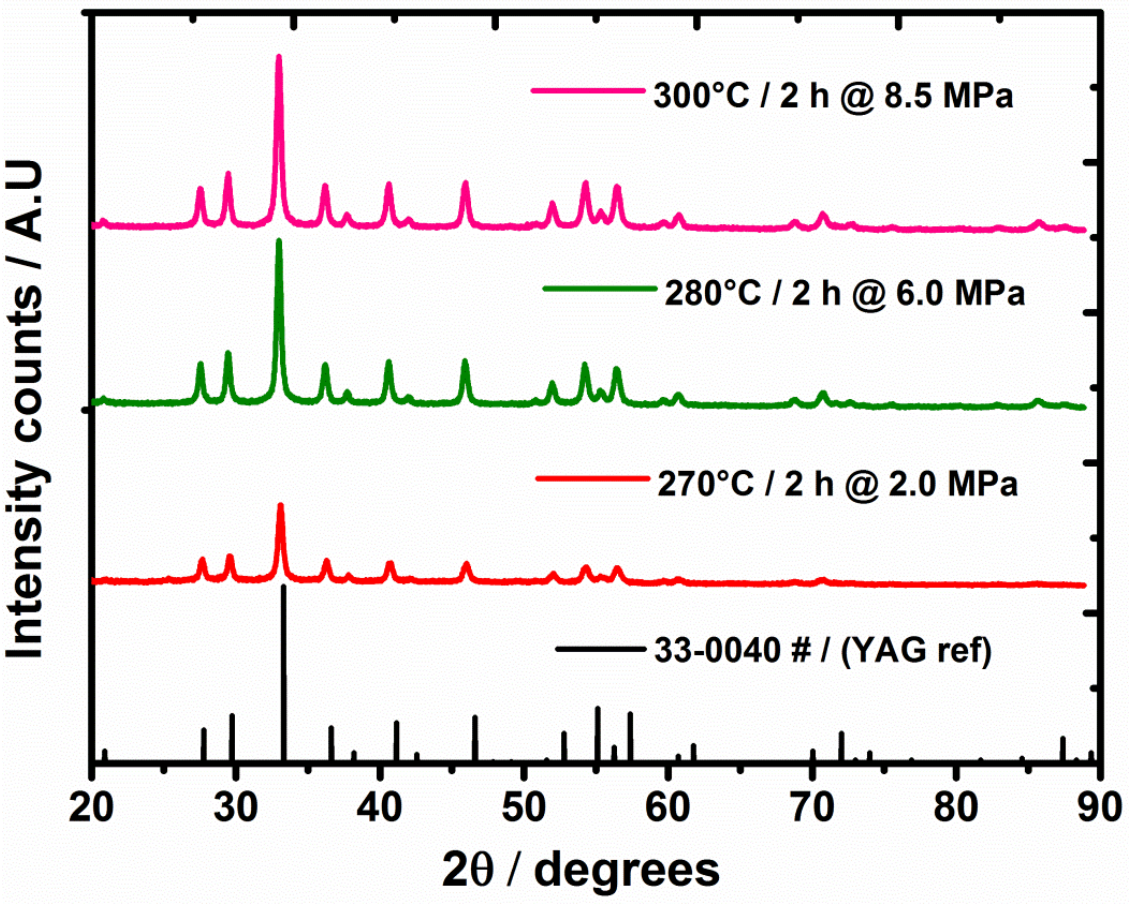


*Figure 72 XRD patterns of ST-nYAG powders obtained using organic precursors at different conditions*

The TEM morphologies of the powders are shown in Figure 73. The particles exhibited different morphologies with varying temperatures and pressures. When they were 270°C and 2 MPa, Figure 73 a and b, the primary particles were about 5 nm in size but were agglomerated in the form of 30 nm clusters. At 280°C, the

autogenous pressure was increased to 6 MPa and the resultant particles were coarser with an irregular structure, Figure 73 c and d. The increase in temperature and pressure further coalesce the 5 nm particles into 30 nm coarser particles. On further increase in temperature to 300°C, the pressure increased to 8.5 MPa and lead to further diffusion to form spherical nanoparticles, Figure 73 e and f. It is worth noting that the particles obtained were homogeneous in structure and no inclusions of secondary particles (platelets, cube-like or rods) with chemical inhomogeneity were formed. This suggests that the organic precursors underwent complete dissolution and crystallised into single phase YAG, within the detection limit of XRD, when the butanediol was used.

To ascertain the effect of temperature on the particle morphology, different volumes of precursors with similar stoichiometry were processed in the autoclave to achieve different pressures at 300°C. All the particles obtained, however, showed similar morphology, Figure 74. Despite the fact that most of the particles were similar in size, at 300°C and 6 MPa some clusters of finer 5 nm particles were still present; arrows indicate these in Figure 74 a. This suggested that it required a higher pressure to form homogenous particles. The absence of such clusters at 7 and 8.5 MPa confirmed this view, Figure 74 b and c.

This study concluded that both the temperature and pressure have a profound effect in determining the particle morphology and suggested that a threshold pressure of about 7 MPa was required to form ~30 nm spherical particles at 300°C. Moreover, the particles had a surface area of about 46.6 ± 0.9 $m^2$ $g^{-1}$ and the calculated BET particle size from equation 19 was ~27 nm. This is also in accordance with the TEM morphology and suggests that the particles obtained using SCF technology exhibited less agglomeration when compared with the other routes investigated.

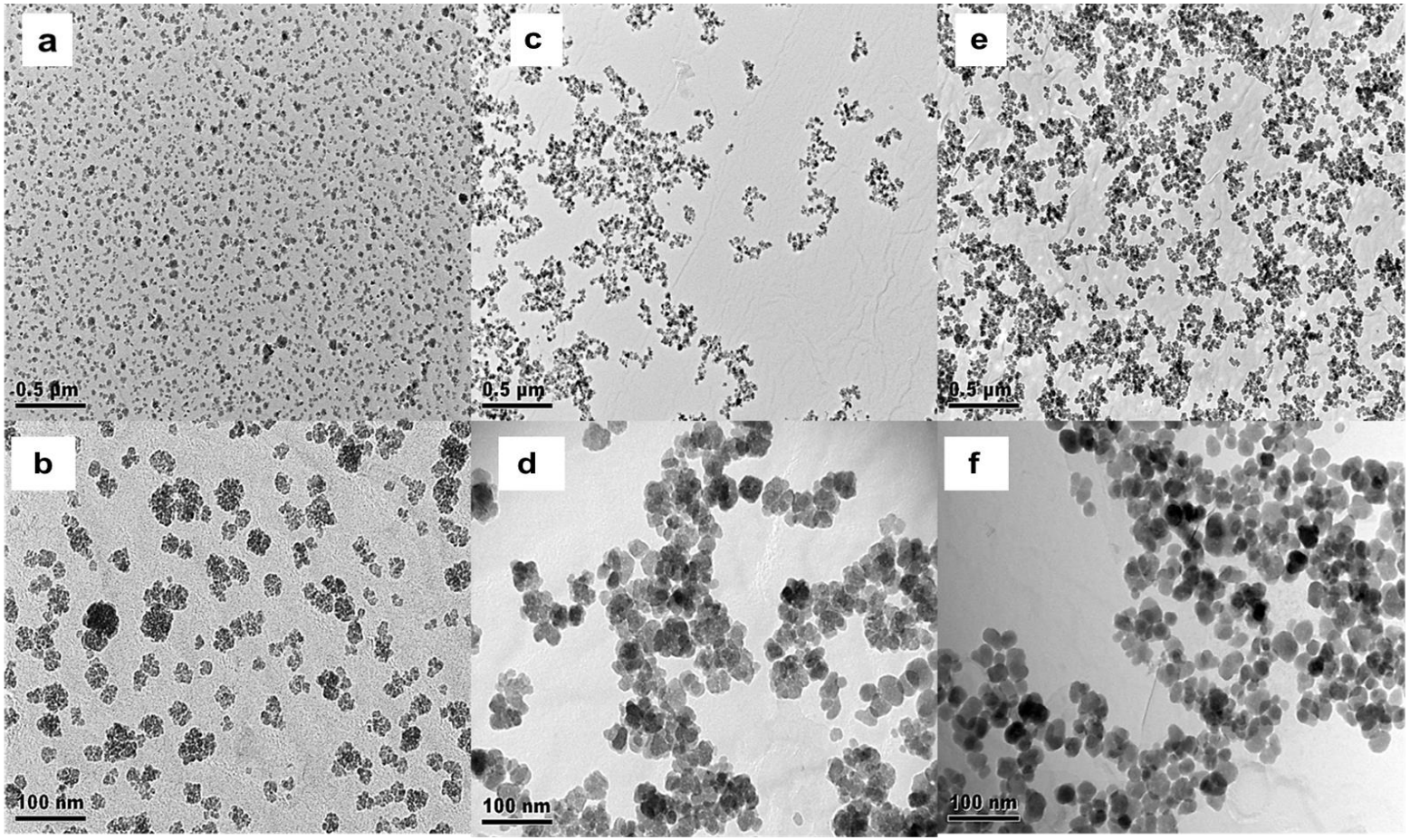


*Figure 73 TEM images of ST-nYAG powders obtained using organic precursors at different conditions.*

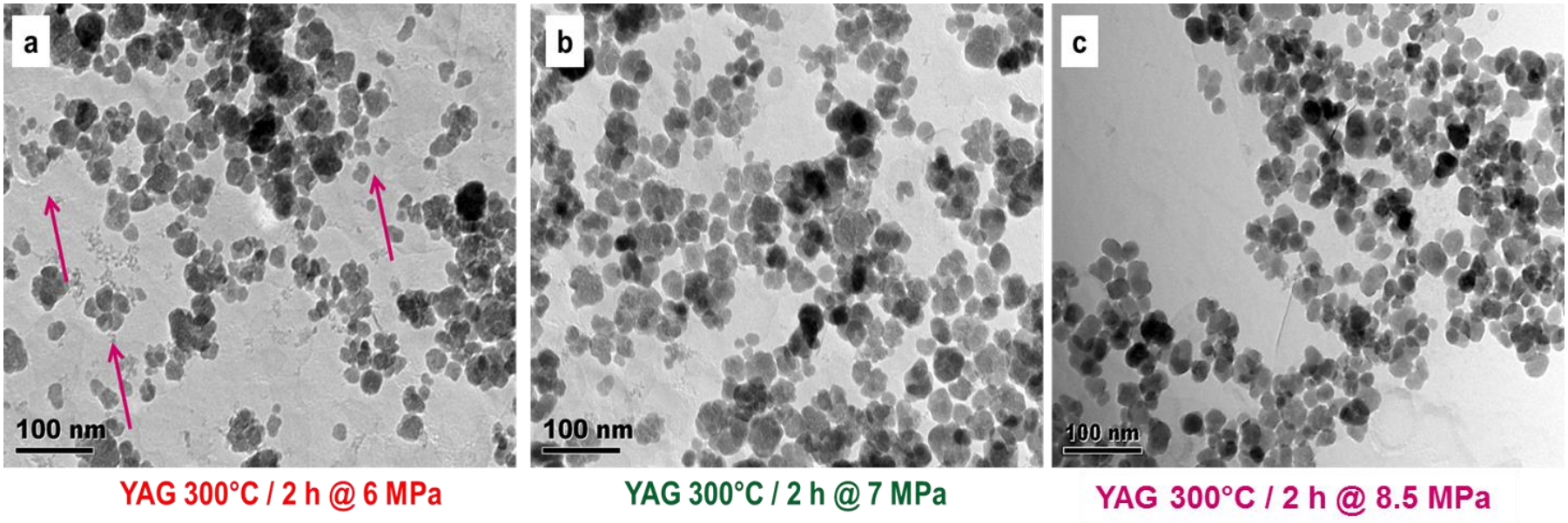


*Figure 74 Effect of pressure on ST-nYAG particles at 300°C for 2 h (arrows showing the small particles).*

## 4.5 Comparison of sol-gel, co-precipitation and solvothermal synthesis of YAG powders

The results obtained from the sol-gel, co-precipitation and solvothermal methods have been discussed in this chapter. These three routes can be compared based on the structural and morphological results to determine the merits and demerits of making YAG using each of the routes.

The XRD results obtained from all the routes exhibited single phase YAG powders when the conditions were optimised, Figure 75. However, with the solvothermal route, there was no need to dry and calcine the precursors to crystallise for the sol-gel and co-precipitation routes.

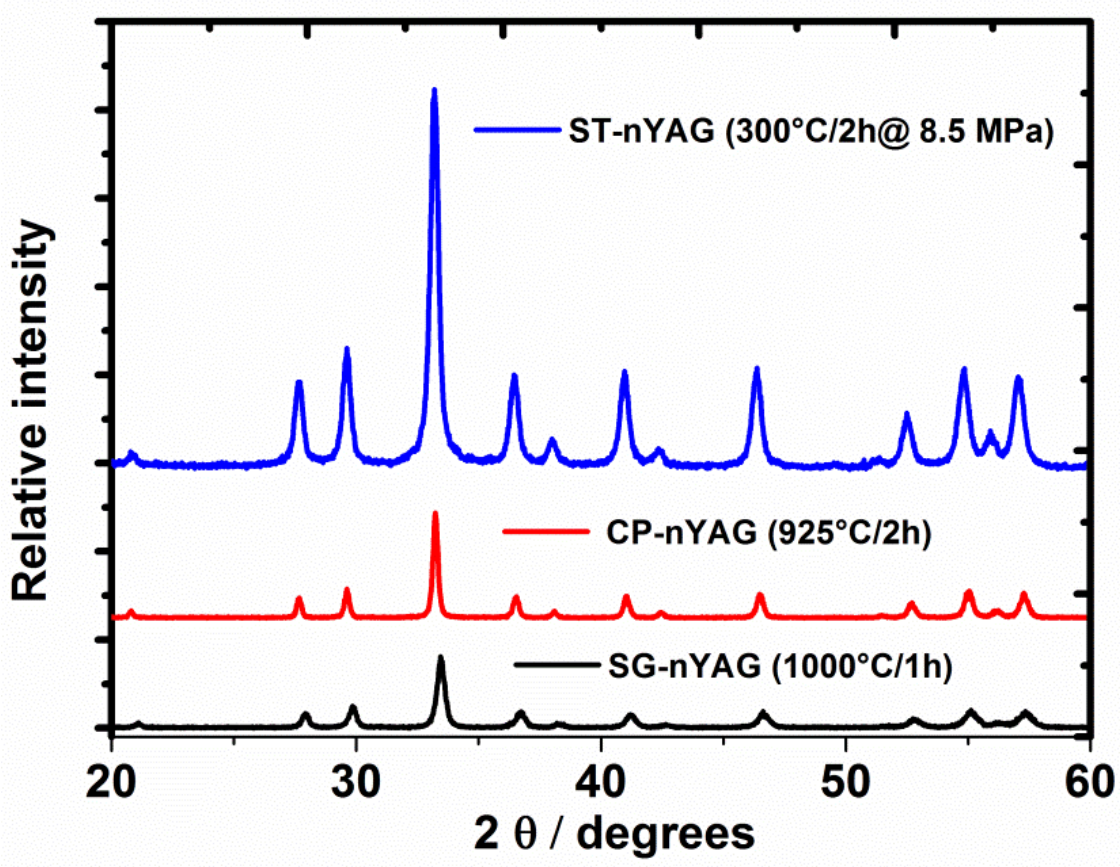


*Figure 75 XRD pattern of sol-gel, co-precipitation and solvothermal YAG powders*

.

*Table 17 Particle characteristics of YAG synthesised using different routes and precursors.*

| **Sample** | **Synthesis route** | **Precursors** | **XRD** | **TEM particle size** | **BET particle size** | **BET Surface area / $m^2g^{-1}$** | **Extent of agglomeration** |
|---|---|---|---|---|---|---|---|
| SG-nYAG | Sol-gel | Nitrate | YAG | 25 ± 5 nm | 694 nm | 1.8 ± 0.1 | Very high |
| SG-YAG | Sol-gel | Metal | YAG | 110 ± 5 nm | - | - | Very high |
| CP-nYAG | Co-precipitation | Nitrate | YAG | 30 ± 5 nm | 347 nm | 3.7 ± 0.1 | High |
| ST-n(YAG+YAH) | Solvothermal | Nitrate | YAG+YAH | 8 ± 2 nm | 8 nm | 156.8 ± 3.2 | Low |
| ST-YAG | Solvothermal | Nitrate | YAG+$Al_2O_3$ | NA | 59 nm | 21.9 ± 0.4 | Low |
| ST-nYAG | Solvothermal | Organic | YAG | 25 ± 3 nm | 27 nm | 46.6 ± 0.9 | Low |

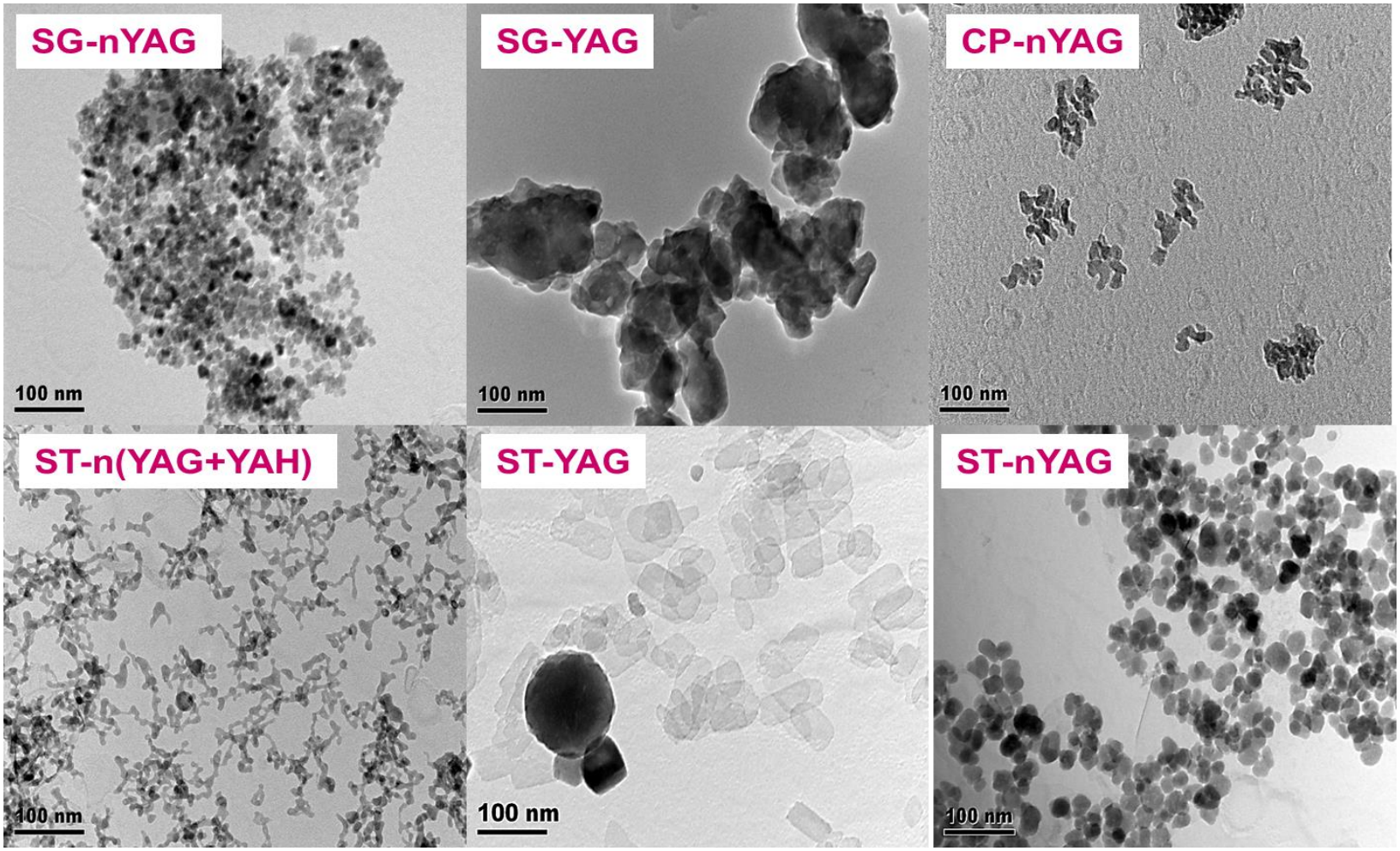


*Figure 76 TEM images of YAG synthesized from sol-gel, co-precipitation and solvothermal methods using nitrate, metal and organic precursors*

The solvothermal route also formed single phase YAG at nearly 700°C lower temperature, albeit with the help of additional pressure, when compared to the other routes. Moreover, the intensities and the peak width from the sol-gel and co-precipitation routes were very low when compared with the solvothermal YAG nanopowders, which suggests that the YAG powders obtained using the solvothermal route were more highly crystalline.

The characteristics of the particles obtained from the different methods are summarised via TEM images, Figure 76, and BET data, Table 17. The former shows that the particles produced by the solvothermal process were finer and exhibited less agglomeration. Although the BET results show that the particles obtained using 2-propanol, ST-n(YAG+YAH), with nitrate precursors exhibited high surface area, the XRD results showed poor crystallinity. Similarly, there was a compositional inhomogeneity in the powders obtained using 1, 4 butanediol with nitrate precursors, ST-YAG, which also showed heterogeneous particle morphology. Only the powder obtained from 1, 4 butanediol with organic precursors, ST-nYAG, exhibited the desired particle characteristics; very high crystallinity, spherical particle morphology with little agglomeration and a high surface area. Hence, suspensions based on this powder are used for colloidal processing to produce YAG green bodies.

## 4.6 Colloidal processing of YAG suspensions

In this section, the electro-kinetic response of $NH_4PAA$ in the YAG suspension and the rheology of the suspensions are discussed together with the analytical evidence. In addition, the effect of ultrasound, solids loadings and ageing effects are discussed with a view to determining the best processing conditions to produce concentrated YAG suspension for subsequent processing.

### 4.6.1 Electro-kinetics and the mechanism underpinning ST-nYAG suspensions

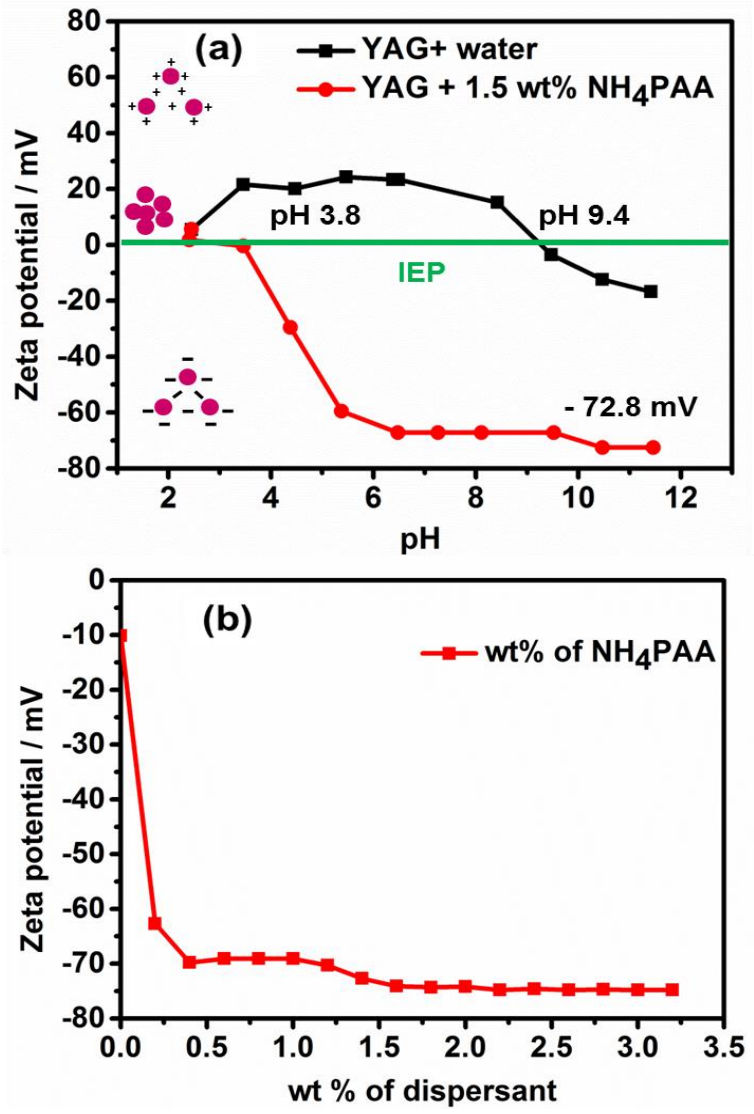


*Figure 77 (a) Potentiometric titration of YAG suspension with (black solid square) and without dispersant ( red solid circle) (b) Concentration series of $NH_4PAA$ in the YAG suspension*

Usually particles in dispersion randomly move with an ionic shell due to gravity or an applied voltage on it. Beyond a distance, the shell or a boundary of the particles don't move due to the hydrodynamic surface shear or the slip plane, which persists within the diffuse layer and the potential that exists at the plane, is called zeta potential. Electrophoresis technique has been widely used for determine zeta potentials by directly measuring the electrophoretic mobility of a particle.

Figure 77a, shows the potentiometric titration from pH 2 to 12 of the YAG suspensions with and without dispersant using the Acoustosizer II. The suspension without dispersant (black curve) displayed the isoelectric point (IEP, i.e. pH at which zeta potential equals zero), where the charge on the surface of the particles is equal, at pH 9.4 and displayed a very low zeta potential in both the acidic and alkaline regions. In this case, cationic dispersants could have been used to increase the positive zeta potential in the acidic region, but the latter could have had a negative impact on the ceramic particles, perhaps the cationic dispersants and the acidic pH can dissolving them. Moreover, cationic dispersants are composed of halogens such as $Cl^-$, $Br^-$ and $I^-$ ions and these tend to remain in ceramics even after sintering. To initiate the electro-steric mechanism using an anionic dispersant, the particles should be negatively charged; as shown by Figure 77a (black curve), this occurred at pHs above 9.5. Therefore, $NH_4$PAA, an anionic dispersant was used to produce stable YAG suspensions under these conditions.

Figure 77b shows the electro-kinetic response of the YAG suspension at pH 10 with varying concentrations of $NH_4$PAA. An initial steep increase in the negative zeta potential occurred, which was followed by a plateau was observed. The former was due to the dissociation of carboxylic acid (COOH) into carboxylic ions, $COO^-$ and gives more negative charge. The plateau region demonstrated that the particles were covered by the dispersant indicating that this occurred at ~1.5 wt.% [230]. Therefore 1.5 wt.% of $NH_4$PAA was used to produce subsequent suspensions.

$$\boldsymbol{RCOO^-NH_4^+ \rightarrow RCOO^- + NH_4^+} \qquad \textit{Eqn 28}$$

The suspension with 1.5 wt.% NH4PAA (red curve) showed a significant difference in the zeta potential compared to the suspension without dispersant, Figure 77a, with the IEP occurring at pH 3.8 when the $NH_4$PAA was added. This shift was due to the adsorption of the disassociated carboxylic ions leading to high negative charges on the surface of the particles, equation 28. Since, equivalent positive charge was required to balance the charges on the surface at the IEP, higher concentrations of the $H^+$ ions from the acid were required.

When the $NH_4$PAA was added to the YAG suspension at a pH above 9.5, the carboxylic acid tail dissociated into carboxylic ions and provided additional negative charge described above. Combined with the absorption of $OH^-$ ions on the particle surfaces, this led to the very high negative zeta potentials measured about up to a maximum of -73 mV. Therefore, pH 10 was chosen as the best pH to produce future YAG suspensions.

To determine the polymer configuration, FT-IR analysis was performed on the YAG suspensions, Figure 78. For the spectra, the peaks near 1650 and 1020 $cm^{-1}$ are caused by $OH^-$ stretching and γ-$NH_3$ rocking vibration, respectively. These are produced by the disassociation of the $NH_4OH$ used to modify the suspension pH into $NH_4^+$ and $OH^-$ ions. The adsorbed $OH^-$ ions on the surface of the YAG particles generate some negative charge and the remnant $NH_4^+$ ions simply dissolved in the water. No other significant peak positions were observed in the sample A. The FT-IR spectrum of sample B supports the proposed polymer configuration. The peaks near 1500 and 1550 $cm^{-1}$ are attributed to the dissociation of carboxylic acid into symmetric and asymmetric carboxylic ions ($COO^-$) respectively [231], which result in the further increase in the zeta potential of the suspension. Spectrum B also showed a reduction in the Al-O-Y peak near 750 $cm^{-1}$, this could be due to the presence of the adsorbed $NH_4$PAA covering the YAG particles and causing the change in the spectrum.

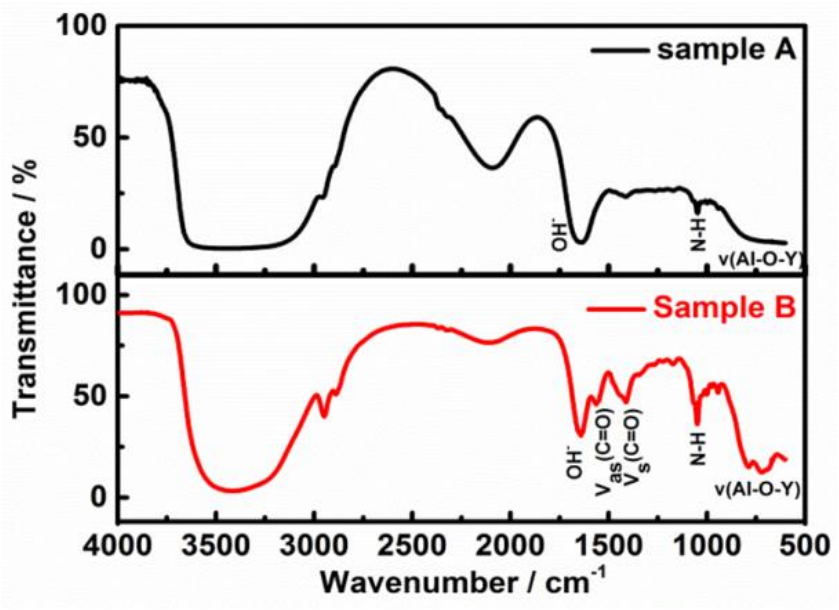


*Figure 78 FT-IR spectra of of 5 wt % aqueous YAG suspensions; Sample A - without dispersant and Sample B – with dispersant (3 wt % $NH_4$PAA).*

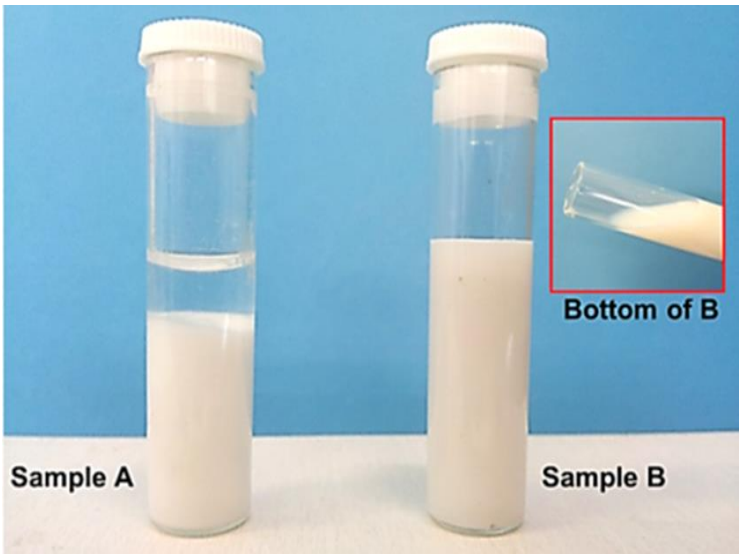


*Figure 79 Sedimentation observation result of 5 wt % aqueous YAG suspensions; Sample A - without dispersant and Sample B – with dispersant (3 wt % $NH_4$PAA).*

The successful effect of the dispersant was observed from the sedimentation of the respective suspensions at pH 10, Figure 79. For sample A, the particles settled to form two distinct phases after 24 h, whilst for sample B no setting was observed, even after 90 days.

## 4.7 Particle size distribution (PSD) of the YAG suspensions

The particle size distributions of the YAG suspensions containing 1.5 wt.% $NH_4PAA$, obtained using the Mastersizer, are shown in Figure 80, both the volume and number percentages of the YAG particles in the suspensions are presented, Figure 80 a and b. The suspension prepared via the solvothermal (ST) route, blue curve, displayed a narrow distribution with a range between 0.1 – 0.4 µm, whilst the suspension prepared using the as-synthesised CP-YAG, red curve, showed a broad distribution from 0.2 to 70 µm. even after ball milling for 48 hours the latter particles ranged from 0.2 to 10 µm. This clearly shows that the YAG agglomerates obtained by the co-precipitation method were hard to break. In contrast the ST-nYAG didn't even require ball milling to achieve particle separation, eliminating a processing step and avoiding contamination.

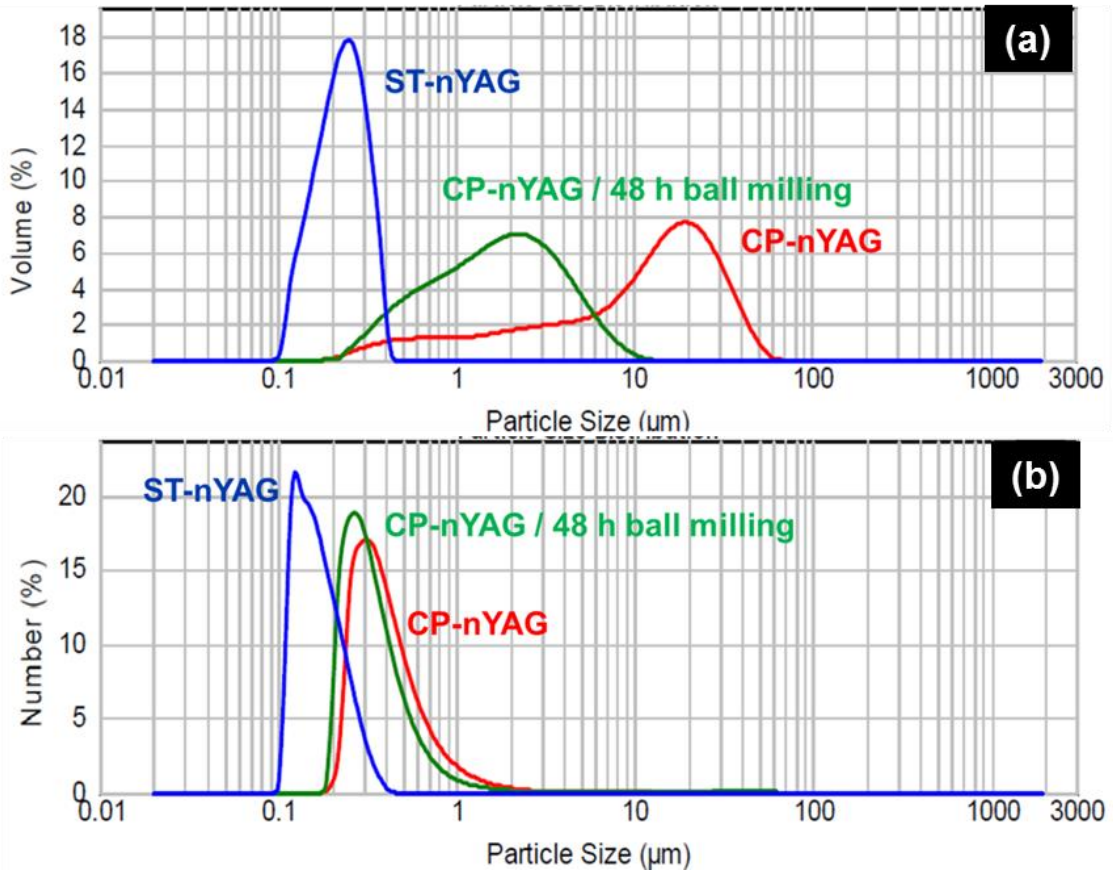


*Figure 80 PSD of the YAG suspensions (a) volume % and (b) number %*

## 4.8 Rheological Behaviour of the YAG suspensions

### 4.8.1 Effect of Ultrasound

The effect of ultrasound on the rheology of the suspensions is shown in Figure 81. The results show a decreasing trend in viscosity with increasing ultrasonic treatment for the first 3 minutes after which there was no further effect. The viscosity of the suspension without ultrasound measured 23 mPa s at a shear rate of 100 $s^{-1}$ and the flow characteristics were shear thinning behaviour with a yield stress of about 2 Pa, Figure 81 a and b, respectively. This shows that the suspension was slightly flocculated and required some shear stress to improve the degree of dispersion. When the suspension exposed to ultrasound for 1 minute, the viscosity reduced from 23 to 7 mPa s at 100 $s^{-1}$ and the flow characteristics were shear thinning behaviour with zero yield stress. This was because during the concentration process the polymer electrolytes cross-linked at 70°C and became entrapped between the flocs, requiring some external force to break them permanently. Thus, the effect that ultrasound produced was used to break the polymer from the network and disperse the suspension uniformly [232]. Since there was no significant difference in viscosity and flow behaviour after 3 minutes of ultrasound exposure, this level was used for preparation of further YAG suspensions.

### 4.8.2 Effect of Ageing

To determine the ability of the suspension to be stored for long durations, the effect of ageing on the rheology of the suspensions was studied after an interval of two weeks, Figure 82 and Table 18.

Table 18 Summary of rheological behaviour of the YAG suspensions

| Ageing Time | Viscosity / mPa s (at shear rate 100 s-1) | Flow Characteristics |
|---|---|---|
| As prepared | 22 | Shear Thinning |
| After 2 weeks | 44 | Shear Thinning |
| After 2 weeks + 3 min ultrasound | 20 | Shear Thinning |

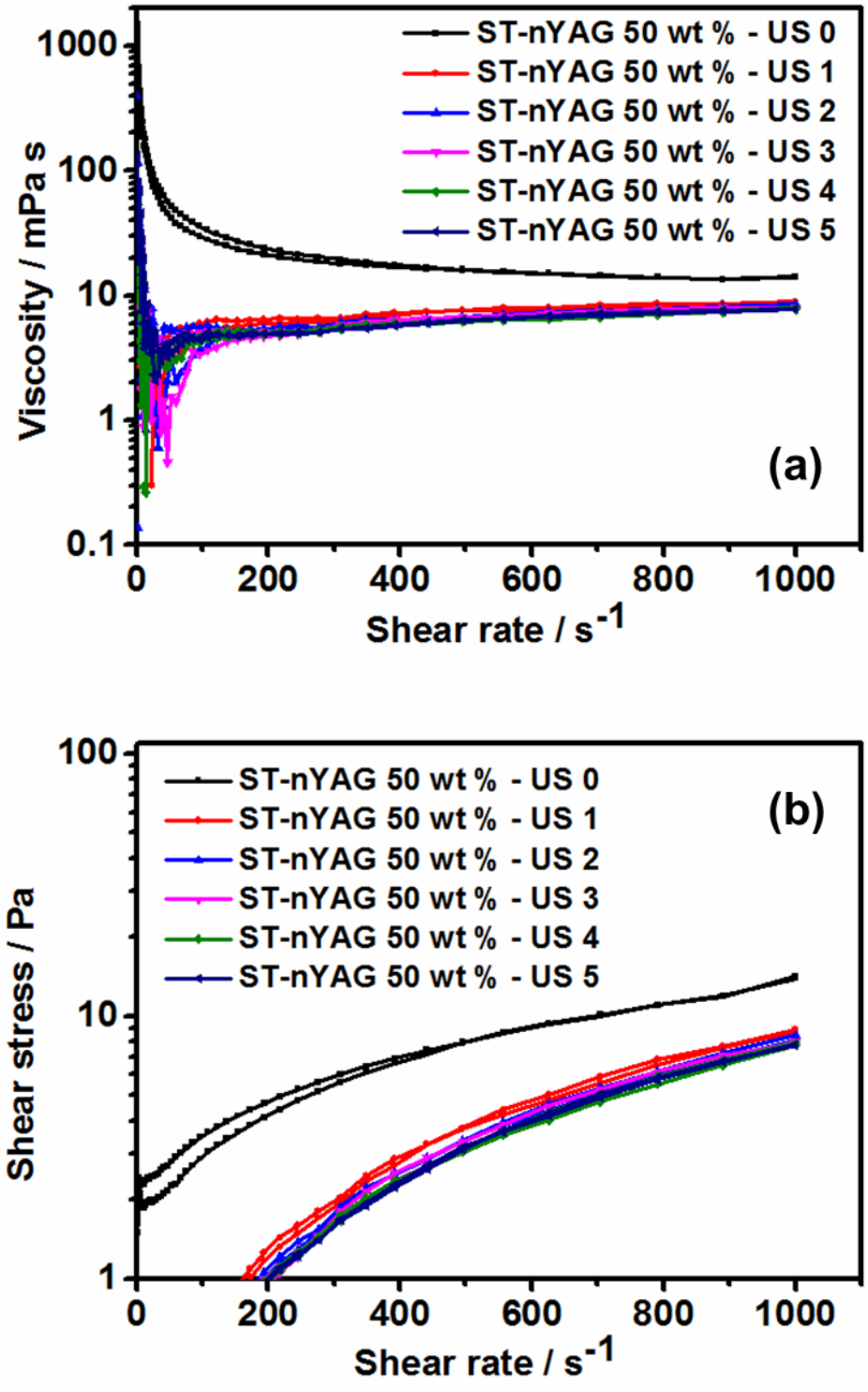


*Figure 81 Effect of ultrasound (US) on (a) viscosity and (b) flow behaviour of ST-nYAG suspensions. (US 0 to 5 mins)*

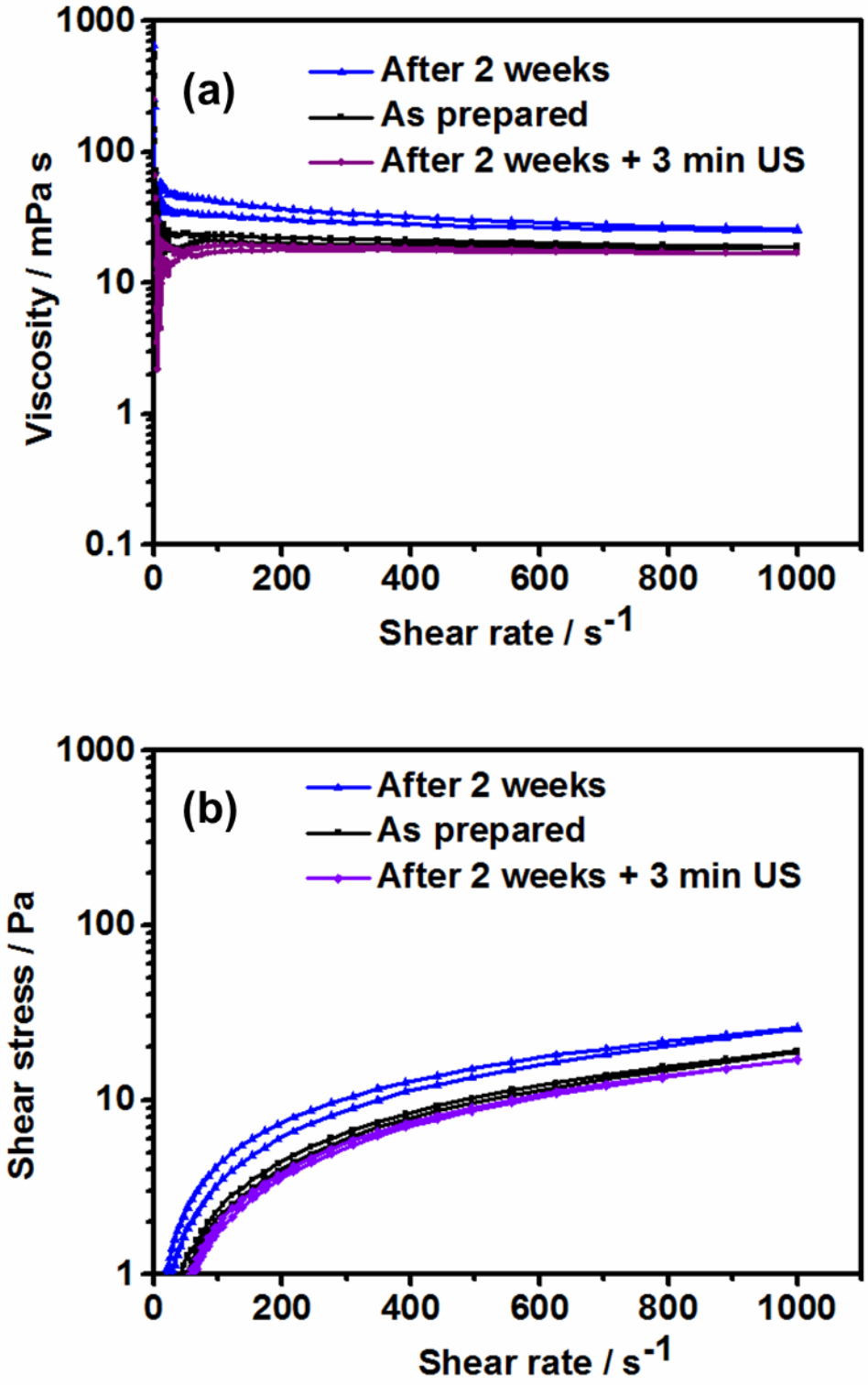


*Figure 82 Effect of ageing on ST-nYAG suspensions, (a) Viscosity and (b) flow behaviour*

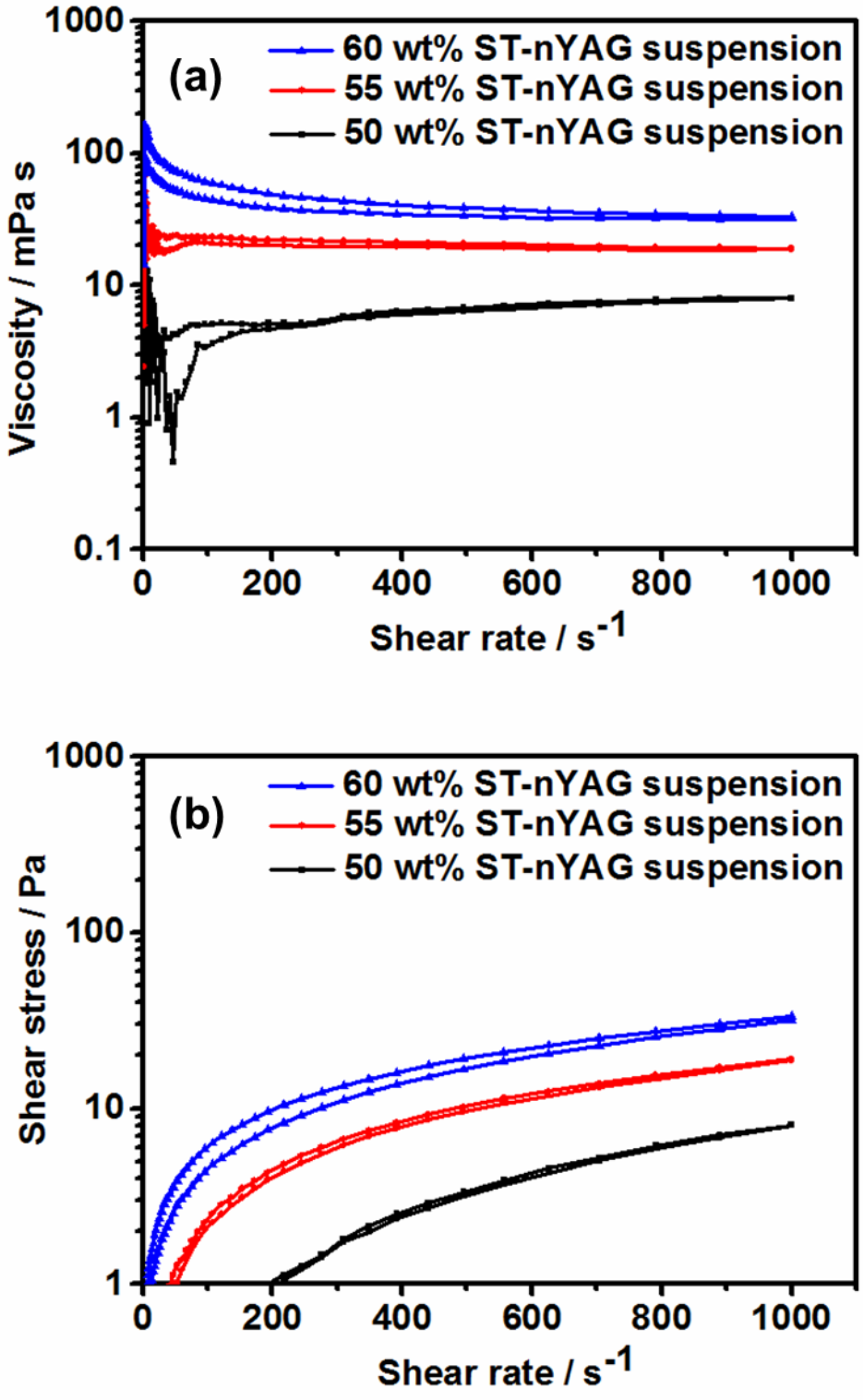


*Figure 83 Effect of solids loading on ST-nYAG suspensions, (a) Viscosity and (b) flow behaviour*

The results show that the suspension increased in viscosity by a factor of two after being aged for two weeks, the flow behaviour was unchanged and there was no settling. The increase in viscosity could be possibly due to the cross linking of the polymer over the period of time [233], forming a network, though since the pH of the suspension was unchanged a strong electro-steric repulsion remained between the particles. The use of 3 minutes of ultrasound on the aged suspensions was sufficient to return them back to their original as-prepared state.

### 4.8.3 Effect of Solids Loading

The effect of solids loading was investigated with three different solid contents of 50, 55 and 60 wt.% ST-nYAG suspensions with dispersant contents of 1.5, 3 and 5 wt.%, Figure 83. Although the 50 wt.% suspension was stable with 1.5 wt.% of dispersant, when the solids content was increased to 55 wt.%, the suspension became highly flocculated making the rheological measurements difficult. Essentially, the particles were so close to each other, the forces of attraction dominated the electro-steric stabilisation. When the dispersant amount was increased to 3 wt.%, the suspension became stable although with a slight increase in viscosity compared to 50 wt.% with 1.5 wt.% dispersant. Increasing the solids content to 60 wt.% again made the rheological measurements difficult; 5 wt.% was required before the rheological characteristics could be measured. Nevertheless, the suspension exhibited a very high viscosity of about 60 mPa s at a shear rate of 100 $s^{-1}$ and shear thinning behaviour with a yield stress of about 2 Pa remained even after 3 min ultrasound. Moreover, after 24 hours of ageing, the suspension displayed gel like behaviour and additional ultrasound was required to re-disperse the suspension.

Both the 50 and 55 wt.% suspensions maintained their stability over time. The most suitable suspension for green forming was found to be the 55 wt.% suspension, due to its higher solids content. The latter plays a vital role in forming spherical granules with porous structure and makes it flowable and crushable during die pressing. Higher solids loading are also preferable to increase the die fill density to minimise the compaction ratio, which reduces the die wall friction volume. The 55 wt.% colloidal ST-nYAG suspension was therefore used to produce granules using the spray freeze drying method for subsequent dry processing.

## 4.9 Spray freeze drying of ST- nYAG granules

In this section, the characteristics of granules obtained from spray freeze drying of ST-nYAG and CP-nYAG suspensions are compared to study the effects they have on the green bodies produced.

### 4.9.1 SFD granule characteristics

The microstructure of the granules obtained from the ST-nYAG and CP-nYAG powder-based suspensions are shown in Figure 84. It can be seen from Figure 84 a and d that a wide range of spherical granule sizes varies from 75 to 250 µm, were produced for both the suspensions. Figure 84 b and e, obtained at a slightly higher magnification, shows the features on the granules. The ST-nYAG granules were soft and porous, whilst the CP-nYAG granules clearly displayed a rough surface with debris of micron level agglomerates present on the surfaces. Figure 84 c and f shows the internal microstructure of the granules at even higher magnification. The ST-YAG granules showed homogenous micron sized pores formed within the granules by the sublimated ice channels; whereas the CP-YAG granules exhibiting a non-homogeneous pore structure due to the fact that the suspension was not stable due to poor dispersion characteristics. Moreover, it is clear from the microstructure that the agglomerated particles also persist inside the CP-YAG granules. The internal porous features formed in the ST-YAG granules was not only influenced by the stability of the colloidal suspension used, but was also attributed to three other factors; the water content, freezing rate and the foaming agent. The water content in the suspension acts as the source for the pore formation; the shape of the pores was determined by the freezing rate of the ice crystals being formed.

As mentioned earlier (see section 2.6.5.1), the rapid freezing of the suspensions resulted in softer granules because of the prevention of the formation of elongated ice crystals [168]. The foaming agent played a vital role in reducing the surface tension of the water by absorbing at the liquid air interface and isolating it into fine droplets, which increased the nucleation density inside the granules. Moreover, the foaming agent acted as defects in the structure, which would have reduced the strength of the granules [164], which makes it to crush during die pressing.

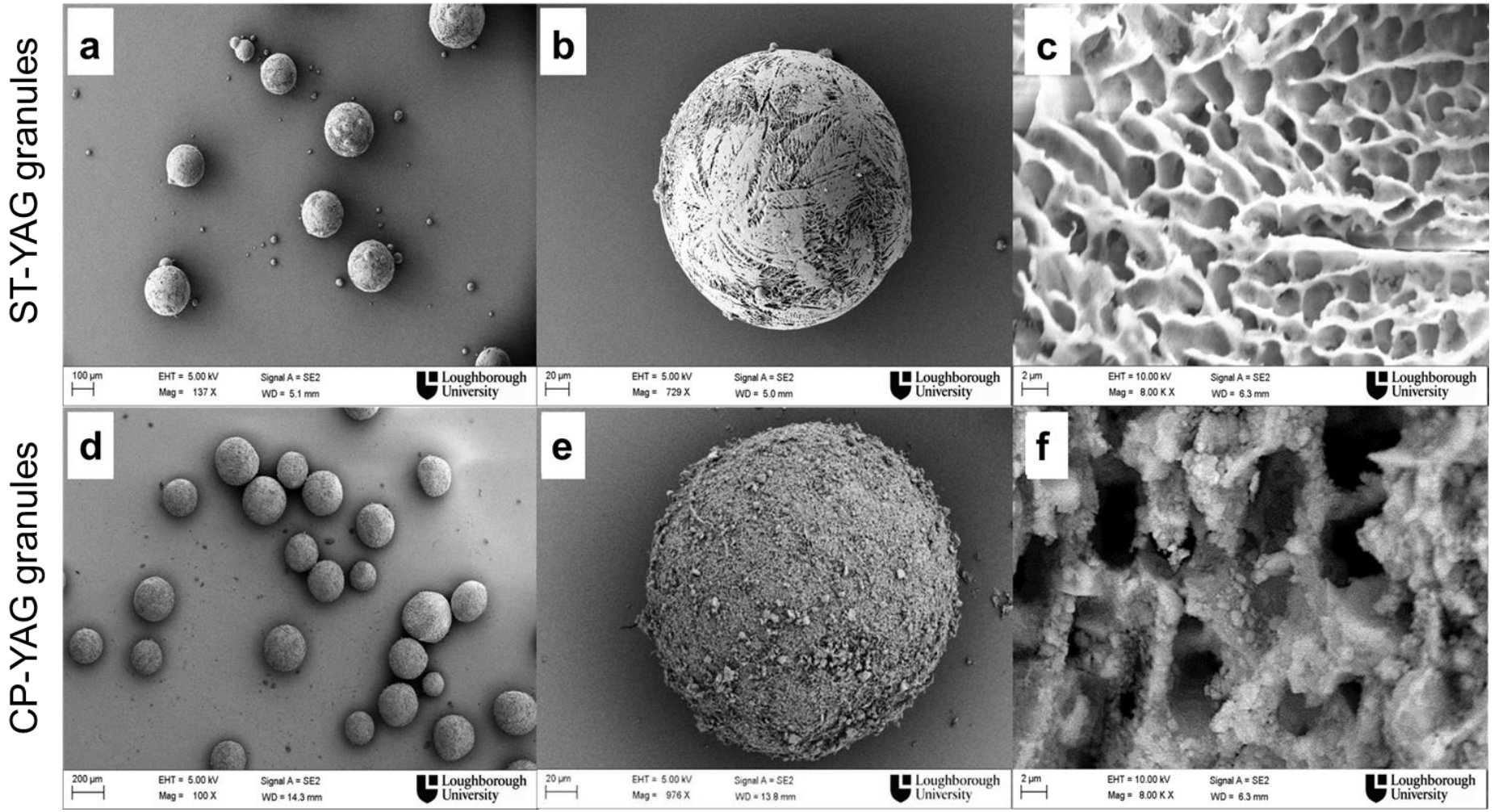


*Figure 84 FEGSEM images; (a,b and c) ST-YAG granules and (d,e and f) CP-YAG granules*

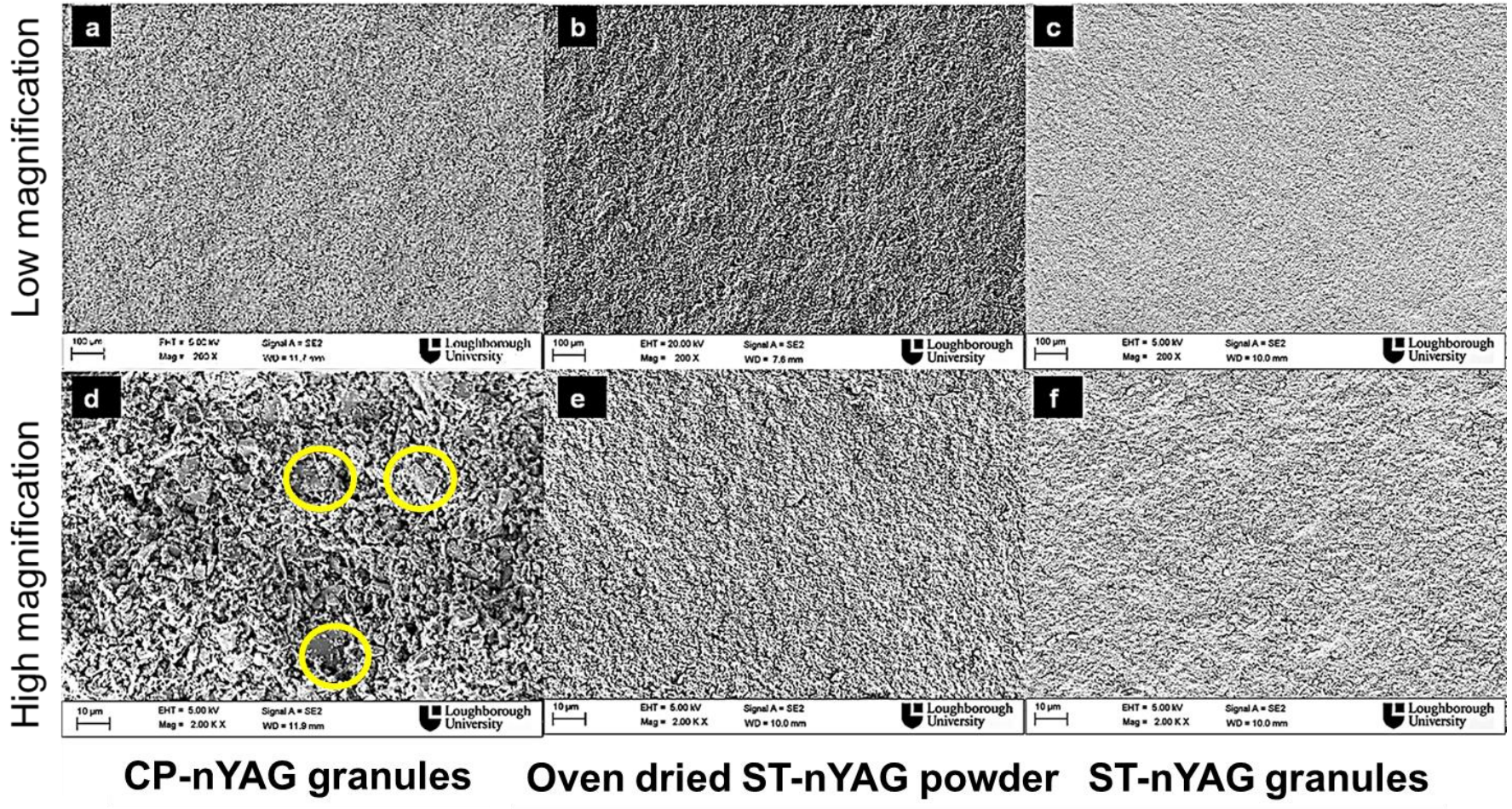


*Figure 85 Fracture surfaces obtained by FEGSEM using, a&d CP-nYAG SFD granules, b&e oven dried ST-nYAG powder and c&f ST-nYAG SFD granules after uniaxial pressing at 70 MPa for 1 min and subsequent isopress at 200 MPa for 2 min.*

### 4.9.2 Fracture surface analysis of YAG green bodies

The consequences of the granule characteristics are very obvious from the comparative microstructures of the fracture surfaces of die pressed green bodies obtained from different SFD YAG granules and the ST-YAG powder oven dried at 80°C, Figure 85. The compacts were produced by uniaxial pressure at 70 MPa for 1 min and subsequent isopress at 200 MPa for 2 min. Figure 85a and d, obtained at different magnifications, show the fracture surfaces of the green samples obtained using CP-YAG granule. The resultant microstructures reveal a rough surface with micron level agglomerates (circled). This reveals that the agglomerated CP-YAG particles cannot be crushed at 200 MPa and requires even higher pressure to crush these hard agglomerates. Although, the resultant green body achieved ~49.9% of theoretical density (TD), the agglomerates would preferentially sinter and have the potential to cause exaggerated grain growth in the YAG ceramics during the final stage of sintering. On the other hand, the dried ST-YAG powder, which had a high surface area of about 46.6 ± 0.9 $m^2g^{-1}$, revealed an homogenous internal morphology though at low magnification the fracture surfaces were slightly rough, see Figure 85. There were no visible uncrushed agglomerates present in the sample, Figure 85 b and e. This could to be attributed to the powder with lesser agglomeration being produced and the resultant green body exhibited ~53.0% of TD. When SFD ST-YAG granules were produced,

Figure 85 c and f, the resultant fracture surfaces yielded a much smoother, homogenous surface with no noticeable agglomerates. The better flowability of the SFD granules allowed efficient die filling whilst the low strength of the granules allowed them to crush back down to their initial powder particle size. Both of these factors allowed the green density to reach ~53.5% of TD and the lack of residual uncrushed granules in the microstructure, meant that a pressure of about 200 MPa was sufficient to produce homogenous green bodies. This pressure range also sits nicely with the current industrial practice.

In summary, for the colloidal processing of YAG, the centrifuged YAG suspension dispersed with $NH_4$PAA formed a stable, aqueous colloidal suspension with a narrow particle size distribution. The electro-kinetics of the $NH_4$PAA was effective and yielded a maximum zeta potential of -72.8 mV at pH 10. The rheology of the

suspension was improved by 3 minutes of ultrasonication yielding a low viscosity. It was also found that 3 wt.% $NH_4$PAA allowed the solids content to be increased to 55 wt.%, which was more suitable for spray freeze drying when ST-YAG powder was used, the resultant green body showed a dense green body without any microstructural defects such as agglomerates, cracks and voids compared with the other processes.

## 4.10 Sintering of YAG ceramics

In this section, the effect of sintering kinetics on YAG powders and granules using three different sintering techniques is discussed. For comparison, CP-nYAG powders and granules are discussed together with their sintered microstructures and their optical properties.

### 4.10.1 Hot presssing of YAG ceramics

Initial sintering trials were performed using loose CP-nYAG powder ball milled for 48 hours and the fracture surfaces of the hot pressed samples obtained using FEGSEM at different magnifications are shown in Figure 86. When the loose YAG powder was hot pressed at 1650°C and 50 MPa for 3 h, resultant sample was resulted in 97.4% of theoretical density (TD). The fracture surfaces of the respective sample, Figure 86 a and b, displayed a coarse microstructure with ~10 µm grain size. The micrograph obtained at relatively higher magnification, Figure 86 b, shows abnormal grain growth with intra-granular pores trapped inside the grains (circled). This is the consequence of agglomerated CP-nYAG powder being used. These agglomerated particles preferentially sintered and caused significant grain growth during the final stage of sintering since agglomerate is already ahead on the sintering curve compared to an individual particle.

When the same loose YAG powder was hot pressed at 1700°C for 3 h and 50 MPa, the sample attained 99.0% of theoretical density (TD). The fracture surfaces of the YAG ceramics, however, show severe grain growth and the grains are very large and non-uniform.

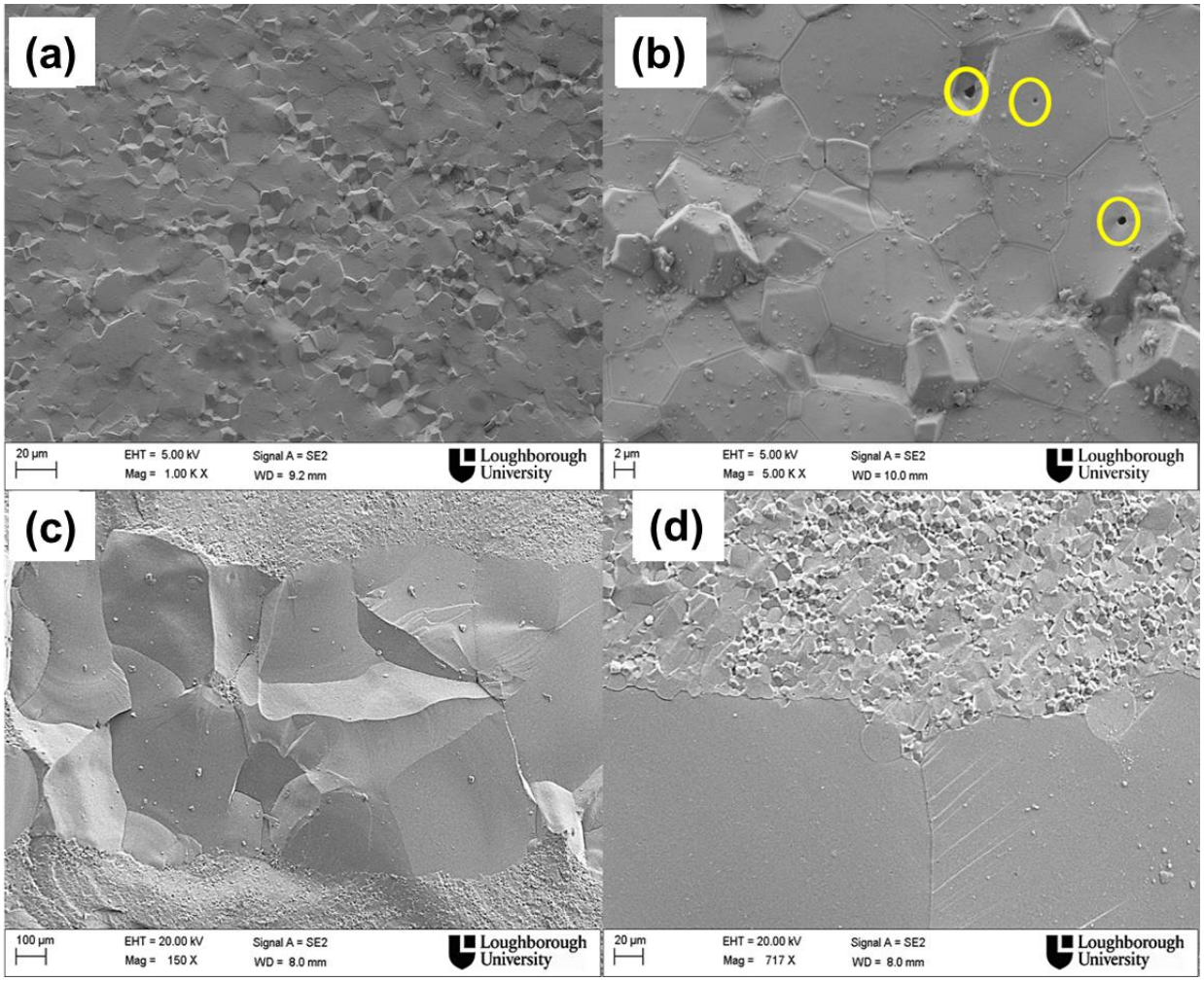


*Figure 86 FEGSEM images of the fracture surfaces of CP-YAG powder sintered using hot pressing, a and b 1650°C and 50 MPa for 3 h and (c and d)1700°C nd 50 MPa for 3 h*

Moreover, Figure 86 c and d show multimodal grain morphology, the top and the bottom layers showed a grain size with ~10 µm, similar to the sample sintered at 1650°C, whilst the middle layer contained ~500 µm grains. This is a clear evidence of enhanced diffusion amongst the particles due to over sintering and plastic flow [234].

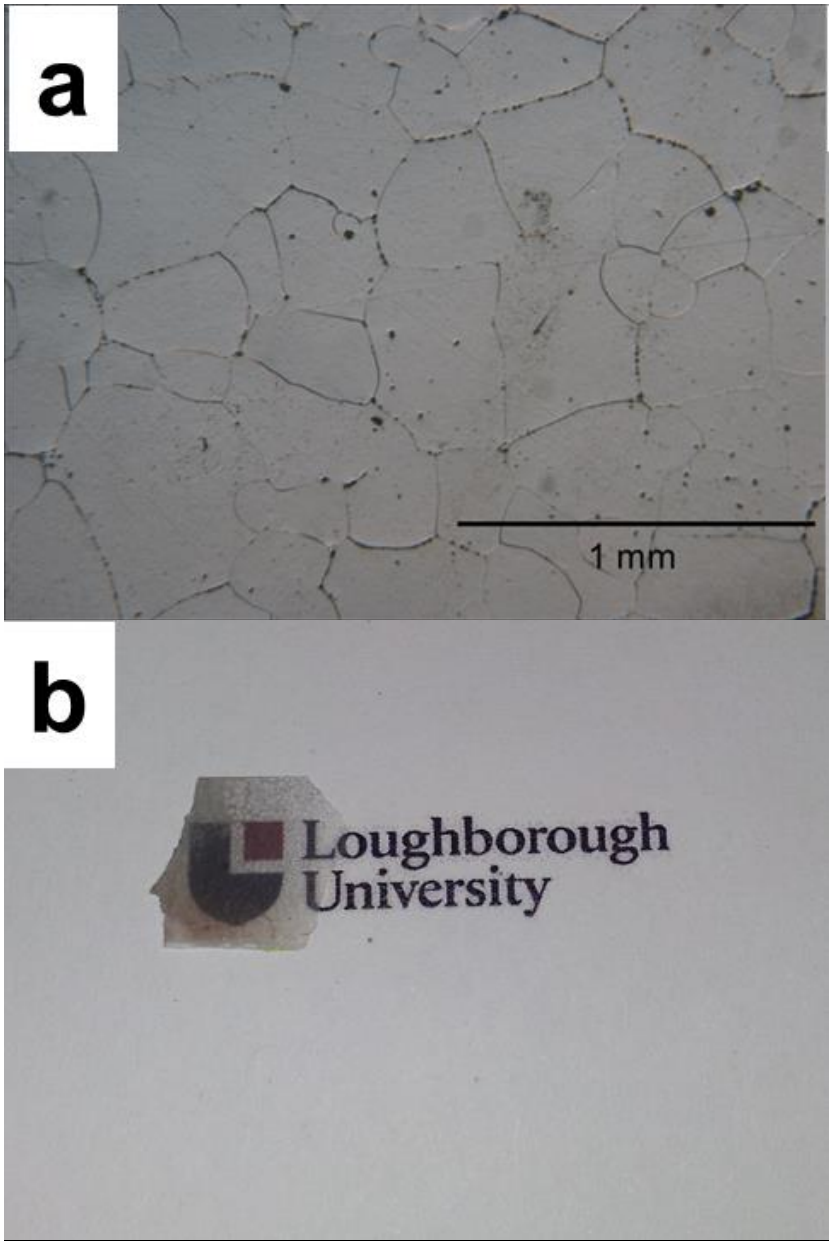


*Figure 87 (a) Microstructure of a polished sample (1700°C and 50 MPa for 3 h) obtained using optical microscopy (b) illustration of transparency of the sample*

The microstructure of a polished sample obtained using optical microscopy, Figure 87a, confirmed that the grains had a 0.5 mm mean grain size. This sample exhibited

some transparency after being polished on both sides, Figure 87b, since there was no grain boundary scattering of the incident light. The slight dark nature on the sample surface is due to the carbon contamination from the graphite die used in the hot press. The transmittance of the sample is shown in Figure 88 a and b. The spectrum obtained from a UV-Visible spectrophotometer showed 80% transmittance from 350 to 800 nm for the sintered sample, which is equivalent to the theoretical transmission of the single crystal Nd:YAG [235]. The FT-IR spectrum shows the transmittance of the sample extended to 6 µm with 60% transmittance. This effect could be attributed to the large grains of the sample with minimal grain boundary scattering.

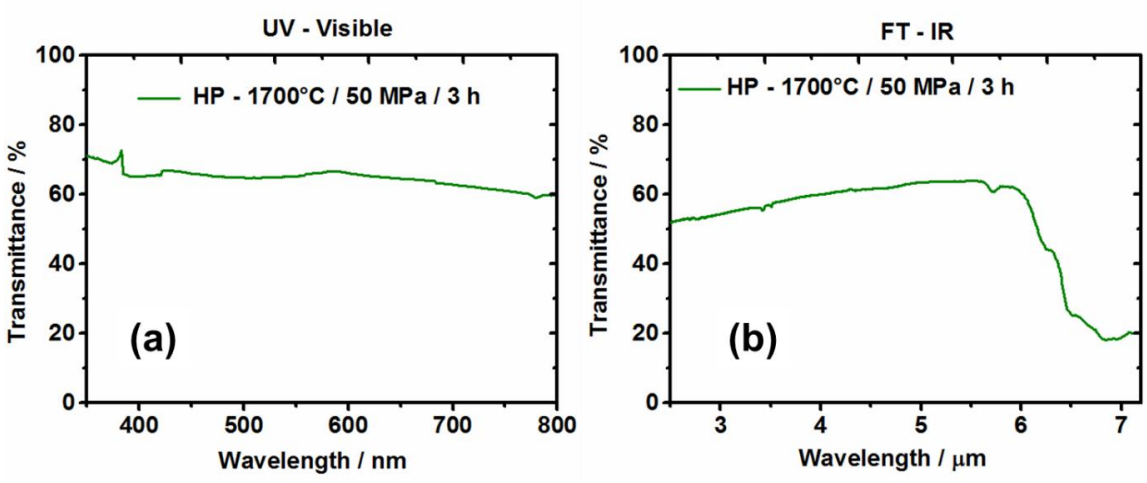


*Figure 88 Optical properties of CP-YAG sintered at 1700°C and 50 MPa for 3 h (a) UV- visible spectrum (b) FT-IR spectrum*

These results led to the conclusion that the sample resulted in large grains due to the excessive grain growth of the agglomerated YAG powder and the low uniaxial pressure being used. In order to decrease the grain size two important changes are required.

First, highly reactive powders without agglomeration were required to avoid preferential sintering of the nanoparticles; note that the powder synthesised using co-precipitation method was not reactive and hence not suitable to achieve a fine grain size. Secondly, much higher pressure was required to reduce the sintering temperature and hence the final grain size.

### 4.10.2 Spark plasma sintering of YAG ceramics

SPS and HIP are alternative methods to densify ceramics at high temperatures and pressures and hence these two were investigated.

Table 19 shows the density and mean grain size of the samples sintered using SPS. Due to restrictions with the equipment, all organics in the granules were removed at 700°C prior to SPS. It is very clear from the table that the densities obtained using the calcined YAG granules were lower compared to the ST-nYAG samples, suggesting that calcination at 700°C was not helpful.

*Table 19 SPS conditions and the density results*

| **Temperature profile** | **CP-nYAG calcined (700°C) granules** | | **ST-nYAG calcined (700°C) granules** | | **ST-nYAG powder oven dried (70°C)** | |
|---|---|---|---|---|---|---|
| | **% of TD** | **Mean grain size** | **% of TD** | **Mean grain size** | **% of TD** | **Mean grain size** |
| 1400°C for 15 min at 70 MPa | 94.8 | ~2 µm | 91.0 | ~400 nm | 99.4 | ~215 nm |
| 1300°C for 15 min at 300 MPa | - | | - | | 99.7 | ~190 nm |

Figure 89 displays the microstructures of the sintered samples. The samples sintered using CP-nYAG granules resulted in larger grain size, ~ 2 µm with intra agglomerated pores (arrowed), as expected, Figure 89a. This is due to the fact that

the as-synthesised CP-nYAG particles were heavily agglomerated, which sintered into large grains with entrapped pores during grain growth. These granules would require higher temperature and pressure to sinter to full density and could lead to a similar result that of the hot pressing results with large grains.

The SPS samples produced using calcined ST-YAG granules resulted in very low density with a mean grain size of about 400 nm, Figure 89b. Since the granules were calcined at 700°C made the particles in the granules agglomerated and the agglomerates wouldn't have crushed during SPS, which resulted in low density. It can also been seen that the pores are at the grain boundaries (hollow circles) and would possibly require much higher temperature or pressure for the complete mass transport to occur at the expense of large grains.

When the non-calcined ST-nYAG powder was used, the SPS process resulted in higher density, 99.4%, and finer microstructure, Figure 89c. when the temperature was dropped to 1300°C but the pressure increased to 300 MPa, again for 15 min, the sample attained 99.7% of TD and the mean grains size was slightly lowered to ~190 nm, Figure 89d. These results support data in the literature (section 2.7), where it is concluded that ceramic powders with high surface area offer high surface energy ($\gamma_{sv}$) and the additional applied pressure ($P_{app}$) enhances the driving force for the closure of the pores during the final stage of sintering.

The SPS technique, however, had an adverse effect on the highly reactive nanopowders through severe carbon contamination of the sintered ST-nYAG samples. Whereas the CP-YAG powder with less surface area turns to clear white after annealing and proves that the ST-nYAG are highly reactive. The use of graphite sheets used to avoid damaging of the graphite die significantly reacted with the sample during sintering and reduced the oxygen in the YAG composition to $Y_3Al_5O_{12-x}$, where x is the carbon that has been replaced [195]. Due to the fact that the SPS generated a reducing atmosphere under huge current, the active species, carbon from the graphite sheet and oxygen from YAG sample, resulted in a carbothermal reduction reaction and the carbon atom easily replaced the oxygen vacancies created under reducing atmosphere.

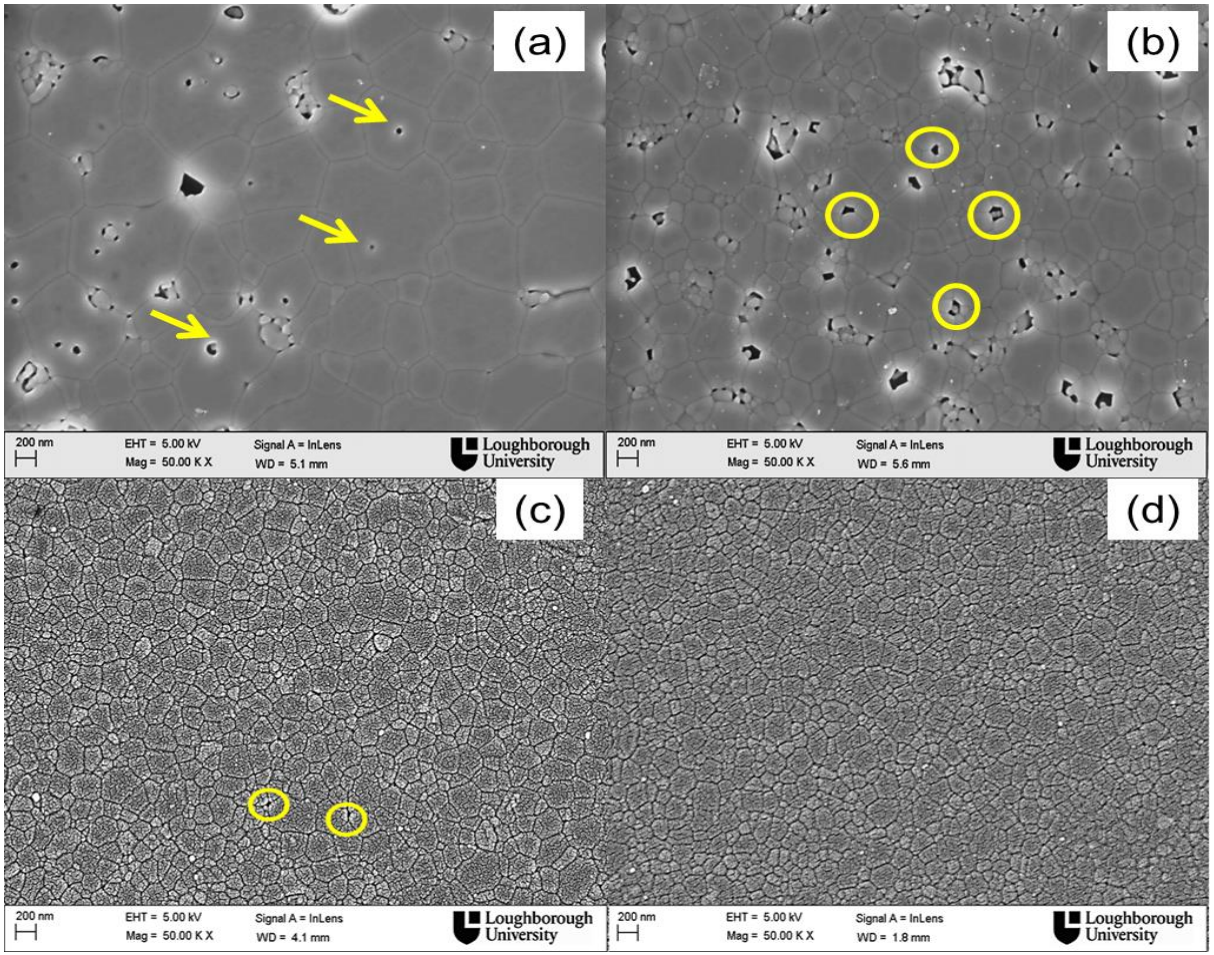


*Figure 89 Microstructure of the SPS samples; a) calcined CP-YAG granules, b) calcined ST-nYAG granules and c&d non-calcined ST-nYAG powders (arrows pointing intra-agglomerated pores and circles showing pores at the grain boundaries)*

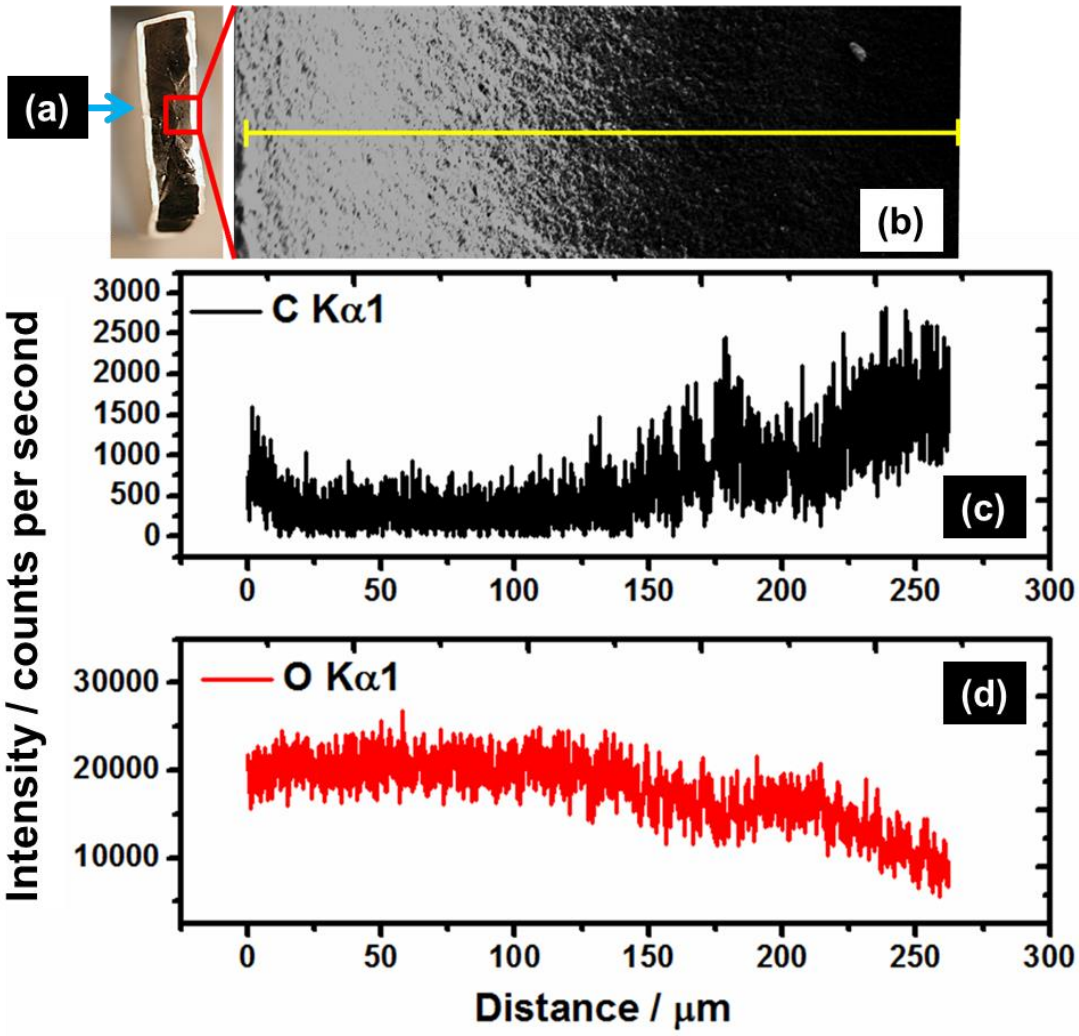


*Figure 90 (a) Fracture surface of YAG ceramics after annealing and FEGSEM image (b) with corresponding EDX line mapping, (c) and (d), across the sample.*

Figure 90a shows the fracture surface of the YAG sample with a contaminated carbon core, which were hardly oxidised even after annealing at 1300°C for 5 hours. Figure 90b shows the FEGSEM image of the fracture surface, the yellow line indicates the length of the EDX line mapping performed for carbon and oxygen Kα1 across the sample. The corresponding maps, Figure 90 c and d, display a clear trend with the C increasing and the O decreasing towards the core.

Due to this carbon contamination, it was concluded that SPS was not suitable for the production of transparent YAG ceramics from highly reactive ST-nYAG powders. HIPing was considered as an alternative sintering approach.

### 4.10.3 Hot isostatic pressing of YAG ceramics

***Pre-sintering of YAG***

Table 20 shows the density of the pre-sintered YAG samples produced using both SFD granules (SFD-YAG) and oven dried powder (OD-YAG) both derived from solvothermal approach. The table clearly shows that the samples attained ~95% of TD at 1350°C for 0 h ($T_1$) and 1100°C for 3 h ($T_2$) using the two step sintering process. Other conditions exhibited higher densities and the focus was to obtain ~95% of TD under the lowest sintering temperature conditions to achieve minimal grain growth.

*Table 20 Pre-sintering results of YAG samples produced using both SFD-YAG granules and oven dried powder (OD-YAG)*

| Temperature profile | SFD-YAG sample | | OD-YAG sample / % of TD | |
|---|---|---|---|---|
| | % of TD | Mean grain size / nm | % of TD | Mean grain size / nm |
| 1350°C for 3 h (single step) | 96.5 | 244 | 97.2 | 248 |
| 1350°C for 0 h (single step) | 93.4 | - | 91.1 | - |
| 1350°C for 0 h (T1) +1200°C for 3 h (T2) | 97.5 | 189 | 98.2 | 227 |
| 1350°C for 0 h (T1) +1150°C for 3 h (T2) | 97.3 | 180 | 97.5 | 214 |
| 1350°C for 0 h (T1) +1100°C for 3 h (T2) | 95.2 (S-1) | 157 | 95.8 (S-2) | 193 |
| 1650°C for 5 h (single step) | 98.1 (S-3) | 464 | 98.7 (S-4) | 470 |

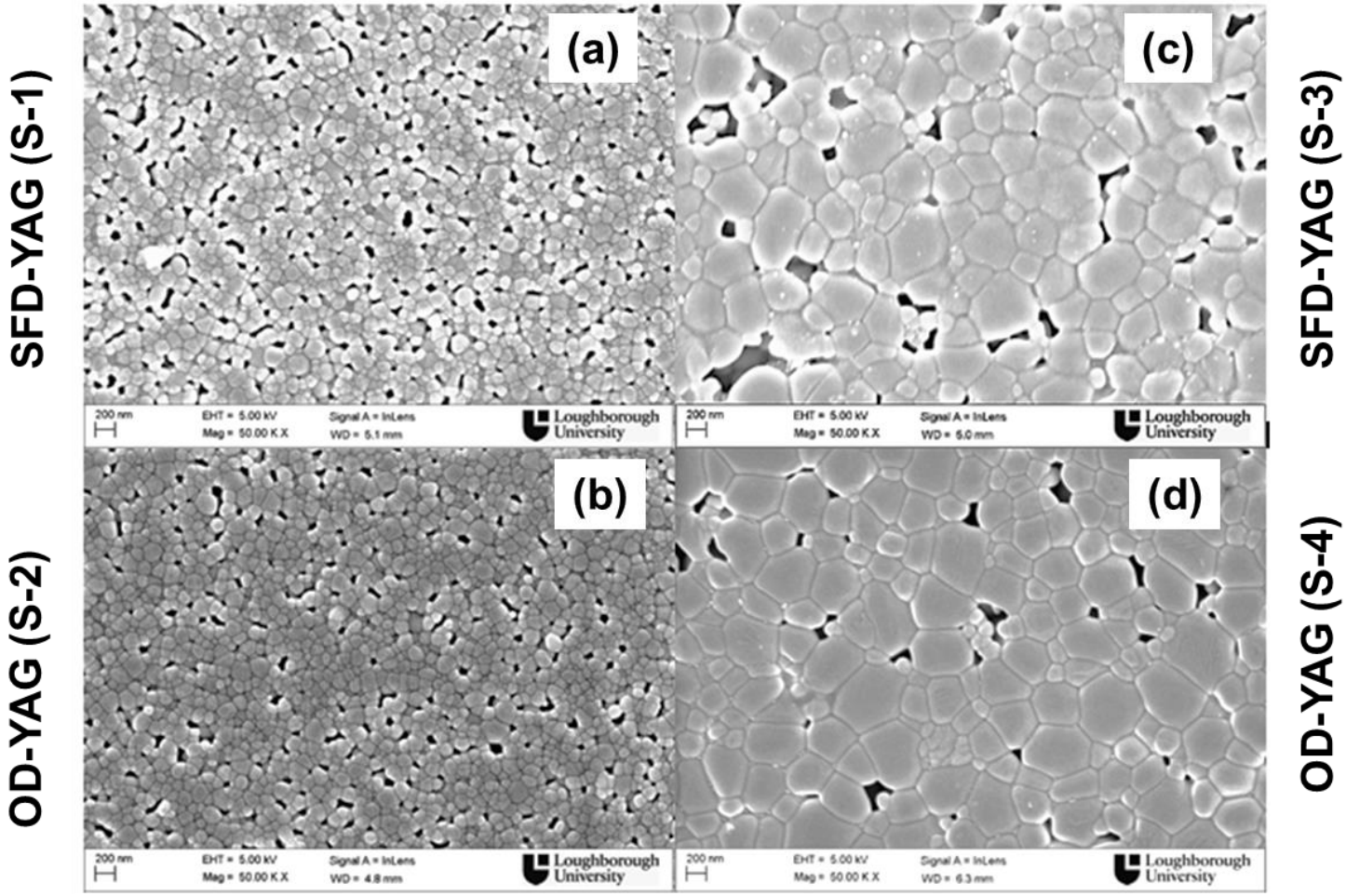


*Figure 91 FEGSEM images of the presintered samples; (a) SFD-YAG and (b) OD-YAG sample obtained at 1350°C for 0 h ($T_1$) and 1100°C for 3 h ($T_2$), (c) SFD-YAG and (d) OD-YAG sample obtained fat 1650°C for 5 h*

Figure 91 a and b show the microstructures of the samples sintered using two step sintering. It is very clear from the microstructures that the pores in the samples were isolated, which is essential for hot isostatic pressing so that an external pressure can be applied to the sample. The sintered samples exhibit grain sizes of about 157 nm and 193 nm from SFD-YAG granules (S-1) and OD-YAG powders (S-2), respectively. The reduction in the grain size at this point of sintering is not only due to the highly reactive powders being used but also due to utilisation of the two step sintering methodology, which supressed the grain growth by pre-coarsening and isolation of the pores in two subsequent steps (see section 2.7.3).

According to Lee et al. [186], ratio of pore diameter to grain diameter plays a vital role during the HIP process. They found that the addition of silica into Nd:YAG ceramic reduced the pore diameter from 1.2 to 0.6 µm, which resulted in the ratio becoming <1 and hence shrunk the pores at dihedral angles of 120° during HIPing. In this work, the average pore diameter was about 118 nm and the pore diameter to grain diameter ratio was ~0.61. This will have reduced the sintering conditions required for the final stage of the densification process, where the final stage sintering depends on the interfacial energy, radius of curvatures of the pores and the applied force, as detailed in section 2.7. On the other hand, single step pre-sintering at 1650°C for 5 h was performed to match with the work done by Lee and Mah [24, 58]. They obtained transparent YAG using HIP at 1550°C and 200 MPa pressure with 0.2 wt % of silica as a sintering aid. The same conditions are examined here for pure YAG and the pre-sintered samples attained ~98% of TD with grain size of about 464 nm and 470 nm for SFD granules (S-3) and OD-YAG powders (S-4), Figure 91c and d, respectively.

### 4.10.4 Microstuctural features of HIPed YAG ceramics

As mentioned earlier, for transparent ceramics the density of the samples should be equivalent to its theoretical values and the mean grain size less than the wavelength of visible light (300 – 700 nm) is desired. Table 21 shows the post HIPing results of the YAG ceramics obtained under different conditions, T-1 to T-6, using both SFD-YAG granules and OD-YAG powders from two different pre-sintering conditions. Micrographs of the samples are shown in Figure 92 to Figure 97.

*Table 21 HIP results of the YAG ceramics obtained under different conditions using both SFD-YAG granules and OD-YAG powders and pre-sintered using both single stage and two stage sintering*

| Sample no. | Pre-sintering conditions | 1350°C for 0 h ($T_1$) +1150°C for 3 h ($T_2$) | | | | 1600°C for 5 h | | | |
|---|---|---|---|---|---|---|---|---|---|
| | HIP conditions | SFD-YAG (S-1) | | OD-YAG (S-2) | | SFD-YAG (S-3) | | OD-YAG (S-4) | |
| | | Density / g $cc^{-1}$ | Mean grain size / nm | Density / g $cc^{-1}$ | Mean grain size / nm | Density / g $cc^{-1}$ | Mean grain size / nm | Density / g $cc^{-1}$ | Mean grain size / nm |
| T-1 | 1500°C and 200 MPa for 3 h | 98.9 | 360 | 99.2 | 383 | 99.9 | 656 | 99.9 | 820 |
| T-2 | 1550°C and 200 MPa for 3 h | 99.7 | 439 | 99.8 | 473 | 99.9 | 813 | 99.9 | 837 |
| T-3 | 1550°C and 200 MPa for 5 h | 99.9 | 1369 | 99.9 | 1954 | 99.9 | 2309 | 99.9 | 2789 |
| T-4 | 1550°C and 300 MPa for 5 h | 98.9 | 2252 | 98.4 | 2334 | 99.1 | 2785 | 98.8 | 3143 |
| T-5 | 1650°C and 300 MPa for 5 h | 97.6 | 2667 | 98.1 | 3881 | 94.3 | 3633 | 94.7 | 3975 |
| T-6 | 1700°C and 300 MPa for 5 h | 97.0 | 3355 | 97.6 | 4422 | 94.1 | 3926 | 94.0 | 4527 |

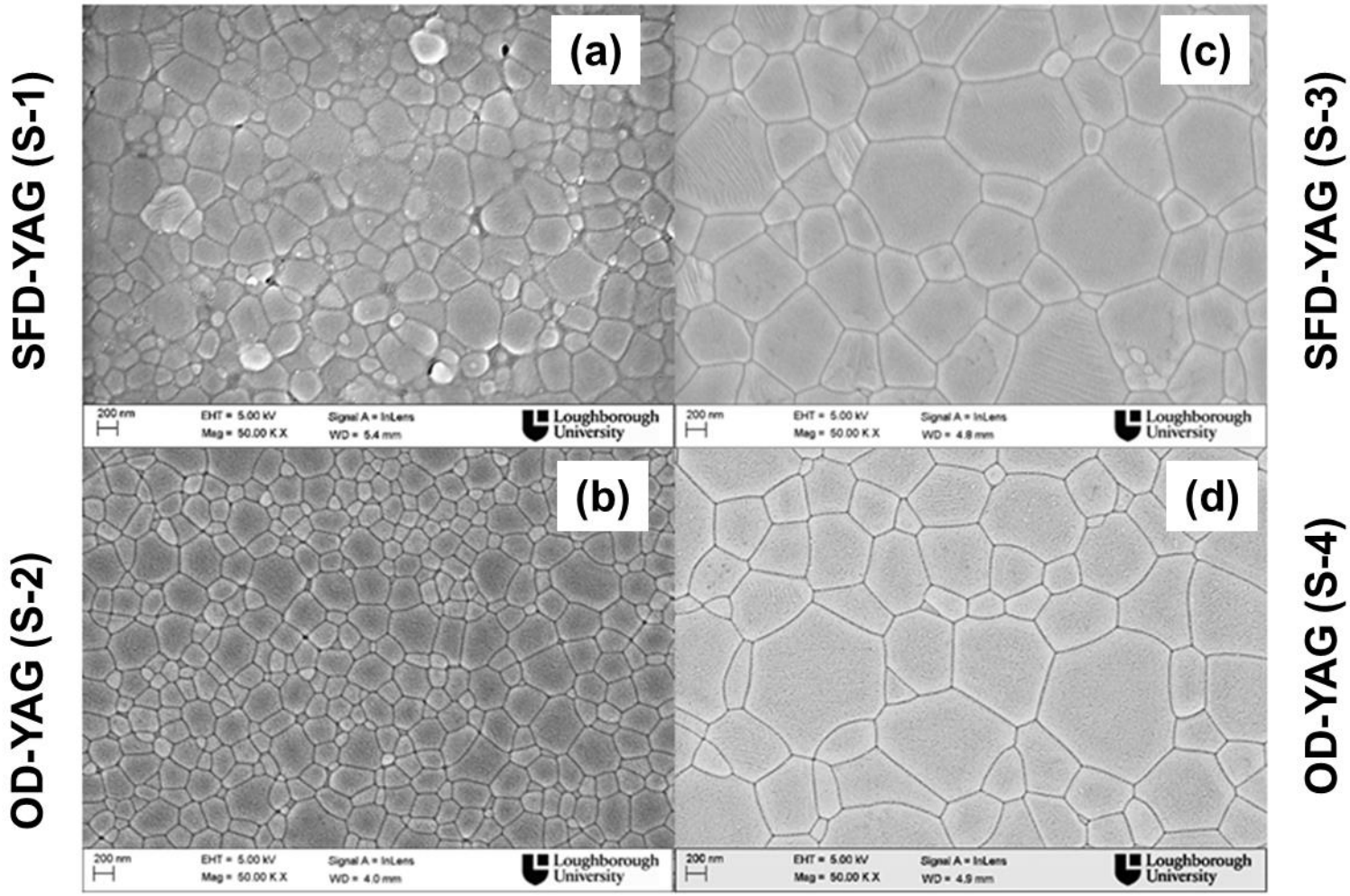


*Figure 92 Microstructure of YAG ceramics after HIPing at 1500°C for 3 h and 200 MPa;(a and b) samples pre-sintered at 1350°C for 0 h ($T_1$) and 1100°C for 3 h ($T_2$) and (c and d), samples pre-sintered at 1600°C for 5 h*

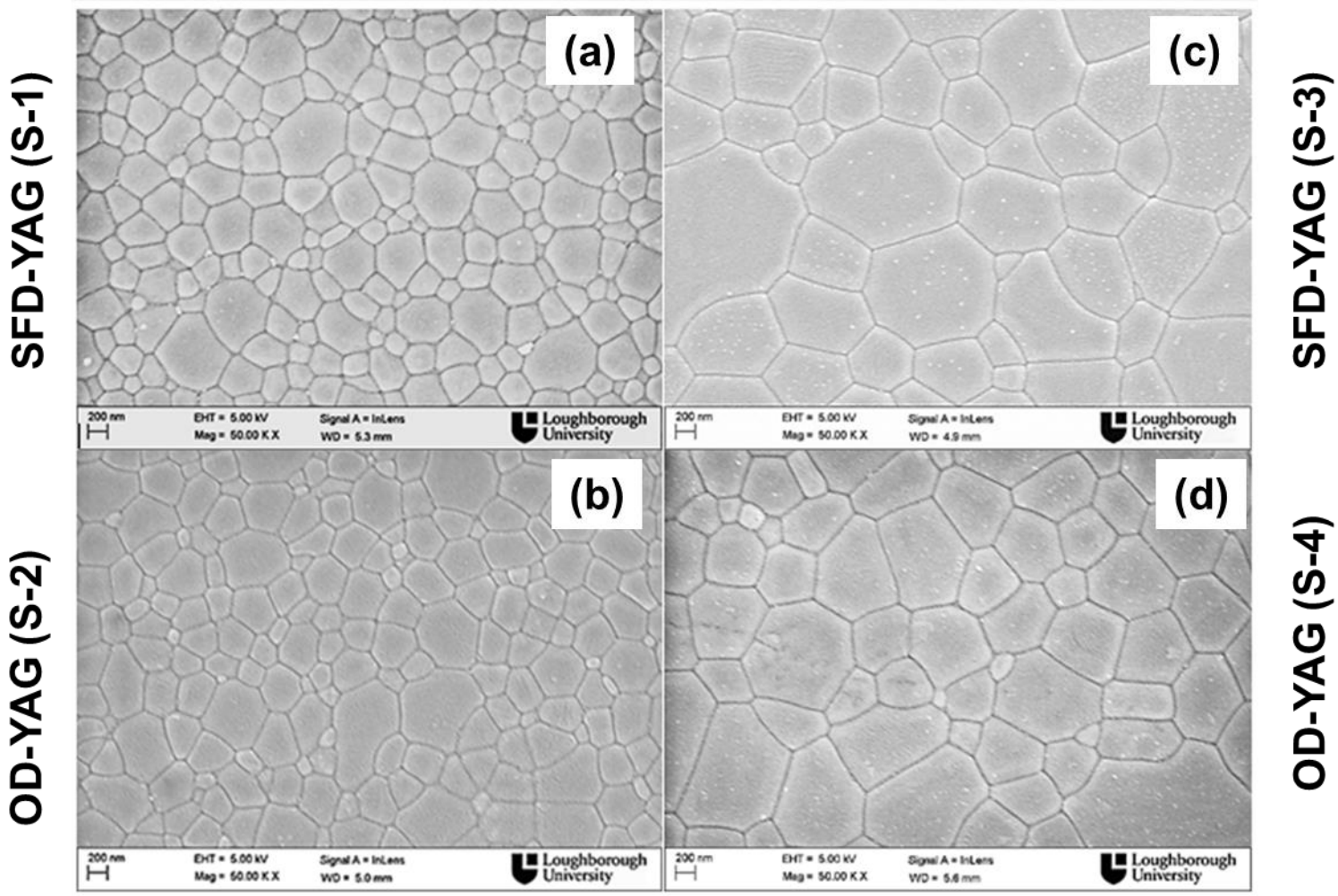


*Figure 93 Microstructure of YAG ceramics after HIPing at 1550°C for 3 h and 200 MPa;(a and b) samples pre-sintered at 1350°C for 0 h ($T_1$) and 1100°C for 3 h ($T_2$) and (c and d), samples pre-sintered at 1600°C for 5 h*

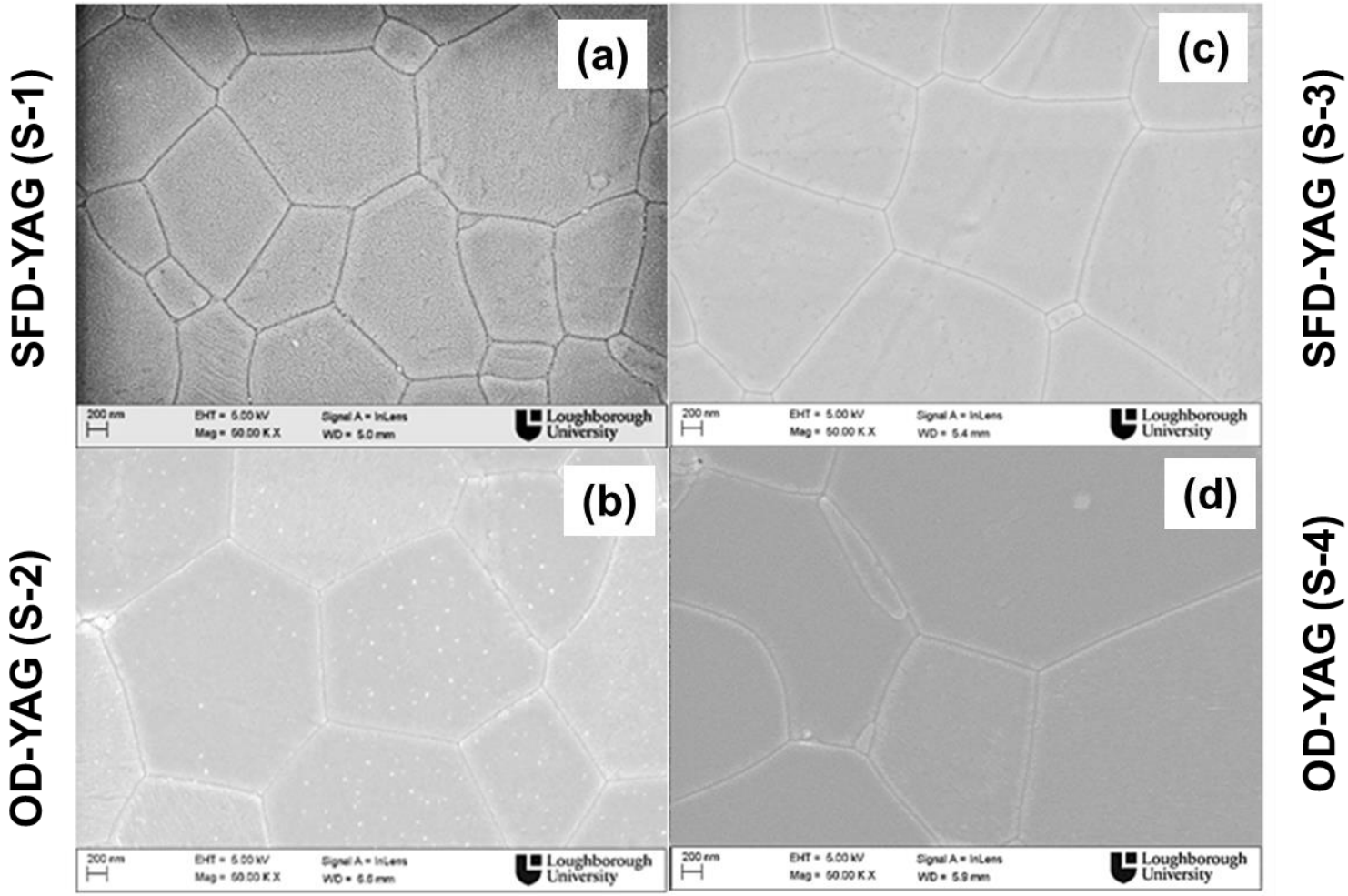


*Figure 94 Microstructure of YAG ceramics after HIPing at 1550°C for 5 h and 200 MPa;(a and b) samples pre-sintered at 1350°C for 0 h ($T_1$) and 1100°C for 3 h ($T_2$) and (c and d), samples pre-sintered at 1600°C for 5 h*

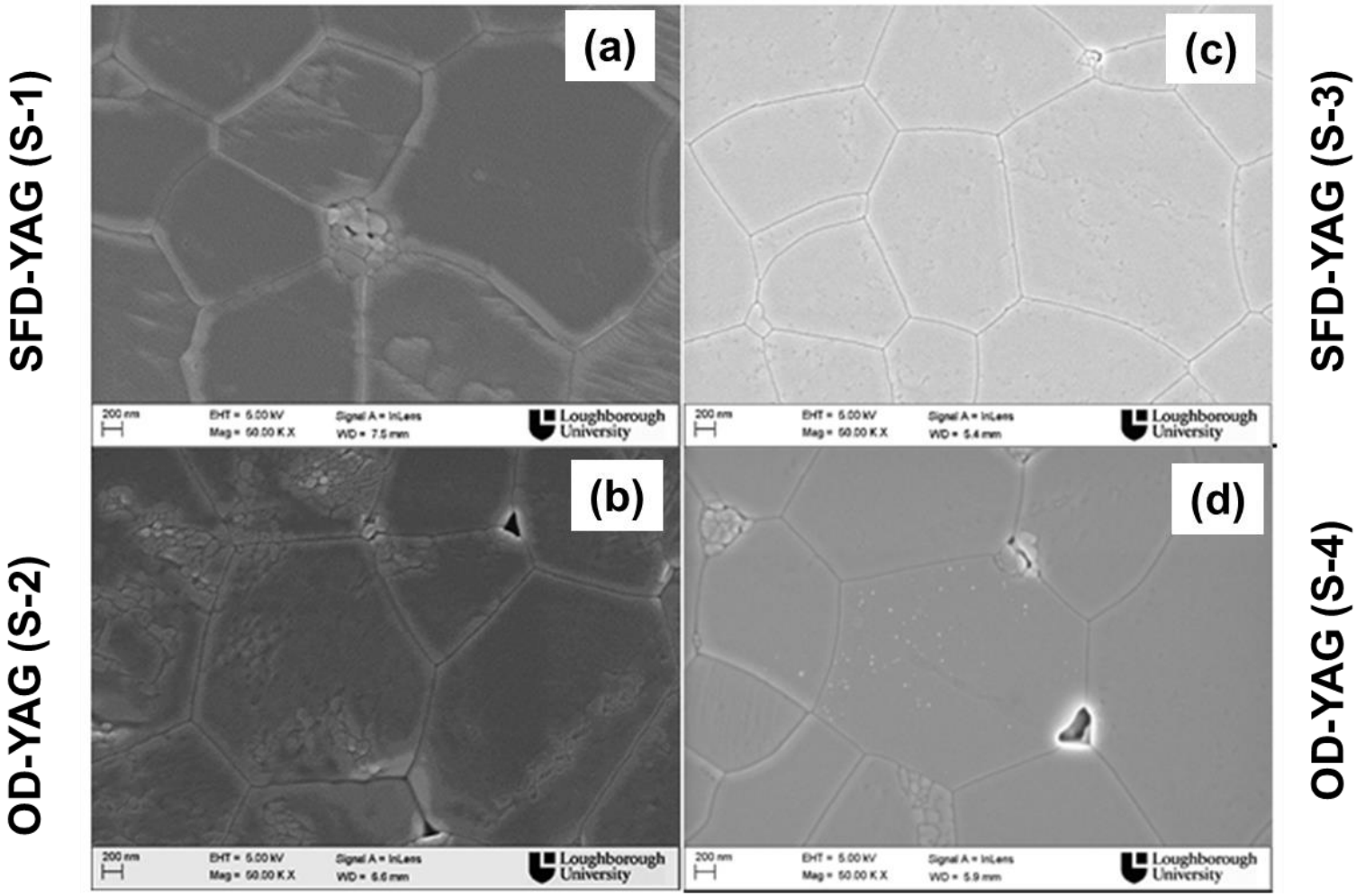


*Figure 95 Microstructure of YAG ceramics after HIPing at 1550°C for 5 h and 300 MPa;(a and b) samples pre-sintered at 1350°C for 0 h ($T_1$) and 1100°C for 3 h ($T_2$) and (c and d), samples pre-sintered at 1600°C for 5 h*

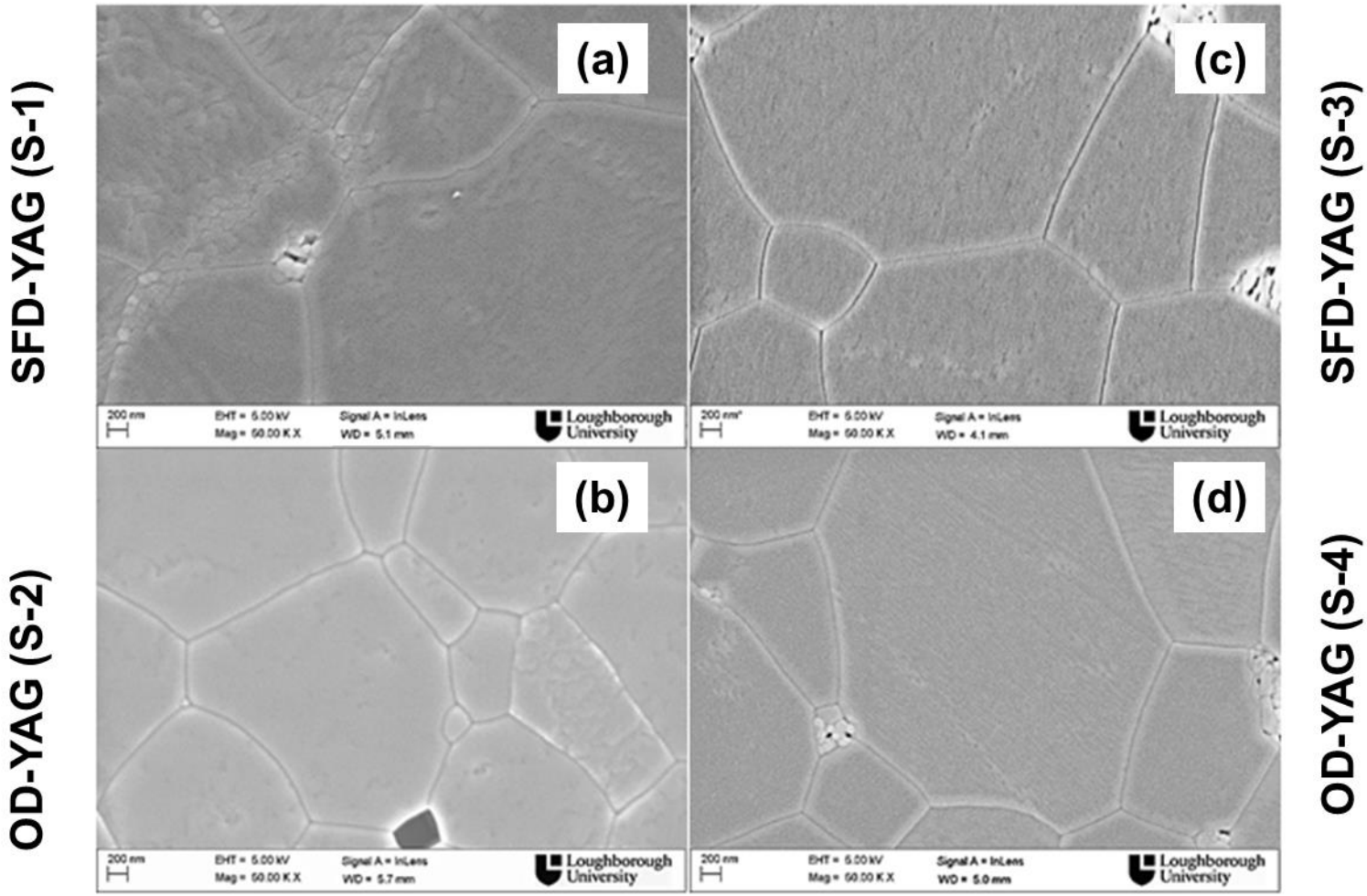


*Figure 96 Microstructure of YAG ceramics after HIPing at 1650°C for 5 h and 300 MPa;(a and b) samples pre-sintered at 1350°C for 0 h ($T_1$) and 1100°C for 3 h ($T_2$) and (c and d), samples pre-sintered at 1600°C for 5 h*

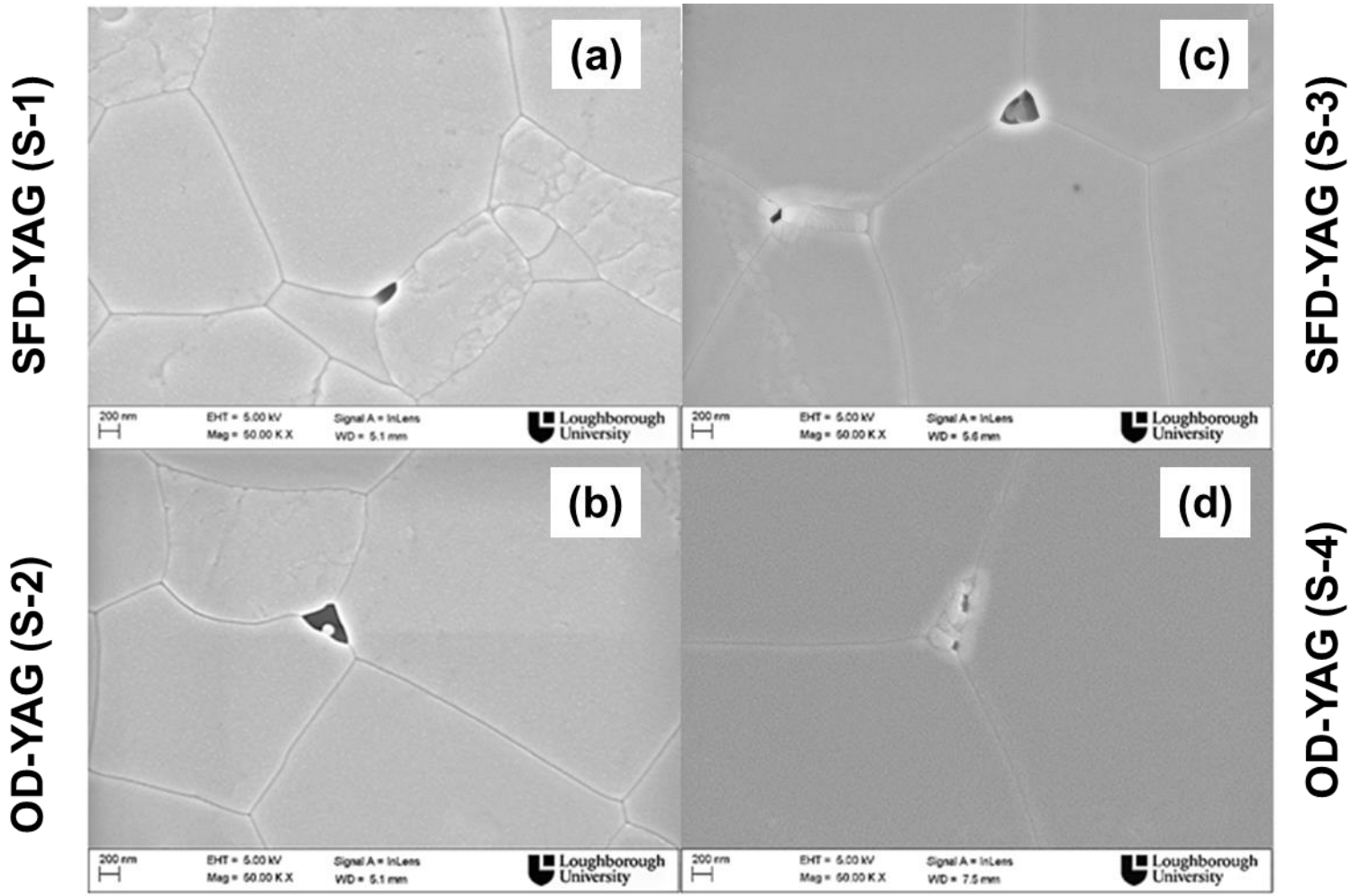


*Figure 97 Microstructure of YAG ceramics after HIPing at 1700°C for 5 h and 300 MPa; (a and b) samples pre-sintered at 1350°C for 0 h ($T_1$) and 1100°C for 3 h ($T_2$) and (c and d), samples pre-sintered at 1600°C for 5 h*

After HIPing at 1500°C and 200 MPa for 3 h, the pre-sintered samples using two step sintering (TSS) approach attained densities about 98.9 and 99.2% with mean grain size about 360 nm and 383 nm for S-1 and S-2, respectively, see Figure 92. Whilst, the samples pre-sintered using single step sintering (SSS) approach resulted in 99.9% density with an increase in grain size of about 656 nm for s-3 and 820 nm for s-4. These results suggest that there was no significant grain growth observed in the TSS samples, but lack of density at 1500°C. When higher temperature, 1550°C, was employed, the sample densities increased to ~99.8% with a mean grain size within the wavelength of light, 439 nm for S-1 and 473 nm for S-2. No significant difference was observed for the samples from the SSS approach.

It is worth noting that the grains are homogenous and no excess grain growth was observed regardless of the samples; see Figure 93, which attributes to the homogeneity of the powders synthesised using solvothermal method.

Regardless of the pre-sintering conditions, all the samples attained 99.9% of TD with micron sized grains when the holding time was increased to 5 hours at 1550°C. When comparing the current samples with Mah and Lee [24, 58], similar conditions were used, the microstructures were similar but the samples were not fully transparent, see Figure 94. This could be due to the absence of rare earth dopant and silica additive, which has improved the transparency of YAG at several instances [157, 186, 235, 236].

It has been clear from the microstructures, Figure 95 to Figure 97, that the increase in temperature above 1550°C and the pressures higher than 200 MPa favoured significant grain growth and causing de-sintering or bloating effects of the YAG ceramics sintered using solvothermal powders. This has been a serious issue whilst sintering fine nanopowders and also been reported by the other researchers [237, 238]. It is very obvious that the samples sintered at conditions T-3 reached a saturation limit regardless of the pre-sintering conditions. As the grains grew above the saturation limit, it forms voids at the triple junction and hence trapping the gas bubbles into the grains during HIPing.

From the HIPing trials, it is very clear that the powders and the granules from the solvothermal method sinter at lower temperatures (200°C lower) when compared to reports in the literature and yield fine microstructures. The study also shows that the

condition, 1550°C and 200 MPa for 3 h, favours finer sub-micron grains with 99.8% of TD being achieved when the two step sintering technique was used for pre-sintering.

### 4.10.5 Optical properties of YAG ceramics

Figure 98 shows the optical transmittance spectra of the samples HIPed at 1550°C and 200 MPa for 3 h, i.e. samples obtained from T-2. The spectra obtained from UV visible spectrophotometry showed transmittance of about 10 – 20% from 350 – 800 nm and a similar range of transmission was extended up to 6 µm from the FT-IR spectra, which is the beginning of mid infrared spectrum.

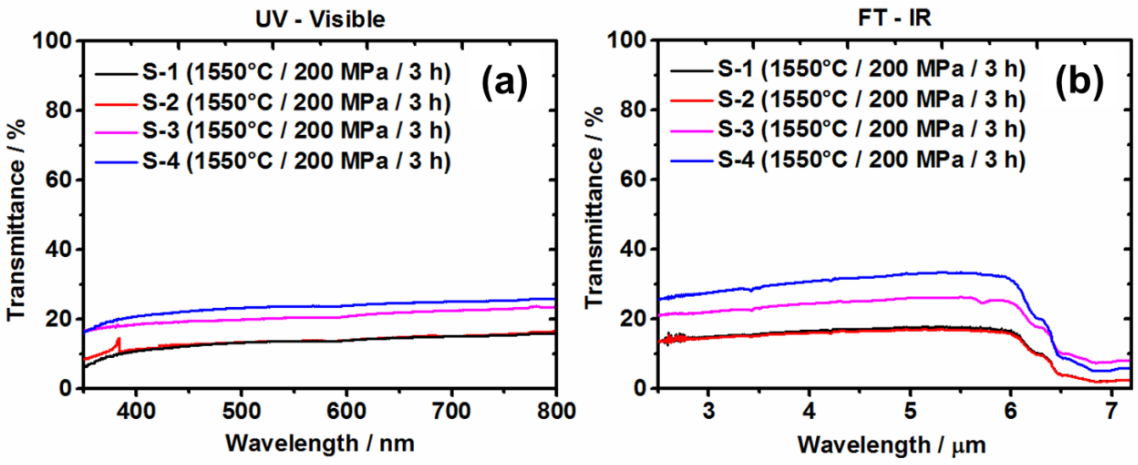


*Figure 98 Optical properties of ST-YAG after HIPing at 1500°C for 3 h / 200 MPa (a) UV- visible spectrum (b) FT-IR spectrum*

The transmittance spectra show that the samples with finer grains (S-1 and S-2) exhibited transmittance that was only about 10 % and which was around half that of the samples with coarse grains (S-3 and S-4). The difference between them could be attributed to the difference in densities and grain sizes of the samples, see Table 21, where the fine pores and the grain boundaries act as primary scattering centres to reduce the in-line transmittance of the polycrystalline ceramics. When comparing the data with the hot pressed CP-YAG ceramics, the fine microstructured samples exhibited transmittance of up to ~60% between 350 – 800 nm, albeit, the density of the CP-YAG was only 99.0% of theoretical density, see Figure 88. This shows that the scattering of the incident light at grain boundaries is predominant in ST-YAG ceramics due to the large surface area of the grain boundaries. Hence in

nanomaterials additive that reduce grain boundary scattering would be hugely beneficial for improving transparency.

Investigation by Sekita et al. [48] revealed that the addition of rare-earth dopant and silica reduced the adsorption co-efficient of pure YAG from 1.7 to 0.25 $cm^{-1}$, which is equivalent to the adsorption co-efficient of the single crystal Nd:YAG, 0.022 $cm^{-1}$. Likewise, Messing et al. [186] and Mah et al. [58] have also reported that the transparency of the Nd:YAG ceramics improved when silica was used as an additive and the latter also influenced both densification and grain growth during HIPing. This literature suggests that the transparency of the pure YAG ceramics can be improved by doping with rare earth elements and using silica as a sintering aid.

This research clearly reveals that the colloidal processing of YAG ceramics certainly decreased the sintering conditions and resulted in fine microstructures, however, the transparency of the samples need to be improved. The lack of transparency in the samples could be due several factors as indicated; lack of dopants, sintering additives, small amount of porosity left and lack of annealing treatments. A detailed future plans to improve transparency are further discussed in section 6.

# 5 Conclusions

The main objectives of the work was to synthesis nanocrystalline YAG particles with minimal agglomeration and investigate the colloidal processing for the production of spray freeze dried granules to facilitate green processing and subsequent sintering of nanostructured YAG ceramics. The following conclusions were drawn from the research work.

**SYNTHESIS**

Initially, chemical synthesis routes such as sol-gel, co-precipitation and solvothermal methods were examined for the synthesis of nanocrystalline YAG with a lower degree of agglomeration than previously achieved. Single phase YAG was obtained using both inorganic (nitrate and metal) precursors and organic (alkoxides) precursors.

It has been reported for the first time that it is possible to use Al metal precursor used as a source to synthesis YAG using the sol-gel method and the conversion yield was increased by a factor of two when compared to the nitrate precursor route. Unfortunately, the 100% metal precursor route lead to coarse YAG particles, 90-150 nm, whilst the nitrate precursor method resulted in fine nanoparticles, 10-25 nm, but with severe agglomeration, as revealed by the BET analysis.

Co-precipitation synthesis involved challenging experimental procedures and the proposed mechanism suggested that an extremely narrow pH range, 8.2 $\pm$ 0.05, and a processing temperature window, 13 ± 3°C, appears to be required for the formation of core/shell precipitates of $Y^{3+}$ and $Al^{3+}$ ions. Whilst the TEM images showed the particle size to range between 25‑30 nm, the BET data suggested that the extent of agglomeration was reduced when compared to the sol-gel route, but was still not good enough to produce fine microstructured YAG ceramics.

Solvothermal route was found to be the most successful for the synthesis of nano YAG particles with minimal agglomeration. Experimental results suggested that ethanol and 2-propanol were not suitable for complete crystallisation of nitrate precursors into single phase YAG within the pressure limit, 8.5 MPa, of the autoclave. Whilst the BET results showed that the particles obtained using 2-propanol exhibited high surface area, the XRD data indicated poor crystallinity. 1, 4

butanediol, a low vapour pressure solvent, however was able to yield nanocrystalline YAG from nitrate and organic precursors below 8.5 MPa pressure. When the nitrate precursor was used, whilst the XRD pattern revealed single phase YAG and BET data resulted in high surface area, 22.0 $m^2g^{-1}$, the TEM images displayed heterogeneous particle morphology and the powders were found chemically inhomogeneous using EDX. When the organic precursors were used, the best conditions resulted in single phase YAG with spherical particle size of about 25 nm with homogenous particle morphology. In addition, the BET data resulted in a very high surface area, 46.6 ± 0.9 $m^2g^{-1}$ and the calculated particle size matching with the TEM morphologies, meaning that the particles are not necking between the adjacent and exhibiting little agglomeration.

This concludes that not only the synthesis methods, but also the solvents and precursors used have a significant influence on the particle morphology, extent of agglomeration and the degree of crystallisation of the YAG powders.

## COLLOIDAL PROCESSING OF YAG

The as-synthesised, non-aqueous YAG suspension was successfully converted into an aqueous suspension without the intermediate drying of the particles. The electro-kinetics of $NH_4$PAA was found to be effective and a zeta potential of about -72.8 mV was achieved at a pH 10. The as-prepared aqueous YAG suspension exhibited a narrow particle size distribution and the suspension was stable for 90 days without any settling behaviour. The rheology of the suspension with 3 wt.% $NH_4$PAA and 55 wt.% solids content was found more suitable for spray freeze drying of YAG granules. The comparative microstructures revealed that the colloidal processing of YAG resulted in dense green bodies without any microstructural defects such as visible cracks and uncrushed agglomerates.

## SINTERING OF YAG CERAMICS

Hot pressing results suggested that the agglomerates in the CP-YAG powders were preferentially sintered and resulted in significant grain growth during the final stage of sintering. These powders required high temperatures and pressures to achieve 99.0% density and the resultant microstructure displayed mean grain sizes of about 0.5 mm. Each grain acted as a small single crystal and so the samples exhibited optical transmittance of about 80% from 350 to 800 nm, which is equivalent to the

theoretical transmission of the single crystal Nd:YAG [235]. This suggests that the light scattering at the pores and along the grain boundaries was minimal when the grain size was large.

SPS technique was found to be successful in terms of producing fine microstructured ceramics, when ST-nYAG powder was used. The sample was sintered to 99.7% of theoretical density and a mean grain size of about ~190 nm was achieved. However, graphite sheet used to avoid damaging the graphite die reacted with the ST-nYAG powder during SPS and the carbon atoms therefore diffused into the YAG ceramics. The latter were hardly oxidised even after annealing. These results suggest that the ST-nYAG powders were not suitable for the processing of transparent ceramics using SPS, unless an alternative to the graphite sheets were used.

The hot isostatic pressing results revealed that the samples pre-sintered using a two stage sintering approach resulted in fine grained ceramics, ~450 nm, and 99.8% of theoretical density. The single step pre-sintering approach resulted in a coarser HIPed microstructure, ~860 nm, and 99.9% theoretical density after sintering at 1550°C and 200 MPa for 3 h. This method avoided the contamination issues associated with the SPS technique and the colloidal processing of YAG resulted in a fine and homogenous microstructure. However, the transmittance of the resultant samples was very low, 10 - 20%, which is probably due to the scattering of light at the grain boundaries. Further increase in the HIPing conditions resulted in de-sintering of the ceramics, which is a major issue during sintering of fine nanoparticles.

# 6 Future work

The current work was focused on the synthesis and processing of pure YAG ceramics, similarly a detailed investigation is now required on the processing of co-doped YAG ceramics in order to improve the transmittance.

To improve the transmittance of the YAG ceramics with fine microstructures, the YAG powders need to be co-doped with rare earth elements and silica additives. For example, it has been shown that 0.28 wt.% $SiO_2$ addition forms a complete solid solution with Nd:YAG and results in high transmittance of the ceramics after HIPing above 80% [236]. Thus co-doped YAG particles with silica need to be synthesised with different concentrations to allow optimisation of the composition. Moreover, addition of rare earth elements such as Pr, Nd, Er and Eu into the YAG system was reported to improve the transmittance of YAG [48]. Amongst the rare earths, Nd and Eu have been widely used to produce colourless YAG ceramics, whereas the other elements undergo selective absorption of the incident light in the visible region causing coloration of the samples. It has been reported that Nd dopant concentrations up to 4 atomic % were found to improve the transmittance of YAG [57]. Therefore, co-doped Nd:YAG particles need to be synthesised using the solvothermal method and a thorough characterisation of the particle morphology, extent of agglomeration and degree of crystallinity will be required.

Although the colloidal processing was successful in producing spray freeze dried granules for pure YAG system, the electro kinetics of the co-doped YAG suspensions could be slightly different. Once the co-doped YAG suspensions were produced, suitable rheology for the SFD process needs to be investigated.

Two step sintering approach followed by HIPing can be used to produce fully dense YAG samples with suitable dopants. Other sintering methodologies such as flash sintering and microwave sintering can also be examined to produce pre-sintered YAG ceramics with even smaller grain size than the TSS approach to achieve fine microstructured samples after HIPing. It is also expected that the sintering conditions will be lowered with the addition of silica in the YAG system. Moreover, to improve the transparency of the as-sintered YAG ceramics, annealing can be done in partial oxygen atmosphere.

Mechanical properties such as hardness, facture toughness and elastic modulus need to be measured for the best YAG ceramics to assess their suitability for demanding applications.

Thus the overall reported work is mainly on the fabrication of pure nanostructured YAG ceramics. The learnings from all the processing stages from a powder to a product can have a significant impact on the development of doped transparent YAG ceramics for optical and other mechanical properties.

# 7 References

[1] H.E. Meissner, Composite optical and electro-optical devices (1998).

[2] C.T. Warner, T.M. Hartnett, D. Fisher, Characterization of AlON optical ceramic.

[3] F.H. Li, J.B. Li, H. Lin, C.X. Huang, M.Y. Lei, H.B. Du, Development of transparent MgAl2O4 spinel ceramics, Key Eng Mat. High-Performance Ceramics VI (2010) 649-652.

[4] A. Krell, J. Klimke, T. Hutzler, Advanced spinel and sub-μm Al2O3 for transparent armour applications, J European Ceram Society. 29 (2009) 275-281.

[5] M. Grujicic, W. Bell, B. Pandurangan, Design and material selection guidelines and strategies for transparent armor systems, Mater Des. 34 (2012) 808-819.

[6] E. Strassburger, Ballistic testing of transparent armour ceramics, J European Ceram Society. 29 (2009) 267-273.

[7] C.F. Cline, L.R. Pinckney, J.J. Zhang, Transparent glass-ceramic armor (2011).

[8] U. Anselmi-Tamburini, J.N. Woolman, Z.A. Munir, Transparent Nanometric Cubic and Tetragonal Zirconia Obtained by High-Pressure Pulsed Electric Current Sintering, Advanced Functional Materials. 17 (2007) 3267-3273.

[9] http://www.raytheon.com/newsroom/technology_today/2009_i1/eye_on_tech_materials.html.

[10] P. Chantikul, S.J. Bennison, B.R. Lawn, Role of grain size in the strength and r-curve properties of alumina, J Am Ceram Soc. 73 (1990) 2419-2427.

[11] I. Ganesh, A review on magnesium aluminate (MgAl2O4) spinel: synthesis, processing and applications, International Materials Reviews. 58 (2013) 63-112.

[12] L. Yang, T. Lu, H. Xu, W. Zhang, B. Ma, A study on the effect factors of sol-gel synthesis of yttrium aluminum garnet nanopowders, J. Appl. Phys. 107 (2010) 064903.

[13] P. Ramanujam, B. Vaidhyanathan, J. Binner, A. Anshuman, C. Spacie, A comparative study of the synthesis of nanocrystalline Yttrium Aluminium Garnet using sol-gel and co-precipitation methods, Ceram. Int. 40 (2014) 4179-4186.

[14] L. Wang, L. Zhang, Y. Fan, J. Luo, P. Zhang, L. An, Synthesis of Nd/Si Codoped YAG Powders via a Solvothermal Method, J Am Ceram Soc. 89 (2006) 3570-3572.

[15] J. Li, Y. Pan, F. Qiu, Y. Wu, J. Guo, Nanostructured Nd:YAG powders via gel combustion: The influence of citrate-to-nitrate ratio, Ceram. Int. 34 (2008) 141-149.

[16] P.D. Cozzoli, T. Pellegrino, L. Manna, Synthesis, properties and perspectives of hybrid nanocrystal structures, Chem. Soc. Rev. 35 (2006) 1195-1208.

[17] X. Li, B. Zhen, T. Odoom-Wubah, Co-precipitation synthesis and two-step sintering of YAG powders for transparent ceramics, Ceram. Int. (2013).

[18] R. Chaim, M. Kalina, J.Z. Shen, Transparent yttrium aluminum garnet (YAG) ceramics by spark plasma sintering, J European Ceram Society. 27 (2007) 3331-3337.

[19] M. Bocanegra-Bernal, Hot isostatic pressing (HIP) technology and its applications to metals and ceramics, J. Mater. Sci. 39 (2004) 6399-6420.

[20] Z. Liu, B. Mei, J. Song, W. Li, Optical Characterizations of Hot-Pressed Erbium-Doped Calcium Fluoride Transparent Ceramic, J Am Ceram Soc (2014).

[21] P. Sharma, K. Hue, H. El-Shall, K. Powers, B. Moudgil, Nano, bio and mineral technologies—mutual leveraging for product and process innovations. 2 (2011) 1232-1238.

[22] M.A. Meyers, A. Mishra, D.J. Benson, Mechanical properties of nanocrystalline materials, P Mat Sci. 51 (2006) 427-556.

[23] N. Wang, Z. Wang, K. Aust, U. Erb, Effect of grain size on mechanical properties of nanocrystalline materials, Acta Metallurgica et Materialia. 43 (1995) 519-528.

[24] T.-. Mah, T.A. Parthasarathy, H.D. Lee, Polycrystalline YAG; structural or functional?, J Ceramic Processing Res. 5 (2004) 369-379.

[25] G.C. Wei, Transparent ceramics for lighting, J European Ceram Society. 29 (2009) 237-244.

[26] M. Suárez, A. Fernández, R. Torrecillas, J.L. Menéndez, Sintering to Transparency of Polycrystalline Ceramic Materials.

[27] G.C. Wei, Transparent ceramic lamp envelope materials, J. Phys. D. 38 (2005) 3057.

[28] H. Yagi, T. Yanagitani, T. Numazawa, K. Ueda, The physical properties of transparent Y3Al5O12: Elastic modulus at high temperature and thermal conductivity at low temperature, Ceram. Int. 33 (2007) 711-714.

[29] T.A. Parthasarathy, T. Mah, K. Keller, Creep Mechanism of Polycrystalline Yttrium Aluminum Garnet, J Am Ceram Soc. 75 (1992) 1756-1759.

[30] D.W. Richerson, Modern ceramic engineering: properties, processing, and use in design, CRC Taylor & Francis, 2006.

[31] Y. Liang, S.P. Dutta, Application trend in advanced ceramic technologies, Technovation. 21 (2001) 61-65.

[32] http://www.lboro.ac.uk/departments/materials/research/groups-areas/advancedceramics/, .

[33] http://www.cerasystem.de/pipe_elbows_coated_steel_4_42_2_1_.html, .

[34] http://www.photonic.saint-gobain.com/transparent-armor.aspx, .

[35] http://www.autoevolution.com/news-image/brutally-reducing-all-kinetic-energy-the-romantic-high-tech-brake-guide-15189-7.html, .

[36] http://www.zxsq.com.cn/category.asp?classid=2, .

[37] http://www.wldiamondtools.com/products/Index_10.html, .

[38] http://www.plusplasticelectronics.com/energy/new-encapsulant-for-high-volume-flexible-solar-module-production-37173.aspx, .

[39] http://www.stockopedia.co.uk/content/ceramic-fuel-cells-interview-with-andrew-neilson-42093/, .

[40] http://www.coringroup.com/medical_professionals/products/hips/minihip/, .

[41] M.W. Barsoum, Fundamentals of Ceramics, IoP publication Ltd, 2003.

[42] S.K. Gupta, J. Singh, J. Akhtar, Materials and Processing for Gate Dielectrics on Silicon Carbide (SiC) Surface (2013).

[43] D. Lee, W. Kingery, Radiation energy transfer and thermal conductivity of ceramic oxides, J Am Ceram Soc. 43 (1960) 594-607.

[44] R.A. Shelby, D.R. Smith, S. Schultz, Experimental verification of a negative index of refraction, Science. 292 (2001) 77-79.

[45] R. Apetz, M.P.B. van Bruggen, Transparent Alumina: A Light-Scattering Model, J Am Ceram Soc. 86 (2003) 480-486.

[46] A. Krell, J. Klimke, T. Hutzler, Transparent compact ceramics: inherent physical issues, Optical materials. 31 (2009) 1144-1150.

[47] B. Kim, K. Hiraga, K. Morita, H. Yoshida, T. Miyazaki, Y. Kagawa, Microstructure and optical properties of transparent alumina, Acta Materialia. 57 (2009) 1319-1326.

[48] M. Sekita, H. Haneda, S. Shirasaki, T. Yanagitani, Optical spectra of undoped and rare-earth-(= Pr, Nd, Eu, and Er) doped transparent ceramic Y3Al5O12, J. Appl. Phys. 69 (1991) 3709-3718.

[49] M. Pokhrel, G. Kumar, P. Samuel, K. Ueda, T. Yanagitani, H. Yagi, D. Sardar, Infrared and upconversion spectroscopic studies of high Er< sup> 3 content transparent YAG ceramic, Optical Materials Express. 1 (2011) 1272-1285.

[50] I. Santacruz, J. Binner, Rheological characterization and coagulation casting of Al2O3–nano zirconia suspensions, J Am Ceram Soc. 91 (2008) 33-40.

[51] J.R. Groza, Nanosintering, Nanostructured Materials. 12 (1999) 987-992.

[52] A. Krell, J. Klimke, T. Hutzler, Advanced spinel and sub-μm $Al_2O_3$ for transparent armour applications, J European Ceram Society. 29 (2009) 275-281.

[53] F.H. Li, J.B. Li, H. Lin, C.X. Huang, M.Y. Lei, H.B. Du, Development of transparent $MgAl_2O_4$ spinel ceramics, Key Engineering Materials. High-Performance Ceramics VI (2010) 649-652.

[54] J.H. Burnett, S.G. Kaplan, E.L. Shirley, P.J. Tompkins, J.E. Webb, High-index materials for 193 nm immersion lithography (2005) 611-621.

[55] R. López, J. Zárate, E. Aguilar, J. Muñoz-Saldaña, Preparation of neodymium-doped yttrium aluminum garnet powders and fibers, J of rare earths. 26 (2008) 670-673.

[56] Q. Liu, M. Gong, F. Lu, W. Gong, C. Li, 520-W continuous-wave diode corner-pumped composite Yb: YAG slab laser, Opt. Lett. 30 (2005) 726-728.

[57] M. Giorgetti, M. Berrettoni, M. Saladino, E. Caponetti, Evidence for a double doping regime in Nd:YAG nanopowders, J. Mater. Sci. 44 (2009) 1572-1579.

[58] H. Lee, T. Mah, T.A. Parthasarathy, Low-Cost Processing of Fine Grained Transparent Yttrium Aluminum Garnet (2008) 147-152.

[59] https://www.llnl.gov/str/April06/Soules.html, .

[60] http://scienceblogs.com/tetrapodzoology/2008/11/03/why-the-lion-grew-its-mane/, .

[61] http://science.howstuffworks.com/transparent-aluminum-armor4.htm, .

[62] http://www.popularmechanics.com/technology/military/weapons/flying-humvees-and-cluster-bombs-from-the-air-force-expo-2#slide-2, .

[63] P.J. Patel, G.A. Gilde, P.G. Dehmer, J.W. McCauley, Transparent ceramics for armor and EM window applications (2000) 1-14.

[64] J. Rheims, J. Köser, T. Wriedt, Refractive-index measurements in the near-IR using an Abbe refractometer, Measurement Science and Technology. 8 (1997) 601-605.

[65] S. Rubini, B. Bonanni, E. Pelucchi, A. Franciosi, Y. Zhuang, G. Bauer, CdTe epitaxial layers in ZnSe-based heterostructures, J. Cryst. Growth. 201-202 (1999) 465-469.

[66] Y. Furukawa, M. Sato, F. Nitanda, K. Ito, Growth and characterization of MgO-doped LiNbO3 for electro-optic devices, J. Cryst. Growth. 99 (1990) 832-836.

[67] I.H. Malitson, Interspecimen Comparison of the Refractive Index of Fused Silica, J. Opt. Soc. Am. 55 (1965) 1205-1208.

[68] R. Thomas, Z. Ikonic, R.W. Kelsall, Plasmonic enhanced electro-optic stub modulator on a SOI platform, Photonics and Nanostructures - Fundamentals and Applications. 9 (2011) 101-107.

[69] A.B.D. Nandiyanto, F. Iskandar, T. Ogi, K. Okuyama, Nanometer to Submicrometer Magnesium Fluoride Particles with Controllable Morphology, Langmuir. 26 (2010) 12260-12266.

[70] L. Baldassare, A. Cingolani, M. Ferrara, M. Lugarà, Dispersion of the linear electrooptic coefficient in ZnS, Solid State Commun. 34 (1980) 237-239.

[71] G.H. Haertling, PLZT electrooptic materials and applications—a review, Ferroelectrics. 75 (1987) 25-55.

[72] J. Lu, K. Ueda, H. Yagi, T. Yanagitani, Y. Akiyama, A.A. Kaminskii, Neodymium doped yttrium aluminum garnet (Y3Al5O12) nanocrystalline ceramics—a new generation of solid state laser and optical materials, J. Alloys Compounds. 341 (2002) 220-225.

[73] Z. Gao, V. Carabelli, E. Carbone, E. Colombo, F. Demaria, M. Dipalo, S. Gosso, C. Manfredotti, A. Pasquarelli, S. Rossi, Y. Xu, E. Vittone, E. Kohn, Transparent diamond microelectrodes for biochemical application, Diamond and Related Materials. 19 (2010) 1021-1026.

[74] M. Stuer, Z. Zhao, U. Aschauer, P. Bowen, Transparent polycrystalline alumina using spark plasma sintering: Effect of Mg, Y and La doping, J European Ceram Society. 30 (2010) 1335-1343.

[75] J. Wahl, T. Hartnett, L. Goldman, R. Twedt, C. Warner, Recent advances in ALON optical ceramic, Proc. SPIE. 5786 (2005) 71.

[76] H. Eilers, Fabrication, optical transmittance, and hardness of IR-transparent ceramics made from nanophase yttria, J European Ceram Society. 27 (2007) 4711-4717.

[77] X. Nie, J.C. Wright, W.W. Chen, L. Fehrenbacher, I. Vesnovsky, Rate effects on the mechanical response of magnesium aluminate spinel, Materials Science and Engineering: A. 528 (2011) 5088-5095.

[78] http://www.crystran.co.uk/optical-materials/diamond-cubic-carbon-c, .

[79] F. Wakai, S. Sakaguchi, Y. Matsuno, Superplasticity of yttria-stabilized tetragonal ZrO 2 polycrystals, Advanced Ceramic Materials. 1 (1986) 259-263.

[80] F. Wakai, Y. Kodama, S. Sakaguchi, N. Murayama, K. Izaki, K. Niihara, A superplastic covalent crystal composite, Nature. 344 (1990) 421-423.

[81] F. Flory, L. Escoubas, G. Berginc, Optical properties of nanostructured materials: a review, J of Nanophotonics. 5 (2011) 052502-052502-20.

[82] A.S. Aricò, P. Bruce, B. Scrosati, J. Tarascon, W. Van Schalkwijk, Nanostructured materials for advanced energy conversion and storage devices, Nature materials. 4 (2005) 366-377.

[83] A.A. Balandin, Thermal properties of graphene and nanostructured carbon materials, Nature materials. 10 (2011) 569-581.

[84] D.L. Leslie-Pelecky, R.D. Rieke, Magnetic properties of nanostructured materials, Chemistry of materials. 8 (1996) 1770-1783.

[85] J. Karch, R. Birringer, H. Gleiter, Ceramics ductile at low temperature (1987).

[86] B.Q. Han, E.J. Lavernia, F.A. Mohamed, Mechanical properties of nanostructured materials, Rev.Adv.Mater.Sci. 9 (2005) 1-16.

[87] J. Binner, B. Vaidhyanathan, Processing of bulk nanostructured ceramics, J European Ceram Society. 28 (2008) 1329-1339.

[88] J.R. Groza, R.J. Dowding, Nanoparticulate materials densification, Nanostructured Materials. 7 (1996) 749-768.

[89] J. Shabanian, R. Jafari, J. Chaouki, Fluidization of ultrafine powders, International Review of Chemical Engineering. 4 (2012) 16-50.

[90] L. Bergström, Colloidal Processing of ceramics, Handbook of Applied Surface and Colloidal Chemistry (2001).

[91] M.M. Kuklja, R. Pandey, Atomistic Modeling of Native Point Defects in Yttrium Aluminum Garnet Crystals, J Am Ceram Soc. 82 (1999) 2881-2886.

[92] http://global.kyocera.com/prdct/fc/list/tokusei/gousei/index.html, .

[93] C. Hammond, The basics of crystallography and diffraction, 3 ed., Oxford University Press, University of Michigan, 2009.

[94] J.F. Shackelford, R.H. Doremus, Ceramic and glass materials: structure, properties and processing, 1 ed., Springer publications, 2008.

[95] J.S. Abell, I.R. Harris, B. Cockayne, B. Lent, An investigation of phase stability in the Y2O3-Al2O3 system, J. Mater. Sci. 9 (1974) 527-537.

[96] P.A. Tanner, P. Law, L. Fu, Preformed sol-gel synthesis and characterization of lanthanide ion-doped yttria-alumina materials, physica status solidi (a). 199 (2003) 403-415.

[97] Z. Li, B. Liu, J. Wang, L. Sun, J. Wang, Y. Zhou, Z. Hu, First-principles Study of Point Defects in Stoichiometric and Non-stoichiometric Y< sub> 4 Al< sub> 2 O< sub> 9, J of Materials Science & Technology. 29 (2013) 1161-1165.

[98] http://www.chemtube3d.com/solidstate/SS-YGarnet.htm, .

[99] A.S. Gandhi, C.G. Levi, Phase selection in precursor-derived yttrium aluminium garnet and related Al2O3–Y2O3 compositions, J. Mater. Res. 20 (2005) 1017-1025.

[100] A.B. Muñoz-García, E. Anglada, L. Seijo, First-principles study of the structure and the electronic structure of yttrium aluminum garnet Y3Al5O12, Int J of Quant Chem. 109 (2009) 1991-1998.

[101] A.S. Gandhi, C.G. Levi, Phase selection in precursor-derived yttrium aluminium garnet and related $Al_2O_3$–$Y_2O_3$ compositions, J. Mater. Res. 20 (2005) 1017-1025.

[102] H. Yagi, K. Takaichi, K. Ueda, Y. Yamasaki, T. Yanagitani, A. Kaminskii, The physical properties of composite YAG ceramics, Laser Physics. 15 (2005) 1338-1344.

[103] M. Panneerselvam, G.N. Subanna, K.J. Rao, Translucent yttrium aluminum garnet: Microwave-assisted route to synthesis and processing, J. Mater. Res. 16 (2001) 2773-2776.

[104] L. Mezeix, D.J. Green, Comparison of the Mechanical Properties of Single Crystal and Polycrystalline Yttrium Aluminum Garnet, Int J App Ceramic Tech. 3 (2006) 166-176.

[105] Akio Ikesue, Yan Lin Aung,Takunori Taira, Tomosumi Kamimura, Kunio Yoshida, Gary L. Messing, Progress in Ceramic Lasers, Annu. Rev. Mater. Res. 36 (2006) 397-429.

[106] F.F. Lange, Powder Processing Science and Technology for Increased Reliability, J Am Ceram Soc. 72 (1989) 3-15.

[107] C. Li, H. Zuo, M. Zhang, J. Han, S. Meng, Fabrication of transparent YAG ceramics by traditional solid-state-reaction method, Transactions of Nonferrous Metals Society of China. 17 (2007) 148-153.

[108] X. Li, H. Liu, J. Wang, H. Cui, F. Han, X. Zhang, R. Boughton, Rapid synthesis of YAG nano-sized powders by a novel method, Mater Lett. 58 (2004) 2377-2380.

[109] S. Ramanathan, M.B. Kakade, S.K. Roy, K.K. Kutty, Processing and characterization of combustion synthesized YAG powders, Ceram. Int. 29 (2003) 477-484.

[110] B.G. Ravi, A.S. Gandhi, X.Z. Guo, J. Margolies, S. Sampath, Liquid Precursor Plasma Spraying of Functional Materials: A Case Study for Yttrium Aluminum Garnet (YAG), J. Therm. Spray Technol. 17 (2008) 82-90.

[111] S.D. Parukuttyamma, J. Margolis, H. Liu, C.P. Grey, S. Sampath, H. Herman, J.B. Parise, Yttrium Aluminum Garnet (YAG) Films through a Precursor Plasma Spraying Technique, J Am Ceram Soc. 84 (2001) 1906-1908.

[112] L. Wang, L. Zhang, Y. Fan, J. Luo, P. Zhang, L. An, Synthesis of Nd/Si Codoped YAG Powders via a Solvothermal Method, J Am Ceram Soc. 89 (2006) 3570-3572.

[113] G. Gowda, Synthesis of yttrium aluminates by the sol-gel process, J. Mater. Sci. Lett. 5 (1986) 1029-1032.

[114] J. Li, T. Ikegami, J. Lee, T. Mori, Y. Yajima, Co-precipitation synthesis and sintering of yttrium aluminum garnet (YAG) powders: the effect of precipitant, J European Ceram Society. 20 (2000) 2395-2405.

[115] J.W.G.A. Vrolijk, J.W.M.M. Willems, R. Metselaar, Coprecipitation of yttrium and aluminium hydroxide for preparation of yttrium aluminium garnet, J European Ceram Society. 6 (1990) 47-51.

[116] H. Gong, D. Tang, H. Huang, J. Ma, Fabrication of yttrium aluminum garnet transparent ceramics from yttria nanopowders synthesized by carbonate precipitation, J of Electroceramics. 23 (2009) 89-93.

[117] A. Ikesue, I. Furusato, K. Kamata, Fabrication of Polycrystal line, Transparent YAG Ceramics by a Solid-State Reaction Method, J Am Ceram Soc. 78 (1995) 225-228.

[118] L. Wen, X. Sun, Z. Xiu, S. Chen, C. Tsai, Synthesis of nanocrystalline yttria powder and fabrication of transparent YAG ceramics, J European Ceram Society. 24 (2004) 2681-2688.

[119] D. Segal, Chemical synthesis of ceramic materials, J.Mater.Chem. 7 (1997) 1297-1305.

[120] A. Pathak, P. Pramanik, Nano-Particles of Oxides through Chemical Methods, Proc. Indian National Science Academy – Physical Sciences. 67 (2001) 47-70.

[121] R.W. Jones, Fundamental principles of sol-gel technology, Institute of Metals, 1989.

[122] B. Vaidhyanathan, J. Binner, Microwave assisted synthesis of nanocrystalline YAG, J. Mater. Sci. 41 (2006) 5954-5957.

[123] M. Rajendran, M.S. Rao, Formation of BaTiO3 from Citrate Precursor, J Solid State Chemistry. 113 (1994) 239-247.

[124] A.?. Costa, L. Esposito, V. Medri, A. Bellosi, Synthesis of Nd-YAG material by citrate-nitrate sol-gel combustion route, Advanced Engineering Materials. 9 (2007) 307-312.

[125] M. Zarzecka, M.M. Bućko, J. Brzezińska-Miecznik, K. Haberko, YAG powder synthesis by the modified citrate process, J European Ceram Society. 27 (2007) 593-597.

[126] M.K. Cinibulk, Synthesis of Yttrium Aluminum Garnet from a Mixed-Metal Citrate Precursor, J Am Ceram Soc. 83 (2000) 1276-1278.

[127] L. Xianxue, W. Wenju, Nanostructured yttrium aluminum garnet powders synthesized by co-precipitation method using tetraethylenepentamine, J. Rare Earths. 27 (2009) 967-970.

[128] P. Apte, H. Burke, H. Pickup, Synthesis of yttrium aluminum garnet by reverse strike precipitation, J. Mater. Res. 7 (1992) 706-711.

[129] H. Wang, L. Gao, K. Niihara, Synthesis of nanoscaled yttrium aluminum garnet powder by the co-precipitation method, Materials Science and Engineering: A. 288 (2000) 1-4.

[130] J. Li, T. Ikegami, J. Lee, T. Mori, Y. Yajima, Co-precipitation synthesis and sintering of yttrium aluminum garnet (YAG) powders: the effect of precipitant, J European Ceram Society. 20 (2000) 2395-2405.

[131] P. Palmero, C. Esnouf, L. Montanaro, G. Fantozzi, Influence of the co-precipitation temperature on phase evolution in yttrium-aluminium oxide materials, J European Ceram Society. 25 (2005) 1565-1573.

[132] C. Marlot, E. Barraud, S. Le Gallet, M. Eichhorn, F. Bernard, Synthesis of YAG nanopowder by the co-precipitation method: Influence of pH and study of the reaction mechanisms, J of Solid State Chemistry. 191 (2012) 114-120.

[133] J.W.G.A. Vrolijk, J.W.M.M. Willems, R. Metselaar, Coprecipitation of yttrium and aluminium hydroxide for preparation of yttrium aluminium garnet, J European Ceram Society. 6 (1990) 47-51.

[134] http://departments.icmab.es/ssc/research-lines/concepcion-domingo, .

[135] http://www.nottingham.ac.uk/supercritical/scintro.html, .

[136] G. Sapkale, S. Patil, U. Surwase, P. Bhatbhage, Supercritical Fluid Extraction.

[137] A. Cabanas, J. Li, P. Blood, T. Chudoba, W. Lojkowski, M. Poliakoff, E. Lester, Synthesis of nanoparticulate yttrium aluminum garnet in supercritical water–ethanol mixtures, J of supercritical fluids. 40 (2007) 284-292.

[138] A. Sahraneshin, S. Takami, D. Hojo, T. Arita, K. Minami, T. Adschiri, Mechanistic study on the synthesis of one-dimensional yttrium aluminum garnet nanostructures under supercritical hydrothermal conditions in the presence of organic amines, CrystEngComm. 14 (2012) 6085-6092.

[139] A. Sahraneshin, S. Takami, K. Minami, D. Hojo, T. Arita, T. Adschiri, Synthesis and morphology control of surface functionalized nanoscale yttrium aluminum garnet particles via supercritical hydrothermal method, P Crystal Growth and Char Mat. 58 (2012) 43-50.

[140] X. Zhang, H. Liu, W. He, J. Wang, X. Li, R.I. Boughton, Synthesis of monodisperse and spherical YAG nanopowder by a mixed solvothermal method, J. Alloys Compounds. 372 (2004) 300-303.

[141] M. Inoue, H. Otsu, H. Kominami, T. Inui, Synthesis of yttrium aluminum garnet by the glycothermal method, J Am Ceram Soc. 74 (1991) 1452-1454.

[142] E.J. Beckman, Supercritical and near-critical CO< sub> 2 in green chemical synthesis and processing, J Supercritical Fluids. 28 (2004) 121-191.

[143] J.A. Darr, M. Poliakoff, New directions in inorganic and metal-organic coordination chemistry in supercritical fluids, Chem. Rev. 99 (1999) 495-542.

[144] C.J. Brinker, G.W. Scherer, The Physics and Chemistry of Sol–Gel Processing, Academic Press, New York ed., New York, 1990.

[145] M.N. Rahaman, Ceramic processing, Wiley Online Library, 2006.

[146] R.J. Hunter, Foundations of colloid science (POD) (2000).

[147] J.A. Lewis, Colloidal processing of ceramics, J Am Ceram Soc. 83 (2000) 2341-2359.

[148] T. Sato, R. Ruch, Stabilization of colloidal dispersions by polymer adsorption, Dekker, 1980.

[149] J.J. Guo, J.A. Lewis, Aggregation effects on the compressive flow properties and drying behavior of colloidal silica suspensions, J Am Ceram Soc. 82 (1999) 2345-2358.

[150] http://commons.wikimedia.org/wiki/File:ColloidalStability.png, .

[151] L.M. Liz-Marzán, M. Giersig, P. Mulvaney, Synthesis of nanosized gold-silica core-shell particles, Langmuir. 12 (1996) 4329-4335.

[152] A. Yethiraj, A. van Blaaderen, A colloidal model system with an interaction tunable from hard sphere to soft and dipolar, Nature. 421 (2003) 513-517.

[153] D. Houivet, J. Fallah, J. Haussonne, Dispersion and grinding of oxide powders into an aqueous slurry, J Am Ceram Soc. 85 (2002) 321-328.

[154] http://www.substech.com/dokuwiki/lib/exe/detail.php?id=stabilization_of_colloids&cache=cache&media=electric_double_layer.png, .

[155] G. Fritz, V. Schädler, N. Willenbacher, N.J. Wagner, Electrosteric stabilization of colloidal dispersions, Langmuir. 18 (2002) 6381-6390.

[156] D. Li, M.B. Müller, S. Gilje, R.B. Kaner, G.G. Wallace, Processable aqueous dispersions of graphene nanosheets, Nature nanotechnology. 3 (2008) 101-105.

[157] K.A. Appiagyei, G.L. Messing, J.Q. Dumm, Aqueous slip casting of transparent yttrium aluminum garnet (YAG) ceramics, Ceram. Int. 34 (2008) 1309-1313.

[158] Y. Lv, W. Zhang, J. Tan, Y. Sang, H. Qin, J. Hu, L. Tong, H. Liu, J. Wang, R. I Boughton, Dispersion of concentrated aqueous neodymia–yttria–alumina mixture with ammonium poly (acrylic acid) as dispersant, J. Alloys Compounds. 509 (2011) 3122-3127.

[159] X. Li, Q. Li, YAG ceramic processed by slip casting via aqueous slurries, Ceram. Int. 34 (2008) 397-401.

[160] J.S. Reed, Introduction to principles of ceramic processing, 2 ed., John Wiley publications, New York, 1938.

[161] M.B. McBride, A critique of diffuse double layer models applied to colloid and surface chemistry, Clays Clay Miner. 45 (1997) 598-608.

[162] M. Hosakawa, K. Nogi, M. Naito, T. Yokama, Nanoparticle technology handbook, Elsevier publications, 2007.

[163] W.D. Kingery, Introduction to ceramics (1960).

[164] J. Binner, B. Vaidhyanathan, K. Annapoorani, Spray Freeze Granulation of Nano Powders for Die Pressing, Adv Sci and Tech. 63 (2011) 1-6.

[165] D. Liu, J. Lin, W. Tuan, Interdependence between green compact property and powder agglomeration and their relation to the sintering behaviour of zirconia powder, Ceram. Int. 25 (1999) 551-559.

[166] N. Uchida, T. Hiranami, S. Tanaka, K. Uematsu, Spray-freeze-dried granules for ceramics fabrication, ACerS Bulletin. 81 (2002) 57-60.

[167] http://www.ceramicindustry.com/articles/ppt-improving-powders-with-freeze-granulation, .

[168] T. Moritz, A. Nagy, Preparation of super soft granules from nanosized ceramic powders by spray freezing, J Nanoparticle Res. 4 (2002) 439-448.

[169] http://o-chemapalooza.wikispaces.com/Sublimation, .

[170] W.S. Cheow, M.L.L. Ng, K. Kho, K. Hadinoto, Spray-freeze-drying production of thermally sensitive polymeric nanoparticle aggregates for inhaled drug delivery: Effect of freeze-drying adjuvants, Int. J. Pharm. 404 (2011) 289-300.

[171] X.C. Tang, M.J. Pikal, Design of freeze-drying processes for pharmaceuticals: practical advice, Pharm. Res. 21 (2004) 191-200.

[172] M. Pikal, M. Roy, S. Shah, Mass and heat transfer in vial freeze-drying of pharmaceuticals: Role of the vial, J. Pharm. Sci. 73 (1984) 1224-1237.

[173] http://www.pharmaceuticalonline.com/doc/a-guide-to-freeze-drying-for-the-laboratory-0002, .

[174] B.P. Raghupathy, J.G. Binner, Spray granulation of nanometric zirconia particles, J Am Ceram Soc. 94 (2011) 42-48.

[175] A. Ketharam, B. Vaidhyanathan, B.P.C. Raghupathy, J.G.P. Binner, Deformable granule production (2013).

[176] B.P. Raghupathy, J. Binner, Spray freeze drying of YSZ nanopowder, J Nanoparticle Res. 14 (2012) 1-15.

[177] http://www.substech.com/dokuwiki/doku.php?id=graphite_manufacturing_process,

[178] S. Strijbos, Friction between a powder compact and a metal wall., J. Powder Bulk Solids Technology. 1 (1977) 83-88.

[179] http://www.designinsite.dk/htmsider/pb1007.htm,

[180] http://what-when-how.com/materialsparts-and-finishes/isostatic-pressing/,

[181] F. Wakai, M. Yoshida, Y. Shinoda, T. Akatsu, Coarsening and grain growth in sintering of two particles of different sizes, Acta materialia. 53 (2005) 1361-1371.

[182] S.L. Kang, Sintering: densification, grain growth and microstructure, Butterworth-Heinemann, 2004.

[183] J.R. Blackford, G. Skouvaklis, M. Purser, V. Koutsos, Friction on ice: stick and slip, Faraday Discuss. 156 (2012) 243-254.

[184] V. Hlavacek, J.A. Puszynski, Chemical engineering aspects of advanced ceramic materials, Ind Eng Chem Res. 35 (1996) 349-377.

[185] H. Tanaka, A. Yamamoto, J. Shimoyama, H. Ogino, K. Kishio, Strongly connected ex situ MgB2 polycrystalline bulks fabricated by solid-state self-sintering, Superconductor Science and Technology. 25 (2012) 115022.

[186] S. Lee, E.R. Kupp, A.J. Stevenson, J.M. Anderson, G.L. Messing, X. Li, E.C. Dickey, J.Q. Dumm, V.K. Simonaitis-Castillo, G.J. Quarles, Hot Isostatic Pressing of Transparent Nd:YAG Ceramics, J Am Ceram Soc. 92 (2009) 1456-1463.

[187] http://spparks.sandia.gov/movies/normal.avi, .

[188] Z. Chen, J. Li, J. Xu, Z. Hu, Fabrication of YAG transparent ceramics by two-step sintering, Ceram. Int. 34 (2008) 1709-1712.

[189] B. Henriques, D. Soares, J. Teixeira, F. Silva, Effect of hot pressing variables on the microstructure, relative density and hardness of sterling silver (Ag-Cu alloy) powder compacts, Materials Research (2014) 0-0.

[190] S.M. Naga, M. Awaad, H.F. El-Maghraby, W.H. Eisa, M. Abou el Ezz, F. Sommer, R. Gadow, Fabrication, Microstructure and Properties of Hot-Pressed Nd:YAG Ceramics. 3 (2012) 35-40.

[191] C. Wang, X. Wang, Z. Zhao, Microstructure homogeneity control in spark plasma sintering of Al2O3 ceramics, J European Ceram Society. 31 (2011) 231-235.

[192] P. Guyot, V. Rat, J. Coudert, F. Jay, A. Maitre, N. Pradeilles, Does the Branly effect occur in spark plasma sintering?, J. Phys. D. 45 (2012) 92001-92004.

[193] D.M. Hulbert, A. Anders, D.V. Dudina, J. Andersson, D. Jiang, C. Unuvar, U. Anselmi-Tamburini, E.J. Lavernia, A.K. Mukherjee, The absence of plasma in “spark plasma sintering”, J. Appl. Phys. 104 (2008) 033305.

[194] R. Chaim, R. Marder-Jaeckel, J.Z. Shen, Transparent YAG ceramics by surface softening of nanoparticles in spark plasma sintering, Mat Sci and Eng: A. 429 (2006) 74-78.

[195] N. Frage, S. Kalabukhov, N. Sverdlov, V. Ezersky, M.P. Dariel, Densification of transparent yttrium aluminum garnet (YAG) by SPS processing, J European Ceram Society. 30 (2010) 3331-3337.

[196] S. Meir, S. Kalabukhov, N. Froumin, M.P. Dariel, N. Frage, Synthesis and densification of transparent magnesium aluminate spinel by SPS processing, J Am Ceram Soc. 92 (2009) 358-364.

[197] M. Bocanegra-Bernal, Hot isostatic pressing (HIP) technology and its applications to metals and ceramics, J. Mater. Sci. 39 (2004) 6399-6420.

[198] N. Loh, K. Sia, An overview of hot isostatic pressing, J. Mater. Process. Technol. 30 (1992) 45-65.

[199] T. Fujikawa, Y. Manabe, M. Yoneda, S. Kofune, T. Nakai, Recent trends of HIP equipment technology in Japan (2004) 27-31.

[200] T. Sato, S. Imaeda, K. Sato, Thermal transformation of yttrium hydroxides to yttrium oxides, Thermochimica Acta. 133 (1988) 79-85.

[201] A. Ikesue, K. Kamata, Microstructure and Optical Properties of Hot Isostatically Pressed Nd:YAG Ceramics, J Am Ceram Soc. 79 (1996) 1927-1933.

[202] M. Blosi, S. Albonetti, M. Dondi, A. Costa, M. Ardit, G. Cruciani, Solâ€“gel combustion synthesis of chromium doped yttrium aluminum perovskites, J. Sol Gel Sci. Technol. 50 (2009) 449-455.

[203] J. Tsay, T. Fang, Effects of Molar Ratio of Citric Acid to Cations and of pH Value on the Formation and Thermal-Decomposition Behavior of Barium Titanium Citrate, J Am Ceram Soc. 82 (1999) 1409-1415.

[204] Q. - Lu, W. - Dong, H. - Wang, X. - Wang, - A Novel Way to Synthesize Yttrium Aluminum Garnet from Metal- Inorganic Precursors, - J Am Ceram Soc. - 85 (2002) - 490-- 492.

[205] M. Shojaie-Bahaabad, E. Taheri-Nassaj, Economical synthesis of nano alumina powder using an aqueous sol–gel method, Mater Lett. 62 (2008) 3364-3366.

[206] M. Alvarez, E.H. Rueda, E.E. Sileo, Simultaneous incorporation of Mn and Al in the goethite structure, Geochim. Cosmochim. Acta. 71 (2007) 1009-1020.

[207] L.J. Beckham, W.A. Fessler, M.A. Kise, Nitrosyl Chloride, Chemical Reviews. 48 (1951) 319-396.

[208] J. Livage, M. Henry, C. Sanchez, Sol-gel chemistry of transition metal oxides, Progress in Solid State Chemistry. 18 (1988) 259-341.

[209] J. Livage, The gel route to transition metal oxides, J of Solid State Chemistry. 64 (1986) 322-330.

[210] Y. Zhang, J. Binner, C. Rielly, B. Vaidhyanathan, Comparison of spray freeze dried nanozirconia granules using ultrasonication and twin-fluid atomisation, J European Ceram Society. 34 (2014) 1001-1008.

[211] P. - Chen, I. - Chen, - Sintering of Fine Oxide Powders: I, Microstructural Evolution, - J Am Ceram Soc. - 79 (1996) – 3129 - 3141.

[212] http://www.shimadzu.eu/sites/default/files/ftir_talkletter_vol_19.pdf, .

[213] E. Alizadeh-Gheshlaghi, B. Shaabani, A. Khodayari, Y. Azizian-Kalandaragh, R. Rahimi, Investigation of the catalytic activity of nano-sized CuO, Co3O4 and CuCo2O4 powders on thermal decomposition of ammonium perchlorate, Powder Technol. 217 (2012) 330-339.

[214] X. Li, W. Wang, Preparation of uniformly dispersed YAG ultrafine powders by co-precipitation method with SDS treatment, Powder Technol. 196 (2009) 26-29.

[215] J. Su, Q.L. Zhang, C.J. Gu, D.L. Sun, Z.B. Wang, H.L. Qiu, A.H. Wang, S.T. Yin, Preparation and characterization of Y3Al5O12 (YAG) nano-powder by co-precipitation method, Mater. Res. Bull. 40 (2005) 1279-1285.

[216] L. Ojamäe, C. Aulin, H. Pedersen, P. Käll, IR and quantum-chemical studies of carboxylic acid and glycine adsorption on rutile TiO2 nanoparticles, J. Colloid Interface Sci. 296 (2006) 71-78.

[217] G. Xia, S. Zhou, J. Zhang, J. Xu, Structural and optical properties of YAG:Ce3+ phosphors by sol–gel combustion method, J. Cryst. Growth. 279 (2005) 357-362.

[218] F.V. Motta, A.P.A. Marques, M.T. Escote, D.M.A. Melo, A.G. Ferreira, E. Longo, E.R. Leite, J.A. Varela, Preparation and characterizations of Ba0.8Ca0.2TiO3 by complex polymerization method (CPM), J. Alloys Compounds. 465 (2008) 452-457.

[219] J. Li, Y. Pan, F. Qiu, Y. Wu, J. Guo, Nanostructured Nd:YAG powders via gel combustion: The influence of citrate-to-nitrate ratio, Ceram. Int. 34 (2008) 141-149.

[220] J.R. van Ommen, J.M. Valverde, R. Pfeffer, Fluidization of nanopowders: a review, J Nanoparticle Res. 14 (2012) 1-29.

[221] P. Vaqueiro, M. Arturo Lopez-quintela, Synthesis of yttrium aluminium garnet by the citrate gel process, J. Mater. Chem. 8 (1998) 161-163.

[222] H.A. Painter, J.E. Loveless, Effect of temperature and pH value on the growth-rate constants of nitrifying bacteria in the activated-sludge process, Water Res. 17 (1983) 237-248.

[223] J. Groeneweg, B. Sellner, W. Tappe, Ammonia oxidation in nitrosomonas at NH3 concentrations near km: Effects of pH and temperature, Water Res. 28 (1994) 2561-2566.

[224] A. Abdel-Halim, Y.K. Afifi, N. Afify, Effects of drying conditions on thermal decomposition behaviour of $UO_3$ gel microspheres, J of Thermal Analysis and Calorimetry. 32 (1987) 1071-1079.

[225] H. Qiu, L. Gao, C. Feng, J. Guo, D. Yan, Preparation and characterization of nanoscale Y-TZP powder by heterogeneous azeotropic distillation, J of Materials Science. 30 (1995) 5508-5513.

[226] Z. Chen, Y. Yang, Z. Hu, J. Li, S. He, Synthesis of highly sinterable YAG nanopowders by a modified co-precipitation method, J. Alloys Compounds. 433 (2007) 328-331.

[227] P.d.S. Santos, A.C.V. Coelho, H.d.S. Santos, P.K. Kiyohara, Hydrothermal synthesis of well-crystallised boehmite crystals of various shapes, Materials Research. 12 (2009) 437-445.

[228] P. Bai, P. Wu, G. Zhao, Z. Yan, X. Zhao, Cation–anion double hydrolysis derived mesoporous γ-Al2O3 as an environmentally friendly and efficient aldol reaction catalyst, J.Mater.Chem. 18 (2007) 74-76.

[229] M. Nyman, L.E. Shea-Rohwer, J.E. Martin, P. Provencio, Nano-YAG: Ce mechanisms of growth and epoxy-encapsulation, Chemistry of Materials. 21 (2009) 1536-1542.

[230] R. Greenwood, Review of the measurement of zeta potentials in concentrated aqueous suspensions using electroacoustics, Adv. Colloid Interface Sci. 106 (2003) 55-81.

[231] L. Zhao, L. Gao, Fabrication and surface characterization of NH< sub> 4 PAA-stabilized HAZ suspensions, J. Colloid Interface Sci. 262 (2003) 428-434.

[232] I. Santacruz, K. Anapoorani, J. Binner, Preparation of high solids content nanozirconia suspensions, J Am Ceram Soc. 91 (2008) 398-405.

[233] J. Besida, D.E. Dunstan, G.V. Franks, , Ceramic and Metallic Components and Methods for Their Production from Flexible Gelled Materials (2005).

[234] S.P. Simner, J.F. Bonnett, N.L. Canfield, K.D. Meinhardt, J.P. Shelton, V.L. Sprenkle, J.W. Stevenson, Development of lanthanum ferrite SOFC cathodes, J. Power Sources. 113 (2003) 1-10.

[235] J. Huie, C. Dudding, J. McCloy, Polycrystalline yttrium aluminum garnet (YAG) for IR transparent missile domes and windows. 6545 (2007) 65450E.

[236] A.J. Stevenson, X. Li, M.A. Martinez, J.M. Anderson, D.L. Suchy, E.R. Kupp, E.C. Dickey, K.T. Mueller, G.L. Messing, Effect of SiO2 on densification and microstructure development in Nd: YAG transparent ceramics, J Am Ceram Soc. 94 (2011) 1380-1387.

[237] M. Mazaheri, A. Zahedi, S. Sadrnezhaad, Two-Step Sintering of Nanocrystalline ZnO Compacts: Effect of Temperature on Densification and Grain Growth, J Am Ceram Soc. 91 (2008) 56-63.

[238] J. Eichler, J. Rödel, U. Eisele, M. Hoffman, Effect of Grain Size on Mechanical Properties of Submicrometer 3Y-TZP: Fracture Strength and Hydrothermal Degradation, J Am Ceram Soc. 90 (2007) 2830-2836.